THE UNIVERSITY
of EDINBURGH

THE UNIVERSITY of EDINBURGH

Human Neutrophil Elastase Phenotyping: Classifying Neutrophils by Function with Novel Imaging Agents

Thane Allardyce Campbell

Doctor of Philosophy with Integrated Study

Optical Medical Imaging with Healthcare Innovation and Entrepreneurship

The University of Edinburgh and The University of Strathclyde
in collaboration with GlaxoSmithKline

2019

DECLARATION

I can confirm that this work is entirely of my own authorship. The work represents experiments and studies undertaken by me, whilst working in a multidisciplinary team whose contributions have been clearly indicated. None of this work has been submitted previously for any degree or qualification, at any university, except the contributions of Filip Angelov submitted for the BSc. in Biomedical Sciences (Hons) at the University of Napier.

In accordance with the University of Edinburgh's dissertation regulations, this thesis does not exceed 100, 000 words and I am the author of all published work included in this thesis.

Thane Campbell ……..

Date ……

DEDICATION

For Jesus, my family, Winston and Barbara, my parents, Winston, my brother and Christy Ringrose.

Exodus 18:5-27: Jethro, Moses' father-in-law, together with Moses' sons and wife, came to him in the wilderness, where he was camped near the mountain of God. Jethro had sent word to him, "I, your father-in-law Jethro, am coming to you with your wife and her two sons." So Moses went out to meet his father-in-law and bowed down and kissed him. They greeted each other and then went into the tent. Moses told his father-in-law about everything the LORD had done to Pharaoh and the Egyptians for Israel's sake and about all the hardships they had met along the way and how the LORD had saved them. Jethro was delighted to hear about all the good things the LORD had done for Israel in rescuing them from the hand of the Egyptians. He said, "Praise be to the LORD, who rescued you from the hand of the Egyptians and of Pharaoh, and who rescued the people from the hand of the Egyptians. Now I know that the LORD is greater than all other gods, for he did this to those who had treated Israel arrogantly." Then Jethro, Moses' father-in-law, brought a burnt offering and other sacrifices to God, and Aaron came with all the elders of Israel to eat a meal with Moses' father-in-law in the presence of God. The next day Moses took his seat to serve as judge for the people, and they stood around him from morning till evening. When his father-in-law saw all that Moses was doing for the people, he said, "What is this you are doing for the people? Why do you alone sit as judge, while all these people stand around you from morning till evening?" Moses answered him, "Because the people come to me to seek God's will. Whenever they have a dispute, it is brought to me, and I decide between the parties and inform them of God's decrees and instructions." Moses' father-in-law replied, "What you are doing is not good. You and these people who come to you will only wear yourselves out. The work is too heavy for you; you cannot handle it alone. Listen now to me and I will give you some advice, and may God be with you. You must be the people's representative before God and bring their disputes to him. Teach them his decrees and instructions, and show them the way they are to live and how they are to behave. But select capable men from all the people—men who fear God, trustworthy men who hate dishonest gain—and appoint them as officials over thousands, hundreds, fifties and tens. Have them serve as judges for the people at all times, but have them bring every difficult case to you; the simple cases they can decide themselves. That will make your load lighter, because they will share it with you. If you do this and God so commands, you will be able to stand the strain, and all these people will go home satisfied." Moses listened to his father-in-law and did everything he said. He chose capable men from all Israel and made them leaders of the people, officials over thousands, hundreds, fifties and tens. They served as judges for the people at all times. The difficult cases they brought to Moses, but the simple ones they decided themselves.

Then Moses sent his father-in-law on his way, and Jethro returned to his own country.

ABSTRACT

This thesis describes approaches taken to classify the functionally diverse neutrophil by its different functions in a live-cell imaging tool. Human neutrophil elastase (HNE) cleaves over 30 substrates, its release is controlled with varying extents of degranulation and its activity is subject to complex modulation. HNE regulation is necessary for the maintenance of health via HNE's multiplicity of functions. Although neutrophils are routinely quantified in assessments of chronic inflammation, we do not have a clinically translatable, integrated tool for measuring HNE in human tissues. Two novel probes have been characterised and multiplexed to form the basis of an imaging technique for understanding the functional implications of neutrophil activity in human tissues, in real-time. Neutrophil Activation Probe (NAP) and VE200 are novel probes for HNE activity and presence. These probes are characterised *in vitro* as sensitive and HNE-specific imaging agents for live-cell imaging and image cytometry.

Multiplexed NAP and HNE are detect neutrophil activation, apoptosis and necrosis. These imaging agents can inform deep profiling techniques to separate neutrophils into untreated, primed, activated and primed-activated states and endogenous vs. exogenous stimulus sub-states. Finally, sections of adenocarcinomatous human lung and whole human lungs, ventilated *ex vivo,* demonstrate the applicability of HNE-based, multiparametric profiling and neutrophil activation detection to clinically relevant platforms.

LAY SUMMARY

Chronic inflammatory diseases can vary so much that it's not always clear which treatment is most appropriate. Sorting patients into the right treatment groups is called patient stratification. The body's white blood cells, work together to respond to disease appropriately, restore health and keep us immune to diseases, they may be a reliable source of patient stratification and disease monitoring information. Extracting this information means accessing diseased tissues, finding white blood cells and understanding their activity. We can use optic fibres as microscopes to do this.

My research describes two new reagents that make neutrophils light-up so that we can count and describe them. These reagents provide clear and sensitive measurements, telling us when neutrophils are activated to fight disease. Just counting neutrophils is already useful in patient stratification. But the enzyme that these reagents interact with is so carefully controlled that it can show us different patterns of light. I found that there was enough information in these images to organise neutrophils into different groups. This means that we can understand what different groups of neutrophils are responding to. These findings may be useful in a range of contexts: Biologists may use them to describe how neutrophils respond to a change, pharmacologists, to describe how neutrophils respond to a drug and clinicians for patient stratification. Further work will be needed to understand how these findings apply to different contexts.

ACKNOWELDEGMENTS

I am sincerely grateful to Professor Kev Dhaliwal, my primary supervisor, tirelessly ambitious in paving the way for many. I am sincerely grateful to Professor Mark Bradley, my second supervisor, leader of the PROTEUS project and a man of inspiring standards. Without Professors Dhaliwal and Bradley none of this would have been possible. Emma Scholefield, Dr. John Marwick and Dr. Trudi Gillespie provided the most patient and practical instructions I received at the bench. Dr. Vikki Evans' enduring determination lead to novel probe synthesis, laying the foundation for much of this work. I would like to thank Dr. Augustine Amour, Dr. Pillar Royo-Jimenez and Dr. Malcolm Begg of GlaxoSmithKline for their technical supervision, penetrating insights and for encouraging innovation.

Dr. Bertrand Vernay gave me fantastic advice, training and assistance in image analysis. Filip Angelov showed great potential at the bench and in an image analysis, it was a privilege to supervise his indomitably passionate work. Thank you to Dr. Adam Marshall, Dominic Norberg and Irene Young for assistance in imaging human lungs and Dr. David Dorward for providing the lung adenocarcinoma tissue slices. Dr. Utsa Karmakar and Dr. Patricia Dos Santos Coelho are skilled and selfless phlebotomists. Pat and Utsa, thank you for being reliable and generous friends. Lyndsey Boswell's technical expertise was instrumental in acquiring the immunohistological data. The Shared University Research Facilities, the Flow Cytometry and Cell Sorting and the Confocal and Advanced Light Microscopy facilities were all essential to this project. Thank you to Dr. Shona Johnstone, Dr. Rolly Weigand, Dr. Will Ramsay and Dr. Mari Pattison. Thank you, Dr. Yi Feng for generously sharing your image analysis software.

I am indebted to Dr. Sonja Vermeren, Professor Ian Dransfield and Professor Adriano Rossi, for sharing unparalleled practical and theoretical insights into neutrophil biology. Thank you, Dr. Tom Craven, Dr. Ahsan Akram, Dr. Calum Ross and Dr. Beth Mills, for their assistance and most of all for your friendship. Dr. Alistair Hayes, a good friend, recommended pivotal data mining software.
Dr. Jean O'Donohughe and Dr. Kirsty Ross made OPTIMA possible with wisdom and encouragement. Thank you to each member of PROTEUS and OPTIMA and the Centre of Inflammation Research, Queen's Medical Research Institute.

ABBREVIATIONS

α-1-PI: alpha-1-protease inhibitor

AAPV-pNA: colourimetric HNE substrate

ARDS: acute respiratory distress syndrome

CG: Cathepsin G

EVLV: *ex vivo* lung ventilation

FCE: fibred confocal endomicroscopy

FLIM: fluorescence lifetime imaging

FLIM: Fluorescence lifetime microscopy

fMLF: N-formylmethionine leucyl-phenylalanine

FMT: Fluorescence molecular tomography

FSC: Forward Scatter

HBSS: Hanks buffer salt solution

HEPES: N-2-Hydroxyethylpiperazine-N-2-Ethanesulfonic Acid

HNE: Human Neutrophil Elastase

IL8: Interleukin 8

LDA: Linear discriminants analysis

LPS: Lipopolysaccharide

LTB4: leukotriene B4

mHNE: membranous Human Neutrophil Elastase

AAPV-AMC – coumarin-labelled HNE substrate

NAP: Neutrophil activation probe

NET: Neutrophil extracellular trap

OEM: Optical endomicroscopy

OI: Optical imaging

PAF: Platelet activating factor, β-Acetyl-γ-O-hexadecyl-L-α-phosphatidylcholine hydrate

PBMC – Peripheral blood mononuclear cell

PBS: phosphate buffer saline

PCA: Principle components analysis

PFA: Paraformaldehyde

PMN: polymorphonuclear cell

PR3: Proteinase 3

RFU: Relative fluorescence units

ROS: reactive oxygen species

SD: standard deviation

SEM: Standard error of the mean

SSC: Side scatter

TAN: Tumour associated neutrophils

TLR: Toll-like Receptor

TPR: True Positive Rate

VE200: HNE-targeted probe (the 200th synthetic attempt of Dr. Vikki Evans)

PUBLICATIONS AND LICENSES

I have contributed, as a joint-first author, to the following article:
Birch, G., Campbell, T., Bradley, M. and Dhaliwal, K., 2019. Optical molecular imaging of inflammatory cells in interventional medicine-an emerging strategy. *Frontiers in Oncology*, *9*, p.882.

Licenses to reuse figures and tables in this thesis from other published works were granted under Creative Commons 3.0 or 4.0 licences or obtained through the Copyright Clearance Centre's RightsLink Service or directly from the publisher. All reused figures and tables have appropriate permissions and are acknowledged in the corresponding legend.

TABLE OF CONTENTS

Chapter 5: HNE Imaging as a Neutrophil Stratification Tool in the Human Lung 167

5.0.0 Introduction,,,

LIST OF FIGRUES

LIST OF TABLES

CHAPTER 1:
INTRODUCTION TO NEUTROPHIL BIOLOGY AND IMAGING

1.1.0 BRIEF HISTORY OF NEUTROPHIL DISCOVERIES

Since its discovery in 1882, by the Russian biologist Ilyia Metchnikoff, the neutrophil has been under constant scrutiny. Inserting rose thorns into starfish, Metchnikoff discovered cells engulfing the distal end of his instrument, which he divided into macrophages and microphages based on their size and phagocytic function. Microphages would later come to be known as neutrophils, and in addition to phagocytosis, many more functions would be revealed as the cellular components of the immune system were classified. With this initial taxonomic step neutrophil biology began, setting the stage for subsequent discoveries. For his pioneering work, Metchnikoff is regarded as the father of natural immunity. 137 years later we have learned much about neutrophil phagocytosis, degranulation, extravasation, apoptosis, necrosis, NETosis and more. The neutrophil has a diverse array of functions, elicited in various activation states, making paradoxical contributions both to health and disease. Neutrophil priming was discovered in 1984 when Guthrie *et al.* added this pre-activated and activation-augmenting state to those known prior: quiescence, activation, apoptosis and necrosis.[1] Neutrophil NETosis, an evolutionarily ancient means of weaponising DNA, was only discovered in 2004 by Brinkman *et al.*, and has gained mechanistic importance in several disease processes since then.[2] Today we know far more about the neutrophil than Metchnikoff did and this leaves greater challenges of knowledge organisation and integration incumbent on the immunologist. Basic and translational research are co-dependent, synergistic disciplines and the recent ten-year commitment to "Transforming UK Translation" of The Wellcome Trust, The Royal Academy of

Engineering, The Royal Society and The Academy of Medical Sciences emphasizes the need for the latter. Many “new” therapies exploit the same mechanisms as existing drugs.[3] And yet immunological research is one of many scientific disciplines which are advancing simultaneously and thereby creating opportunities to harness neutrophil biology for truly innovative therapeutic interventions. Image cytometry has realised previously unimaginable rates of learning from large biological datasets. Machine-learning techniques may provide tools of sufficient sophistication to characterise the pleiotropic set of neutrophil behaviours. With such a taxonomy, neutrophil states could be classified in real-time, using molecular imaging, in the changing inflammatory milieu of the patient. Numerous studies have demonstrated the prognostic power of simple neutrophil enumeration.[4–9] A qualitative understanding of each neutrophil in a population is the logical consequence of neutrophil enumeration, refining quantitation with precision that may enhance its application in academic research, drug development and clinical trials. I sought to create this precise tool by leveraging the informative pleiotropism of human neutrophil elastase (HNE), visualized using two novel imaging probes, synthesized in house.

1.1.1 NEUTROPHILS

Their capacities to respond *en masse* and rapidly, underscore their potential as biomarkers, capable of producing large readouts in short time-frames – properties that are particularly desirable for surgical guidance and drug development assays. The relatively short neutrophil half-life acts to limit any off-target consequences of labelling to timeframes of days or hours whilst the persistence of the neutrophilic influx in inflamed tissues, makes neutrophil readouts useful over the entire disease monitoring period, irrespective of its duration. Overall, neutrophil imaging creates an ideal paradigm for patient-specific disease monitoring and intervention.

1.1.2 NEUTROPHIL RECRUITMENT

Circulating neutrophils can be divided into circulating and marginated pools as the Wintrobe group first demonstrated. The finding that nearly 50% of ^{32}P-labelled, autologous neutrophils disappear from circulation following infusion lead the group to postulate technical errors or redistribution of infused neutrophils between the circulation and an additional pool.[10] Subsequent work demonstrated that the missing neutrophils could be restored to the circulation with the addition of adrenaline, providing good support for the margination of infused neutrophils.[11] The release of neutrophils from marginated pools into the systemic circulation helps to explain their accumulation at an inflammatory site and sustained numbers in circulation following recruitment, a processes that classically follows five phases. With respect to the endothelium, recruited neutrophils are first captured, that is they form initial attachment, before executing rolling adhesion, firm adhesion -

accompanied by cell spreading, crawling motility and finally transmigration. Following transmigration into the tissue, the neutrophil may be exposed to a range of pro-inflammatory stimuli which lead to neutrophil activation and the sequelae thereof. The range of chemoattractants, their combination with different humoral factors and the specialisations of different marginated pools may each contribute to detectable differences in recruited neutrophils. Quantifying these differences could enable data-driven classification of phenotypes and reveal the recruiting conditions.

During rolling adhesion, the majority of leukocytes can withstand sheer stresses of 1 dyn/cm^{-2}. Neutrophils have a unique capacity to withstand up to 10 dyn/cm^{-2} during rolling adhesion, and 30 dyn/cm^{-2} in the presence of P-selectin. To achieve such sheer stress resistance neutrophils have a range of strategies. Flattening out increases adhesion molecule engagement, and neutrophils employ more selectins. Selectin “catch-bonds” are strengthened by increased sheer stress.[12] Finally neutrophils employ specialised membranous protrusions: slings and tethers, increasing the force of their adhesion and slowing rolling motility at high sheer stress.[13,14]

1.1.3 EXTRAVASATION

A critical role for HNE in neutrophil biology is extracellular matrix (ECM) digestion, allowing neutrophils to leave the blood space, enter the tissue space and effect their characteristic pro-inflammatory roles. This is extravasation and it makes use of HNE's unusual multiplicity of targets and plasma membrane affinity, simultaneously. Neutrophil extravasation, or transendothelial migration, can take paracellular[15] or transcellular[16] forms moving between or through endothelial cells respectively. HNE is localized to the leading edge of transmigrating neutrophils[17] where it cleaves intercellular adhesion molecules[18] and ECM components including elastin, laminins, decorin, collagens and fibronectin.[19–25] These proteolytic events allow neutrophils to traverse the ECM but also produce a range of neutrophil, monocyte and macrophage chemoattractants[24,26–28] and release vascular endothelial growth factor.[29]

Under the influence of a chemotactic gradient neutrophils use high affinity chemokine receptors to move towards a chemoattractant source and low affinity receptors to halt chemotaxis.[30] However, neutrophils execute different migration patterns with chemoattractant specificity. Leukotriene B4 (LTB4) and fMLF elicit highly directional neutrophil migration, so called convergent migration, as it facilitates rapid convergence on the source of chemoattractant. LTB4 is released in a paracrine fashion, increasing the number of migrating neutrophils and their overall migratory distance.[31] LTB4 stimulation also promotes paracrine LTB4 release and the resultant positive feedback loops are important in facilitating neutrophil

swarming motility.[32] C5a and IL8 however, stimulate a more meandering, divergent, chemotaxis. Convergent and divergent migration are chemokine concentration-independent processes. Neither convergence or divergence are precipitated by one signalling cascade but by more complex mechanisms that allow signal integrations and modulated receptor expression in the presence of competing chemokines.[33] Competing chemokinetic signals are integrated hierarchically as signalling from certain chemokines supervenes that of others. Unlike platelet-activating factor (PAF) receptors, fMLF receptors are stored in mobilisable intracellular pools and their increased expressions enable fMLF signalling to become dominant in a PAF-laden milieu.[34] Whereas convergent migration may be expected of neutrophils seeking a bacterial target, divergent migration may serve a more exploratory/surveillance function.[31] Convergent and divergent migration and dynamic chemokinetic signal processing demonstrate the neutrophil's ability to employ detectable behaviours with stimulus specificity.

1.1.4 NEUTROPHIL LIFESPAN

The view that neutrophils circulate with a half-life of 6-8 hours under normal physiological conditions, is widely-held and yet in a seminal report (Mauer *et al.* 1960) neutrophils were labelled with a reagent which was both radioactive and a structural analogue of the nerve gas, sarin.[10] More early support for the 6-8 hour half-life came from studies of neutrophils following allogeneic blood transfusion.[35] In 1971, Dresch, Najean and Beauchet reported that the sarin analogue, $DF^{32}P$ has

the cytotoxic effect of reducing neutrophil half-life.[36] Pillay *et al.* reported a 90 hour half-life claiming that such extensive lifespans can only be observed using *in vivo* methods.[37] However off-target labelling can confound *in vivo* measurements and Pillay *et al.*'s work has been criticised as an over-estimate of neutrophil half-life by labelling bone-marrow neutrophils.[38] Neutrophils can become primed by a variety of methods for their isolation from whole-blood and so differences in measured half-lives may be methodological in origin.[39] Indeed, in their 2013 review of neutrophil lifespan studies from 1960 to 2010 Tak *et al.* decry a variety of methodological limitations confounding reported half-life measurements, from toxic neutrophil labels, to manipulative *ex vivo* conditions, to uncertainty between measurements arising from the systemic circulation and the bone marrow.[40] More conclusive work on the *in vivo* lifespan of neutrophils is required to establish this fundamental question of neutrophil kinetics and thanks to a wealth of fluorescent neutrophil labelling techniques (discussed in **1.3.2 Neutrophil Imaging Probes**) this data may not take another fifty years to acquire. In the field of neutrophil kinetics, it is well accepted that neutrophil lifespan extends several-fold following neutrophil activation, in response to various endogenous and exogenous stimuli.[41]

1.1.5 NEUTROPHIL ACTIVATION

Circulating in a quiescent state, neutrophils become partially activated on transmigration through the vascular endothelium. Upon activation neutrophils gain, pinocytic, phagocytic, degranulating and NET-releasing functions. If neutrophils are exposed to priming and subsequent activating stimuli their activation-dependent functions are augmented. Neutrophils detect activating stimuli through numerous cell-surface receptors which are comprehensively reviewed by Futosi *et al.*[42] Briefly these include receptors for pathogen-associated molecular patterns, opsonization, chemokines, cell signalling and complement. Neutrophils also express a range of intracellular receptors sensitive to nucleotides and viral RNA.[43,44] Receptor occupancy activates intracellular signalling leading neutrophils to execute their effector functions. Neutrophil activation has been described in sterile and non-sterile inflammatory paradigms.

1.1.6 HNE RELEASE IN STERILE INFLAMMATION

Although commonly considered in its pathogen-response paradigm, the immune system also responds to sterile host-tissue damage. In fact, recent research indicates that host-tissue damage may be necessary for the neutrophil response to bacterial infection.[45] In under an hour, neutrophils, responding to a diffusion of lytic cell contents or a fragmenting extracellular matrix, begin infiltrating damaged tissue.[25,46] These chemoattractant factors are known as damage associated molecular patterns (DAMPs), a diverse and growing number of molecules capable of

stimulating leukocyte recruitment including adenosine, mitochondrial formylated peptides and collagen fragments. Instead of traversing the parenchyma or interstitium, their intravascular migration allows neutrophils to approach the damaged lesion.[46] Extravasation can incur collateral host-tissue damage and sustained intravascular migration mitigates this effect.[46] Similarly, DAMPs and paracrine signalling help neutrophils to accumulate, even swarm, at sites of injury, away from healthy tissue.[32]

However neutrophil swarming does not prevent reverse transmigration, as these cells re-enter the systemic circulation and become widely dispersed throughout the body. Endogenous LTB4, which facilitates swarming, can also lead to reverse-transmigration by promoting HNE-mediated proteolysis of intercellular adhesion molecules (JAM-C).[18] The dissemination of activated neutrophils to multiple organs via reverse transmigration can have wide-spread, deleterious effects on healthy tissue. The Nourshargh group found that injecting LTB4 into mouse cremaster muscles lead to neutrophil accumulation and organ damage in the lungs, heart and liver.[18] Increased plasma HNE, LTB4 and soluble JAM-C may implicate this mechanism of deleterious neutrophil dissemination in several sterile inflammatory diseases, including trauma-induced secondary acute respiratory distress syndrome, rheumatoid, psoriatic and osteoarthritis and systemic sclerosis.[47–50]

The heterogeneous causes of sterile inflammation can result in varying neutrophil responses. Dry-eye disease, atherosclerosis and lung cancer represent three distinct patterns of sterile inflammation in which HNE serves pathological and reparative

functions. In dry-eye disease HNE's reparative mucin stimulation is overwhelmed by HNE-rich neutrophil NETs, a key pathological factor as demonstrated by Mun *et al.*'s recent clinical trial.[51–54] In atherosclerosis neutrophil infiltration occurs soon after fatty streak deposition and persists. Unfortunately increased neutrophil count in atheroma is a negative prognostic indicator with HNE promoting plaque destabilisation and pathological neovascularisation.[55,56] In various solid tumours neutrophils may demonstrate anti- and pro-tumorigenic phenotypes, N1 and N2 respectively.[57] Although the existence of these two phenotypes in humans is contested as an oversimplification, the extremes of a spectrum of activated neutrophils.[57] Supraphysiological HNE concentrations may kill cancer cells, however in lung cancer HNE alleviates growth-inhibiting signals and promotes metastasis.[58,59]

1.1.7 HNE RELEASE IN NON-STERILE INFLAMMATION

To detect pathogen associated molecular patterns neutrophils have pattern recognition receptors such as the toll-like receptors (TLRs). The well characterized LPS-TLR4 interaction precipitates increased TLR4 expression, ROS production, pinocytosis, phagocytosis and degranulation.[60] Following TLR4 occupancy neutrophils engulf bacteria, forming the intracellular phagosome. Lysosomes and azurophil granules fuse with the phagosome forming the phagolysosome which undergoes proton-pump-mediated alkalinisation reaching an optimal pH range (pH 8.5-9.0) for HNE activity.[61] Phagolysosomal alkalinisation depends on potassium ion influx and this also results in phagolysosomal hypertonicity which displaces HNE

from anionic sulphonated proteoglycans.[62] Dispersed through the alkaline phagolysosome HNE accesses and degrades microbes with maximal efficiency. Interestingly LPS exposure also facilitates hierarchical chemotaxis by preventing chemotaxis in response to C5a, IL8 and LTB4 and not fMLF.[63]

Phagocytosis is not the only antimicrobial process which employs HNE activity. HNE is degranulated into the extracellular space and weaponizes ejected DNA in antimicrobial NETosis. Early in NETosis HNE translocates to the nucleus to cleave histones, decondensing chromatin.[64] Following chromatin decondensation, the nuclear envelope disintegrates forming a chain of vesicles which deteriorate to allow positively charged proteases like HNE to associate with negatively charged chromatin.[65] Neutrophils then round up and contract until the cell membrane ruptures allowing the intracellular homogenate to erupt and spread from this focal point. With associated endothelial cell toxicity in vitro, NETs may represent a high-risk strategy for antimicrobial defence which requires careful regulation.[66] The Papayanopulous group have demonstrated that when pathogens are too large for phagocytic clearance, the absence of phagosomes is detected in a dectin-1 mediated fashion. HNE not sequestered to the phagolysosome translocates to the nucleus leading to NETosis.[64] However Papayanopulous *et al.* do not explain how NETs are produced in the presence of smaller targets such as Staphylococcus aureus.[67] Since its discovery in 2004 there are at least two forms of NETosis, suicidal and vital and work to more clearly describe NETotic mechanisms is ongoing.[67,68]

1.2.0 FLUORESCENCE

Aleksander Jablonski first proposed the schematic illustration known as the "Jablonski Diagram" in 1933 to describe the electronic states of a molecule and its transitions between them. Molecules have a ground state (S_0) and excited states (S_1 – S_n). Each state subdivides into vibrational levels. Energy entering the system as light is absorbed (a), driving electrons into higher energy excited states, but excited electrons will return to the ground state. Between vibrational levels of an excited state electrons may lose energy as heat or movement via internal conversion (d). Internal conversion can explain the descent of electrons from higher to lower energy excited states and electrons can return to the ground state via non-radiative transitions (b). When an electron is in the lowest vibrational level of the lowest excited state it may lose energy as fluorescence (c) returning to (any of the vibrational levels of) the ground state. The range of ground state vibrational levels an electron may fall to explains the flourescence specturm of a given molecule, as photons of various wavelengths are released as a consequence.

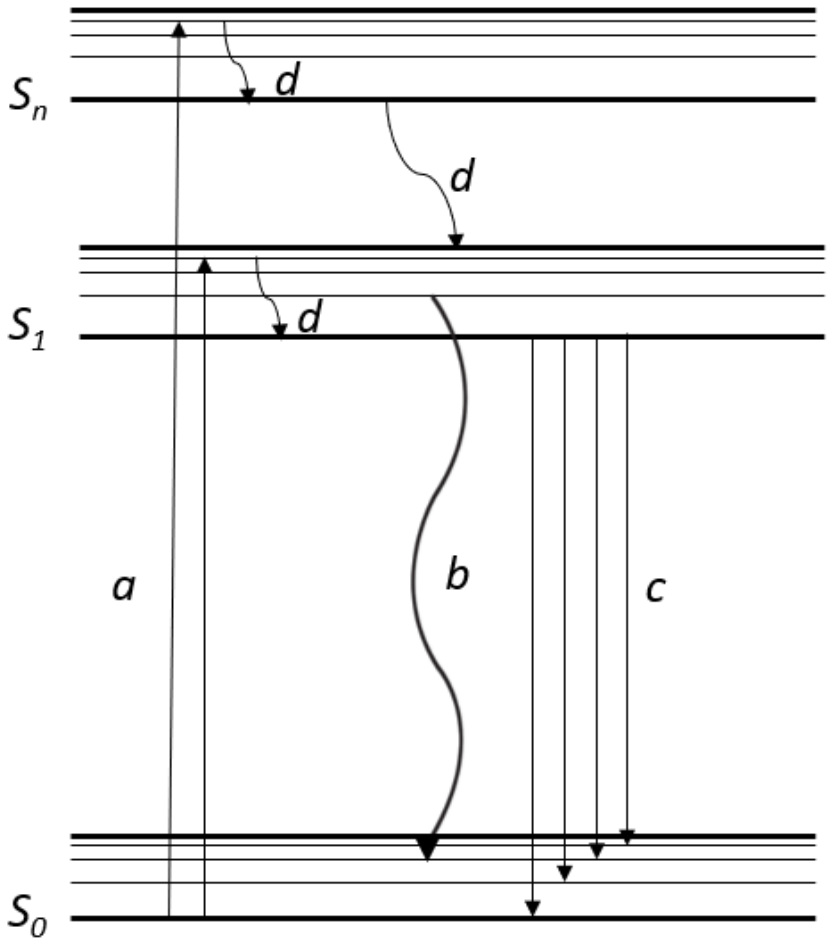

Figure 1.1 Energy Transitions of Fluorescence
An adapted Jablonski diagram shows light absorption (a), non-radiative transition (b) and light emission (c) internal conversion (d) and thte electronic states (S_0 -S_n).

Hence absorption (a), non-radiative transitions (such as internal conversion) and fluorescence emission help to explain the effects of incident light on a fluorescent molecule. Importantly, in single photon imaging techniques, emission photons always have less energy than excitation photons and hence emitted light is longer in wavelength than absorbed light. This helps to design multispectral imaging protocols without exciting multiple fluorophores with a single excitation laser.

1.2.1 OPTICAL IMAGING

Biological research uses fluorescent proteins and fluorophore-conjugated antibodies, it combines imaging and fluorescence sensing techniques, and so it relies heavily on optical imaging (OI) techniques. Utilising the 400-700 nm wavelengths of visible light allows OI to achieve sub-cellular microscopic resolution. Meso and macroscopic images are also accessible to the investigator via OI. Fluorophore synthesis is relatively cheap, antibody conjugation is readily achieved at the bench, and a variety of fluorescent reagents are commercially available so that OI can be implemented at low cost. OI is minimally invasive and highly versatile with a range of signal accumulating strategies and spectrally distinct fluorophores for multiplexed OI. Capitalising on the advantages of OI, a range of imaging techniques have emerged, adapting the utility of light microscopy to a variety of purposes and introducing alternative imaging platforms.

1.2.2 DEPTH AND RESOLUTION

Fluorescence microscopy became three-dimensional with the introduction of confocal scanning microscopy in 1955. Marvin Minsky's invention could sample in-focus light across a range of lateral positions and at a series of depths, stacking two-dimensional cross-sections in the axial plane.[69] Thirty-five years later the shallow penetration depths of OI would be overcome as Denk and Strickler combined two-photon absorption with laser scanning technology to create multi-photon microscopy. High resolution imaging could now be acquired at 0.5 – 1.0 mm penetration depths instead of the 0.25 mm depth, previously attainable.[70,71] Through optical windows, multiphoton microscopy advanced *in vivo* imaging making cellular and molecular dynamics visible in diseased tissues with multispectral, sub-cellular resolution imaging.[72] Since 1999, with stimulated emission-depletion (STED) microscopy, super-resolution microscopy has emerged in a range of formats extending the lateral resolution of OI beyond the 100 nm diffraction limit of light and visualising intracellular organelles such as the endoplasmic reticulum with ≈50 nm resolution.[73]

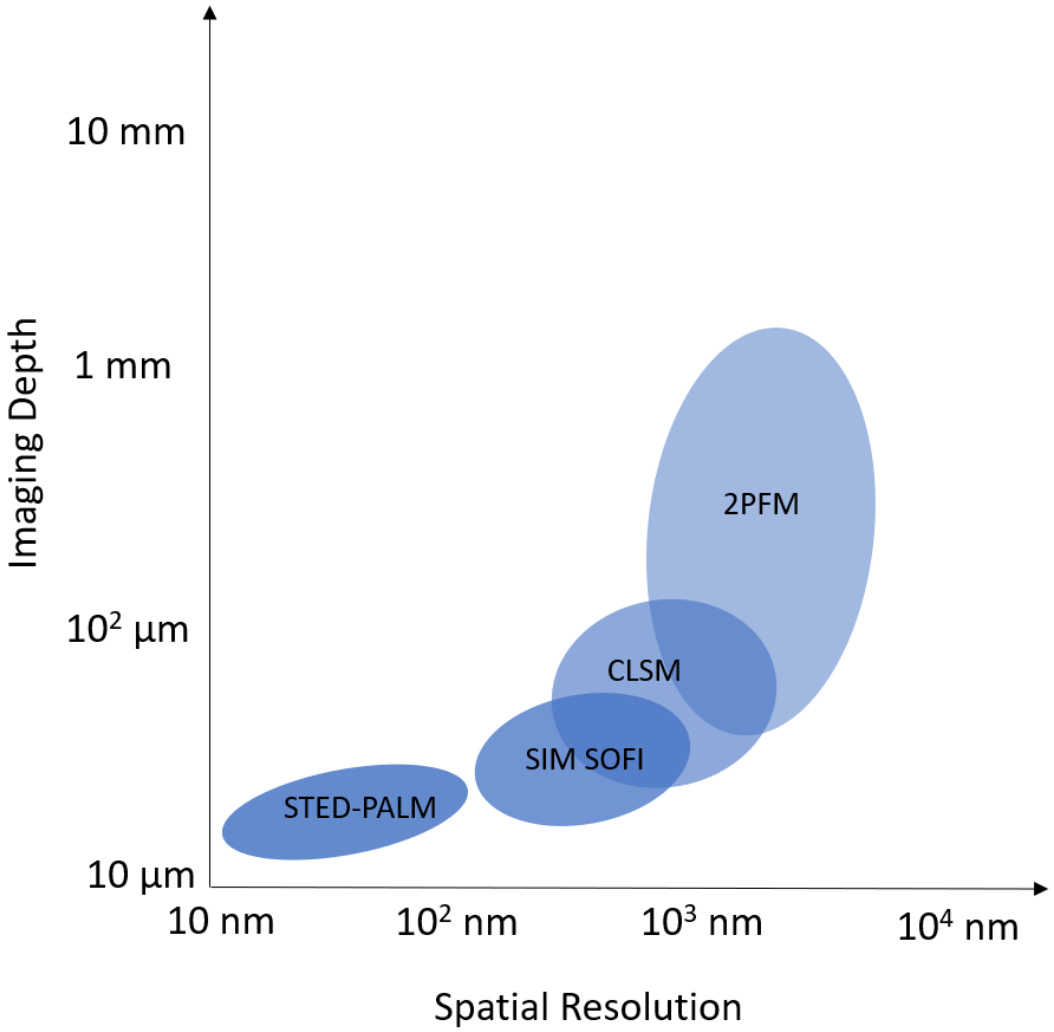

Figure 1.2 Comparison of Optical Imaging techniques
Imaging depth vs. spatial resolution for super-resolution techniques (STED, PALM, SIM and SOFI) Confocal laser scanning microscopy (CSLM) and multiphoton microscopy (2PFM).

1.2.3 THROUGHPUT

Although OI became increasingly sophisticated to achieve greater lateral resolution and penetration depths, the new platforms were inherently, extremely low-throughput. High-throughput imaging platforms emerged to capture population-level metrics which could generalize more reliably across biological phenomena. Numerous plate-reader spectrometers have integrated CMOS camera technology to

offer high-throughput imaging for more comprehensive investigations. And digital flow cytometry has employed a similar strategy to simultaneously capture fluorescent images and per cell fluorescence intensity measurements across large populations of cells. These integrated systems failed to deliver high-resolution, multidimensional imaging that makes traditional confocal microscopy such a useful technique. Finally, by using cell-segmentation image analysis, the microscopic field of view could be dissected into its component cells, now individual regions of interest. Image cytometry developed to describe populations of cells, at the level of the individual cell, without compromising microscopic resolution or dimensionality.

1.2.4 REPRODUCING IN VIVO CONDITIONS

With OI observations becoming more representative of *in vivo* molecular events, more recent OI efforts have focused on reducing the perturbations required in image acquisition. Fluorescence molecular tomography uses sequential scanning and a series of detector pairs to describe fluorescence emission from stained, excised tissues and whole animal models *in vivo*.[74] Using three-dimensional, sequential scanning and image reconstruction, image acquisition times are relatively long for fluorescence molecular tomography and resolution is limited by ≈4 mm^3 voxels.[75] Label-free phase microscopy achieves a 90 nm lateral resolution, reconstructing live samples as three-dimensional refraction tomograms using image analysis and complex deconvolution techniques.[76]

Fibred confocal endomicroscopy (FCE) is used in humans to access cells *in situ* and is

capable of multiplexing intrinsic autofluorescence, targeted and functional labelling.[77]

1.2.5 OPTICAL IMAGING PROBES

Four classes of fluorescent contrast agents are free dyes, targeted probes, activable probes and sensor probes. Free dyes are designed to avoid molecular interactions *in vivo*, instead they label entire fluid volumes illuminating the structure of fluid-filled compartments in a variety of organs. Indocyanine green (ICG) is a near-infra red fluorophore with FDA approval. Cheap, and non-toxic, ICG enables repeat-measurements and is used in a variety of clinical settings including angiography, tumour resection and ophthalmic examination.[78,79] For targeted, activable and sensor probes, target specificity becomes an important consideration if measurements are to be reliable. Targeted probes are designed to remain in solution until the molecular target is bound. Unbound targeted probe remains diffuse so that signal accumulation at target sites creates signal to noise contrast appropriate for imaging. Unbound probe may also be washed from off-target sites to enhance image contrast. Activable probes have a more sophisticated signal generation mechanism. Fluorescently quenched prior to encountering their molecular target, large signal to noise ratios can be generated by these probes.[80] Activable probes are often designed with in-built substrates for specific enzyme cleavage and generate higher resolution, more specific images when a mechanism to accumulate activated fluorescent fragments is employed.[81] These properties make activable probes useful for cell tracking and describing varying extents of

probe activation within a cellular population. Finally, sensor probes rely on environmental changes, for example, in pH or redox state, to activate fluorescence.[82] Like activable probes, sensor probes enable functional imaging in addition to the structural information they relay. The transient signals of sensor probes are lost as environmental conditions revert or exceed their detection ranges making these probes useful for kinetic studies but also increasing the likelihood that signalling events will go unnoticed. Different classes of contrast agent can be multiplexed towards different aims, for example, combined cell tracking and functional imaging. The mechanisms of signal generation in these four classes of contrast agent can be recombined to create variants such as the recent BODIPY probe for detecting fungal infection *in vivo*. Medive-Tapia *et al.* used an environmentally sensitive fluorophore to render a targeted probe fluorescently silent until interaction with its fungal target.[83]

1.3.0 CLINICAL OPTICAL MOLECULAR IMAGING

Recent developments in optical molecular imaging are enabling the identification and evaluation of inflammatory cells such as neutrophils in a variety of imaging scenarios. This is important as these leukocytes are an important part of host defence and immune homeostasis. The pivotal role of neutrophils as professional phagocytes in acute and chronic inflammatory disease may allow their use as versatile interventional biomarkers and as such fluorescent imaging of these cells has the potential to advance disease treatment and management, producing sub-

cellular information in real-time. Intrinsic tissue autofluorescence adds further value when the structures of the extracellular matrix or metabolic activities are of interest. The predominant modality of fluorescence intensity measurements, coupled with recent technological developments such as label-free nonlinear optical images and Raman analysis,[84,85] have opened up the possibility of giving the surgeon functional images of the surgical site in real time. Furthermore, exciting developments are resulting from the integration of cell classification and machine learning techniques, allowing deeper analysis of the richness of the datasets of each image.

Macroscopic widefield open fluorescence systems and high-resolution endomicroscopy are the predominant systems that have been used clinically to detect optical molecular tracers and recent advancements in imaging technology mean that fluorescence guided surgery is becoming a reality in cancer resection.[86] Complete tumour removal is crucial for patient outcomes, but difficult to ensure by conventional microscopy as visual characteristics and palpitation are inadequate to determine tumour-free margin. With fluorescence systems, surgeons will have the future ability to assess the extent of tumour excision and local metastases in real-time using a fluorescent label that “lights-up” the tumour and hence delineates its margins. Optical endomicroscopy (OEM) enables optical imaging at high resolution typically via a bundle of optical fibres to enable imaging with microscopic resolution, with the added ability to explore within a variety of cavities. Recently fibre-bundle endomicroscopy has been used in the lung to assess alveolar structure in emphysema, neoplastic changes in epithelial cells and real-time in vivo detection

of bacteria.[87–89] As well as in the GI tract where it has been used to detect changes associated with squamous cell carcinoma and colorectal polyps.[90] There are a range of OEM platforms, spanning clinical use and developmental systems,[89,91] although standardisation is necessary to generate meaningful diagnostic data.[92]

To maximise the utility of real-time fluorescence imaging devices, optical molecular probes that provide contrast and are suitable for use *in vivo* are required. Although extensive libraries of optical tracers for many targets have been developed,[93,94] none have been licensed for routine clinical use. Here I will focus on fluorescent molecular probes for neutrophils. Recent agents allow the identification of neutrophils, as well as providing information on dynamic cellular processes such as enzymatic activity, redox processes and phagocytic ability; processes that impact pathophysiology. Overall, inflammatory cell imaging creates an ideal paradigm for patient-specific disease monitoring and intervention (**Table 1.1**). Recent advances in fluorescent and Raman imaging are enabling neutrophil burden and activity to be described noninvasively and dynamically with tissue-level resolution.

Information	Method [Cohort size]	Disease	Reference
Disease Stage	Meta-analysis [45,905]	Gastrointestinal tumours	5
	Meta-analysis [40,559]	Solid tumours	6
	Patient Study Zhao et al. [270]	Inflammatory bowel disease	7
Disease Onset	Patient study [184]	Bacteraemia	95
	Patient study [118]	Sepsis-induced acute kidney injury	96
Critical Event	Meta-analysis [76,002]	Cardiovascular	97
	Patient study [557]	Diabetic neuropathy	98
	Patient study [698]	Chronic obstructive pulmonary disease	99
	Patient study [189]	Pesticide Poisoning	100

Table 1.1 Evidence for the role of neutrophils as biomarkers in various diseases. Data referenced to meta-analyses or patient studies in the literature. Copyright Birch *et al.* 2019[101]

1.3.1 NEUTROPHILS AS BIOMARKERS

As cells that migrate to diseased tissues and accumulate, both over the course of a disease and due to chemotactic stimuli, neutrophils can provide meaningful prognostic data just by their enumeration. Neutrophil counts have long been used to stratify patients by scoring disease, for example in ulcerative colitis.[102] Several large patient studies and systematic reviews, show the more recent neutrophil to lymphocyte ratio useful in staging inflammatory bowel disease (IBD) and numerous solid tumours[6,103] as well as predicting cardiovascular disease, diabetic neuropathy, glaucoma, sepsis-induced acute kidney injury and bacteremia.[95–97,99,104,105] Simple

neutrophil enumeration may even resolve the controversial question of when to intervene in carotid artery disease.[106] Using explanted human tissues Ionita *et al*. evidenced correlations between neutrophil count and several critical factors in atherosclerotic plaque stability.[107]

More sophisticated pathological insights can be drawn from qualified neutrophil enumeration, considering the viability status of neutrophils and quantifying neutrophil extracellular traps (NETs) independently of neutrophils in altered activation states. The accumulation of neutrophils on the ocular surface in dry-eye disease (DED) is thought to result in pathological NET formation.[108,109] With the recent success of a phase I/II study evaluating DNAse treatment, NET burden is becoming an important clinical parameter in this disease.[54] Impression cytology is a standard technique employed in the diagnosis of DED. However, there is now a convincing case for the replacement of the poorly standardized and potentially damaging impression cytology technique with *in* vivo laser scanning confocal microscopy, a technique which may itself be superseded by the rapidity and operational ease of OEM devices.[110] Neutrophil nuclei undergo morphological changes in DED that can assist the detection of DED-related hyperosmolarity.[109] With the abundance of HNE in NETs and this enzyme's stimulatory role in mucin production HNE may allow diagnostic disease monitoring in DED.[51,111] Beyond the conjunctiva, the eye has vascular and neural similarities to the brain which are optically accessible. Through non-invasive eye examination, Alzheimer's-related neurodegeneration has been linked to the development of retinal vasculature

abnormalities[112] and Ramierez *et al.* have highlighted the retina's biomarker potential in Alzheirmer's, glaucoma and Parkinson's disease.[113] Neuroprotectin D1 halves cerebral infarct size and counteracts neutrophil influx.[114] Taken together these findings may indicate a role for retinal neutrophil monitoring in neurodegenerative disease.

Another layer of insight may be accessible via measurement of neutrophil activity as studies of patients with inflammatory bowel disease have demonstrated. Patient studies found changes in faecal lactoferrin, calprotectin and HNE were significantly correlated with endoscopy and could be used to distinguish between mild disease, mucosal healing and clinical remission, and even predict flare onset.[115] HNE is further implicated in IBD treatment by cleaving therapeutic monoclonal antibodies Infliximab, Adalumimab, Vedolizumab.[116] The varied and clear benefits of such simple and direct analyses highlight the precision of the inflammatory response and the diagnostic potential of optical probes for neutrophil imaging.

Where the inflammatory response yields more nuanced information, sophisticated neutrophil imaging techniques may be required for accurate disease monitoring. Tumour associated neutrophils (TANs) may produce particularly unintelligible neutrophil imaging readouts. TANs execute varied and oppositional roles in tumoral inflammatory milieu. In early stage lung cancer TANs help to limit disease progression however animal models have elucidated several pro-tumoral mechanisms for neutrophils.[29,117,118] Some of the heterogeneity measured may come from relying on

the expression of TAN markers which can vary in different tumour microenvironments. Although yet unproven, N1 and N2 neutrophils may exert anti- and pro-tumoral effects respectively in humans, however there is no suitable marker exists for distinguishing between these phenotypes in the tumour.[119] Label-free OEM could assist in the identification of neutrophils by accessing more stable features such as their polymorphic nuclei. Similarly, lymphocyte numbers have proven a useful means of gauging neutrophilia. The versatile NLR has become an attractive stratification tool for understanding patient risk in a variety of cancer settings. But the reported high and low risk thresholds are inconsistent and the prognostic value of NLR for individual patients is unclear.[57] Imaging local inflammatory infiltrates may provide a necessary level of contextualisation for NLRs. Easily multiplexed and providing real-time, functional information at sub-cellular resolution neutrophil imaging probes may be uniquely capable of revealing an N1 to N2 ratio in the tumour microenvironment *in vivo*.

1.3.2 NEUTROPHIL IMAGING PROBES

Neutrophils make ideal biomarkers for several reasons. Constantly circulating and rapidly chemotaxing, neutrophils are the first leukocytes recruited to an inflammatory site. Neutrophil accumulate at the site of inflammation such that signal can be rapidly amplified. These properties are particularly desirable for fluorescence guided surgical operations. The neutrophilic half-life also benefits its biomarker potential as a relatively short neutrophil half-life limits any off-target effects which labelling might incur to days or hours. And neutrophils persist in inflamed tissues, providing information over the entire disease monitoring period, irrespective of its duration. Disease monitoring and intervention could benefit from such a biomarker. While fluorescence represents a cheap and versatile signal mode, recent advances in fluoresecence lifetime and Raman spectroscopic are also promising modes of optical imaging for non-invasive, real-time measures of neutrophil activity in man.

Target	Molecule	Optical Modality	Models	References
Serprocidins	Quenched Dendrimeric probe	Fluorescence	Human Cells *ex vivo*	81
HNE	Quenched probe		Mouse	120
	Quenched Dendrimeric probe		Sheep, Human	121
FPR1	Peptide		Human	122
	Radioactive nanoparticle	Dual PET/MRI	Mouse	123
Nucleus	Label-free	Raman	Human Cells *ex vivo*	124
		2-Photon FLIM	Human	125

Table 1.2 Overview of optical probes developed for neutrophil imaging. Copyright Birch *et al.* 2019[101]

1.3.3 PROBING SERINE PROTEASES

As the only class of optical imaging agents being developed for clinical optical molecular imaging of neutrophils to date, the serine protease-targeting probes are an exciting area of research. Of prime importance is the question of specificity between the serprocidins, the serine proteases with antimicrobial activity. There are three serprocidins, cathepsin G, protease 3 and HNE. Neutrophil serine protease 4 is the recently discovered forth member of this class of enzyme and its antimicrobial status is yet to be established. Great advances have been made in structure-activity studies for the fine-tuning of substrates[126,127] and inhibitors[128–131] specificity targeting only HNE *in vitro*. These advances have yielded excellent starting points for the development of targeted and activable imaging probes to be subjected to *in vivo* performance evaluation. The relative quantities and activities of each enzyme upon co-release must also be considered for clinical applications as HNE is the most abundant and often the fastest serine protease.[132] These factors of serprocidin probe specificity will be discussed further in **Chapter 4.1.2**.

1.3.4 PROBING FORMYL PEPTIDE RECEPTOR 1

NIR imaging is often superior to other wavelengths as tissue autofluorescence is lowest in this region of the visible spectrum. Zhou *et al*. synthesized a NIR fMLF receptor 1 targeting nanoprobe for imaging inflammation.[122] The issue of inflammatory site access was solved by building the labelling (cFLFLF) and fluorophore (Oyster-800) components onto a hydrophilic 8-arm PEG scaffold. There

are many benefits to using the cFLFLF ligand: its high affinity FPR1 binding (Kd = 2 nM) generates a sensitive readout of leukocyte distribution.[133] The ability of cFLFLF probes to access inflammatory sites with either PET (Cu18, Tec) or NIR (Cy5,Cy7) labels has also been demonstrated. However FPR1 is not cell-type specific and these probes bound macrophages and neutrophils.[134–136] cFLFLF probes may generate a useful readout when information on inflammatory cell accumulation is sought in broad terms but they may fail to clarify whether clinical intervention should focus on altering neutrophil or macrophage activity.

Pellico *et al.* combined radiochemistry and nanotechnology to create neutrophil-specific radiotracers by coating gallium-doped nanoparticles with cFLFLF for FPR1 labelling, a radiotracer for murine neutrophils was generated with dual PET and MRI utility.[123] Coating with peptide can produce significant probe hydrophobicity which has prevented other radiotracers from reaching the inflammatory site. By citrate-coating nanoparticles, the relatively large nanoparticle surface confers the necessary solubility for targeting neutrophils in vivo. Although the authors showed neutrophil depletion was capable of removing signal, it also removes important crosstalk from the LPS inflammatory response such that nonspecific signalling may be harder to detect.

A truly neutrophil specific target for biomarker development has proved elusive. Instead neutrophil specificity has arisen from combinatorial strategies exploiting the unique properties of certain targets within neutrophils. For example, HNE reaches such high concentrations in neutrophils that most systems will fail to detect the

minority of HNE positive monocytes bearing far lower quantities of the enzyme.[137] Neutrophil specific functions can also be exploited by careful probe design. Phagolysosome alkalinisation, which enhances the fluorescence signal of some fluorophores does not occur in monocytes. A novel, super-silent FRET probe[81] combines these structural and functional cellular characteristics to achieve neutrophil specificity (discussed in **4.1.1 Serine Proteases**). Label-free methods of cell identification have also sought neutrophils using targets found in other cell types but uniquely arranged in neutrophils.

1.3.5 LABEL FREE NEUTROPHIL IMAGING

Neutrophil imaging in the context of inflammatory research has aimed at understanding the relevance of cellular components to cell function. Questions of molecular colocalization and characterization are well served by fluorescent labels for elucidating the spatiotemporal relationships of cells and subcellular structures without altering the processes for investigation. As translational research influences surgical guidance questions of long-term cytotoxicity and ease-of-adoption are more important. Label-free imaging, which may seem imprecise for research purposes, is often cheaper, safer and does not require the considerable translational effort of alternative techniques. Molecules such as NADH, elastin and haemoglobin are established sources of intracellular and extracellular autofluorescence, but an amalgamation of signatures from yet more analytes may also contribute. Much characterisation is still required to generate clinically

meaningful autofluorescence imaging and techniques such as fluorescence lifetime imaging may become an important source of differentiation. Reflectance microscopy, which distinguishes between matter of different refractive indices, is now also capable of cellular resolution. For high-resolution imaging, individual molecules can be detected and quantified via Raman spectroscopy. Label-free imaging is *en route* to becoming as informative as fluorescence image-guided surgery can be, a limit it may exceed in a multi-modal platform.

1.3.6 RAMAN SPECTROSCOPY

By measuring the minute proportion of photons which interact with molecules inelastically, Raman spectroscopy can, non-destructively, describe the chemical composition of unlabelled matter. The first look at a leukocyte using Raman spectroscopy was when Puppels *et al*. compared eosinophils and Chinese hamster lung cells.[138] The group found nuclei spectroscopically distinct from cytoplasm and that distinctions between granulocytes may be made on the basis of their cytoplasmic contents.[139] In 1998, Otto *et al.* collected the first Raman spectrum of activated neutrophils.[140] More recently Ramoji *et al.* demonstrated the ability to discern between lymphocytes and neutrophils with concomitant Raman mapping of nuclear morphology.[124] With the application of principal components analysis (PCA) cells could be classified with 94% accuracy in the validation dataset and predicted with, 81% accuracy, in a new dataset from a completely different donor. Because Raman spectroscopy can describe intracellular contents it may be better suited to

quantifying cell function. Instead of identifying cells Harz *et al.* used spectrally distinct Raman and fluorescence excitation wavelengths to successfully multiplex these spectroscopic and microscopic techniques.[85] Particularly in such a multiplexed system, intracellular localization and oxidation states of functionally significant molecules may be revealed through Raman mapping to intimate whether or not neutrophils are effecting clinically meaningful processes such phagocytosis and to what extent.[141]

1.3.7 TWO-PHOTON ENDOGENOUS FLIM

The question of whether or not technology as nascent and complex as two-photon microscopy can be translated into a clinical endomicroscopy technology is unanswered. Although confocal endomicroscopy is in clinical use, two-photon endomicroscopy (TPEM) carries additional fibre optics challenges such as fibre non-linearity distorting the two-photon excitation light and the low quantum yields of intrinsic fluorophores.[91] These and other hurdles were overcome in 2008 when TPEM of human and mouse sarcomeres was conducted using a GRIN lens.[142] The technique involved a minimally-invasive needle clad fibre capable of imaging directly beneath the skin. In vivo TPEM was performed laparoscopically with a "stick" lens which avoids GRIN lens associated spherical aberrations revealing ovarian cancer through a laparoscopic procedure, centimetres into the body.[143] However murine tissues were investigated *in vivo* with a flexible Fluorescence

lifetime imaging microscopy (FLIM) endomicroscope, of working distance 135 µm in 2011, and the field continues to rapidly improve this label-free technology.[144]

Using two-photon excited fluorescence (TPEF) Zeng *et al.* characterised blood cells by their endogenous fluorescence lifetime signals. TPEF fluorescence lifetime imaging can detect differences in bound and unbound NADH such erythrocytes, agranulocytes and granulocytes are distinguishable.[125] As proportions of bound and free NADH vary by the dominant metabolic pathway employed by the cell – TPEF FLIM is functional imaging. Metabolic functional imaging may be able to identify granulocytes undergoing phagocytosis but whether or not phagocytosis and other factors affecting the NAD/NADH ratio, such as oxygen availability, can be dis-entangled remains unclear. By visualising cytoplasmic protein, TPEF FLIM can identify the size and shape of cells and (as absences in the cytoplasmic image) their nuclei - detailing the characteristic lobular structure of granulocyte nuclei. With neutrophils comprising 95% of the granulocytes population, these morphological distinctions give TPEF FLIM neutrophil specificity to rival the best ligand-based, fluorescent probes. Although the distinction between phagocytic and untreated neutrophils is subtle, this technique can separate untreated from activated neutrophils on morphological grounds. Quiescent neutrophils have a rounded morphology but membrane ruffling, characteristic of neutrophil activation was visualized when neutrophils phagocytosed E coli.[125]

1.4.0 IMAGE CYTOMETRY AND DATA SCIENCE

Cell segmentation was an important development in image analysis which enabled each individual cell to be analysed as a separate image. Because of cell segmentation cell-specific features such as ferret diameter and plasma membrane vs. cytoplasm comparisons could be quantified. Individual cell segmentation is commonly achieved when image analysis is applied to immunohistochemical images and images of cell monolayers such that hundreds or even thousands of cells, per image, can produce multiparametric quantitative data. Because so many individual parameters can be measured, data can be visualised in scatter plots, using parameter pairs as axes, and gating strategies can be applied using subsequent parameter pairs for multivariate analysis. Although this approach resembles flow cytometric data analysis, the challenges of multiplexing antibodies and fluorophores with similar properties do not constrain the generation of parameters in image cytometry to the same extent. For each imaging channel the distribution of pixels representing one cell and the application of mathematical functions may produce more meaningful visualizations than raw data. Positional data exists to describe the size and shape of cells and textural feature analysis combines pixel values and positions to understand the presence of patterns in the data. Such large datasets can be generated that statistical analysis becomes a necessary means of selecting optimal features for a data scientist's understanding of cellular populations. When using clustering techniques, features are optimal when the variance between cells of different treatment groups or phenotypes is maximised and to this end PCA enables more powerful data visualisation than serial gating. Although both PCA and

gating strategies provide linear combinations of multiple variables, PCA need not exclude data. The contributions of raw variables to new combinatorial variables (principal components) can be weighted by the extent of sample variance explained by each raw variable. So organised, multiparametric data becomes a powerful tool for the discovery and classification of cellular phenotypes.

CHAPTER 2:
MATERIALS AND METHODS

2.1.0 ETHICAL STATEMENT

All experiments using human samples were performed following approval of the appropriate accredited medical regional ethics committee (AMREC) and with informed consent of the patients. Whole blood for leukocyte isolation was taken from healthy volunteers following consent (AMREC ref no: 15-HV-013, CIRBRP004). COPD patient blood samples were collected following patient consent (REC reference 15/ES/0094, SR1063). Sectioned human lung samples were obtained from the lungs (cancerous and non-cancerous regions) of patients undergoing resection for lung cancer, approved by the NHS Lothian AMREC and facilitated by NHS Lothian SAHSC Bioresource (REC reference 15/ES/0094, SR1063). Whole human lungs for *ex vivo* lung ventilation studies were obtained from deceased organ donors whose lungs were not accepted for transplantation as part of the ENLIGHTEN programme (Universities of Edinburgh Glasgow and Newcastle) and with REC approval (REC No:16/LO/1883, SR1063). Next of kin gave consent for the lungs of the deceased to be used for research purposes.

2.1.1 MATERIALS

The following reagents were purchased from Sigma-Aldrich, St. Louis, MO, USA: Proteinase 3 from human leukocytes (P0615), Human leukocyte Cathepsin G (C4428), Fibronectin (F1141), Paraformaldehyde 4% (158127), 10% neutral buffered formalin (HT501128), HEPES (3375), Sodium Chloride (NacCl) (S5886), DAPI (D9542), AAPV-pNA (M4765), AAPV-AMC, (M9771), Phorbol 12-myristate 13-acetate (79346), calcium ionophore (A23187, C7522) Interleukin-8 (I1645-10UG), Leukotriene B4 (L0517-10UG) β-Acetyl-γ-O-hexadecyl-L-α-phosphatidylcholine hydrate (P49904) LPS (L3129), fMLF (F3506).

Antibodies against HNE (ab67682), Glut1 transporter (ab115730) and rabbit IgG (ab7171) were purchased from Abcam Cambridge, UK.

The following reagents were purchased from ThermoFisher Scientific, Waltham, MA, USA unless otherwise stated: CellMask™ orange plasma membrane stain (C10045), Hank's Balanced Salt Solution without Phenol Red (14025092, Gibco), Dulbecco's Phosphate Buffered Saline (PBS) (14190144, Gibco), Dulbecco's Phosphate Buffered Saline with Calcium and Magnesium (14040091, Gibco), [10x] PBS (14080048, Gibco), Cy3 tyramide (NEL 744Boo1kt, PerkinElmer, MA, USA), normal goat serum (GO-605/500, Biosera, Heathfiled, UK), ER1 buffer (AR9961, Leica biosystems), H202 (23622.260, VWR), Sputum purified Human Leukocyte Elastase (SE563, Elastin Products Company, MO, USA), Sivelestat (ONO-5046; Tocris Bioscience, Bristol, UK).

2.1.2 SMARTPROBE SYNTHESIS

The dendrimeric SmartProbe, Neutrophil Activation Probe (NAP), was synthesized by collaborators in the Bradley Group.[145]

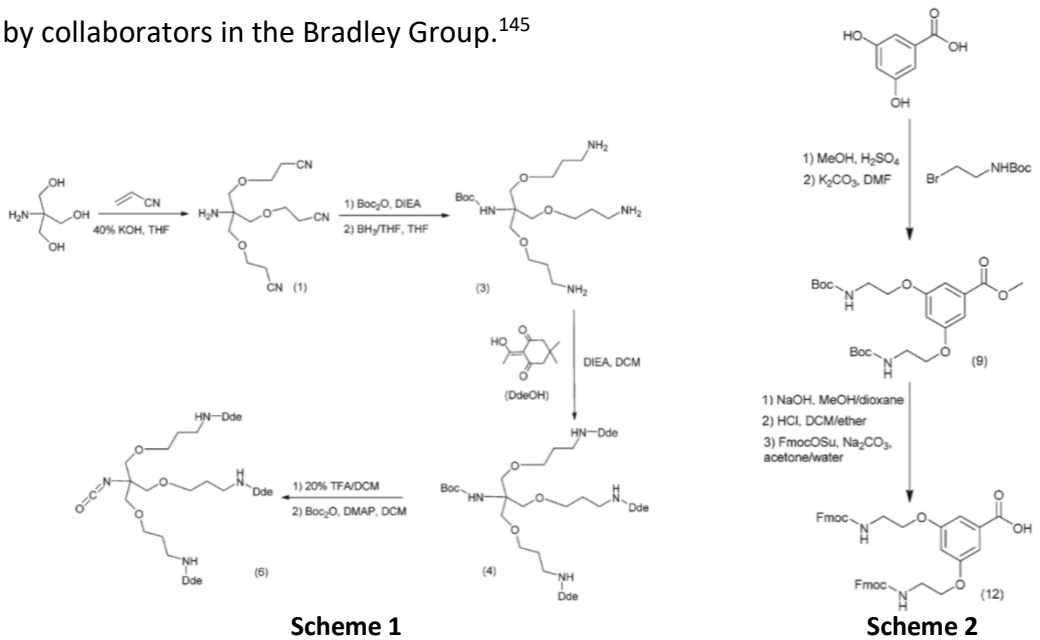

Scheme 1 **Scheme 2**

Figure 2.0 Synthetic Schemes for Neutrophil Activation Probe development
Monomers from schemes 1 and 2 were used to synthesis precursors to Neutrophil Activation Probe.

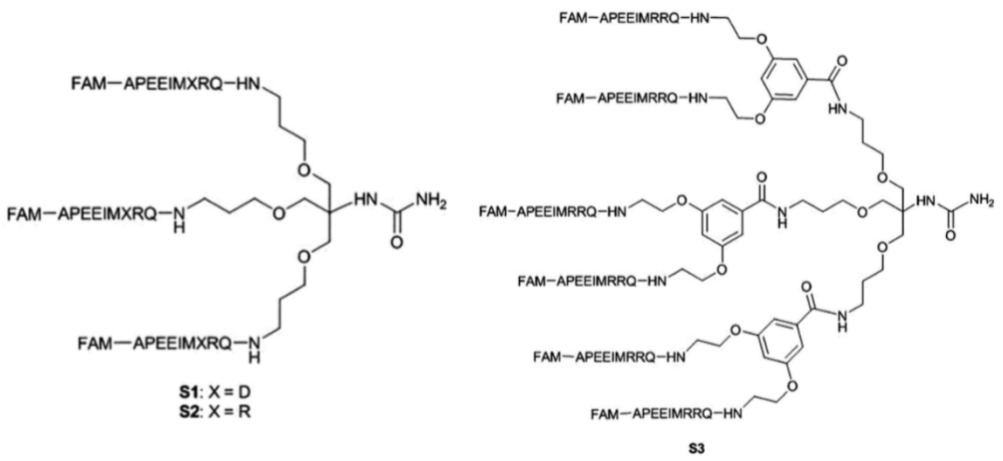

Figure 2.1 Synthetic precursors to Neutrophil Activation Probe
S1-S3 incorporate peptide sequences APEEIMDRQ and APEEIMRRQ optimised by Gauthier *et al.* with a single fluorescein label on trivalent (S1 and S2) and hexavalent (S3) scaffolds.

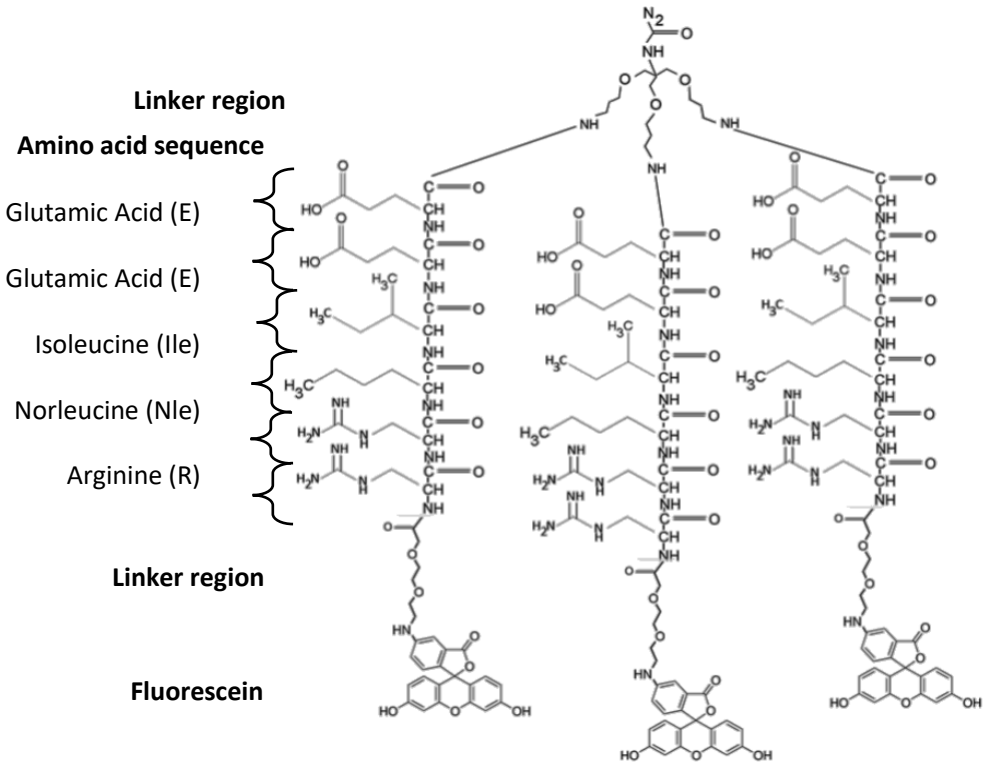

Molecular mass = 4236.56 Daltons

Figure 2.2 Chemical Structure and Molecular Mass of Neutrophil Activation Probe
Diagram of NAP chemical structure with linker regions, amino acid sequence regions and fluorescein moieties labelled.

2.1.3 SPECTROPHOTOMETER ASSAYS

Samples were prepared in a 50 mM HEPES, 50 mM NaCl buffer (S7653, Sigma-Aldrich) and data were acquired via the Synergy H1 hybrid reader, BioTek, Potton, UK.

2.1.4 DETERMINING KINETIC RATE CONSTANTS

HNE (100 nM) was added to colorimetric elastase substrate (1 µM, M4765, Sigma-Aldrich) at room temperature and read, immediately after preparation, at 37 ^{o}C. Absorbance readings were performed at one-minute intervals.

2.1.5 DATA-REDUCTION

Enzyme velocities were calculated as

$$E_V = \frac{AV}{\varepsilon l t}$$

Where E_v = Enzyme velocity A = Absorbance ε = substrate extinction coefficient l = path length t = time and V = reaction volume.

Enzyme velocity was plotted against substrate concentration to fit a rectangular hyperbola, using GraphPad Software (version 5.01, La Jolla California, USA), whereby maximum velocity (V_{max}) is the asymptote and the Michaelis-Menton constant (K_M) is the gradient. The catalysis constant was calculated using equation (10) from the following derivation.

2.1.6 DERIVATION OF THE MICHAELIS MENTEN EQUATION

$$E + S \underset{k_{-1}}{\overset{k_1}{\rightleftarrows}} ES \xrightarrow{k_{cat}} E + P \quad (1)$$

$$v_0 = k_{cat}[ES] \quad (2)$$

$$k_{-1}[ES] + k_{cat}[ES] = k_1[E][S] \quad (3)$$

$$\frac{k_{-1}+k_{cat}}{k_1} = \frac{[E][S]}{[ES]} \quad (4)$$

$$\frac{k_{-1}+k_{cat}}{k_1} = K_M \quad (5)$$

$$[E] = [E]_{total} - [ES] \quad (6)$$

Substituting 5 and 6 into 4:

$$K_M = \frac{([E]_{total}-[ES])[S]}{[E]} \quad (7)$$

$$K_M[ES] = [E]_{total}[S] - [ES][S]$$

$$K_M[ES] + [ES][S] = [E]_{total}[S]$$

$$[ES](K_M + [S]) = [E]_{total}[S]$$

$$[ES] = \frac{[E]_{total}[S]}{K_M+[S]} \quad (8)$$

Substituting 8 into 2:

$$v_0 = k_{cat}\frac{[E]_{total}[S]}{K_M+[S]} \quad (9)$$

$$v_{max} = k_{cat}[E]_{total} \quad (10)$$

Substituting 10 into 9:

$$v_0 = \frac{v_{max}[S]}{K_M+[S]} \quad (11)$$

Concentrations	Constants	Velocities
$[E]_{total}$ = total enzyme	k_{cat} = catalysis	v_{max} = maximum enzyme
[E] = enzyme	k_1 = association rate	v_0 = initial enzyme
[S] = substrate	k_{-1} = disociation rate	
[ES] = enzyme-substrate complex	K_M = Michaelis-Menton	
[P] = Product		

$$T_{1/2} = \frac{ln_2}{k_{inact}}$$

Where $T_{1/2}$ = half-life, k_{inact}= inactivation constant

To compare the effect of dose on fluorescence intensity, Neutrophil Activation Probe (NAP 0.5, 1, 2.5, 5 µM), flat-bottomed 96 well plates (Corning, NY, USA) were prepared with HNE 100 nM (SE563, Elastin Products Company, MO, USA) at room temperature and read, immediately after preparation, at 37 ^{o}C. Fluorescent intensity readings were performed at one-minute intervals.

2.1.7 NAP SELECTIVITY FOR SERINE PROTEASES

To compare serine protease activities with NAP (3 µM), flat-bottomed 96 well plates (Corning, NY, USA) were prepared on ice and read immediately after preparation at 37 ^{o}C. Temperature fluctuation artefacts were removed by subtracting fluorescence changes of enzyme-free, NAP controls. Fluorescence intensity was read using $\lambda_{ex}/\lambda_{em}$ 488/525 nm light for fluorescein and fluorescein-based dyes in solutions of boron and potassium titrated to pH 5, 7 and 9. Detector gain was internally calibrated with each experimental replicate so that 488 nm light stimulation, of 5,6

carboxyfluorescein (15 µM) in freshly made up pH 12 buffer, was equal to 100,000 relative fluorescence units. Fluorescence intensity reads were performed at one-minute intervals. Proteinase 3 (E3539, Sigma-Aldrich), Cathepsin G (Sigma-Aldrich, C4428) and HNE (SE563, Elastin Products Company, MO, USA) concentrations were prepared by serial dilution. HNE was stored at 10 µM, at -20 ^{o}C in a 0.02M NaoAC, 50% glycerol v/v buffer (G5516, Sigma-Aldrich) made up at pH 5. To investigate the effect of pH on HNE enzyme activity, fluorogenic elastase substrate (1 µM M4765, Sigma-Aldrich) fluorescence intensity was read at 37 ^{o}C, using $\lambda_{ex}/\lambda_{em}$ 370/460 nm.

To determine kinetic constants measurements of enzyme velocity were performed when HNE 100 nM (SE563, Elastin Products Company, MO, USA) was added to fluorogenic elastase substrate (1 µM, 324740, Sigma-Aldrich) in the presence of irreversible elastase inhibitor (GW457427, GlaxoSmithKline) or HNE targeted probes (0.1, 0.2, 0.5, 1, 2, 5, 10 µM). Samples were prepared in flat-bottomed 384 well plates (Corning, NY, USA) with optically transparent seals (Sigma-Aldrich). Fluorescence intensity read at 37 ^{o}C, using $\lambda_{ex}/\lambda_{em}$ 370/460 nm and gain was set to 90 arbitrary units with fluorescence intensity reads were performed at twenty-second intervals. Experimental conditions for absorbance measurements differed by the use of flat-bottomed 96 well plates (Corning, NY, USA) and fifteen-second intervals.

Spectral Characterisation of HNE-targeted Probes

Spectral scanning was performed using 500 nm light, with the monochromator fixed at 750 nm, to ensure spectra could be seen across the excitation and emission peaks. 10 µM solutions of Cy5-based dyes were prepared in distilled water or PBS with cations. Fluorescent emissions were detected at 10 nm intervals from 400 nm to 800 nm, at room temperature and with gain set to 100 arbitrary units. Samples were illuminated top down, with the light source aligned above detectors.

2.1.8 PRIMARY HUMAN NEUTROPHIL SUPERNATANTS AND LYSATES

To prepare supernatants and lysates, healthy human neutrophils, freshly isolated at $2x10^7$/mL, were incubated in PBS with cations at room temperature for 30 minutes before exposure to the relevant pharmacological stimulus for another 30 minutes. Cell suspensions were centrifuged at 350 rpm for 5 minutes and the supernatants removed were mixed with glycerol, 50% v/v. Supernatants were replaced with equivalent volumes of PBS without cations and cell lysates were obtained by using repeated dry ice/acetone baths. The resulting suspension was centrifuged at 13,000 rpm for 20 minutes to remove debris. Aliquots of supernatant and lysates were placed in the chambers of a 96 well flat-bottomed plate. Samples were mixed with a stock solution of NAP (100 µM) to a final volume of 100 µL with final NAP concentrations of 3 µM. Where indicated, Sivelestat (ONO-5046; Tocris Bioscience, Bristol, UK) was used at concentrations of 1, 0.5 and 0.25 µM.

2.1.9 DETERMINING FIXED PURIFIED HNE ACTIVITY

To determine the effect of fixation on HNE, samples of purified HNE (100 nM), formaldehyde (0, 1, 2, 4, 8, 16%, Sigma-Aldrich) and NAP 3 (μM) were measured using $\lambda_{ex}/\lambda_{em}$ 488/525 nm light. Fluorescent measurements were performed at one-minute intervals in 96 well plates (Corning, NY, USA) well plates.

2.2.0 PREPARATION OF HUMAN POLYMORPHONUCLEAR CELLS AND PERIPHERAL BLOOD MULTI AND MONONUCLEAR CELLS FROM WHOLE BLOOD

Whole blood was separated into serum, polymorphonuclear cells (PMN) and peripheral blood mononuclear cells (PBMC) using a method previously described by our group[39]. In summary, whole blood was mixed with 3.8% sodium citrate before plasma was separated by centrifugation. Dextran sedimentation was used to remove erythrocytes and produce a leukocyte suspension which results in PMN and PBMC layers upon centrifugation in a discontinuous, isotonic Percoll gradient. PBMC and PMN accumulate at the 55/70% and 70/81% Percoll interfaces respectively. Autologous serum was prepared by missing 10 mL plasma with 220 μL calcium chloride 1 M. The PMN layer was used in neutrophil experiments without further purification for practical purposes. The PMN layer typically contains 95% neutrophils or more with a small minority of eosinophils and even less or no basophils.[77] PMN and PBMC purity were determined after each isolation by mixing

198 µL, of 50 mL PMN or PBMC solutions in PBS without cations, with 2 µL autologous serum for cytospins.

For COPD preparations, reagents volumes were quartered to correspond with 10 mL whole blood, excluding wash steps. Whole blood was mixed with 0.75 mL 3.8% sodium citrate. 5 mL plasma was reduced to serum with 110 µL calcium chloride 1 M prior to dextran sedimentation.

2.2.1 PREPARATION OF ISOLATED LEUKOCYTE CYTOSPINS

200 µL cell suspensions, containing 2% autologous serum, were spun at 300 rpm for 3 minutes, allowed to dry, methanol fixed and stained in Diff-Quik. Autologous serum prevents cell from rupturing during the spin. Slides were allowed to air-dry for 10 minutes and a cell differential was calculated using an EL-Einsatz upright Axioskope microscope (Carl Zeiss, Jena, German) to count at least 200 cells.

2.2.2 FLOW CYTOMETRIC ANALYSES OF PMN

For the following flow cytometric analyses cell suspensions were preincubated for 30 minutes at room temperature in PBS with cations. Flow cytometric measurements were performed on the BD FACSCalibur flow cytometer, with 1.5 mL Eppendorf tubes. Fluorescence cross-over compensation using single-stained samples and data-analysis was performed using FlowJo software (version 10.0.0 Ashland, OR, USA).

HNE measurements across the PMN lifespan

To investigate the effects of PMN apoptosis, primary and secondary necrosis on NAP signal PMN suspensions were resuspended at $1x10^7$ cells/mL and incubated for 30 minutes at room temperature in PBS with cations. PMN suspensions were incubated at 37 ^oC, 5% CO_2 for 0, 2, 6 and 20 hours before transferring samples to 1.5 mL Eppendorf tubes. Annexin-V-Alexa Fluor 647 antibody (1:200, 640912, Biolegend, San Diego, CA, USA) and propidium iodide (1:300, 556463, BD Biosciences Oxford, UK) were added to samples 20 minutes and immediately prior to flow cytometric analysis, respectively. Individual samples were briefly vortexed, immediately before measurement.

2.2.3 DETERMINING HNE ACTIVITY FOLLOWING PMN FIXATION

To determine how paraformaldehyde fixation effects NAP labelling, PMN were seeded into round bottom 96 well plates (Corning, NY, USA) well plates and incubated at, 37 ^oC, 5% CO_2, in 50 µL HBSS with cations and 10% auotologous serum, with or without stimuli (25 µg/mL LPS for 30 minutes, then 100 nM fMLF for 15 minutes), NAP (3 µM) and anti-CD11b antibody (5 ug/mL 301414 Biolegend, San Diego, CA, USA). To fix PMN, suspensions were centrifuged at 300 g for 4 mins and resuspended in 4% paraformaldehyde, for 5 mins on ice before repeating centrifugation and washing twice in PBS without cations. Individual samples were transferred to 1.5 mL Eppendorf tubes and briefly vortexed, immediately before measurement.

For the following flow cytometric analyses cell suspensions were preincubated for 30 minutes at room temperature in PBS with cations. Flow cytometric measurements were performed on Flow cytometric measurements were performed on the automated Attune NxT acoustic focusing cytometer, shaking round bottom 96 well plates (Corning, NY, USA) well plates, between measuring each sample:

Adhesion molecule expression following pharmacological stimulation

To describe the activation assay window with calcium ionophore stimulation PMN suspensions were resuspended at $1x10^7$ cells/mL. PMN were incubated with anti-CD11b-Alexa Fluor 647 labelled antibody (5 µg/mL 301414 Biolegend, San Diego, CA, USA), anti-CD62L antibody (5 µg/mL 304806 Biolegend, San Diego, CA, USA) and calcium ionophore (final [1 µM], A23187) for 30 minutes at room temperature. 350 µL PBS with cations were added to samples before spinning at 300 g for 4 minutes and resuspending in 200 µL PBS without cations for flow cytometric analysis using $\lambda_{ex}/\lambda_{em}$ 640/660 light and $\lambda_{ex}/\lambda_{em}$ 450/488 light.

HNE targeted-probe cell-type specificity with varying PMA concentration

To compare PMA dose responses in PMN and PBMC, 20 µL cell suspensions were resuspended at 1.25 $x10^7$ cells/mL and added to cyanine-based dyes with or without, phorbol myristate acetate (0, 10, 50, 100, 250, 500, 1000, 2000 nM, 79346, Sigma-Aldrich) or calcium ionophore (final [10 µM], A23187). PMN and reagents were briefly titurated in a final volume of 40 µL and incubated at room temperature for 10 minutes before adding 260 µL PBS with cations, spinning at 300g for 4

minutes and washing into 200 µL PBS without cations. PMN underwent flow cytometric analysis using $\lambda_{ex}/\lambda_{em}$ 640/660 light.

Cell-type specificity comparison of HNE targeted-probes

To investigate the cell-type and HNE specificity of cyanine-based dyes PMN suspensions were resuspended at 1.25 x10^7 cells/mL and 30-minute preincubations included Sivelestat (100 µM, ONO-5046; Tocris Bioscience, Bristol, UK) where indicated. 20 µL aliquots of PMN suspensions were added to the relevant combinations of cyanine-based dyes (final [1 µM]), calcium ionophore (final [1 µM], A23187) and Sivelestat (final [50 µM], ONO-5046; Tocris Bioscience, Bristol, UK). PMN and reagents were briefly titurated in a final volume of 40 µL and incubated at room temperature for 10 minutes before adding 260 µL PBS with cations, spinning at 300g for 4 minutes and washing into 200 µL PBS without cations. PMN underwent flow cytometric analysis using $\lambda_{ex}/\lambda_{em}$ 640/660 light.

2.2.4 LASER SCANNING CONFOCAL MICROSCOPY OF PMN

In the following experiments cell suspensions were preincubated for 30 minutes at room temperature in PBS with cations and imaged using a Zeiss LSM 510-META confocal laser scanning microscope (Carl Zeiss, Jena, German). 8 well LabTek II confocal chambers (VWR, PA, USA) were coated in 1 µg/mL fibronectin (Sigma Aldrich) for 10 minutes and air-dried prior to the addition of cell suspensions.

2.2.5 INTRACELLULAR NAP SIGNAL GENERATION

PMN suspensions were incubated for 30 minutes at room temperature in PBS with cations and, where indicated, with Sivelestat (100 µM, ONO-5046; Tocris Bioscience, Bristol, UK). Inhibitor concentrations were kept constant throughout the experiment and 192.5 µL PMN suspensions were added to each well. Wells seeded with PMN were washed once in PBS with cations and co-incubated with 7.5 µL NAP (final [3 µM]). PMN were imaged, at their interface with the well bottom, over a 10 minutes time-course at 30 second intervals and 50 µL calcium ionophore (final [10 µM], A23187) was added at 90 seconds.

2.2.6 PRIMARY HUMANY NEUTROPHIL HNE IMMUNOFLUORESCENCE

PMN incubated in PBS with cations or calcium ionophore (final [1 µM], A23187) for 10 minutes at 37 ^{o}C, 5% CO_2. PMN were fixed in 4% paraformaldehyde for 5 mins on ice and twice washed in PBS without cations. Fixed PMN were coated in 0.3 M glycine for 15 minutes at 37 ^{o}C, and blocked in 0.2 µM filtered, 10% goat serum for 30 minutes at 37 ^{o}C. After incubating in anti-HNE antibody (1:200, ab68672, Abcam Cambridge, UK) for 1 hour at room temperature and washed five times in PBS without cations. After primary antibody labelling PMN were then incubated in Cy5-labelled anti-rabbit antibody (1:1000 in PBS without cations, A-21206, ThermoFisher Scientific, Waltham, MA, USA) for 1 hr at room temperature and washed four times in PBS without cations before its replacement with 50 µL DAPI (1 µM) for 5 mins at room temperature. After secondary antibody labelling DAPI

solutions were replaced by 50 µL CellMask™ Orange (1:5000 in PBS without cations) 10 mins at 37 °C and PMN were imaged in z-stacked planes.

2.2.7 LASER SCANNING CONFOCAL MICROSCOPY IMAGE ANALYSIS

ImageJ (version 1.52n, Rasband, National Institute of Health, USA) was used to objectively quantify intracellular and extracellular enzyme velocities via change in pixel intensity following pharmacological cellular stimulation with and without enzymatic inhibition. Algorithms to extract numerical pixel intensity values from image batches and process these values for time-dependent frame averages, for individual time-lapse videos, were employed using ImageJ (version 1.52n, Rasband, National Institute of Health, USA) and MatLab (version 2015b) respectively. To calculate intracellular NAP signal maxima using ImageJ, extracellular pixel intensities were removed from each image, as values above a fixed threshold, producing binary masks of images. Binary masks underwent image multiplication with raw images and pixel intensity maxima were measured. The resultant images were divided into an 8x8 grid of square regions of interest. Region of interest measurements were averaged, to calculate frame averages at each timepoint, which were divided by frame cell number.

2.3.0 SPINNING DISK CONFOCAL MICROSCOPY OF LEUKOCYTES

In the following experiments cell suspensions were preincubated for 30 minutes at room temperature in PBS with cations and imaged, in z-stacked planes, using the Olympus IX83 spinning disk confocal laser scanning microscope (Carl Zeiss, Jena,

German). Black, Ibidi 96 well plates (Thistle Scientific, Glasgow, UK) were coated in 1 µg/mL fibronectin (Sigma Aldrich) for 10 minutes and air-dried prior to the addition of cell suspensions.

2.3.1 HNE-TARGETED PROBE DOSING

This study was undertaken by Mr. Filip Angelov. 100 µL PMN suspensions (10^7/mL) were plated in PBS with cations. 100 µL VE200 in PBS with cations was added to wells (final [0.1, 0.2, 0.5, 1 and 2 µM]) with or without calcium ionophore (final [10 µM]).

2.3.2 INTRACELLULAR NAP SIGNAL GENERATION UNDER BACTERIAL PRODUCT STIMULATION

This study was undertaken by Mr. Filip Angelov. Altering the method for *Intracellular NAP signal generation* (**Method 2.1.5**), instead of calcium ionophore stimulation all PMN were treated with 25 ng/mL LPS for 30 minutes, followed by 100 nM fMLF.

2.3.3 INTRACELLULAR NAP SIGNAL GENERATION UNDER INHIBITION

This study was undertaken by Mr. Filip Angelov. Altering the method for *Intracellular NAP signal generation* (**Method 2.1.5**), PMN were stained with CellMask™ Orange (1:10,000, ThermoFisher Scientific, Waltham, MA, USA) and three HNE inhibitor conditions (0.02 µM, 0.2 µM and 2 µM, GW447631, GlaxoSmithKline) were added, to the Sivelestat and uninhibited conditions.

2.3.4 HNE LABELLING OF VIABLE, APOPTOTIC AND NECROTIC NEUTROPHILS

This study was undertaken by Mr. Filip Angelov. 100 µL PMN suspensions (10^7/mL) PMN were plated in solutions of CellMask™ Orange (1:10,000, ThermoFisher Scientific, Waltham, MA, USA) and DAPI (1 µM, ThermoFisher Scientific, Waltham, MA, USA). PMN were untreated or treated with GW447631 (final [10 µM]) or Q-VD-OPh hydrate (final [15 µM], Sigma Aldrich, SML0063). At 0, 4 and 18 hrs following plating, solutions of NAP (final [3 µM]) and where relevant, VE200 (final [100 nM]) were added to wells with or without calcium ionophore (final [5 µM]). At intervals between imaging plated PMN were incubated at 37 ^oC, 5% CO_2.

2.3.5 NAP AND HNE-TARGETED PROBE MULTIPLEXED LABELLING

100 µL PMN suspensions (10^7/mL) were plated and PBS with cations was replaced with reagent solutions of NAP (3 µM) and cyanine-based dyes (0.2, 2 µM) with or without calcium ionophore (final [1 µM], A23187) for 10 minutes before cells were washed in 100 µL PBS with cations and imaged.

2.3.6 HNE PRESENCE AND ACTIVITY UNDER VARYING CHEMOKINETIC STIMULATION

100 µL PMN (10^7/mL) incubated in PBS with cations or chemokine (LPS 25 µg/mL, IL8 3 nM, PAF 100 nM, LTB4 1 nM) for 30 minutes at, 37 ^oC, 5% CO2 after which, 25 µg/mL LPS solution in one of the two LPS conditions was replaced with fMLF and all conditions were incubated for a further 15 minutes. PMN were fixed in 4% paraformaldehyde for 5 mins on ice and twice washed in PBS without cations. Fixed PMN were coated in 0.3 M glycine for 15 minutes at 37 ^oC, and blocked in 0.2 µM filtered, 10% goat serum for 30 minutes at 37 ^oC. After incubating in anti-HNE antibody (1:200, ab68672, Abcam Cambridge, UK) for 1 hour at room temperature and washed five times in PBS without cations. After primary antibody labelling PMN were then incubated in Cy5-labelled anti-rabbit antibody (1:1000 in PBS without cations, PA45004, Amersham Bioscience) for 1 hr at room temperature and washed four times in PBS without cations before its replacement with 50 µL DAPI (1 µM, ThermoFisher Scientific, Waltham, MA, USA) for 5 mins at room temperature. After secondary antibody labelling DAPI solutions were replaced by 50 µL CellMask^{TM} Orange (1:5000 in PBS without cations) 10 mins at 37 ^oC. NAP/HBSS (final [3] µM,

14175-053, ThermoFischer Scientific, Waltham, MA, USA) was added to wells with immunolabelled PMN. After 1 hr incubation at room temperature PMN were imaged.

2.3.7 HNE PRESENCE AND ACTIVITY IN COPD NEUTROPHILS UNDER VARYING CHEMOKINETIC STIMULATION

To investigate chemokinetic response in healthy young, COPD patient PMN, 50 µL PMN (10^7/mL) suspensions were preincubated with CellMask™ Orange (1:10,000, ThermoFisher Scientific, Waltham, MA, USA) and DAPI (1 µM, ThermoFisher Scientific, Waltham, MA, USA) before plating. Unstained PMN were washed once. CellMask™ Orange and DAPI solutions were replaced in the relevant conditions, directly before imaging, with NAP (3 µM) and VE200 (100 nM) solutions with or without chemokine (LPS 25 µg/mL, IL8 3 nM, PAF 100 nM, or LTB4 1 nM) or LTB4 with Sivelestat (50 µM). Z-stacked images were acquired at 37 ^{o}C, 5% CO2, with 0, 45 and 90 minute intervals and LPS/NAP/VE200 solution was replaced by fMLF/NAP /VE200 solution after 30 mins.

2.3.8 IMMUNOHISTOCHEMISTRY OF PARAFFIN-EMBEDDED HUMAN TISSUES

This study was undertaken by Miss. Lyndsey Boswell and the Shared University Research Facilities. Following dewax and rehydration samples were incubated in ER1 citrate buffer, ph6 (AR9961, Leica Biosystems, Milton Keynes, UK) for 20

minutes. Samples were treated with H2O2 1:10 (236220.260, VWR, Leicestershire, UK) for 10 minutes and incubated in normal goat serum 1:5 (GO-605/500 Biosera, Heathfield, UK) for 10 minutes. Samples were incubated with anti-HNE primary antibody 1:1000 (ab68672) for 60 minutes before incubation with goat anti-rabbit secondary antibody 1:500 (ab7171) for 30 minutes. For tyramide signal amplification, Cy3-labelled tyramide (PerkinElmer, MA, USA, NEL 744Boo1kt, 1:50) was added to samples for 10 minutes. Nuclei were stained by incubation with DAPI 1:1000 (Sigma-Aldrich, D9542) for 10 minutes. Fluorescent stains were applied to samples using the BOND Max automated immunohistochemistry machine (Leica Biosystems, Milton Keynes, UK).

2.4.0 FIBRED CONFOCAL ENDOMICROSCOPY OF LEUKOCYTES

The following experiments were conducted using the Versicolour fibred endomicroscopic system, designed in house, and imaged via the catheterised Panoptes fibre. Versiplayer version 3.0 software provided a graphic user interface.

2.4.1 FIBRED CONFOCAL HNE IMAGING IN VITRO

100 µL PMN suspensions (10^7/mL) were plated into black, Ibidi 96 well plates (Thistle Scientific, Glasgow, UK), and PBS with cations was replaced with reagent solutions of NAP (3 µM) and cyanine-based dyes (2 µM) with or without calcium ionophore (final [1 µM], A23187) for 10 minutes before cells were washed in 100 µL PBS with cations and imaged. A catheterised Panoptes fibre was applied directly to the bottom of each well for point-of-contact imaging.

2.4.2 FIBRED CONFOCAL HNE IMAGING IN AN EX VIVO VENTILATED LUNG MODEL

PMN were separated from whole blood by Percoll blood preparation and resuspend at 10^7/mL. *Ex vivo* human lungs were connected to ventilation apparatus and probed with a bronchoendoscope past the primary bronchi. A catheterised Panoptes fibre was inserted down the auxiliary port of the bronchoendoscope and into the alveolar airspace for imaging using the in-house Versicolour fibred confocal endomicroscope. Solutions of PMN, NAP (final [3 µM]) and VE200 (final [200 or 400 nM]) were prepared with or without calcium ionophore 10 µM and instilled, via catheter, into the alveolar space of *ex vivo* human lungs, under ventilation.

2.5.0 IMAGE ANALYSIS OF SPINNING DISK CONFOCAL MICROSCOPY OF LEUKOCYTES

Image analysis was performed using ImageJ (version 1.52n, Rasband, National Institute of Health, USA) unless otherwise stated. Three-dimensional image stacks were converted to two-dimensional maximum projections and underwent mean-limited thresholding.

2.5.1 INTRACELLULAR NAP SIGNAL GENERATION UNDER BACTERIAL PRODUCT STIMULATION

The image analysis method described in 2.2.7 was repeated.

2.5.2 HNE TARGETED PROBE DOSING

Following mean-limited thresholding images were analysed by two methods, firstly by whole frame mean fluorescence intensity whereby the sum of pixel intensities was divided by the number of pixels. Secondly by integrated density, whereby images were thresholded to include only intracellular pixels and these areas were measured. Each intracellular pixel area was multiplied by its mean fluorescence intensity.

2.5.3 NEUTROPHIL APOPTOSIS AND NECROSIS

Following mean-limited thresholding a binary mask for cellular pixel area was constructed using CellMask^{TM} Orange images and the percentile algorithm. The binary mask was applied to NAP, VE200 and DAPI images, measuring mean fluorescence, the sum of pixel values divided by the number of contributing pixels.

2.5.4 IMAGE CYTOMETRIC ANALYSIS

Three-dimensional image stacks were converted to two-dimensional maximum and sum projections using ImageJ (version 1.52n, Rasband, National Institute of Health, USA). CellProfiler (version 2.2.0) maximum projections were used to identify individual cells as primary objects in the DAPI channel and secondary objects in the CellMask™ channel respectively. Intensity, textural and positional features secondary object were measured and ranked using statistical analyses in Orange (version. 3.0), for objective feature selection. Data were visualised using GraphPad Prism (version 5.01, La Jolla California, USA) or Orange (version. 3.0).

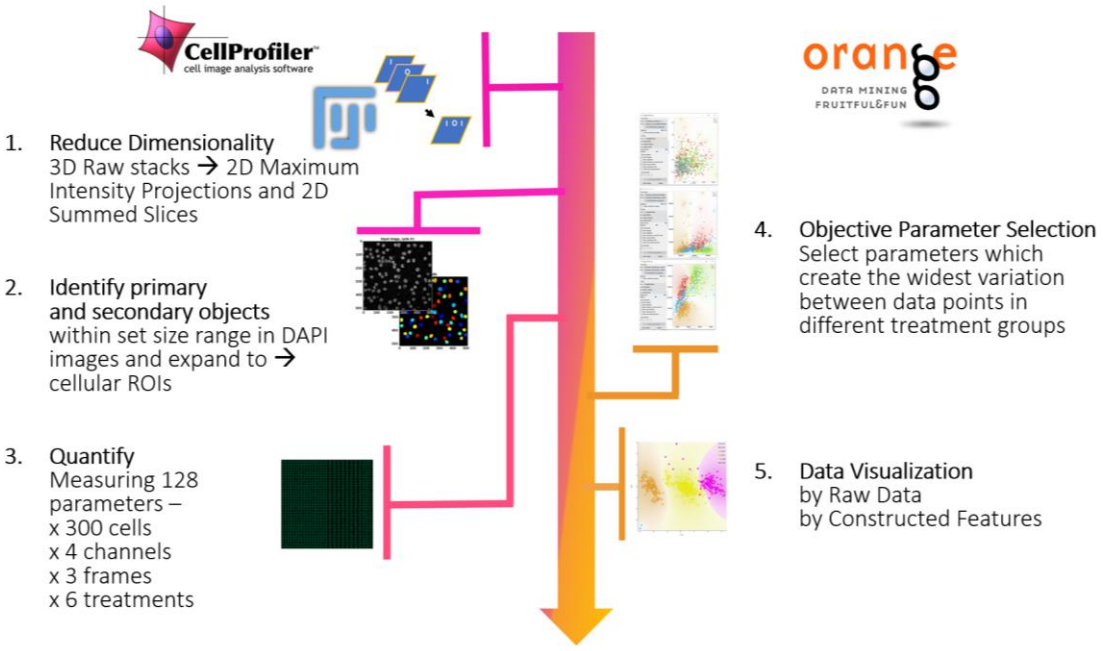

Figure 2.3 Diagram of a data analysis workflow for image cytometric analyses
ImageJ, CellProfiler and Orange software are combined to create two-dimensional projections of three-dimensional image stacks, extract individual cellular data across several imaging features and objectively extract features for data visualisation. For complex classification tasks features are recombined, to visualise data clusters in multidimensional hyperplanes, using principle components analysis.

2.5.5 IMMUNOHISTOCHEMISTRY OF HUMAN TISSUES

488 channel images were analysed in an image cytometric format using CellProfiler (version 2.2) and data was processed using Orange (version 3.0) for visualisation using GraphPad Prism (version 5.01, La Jolla California, USA).

2.5.6 NEURAL NETWORK MODELLING

This study was undertaken by Mr. Peter McGregor. Images were analysed in an image cytometric format using CellProfiler (version 2.2) describing 277 numerical features for six classes, each of approximately one thousand cells, imaged in four channels. Imaging data was class annotated and split into training and evaluation data sets. For each feature the standard score of the training set was calculated and data was normalized to the standard score. The training data set was used to train a neural network with a single hidden layer of size 20 and an output layer of size 6. The training was performed using stochastic gradient descent with a categorical cross entropy loss function for 100 epochs. Using the evaluation data set, the model was evaluated to determine the generalisation accuracy for each class, populating the confusion matrix. The neural network code was created with Python 3.6, using TensorFlow (version 1.14) and numpy (version 1.17).

2.5.7 FIBRED CONFOCAL ENDOMICROSCOPY

Using Versiplayer version 3.0 software consistent pixel minimum and maximum vales were applied to all images of a given data set to prevent image saturation. Framewise histogramming was applied to single-channel 630 or 470 nm images using ImageJ (version 1.52n, Rasband, National Institute of Health, USA).

2.6.0. STATISTICAL ANALYSIS

All experiments were performed at least three times unless otherwise stated and results expressed as mean ± SD where replicates from independent experiments are compared, or mean ± SEM where means of independent replicates were not assessed. Using GraphPad Prism (version 5.01, San Diego California USA) data was analysed by Student's t-test for normally distributed data or Mann-Whitney U test or ANOVA and significance was determined as $p<0.05$ for all laboratory data. Principal components analysis and linear discriminants analysis of data were conducted using Orange (version 3.0).

CHAPTER 3:
CHARACTERISING NEUTROPHIL ACTIVATION WITH NEUTROPHIL ACTIVATION PROBE IN VITRO

3.0.0 INTRODUCTION

NAP is a novel, dendrimeric SmartProbe designed to detect active HNE. This chapter aims to characterise the NAP-HNE interaction, evaluating NAP as a HNE biomarker. This chapter aims to address how NAP signal is affected by conditions that modulate HNE activity *in vivo*, HNE concentration, inhibition and pH change. NAP signal is evaluated as a result of neutrophil activation, due to both pharmacological and physiological stimuli, along with the influence of apoptosis and necrosis as these deviations from the quiescent state may provide clinically meaningful NAP signal. Of particular interest is NAP signal specificity for HNE, at the molecular and cellular level, evaluated in terms of co-released serprocidins and specific inhibition. NAP characteristics established in this chapter inform its utility as a biomarker and experimental design in subsequent chapters.

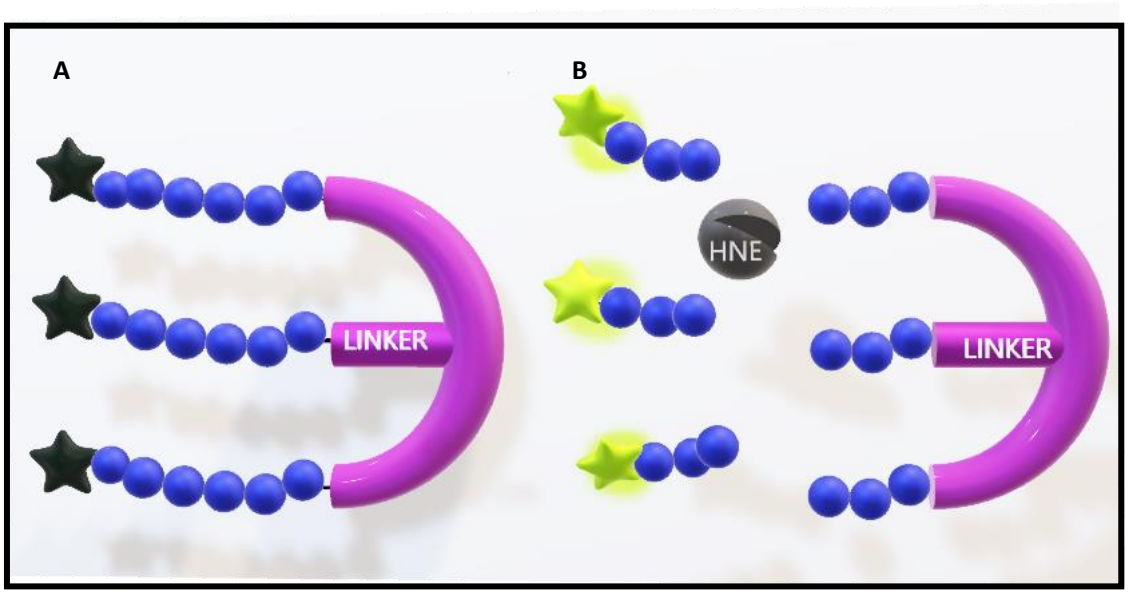

Figure. 3.0 Structure and Function of Neutrophil Activation Probe
Structure of Neutrophil Activation Probe (NAP) **A**) before cleavage, showing fluorescein (green stars), amino acids (blue spheres) and linker (purple). **B**) In the presence of active human neutrophil elastase (HNE, grey, notched sphere) peptide sequences are cleaved alleviating fluorescein vertical quenching.

3.1.0 PHARMACOLOGICAL NEUTROPHIL ACTIVATION

Pharmacological stimuli commonly used to activate neutrophils include phorbol myristate acetate (PMA), calcium ionophore (A23187) and ionomycin. PMA is a potent protein kinase C (PKC) activator.[146] Although PKC is typically calcium-dependent, in the presence of PKC calcium ions are not required for PKC activation. Soluble PKC is auto-inhibited and located in the cytosol.[147] Upon PMA-induced activation PKC undergoes conformational change and translocates from the cytosol, irreversibly inserting into the cellular endo-membrane and dissociating from calcium and PMA.[146] Acting on several targets, activated PKC activates signalling cascades associated with neutrophil activation.[148] In the absence of pharmacological stimulation, PKC isozymes are activated by calcium ions, diacyl glycerol and/or phosphatidyl serine, depending on the class of isozyme.[149]

Ionomycin, a product of *Streptomyces congloblatus*, is a calcium ionophore which facilitates calcium efflux and influx.[150] By increasing intracellular Ca^{2+} ionomycin triggers several neutrophil activation processes including reactive oxygen species generation and NETosis.[151–153] Although PMA and ionomycin both activate PKC and are often used in conjunction in some assays this may prove counterproductive for neutrophil activation. When stimulating NETosis PMA has been found to counter ionomycin induced pro-NETotic signalling highlighting the importance of characterising activation responses in this peculiar cell-type.[154,155]

A23187, referred to as calcium ionophore hereafter, is a calcium ionophore and an antibiotic derived from *Streptomyces charteusensis* fermentation.[156] Stimulating

intracellular Ca^{2+} concentration increase by carrying Ca^{2+} across cell membranes, calcium ionophore relies on extracellular Ca^{2+} concentration to be effective.[157] Calcium ionophore and ionomycin are very hydrophobic and hence are readily rendered ineffective by binding to serum proteins.[158] This technicality can be resolved by avoiding the use of serum proteins or increasing the concentration of calcium ionophores. Calcium ionophore has a long history of use as a stimulus of neutrophil degranulation, eliciting its effect rapidly and at low concentrations.[159,160]

3.1.1 SERINE PROTEASES IN APOPTOSIS

Gilligan *et al.* found that all granules translocate to the neutrophil plasma membrane during priming and late apoptosis, externalising total serine protease content. However Witko-Sarsat *et al.* demonstrated that PR3 is expressed on the surface of a subset of unactivated neutrophils, promoting vasculitis.[161] The Witko-Sarsat group found that PR3 exists in a granule-independent secretory vesicle pool which is externalized during apoptosis by PR3-phospholipid scramblase 1 interaction.[162] PR3 externalization impairs macrophage efferocytosis of neutrophil apoptotic bodies.[162] PR-3 coated microvesicles enhance neutrophil respiratory burst and remove the inhibitory effect of apoptotic microvesicles on respiratory burst in a combination that may potentiate systemic oxidative endothelial cell damage.[163]

Macrophage-mediated efferocytosis of neutrophil apoptotic bodies is hindered not only by PR3 but also HNE which cleaves phophatidyl serine receptor.[164] Efferocytosis stimulates anti-inflammatory cytokine release and is necessary for the

resolution of inflammation. Uncleared apoptotic bodies are prone to proinflammatory necrotic decay and further release of PR3 and HNE. Secretory leukocyte inhibitory protein (SLPI) inhibits cathepsin G and HNE. Following gene delivery Henriksen *et al.'s* macrophages overexpressed SLPI and regained efferocytotic function.[165] HNE also impairs efferocytosis by cleaving surfactant protein-D.[166] In addition to its effects on neutrophils, HNE promotes and smooth muscle cell apoptosis while inhibiting leukaemia and lung adenocarcinoma cell apoptosis.[59,167,168] HNE also promotes lung epithelial cell apoptosis in a mechanism that may promote emphysema.[169] And endothelial cell apoptosis and autophagy but not necrosis or necroptosis were stimulated by HNE.[170]

Cathepsin G (CG) induces apoptosis of bone-marrow neutrophils in the absence of serpin B1, a PR3, HNE and CG inhibitor. This was demonstrated by Benefara *et al.* when their serpin B1 knockout mice developed CG-dependent neutropenia.[171] The Benefara group also showed serpin B1 was necessary for neutrophil survival in a murine model of bacterial lung infection. The relative importance of CG, PR3 and HNE in neutrophil apoptosis and necrosis at the inflammatory site is less clear particularly as PR3 and HNE-mediated decrements in efferocytosis could potentiate neutrophil necrosis *in vivo*. It seems dis-regulated CG release can also lead to cardiomyocyte detachment-induced apoptosis (anoikis). A detailed mechanism for CG-mediated cardiomycotye anoikis has been elucidated by Rafiq *et al.* who show CG acts through EGFR, SHP2 and finally focal adhesion kinase.[172]

3.1.2 SERINE PROTEASE KINETICS

For biomarker development, an important consideration is specificity. Off-target effects can generate false positive readouts or simply interfere with true positive signal generation. HNE is one of a family of enzymes known as serine proteases. The serine proteases are stored in the azurophil granules and released simultaneously. By measuring the effect of each serine protease on probe signal generation important concerns about probe specificity can be addressed. Understanding the relative activities of similar proteases may help to explain findings pertaining to activated neutrophil supernatants. HNE is the most abundant serine protease stored in neutrophils such that it is likely to outcompete protease 3 (PR3) and cathepsin G (CG) for common substrates upon degranulation. HNE's rate of substrate cleavage (enzyme velocity) is often reported as faster than that of PR3 or CG. When Korkmaz *et al.* derived fluorescent substrates from the reactive site loops of endogenous inhibitors, alpha-1-protease inhibitor (α-1-PI) and serpin B1, HNE showed 14 and even 50 fold increases against the next fastest serine protease.[132] Such evidence supports the view that HNE is the "fastest" serine protease however relative enzyme velocities can be altered with changes in peptide sequences and lengths to preferentially expedite interactions with a particular protease.

3.1.3 NAP TOXICITY

The toxicity of NAP was comprehensively assessed prior to the characterisation presented here, in preparation for an early phase 1 clinical trial. NAP toxicity was assessed via single dose studies in rats, *In vitro* genotoxicity and local tolerance in rat lungs as well as gathering information from studies of fluorescein and poly-ethylene glycol constituents. NAP did not induce mortality, pathological events or mutagenesis and its constituents are non-toxic (unpublished results). The early phase 1 clinical study confirmed the safety of micro-dosed NAP (10 µg) in man. (NCT01532024)

3.1.4 HYPOTHESIS AND AIMS:

Hypothesis: Neutrophil Activation Probe can sensitively and specifically detect HNE activity *in vitro* and intracellularly in primary human neutrophils.

Aims:

1) Molecularly characterise NAP signal in terms of:

i. Dose dependence

ii. pH dependence

iii. Temperature dependence

iv. HNE selectivity

2) Cellularly characterise NAP signal in terms:

i. Neutrophil activation with 1 µM Calcium Ionophore

ii. Concomitant neutrophil activation and HNE inhibition

iii. Imaging intracellular HNE activity in Neutrophils

   a. by pharmacological stimulus

   b. by physiological stimulus

iv. Detecting HNE activity in ageing, apoptotic, necrotic and activated neutrophils

   a. by whole-cell fluorescence via flow cytometry

   b. by intracellular fluorescence via image cytometry

3.2.0 RESULTS

3.2.1 CHARACTERISING THE DOSE-FLUORESCENCE RELATIONSHIP FOR NAP

To establish a concentration of NAP which would be useful for enzymatic studies with HNE, 100 nM HNE was incubated with a range of NAP doses. At 0.5 µM NAP, enzyme activity was not readily observable after 60 minutes incubation at 37^{o}C. Significant differences between all NAP concentrations developed after 20 minutes of incubation, in a dose dependent fashion, and the limit of detection in this system was 1 µM NAP. In agreement with previous work in the group and for practicable purposes, a 3 µM concentration of NAP was selected for use in future experiments.

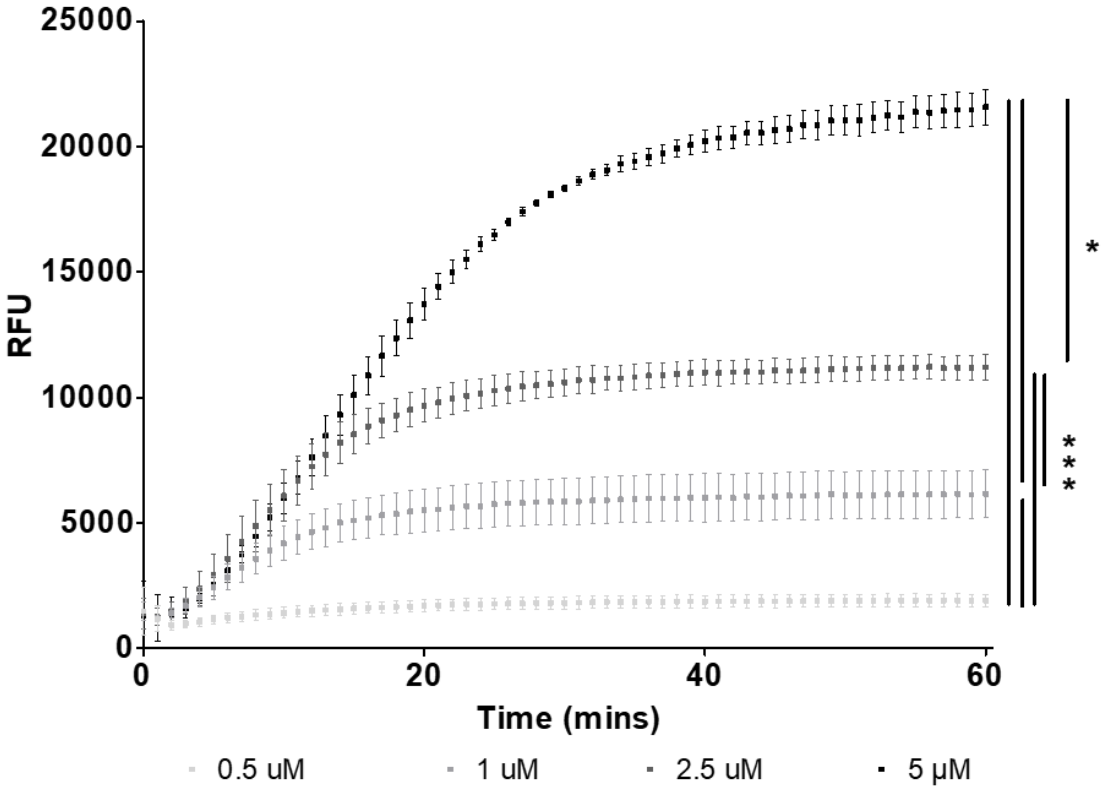

Figure 3.1 NAP signal is dose dependent
Dose-dependence of NAP signal was demonstrated by measuring fluorescence at 0.5, 1, 2.5 and 5 µM of NAP incubated with 100 nM HNE. Values in the graph represent mean ± SEM, *P* values were calculated using Friedman test and a Dunn's multiple comparisons, ** *P* <0.01, n=3.

3.2.2 CHARACTERISING NAP: TEMPERATURE-FLUORESCENCE RELATIONSHIP

Prior to cleavage by active HNE, NAP emits dim, background fluorescence at 525 nm when excited by 488 nm light. Each molecule of NAP contains 3 fluorescein moieties and fluorescein is a pH indicator.[61] To understand how fluorescein's and hence NAP's pH dependent quantum yield may influence subsequent measurements and to look for any temperature dependence in baseline fluorescence, the effect of pH and temperature variations were investigated. When uncleaved NAP was heated to 20, 25 and 30 ^{o}C in pH 5, 7 and 9 solution, NAP fluorescence intensity in pH 5 solution was similar to that of distilled water. Fluorescence emissions of NAP at pH 7 and 9 were both significantly greater than that of pH 5 and the trend between temperature points indicates quantum yield is optimal at 25^{o}C. pH produces the majority of variation between samples and only 0.2% variation can be attributed to effect of temperature in this assay. To further understand the effect of temperature on the fluorescent properties of NAP the amount of light NAP can absorb across a temperature range was measured. NAP absorption of 488 nm light at 26.1^{o}C was significantly greater than that of higher temperatures. NAP quantum yield is most efficient under alkali pH, at 26.1 ^{o}C.

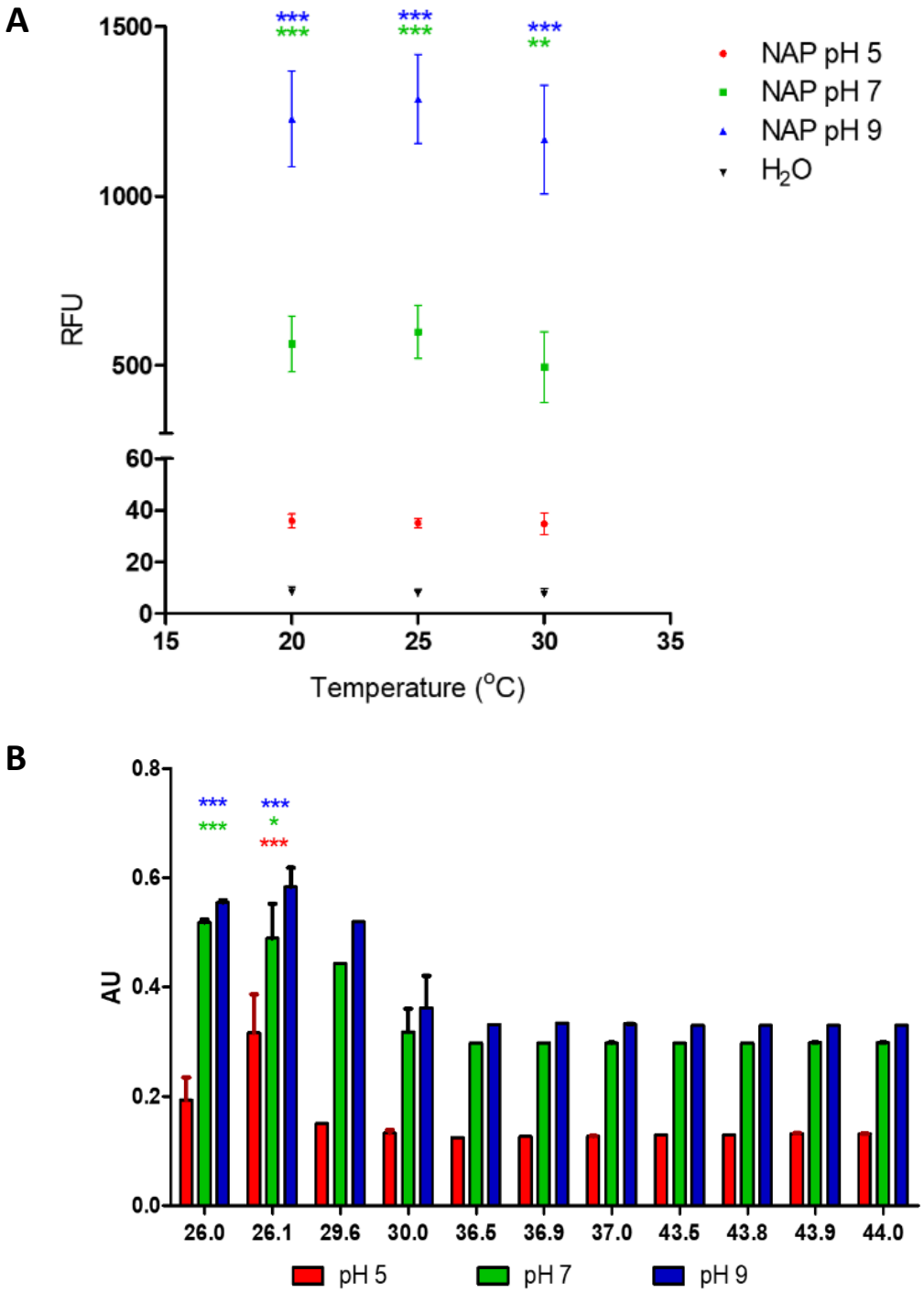

Figure 3.2 Baseline NAP signal varies with pH and temperature
A) NAP fluorescence was measured at 20, 25 and 30°C at pH 7. n=4 **B)** NAP absorbance at 485 nm was measured with increasing temperature.
Values represented are mean ± SEM and *P* values were calculated using one-way ANOVA and Bonferroni multiple comparisons test. * *P* <0.05 ** *P* <0.01 *** *P* <0.001, n=3

3.2.3 CHARACTERISING NAP: THE PH-FLUORESCENCE RELATIONSHIP

As seen in **Fig. 1.2**, alkali conditions increase NAP quantum yield, in addition, alkali conditions are reported to increase HNE catalytic rate[61] and both these effects will promote increased NAP signal. To measure the effect of alkalinisation on HNE activity, a range of HNE concentrations were incubated at 37^{o}C in pH 7 and 9 buffer with a coumarin labelled HNE substrate. Unlike NAP, a coumarin labelled HNE substrate can be taken as a measure of HNE activity alone because coumarin displays pH invariant fluorescence emission. HNE activity at pH 9 was significantly greater than that of pH 7 at each enzyme dose with a strict linear relationship (r^2=0.98) whereby a 2-log increase in pH, from pH 7 to pH 9, produces a 4-fold increase in HNE activity (see equation, V = RFU at a given HNE concentration). Because of the significant differences in enzyme activity at pH 7 and 9, the relatively suppressed activity of HNE at pH 7 approaches maximal enzyme activity, for this concentration of coumarin-labelled substrate, at 100 nM HNE. HNE activity at pH 9 shows direct proportionality between HNE concentration and HNE activity at these physiologically relevant HNE doses.

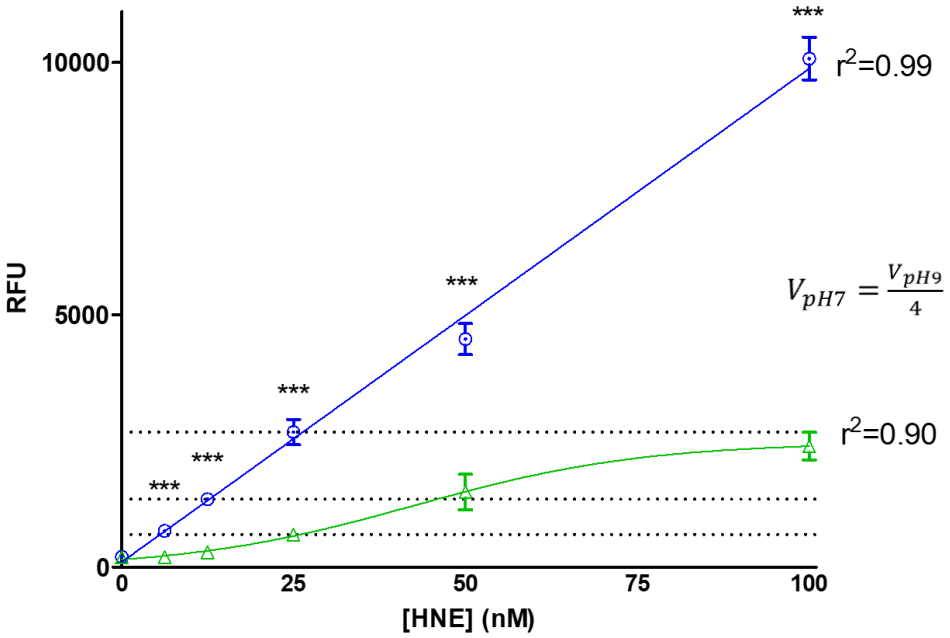

Figure 3.3 HNE activity increases in alkali pH.
Activity of 6.25, 12.5, 25, 50 and 100 nM purified HNE with 1 µM AAPV-AMC at pH 7 (green) and pH 9 (blue). Values in the graph represent mean ± SEM, *P* values were calculated using two-way ANOVA and Bonferroni multiple comparisons test, *** *P* <0.0001 n=3.

3.2.4 CHARACTERISING THE SERPROCIDIN SPECIFICITY OF NAP: ABSOLUTE FLUORESCENCE

In addition to temperature and pH fluctuation, competition with serprocidins is a physiologically relevant parameter to consider for NAP characterisation. Due to the effect of pH on serprocidin activity, HNE was compared to cathepsin G (CG) and proteinase 3 (PR3) at physiologically relevant HNE doses, 6.25 and 100 nM and at pH 5, 7 and 9 at 37^{o}C. At 6.25 nM serprocidins elicit negligible NAP signals at pH 5, 7 and 9, instead NAP background fluorescence (dotted lines) contributes the majority of measurements for each enzyme. At 100 nM CG and PR3 generate modest increases in NAP signal after background subtraction however HNE-derived NAP signal is significantly increased above that of CG and PR3 respectively by the following fold changes: 4.06 and 3.35 at pH 5, 2.41 and 3.86 at pH 7, 5.73 and 5.52 at pH 9.

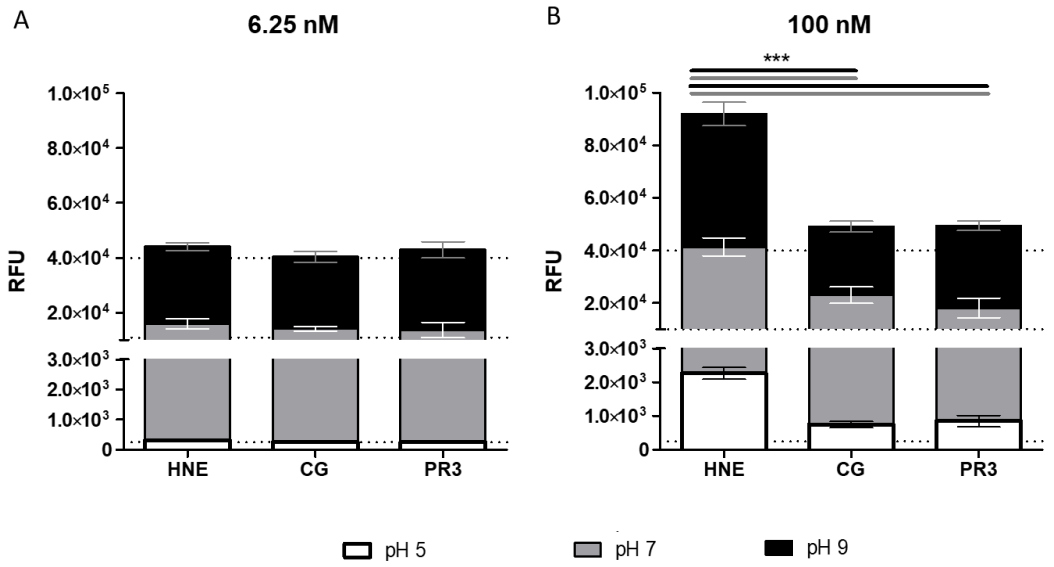

Figure 3.4 NAP selects for HNE activity at high physiological enzyme concentrations
Average of NAP fluorescence over 10 minutes, after 50 mins incubation with HNE, proteinase 3 or cathepsin G at **A)** 6.25 nM **B)** 100 nM at pH 9 (black bars), pH 7 (grey bars) and pH 5 (white bars). Dotted lines indicate uncleaved NAP signals of 2.5, 100 and 400 x10^2 RFU at pH 5, 7 and 9 respectively in both graphs. Values represent mean ± SEM and *P* values were calculated using two-way ANOVA and Bonferroni multiple comparisons test, *** *P* <0.001, n=3

3.2.5 CHARACTERISING THE SERPROCIDIN SPECIFICITY OF NAP: ENZYME ACTIVITY

Investigating the enzyme selectivity of NAP among the serprocidins reveals that NAP can be cleaved by HNE, PR3 and CG. NAP is cleaved more rapidly by HNE than competing serprocidins in five of six cases where enzyme concentration and pH are comparable. When enzyme concentration or pH are increased to enhance the enzyme velocity of HNE, and competing serprocidins, HNE-selectivity increases. The ability to augment HNE selectivity in this manner is pertinent to the intracellular dynamics of phagocytosis during which phagolysosomal pH and serprocidin activity increase.[61] At 6.25 nM all serprocidins demonstrate relatively slow enzyme velocities ranging from 0.5 – 171.7 RFU/min (**Fig.3.5 A-C**). Under these conditions, only one of the 9 comparisons of serprocidin-generated NAP signal (3 comparisons for pH 5, 7 and 9 respectively) is significant, the PR3 to CG comparison at pH 9 (**Fig.3.5 C**). At the 100 nM serine protease concentration, NAP demonstrates a high degree of HNE-selectivity as HNE-derived NAP signals are significantly higher than PR3 and CG irrespective of pH (**Fig.3.5 D-F**). In contrast to HNE, there are no significant differences between PR3 and CG at 100 nM.

Although 6.25 nM HNE-derived NAP signal is not significantly different from 6.25 nM PR3 or CG-derived signals, there is a trend towards increased selectivity for HNE. 4 of the 6 possible HNE-PR3 or HNE-CG comparisons, trend towards increased NAP signal generation with HNE, with fold increases ranging from 1.4 - 2.6 (**Fig.3.5**

G). At 100 nM, these trends become significant fold-increases ranging from 2.7 to 34, largely dependent on pH (**Fig.3.5 G**).

At constant enzyme concentration pH also influences the rate of NAP cleavage. CG enzyme velocity decreased from 106.7 at pH 7 to 28.8 at pH 9, however in all other instances increasing pH, increased the enzyme velocity of the serprocidins, whether this increase was from pH 5 to 7 or pH 7 to 9. The influence of pH on fluorescein fluorescence can contribute to these measurements and was investigated with respect to HNE (see **Fig. 3.3**). Despite the pH sensitivity of fluorescein, increasing pH appears to increase NAP's ability to select for HNE. There is a growing disparity between HNE-derived NAP signal and that of other serprocdidins as average fold increases increase with alkalinisation from 2.6 (pH5) to 6.3 (pH7) to 19.6 (pH 9).

Finally, among the serprocidins, HNE demonstrates the greatest capacity to accelerate enzyme velocity in response to increased enzyme concentration. HNE's greater intrinsic ability to cleave NAP is demonstrated across pH 5, 7 and 9 with fold changes that range from 9.9 at pH7 to 19.2 at pH9 (**Fig.3.5 H**). Five of the six fold changes generated by PR3 and CG are less than the lowest of the HNE fold changes. And the single PR3 fold increase which falls within the HNE range, relies on a low baseline, its enzyme velocity being 2.6-fold less than that of HNE at 6.25 nM (PR3 =0.5 RFU/min, HNE= 1.3 RFU/min) as opposed to high enzyme velocity at 100 nM (PR3 8.7 RFU/min, HNE 23.1 RFU/min).

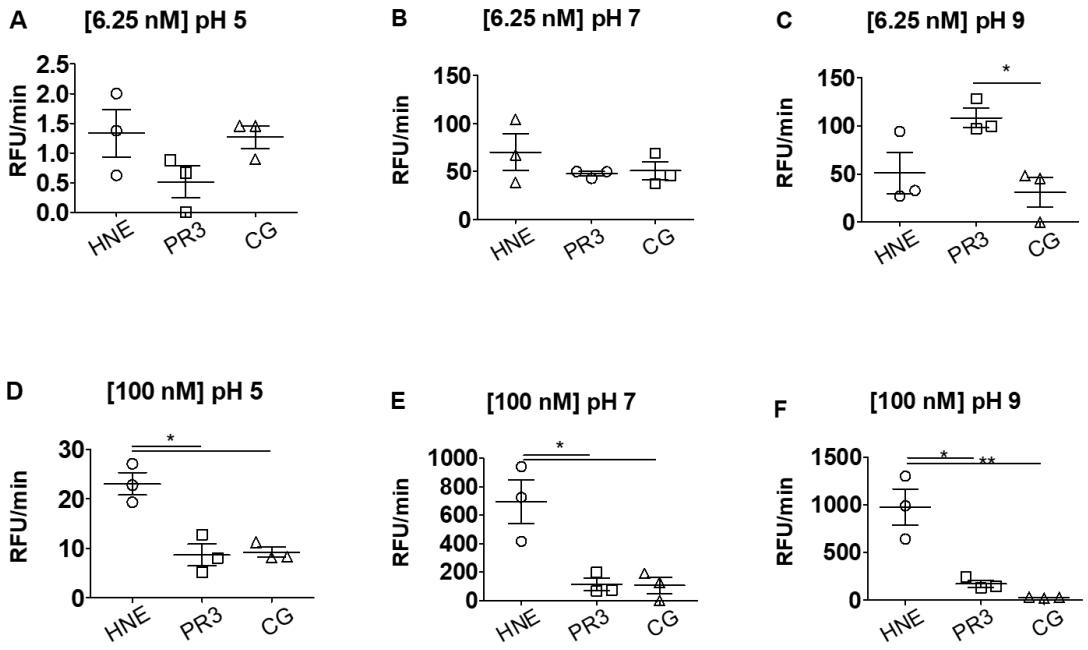

G **HNE enzyme velocity fold increase over other serprocidins**

	6.25 nM			100 nM		
pH	**PR3**	**CG**	**Mean**	**PR3**	**CG**	**Mean**
5	2.6	1.0	1.8	2.7	2.5	2.6
7	1.5	1.4	1.5	6.1	6.5	6.3
9	0.5	1.7	1.1	5.7	34.0	19.9

H **Enzyme velocity fold increase between 6.25 and 100 nM conditions**

pH	**HNE**	**PR3**	**CG**
5	17.3	16.9	7.3
7	9.9	2.4	2.1
9	19.2	1.5	0.9

Figure 3.5
HNE selectivity of NAP signal increases with increasing serprocidin concentration and pH
The tangents of progress curves, describing enzyme activity over time, were averaged after 5 mins incubation with HNE, proteinase 3 or cathepsin G at **A-C)** 6.25 nM and **D-F)** 100 nM. **G**) Table showing fold-increase of HNE enzyme velocities over PR3 and CG. **H)** Table showing fold-increase between 6.25 and 100 nM enzyme velocities. Values represent mean ± SEM and *P* values were calculated using two-way ANOVA and Bonferroni multiple comparisons test, * *P* <0.05 *** *P* <0.001, n=3

3.2.6 THE EFFECT OF CALCIUM IONOPHORE ON NEUTROPHIL ADHESION MOLECULE EXPRESSION

From an initial MFI of 5 μg/mL CD11b expression and 5 μg/mL CD62L expression, neutrophils stimulated with 1 μM calcium ionophore showed 9.33 fold increase in CD11b expression and concomitant 3.10 fold decrease in CD62L expression by flow cytometric analysis. Following Percoll blood preparation there is a significant difference between untreated and 1 μM calcium ionophore activated neutrophils.

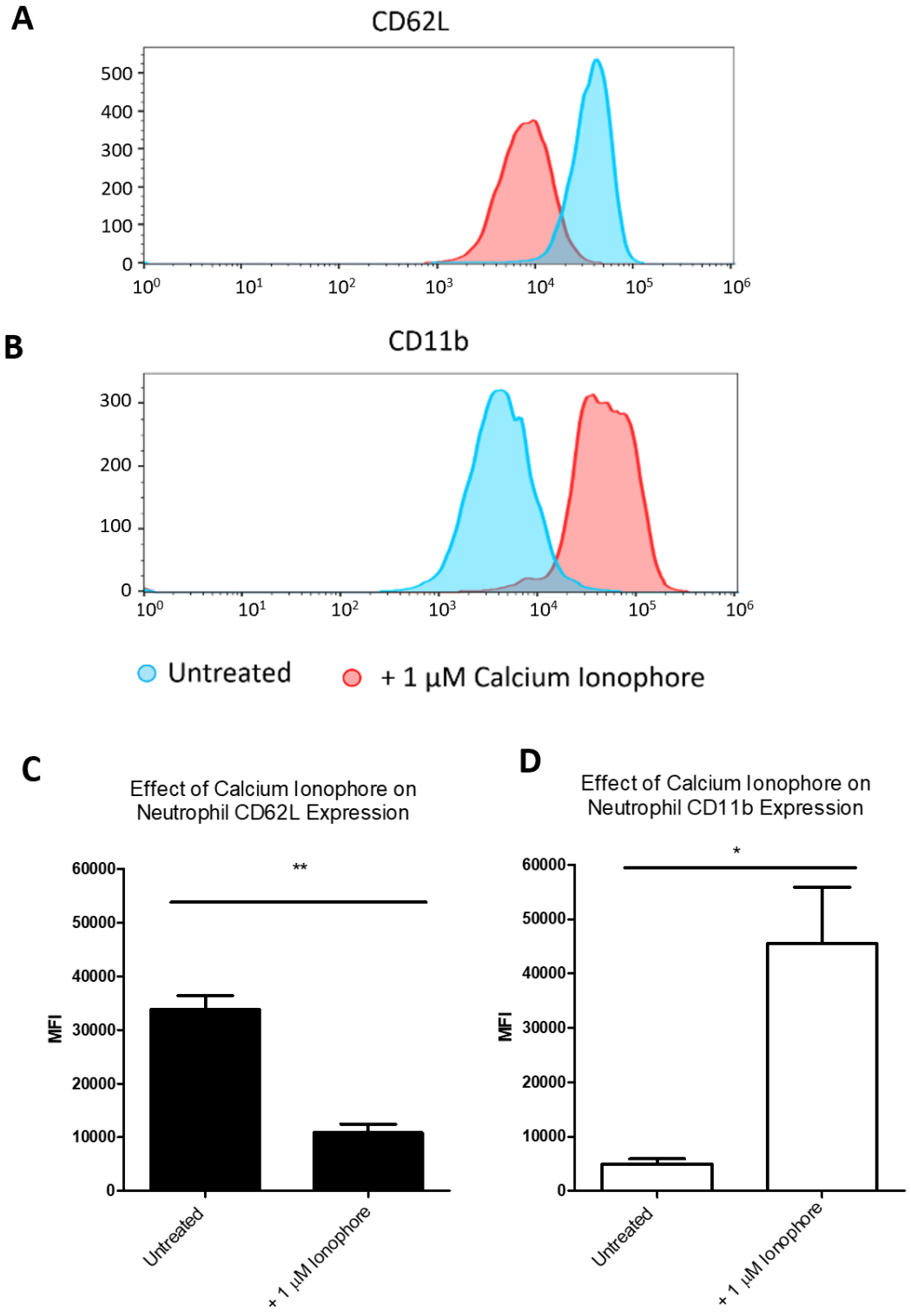

Figure 3.6 Percoll blood preparation derived neutrophils are sensitive to activation
Median fluorescence intensities of neutrophil populations labelled for cell surface **A)** CD62L expression and **B)** CD11b expression, analysed by flow cytometry. Graph values represent mean ± SEM, *P* values were calculated by t test, **P*<0.05 ***P*<0.01 n=3.

3.2.7 THE SENSITIVITY OF NAP TO PHARMACOLOGICAL HNE INHIBITION

Following stimulation with calcium ionophore, NAP signal is detectable in neutrophil-derived supernatants over a range of active HNE concentrations. When Sivelestat, a small-molecule inhibitor, specific for HNE, is added to activated neutrophil derived supernatants dose dependent inhibition is detectable using NAP. As varying active HNE concentration in neutrophil-derived supernatants produces significant differences in NAP fluorescence, NAP can be used to distinguish between these conditions as a sensitive measure of extracellular HNE.

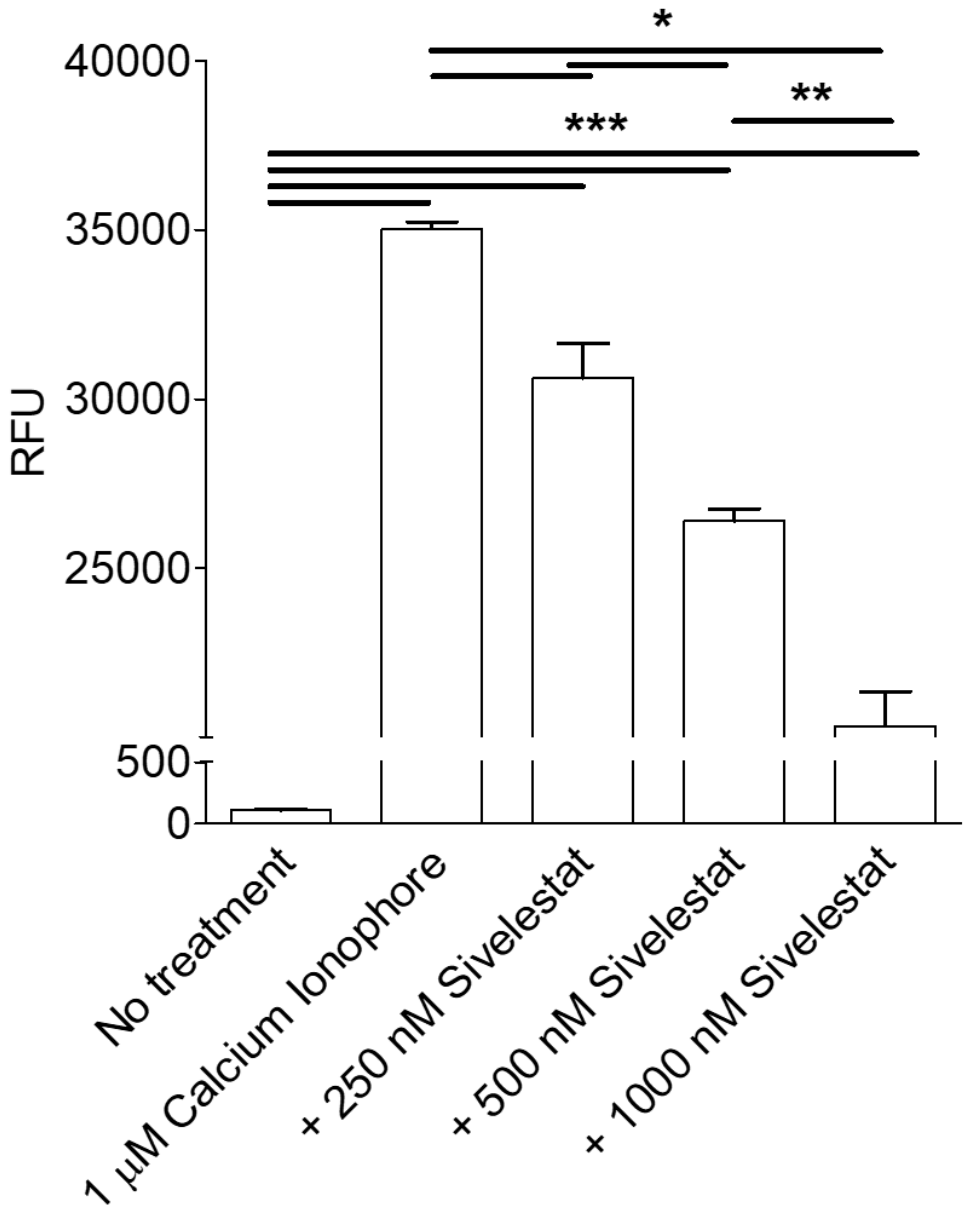

Figure 3.7 NAP detects HNE release and pharmacological inhibition
Measuring HNE activity of $2x10^7$/mL neutrophil supernatant under increasing pharmacological inhibition (Sivelestat). Values in the graph represent mean ± SEM, *P* values were calculated using repeated measures one-way ANOVA and Bonferroni's multiple comparison test, ***P*<0.01 *** *P* <0.001 n=3.

3.2.8 INTRACELLULAR NAP SIGNAL KINETICS DURING PHARMACOLOGICAL NEUTROPHIL ACTIVATION

Confocal microscopy reveals that in addition to extracellular fluorescence increase, NAP enters neutrophils upon calcium ionophore stimulation, generating bright intracellular puncta. NAP signal was blocked when calcium ionophore is added to cells preincubated with Sivelestat (100 µM), a specific and irreversible HNE inhibitor. Image analysis reveals that neutrophils incubated with and without Sivelestat show the same dim fluorescence prior to the addition of the calcium ionophore stimulus, which dilutes NAP to a 3 µM final concentration, decreasing all fluorescence values. Neutrophils without Sivelestat rapidly increase intracellular fluorescence, 0.047 – 0.463 mean pixel intensity (MPI), becoming significantly different from the Sivestat condition (0.010 – 0.011 MPI) at 2 minutes after adding stimulus. Neutrophils without Sivelestat continue to increase to a plateau of 0.824 MPI over the next 3 minutes, stable for the duration of the 10-minute time course. Sivelestat inhibition prevents signals from exceeding 0.06 MPI over the time course so that differences between both conditions remain significantly different. The removal of NAP signal by the addition of Sivelestat alone, demonstrates that NAP signal is a specific indicator of HNE activity in primary human neutrophils *in vitro*.

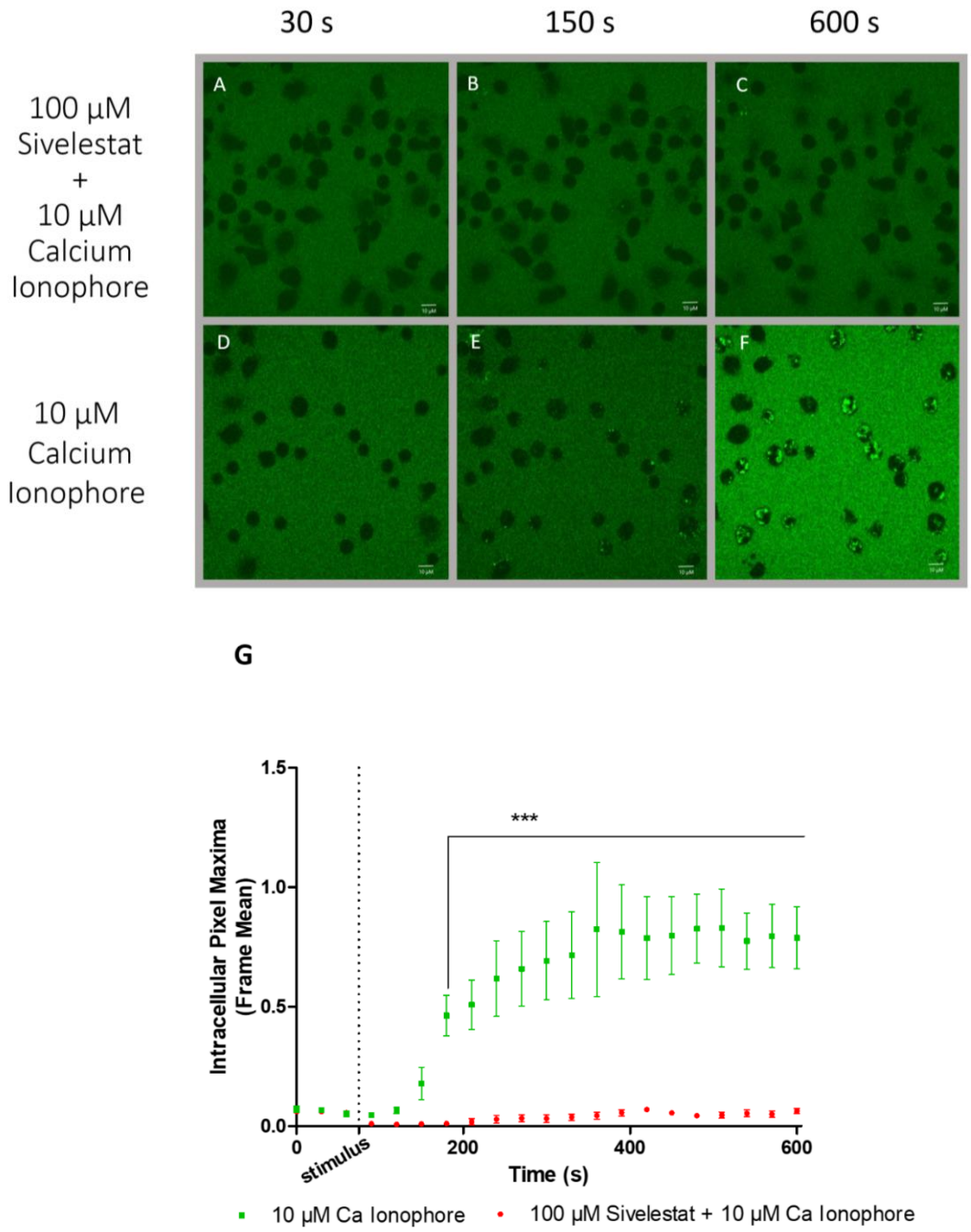

Figure 3.8 HNE is required for Neutrophil Activation Imaging using NAP
Images represent 10-minute time lapse of neutrophils stimulated with 10 µM calcium ionophore **A-C)** with and **D-F)** without 100 µM Sivelestat. **G)** Image analysis plotting mean intracellular fluorescence intensities of neutrophil populations at 30 second intervals. Graph values represent mean ± SEM, *P* values were calculated by two-way ANOVA and Bonferroni multiple comparisons test, **P*<0.05 ***P*<0.01 ****P*<0.001 n=3.

3.2.9 INTRACELLULAR NAP SIGNAL KINETICS DURING BACTERIAL PRODUCT-INDUCED NEUTROPHIL ACTIVATION

The previous time lapsed, intracellular NAP signal experiment was modified to understand the implications of HNE imaging in neutrophils under more physiologically relevant conditions. All conditions appear similar in morphology and fluorescence prior to fMLF stimulation (**Fig. 3.9.A,D,G**). Image analysis of intracellular fluorescence revealed similar values across all conditions prior to fMLF stimulation (0.00 - 0.02 intracellular pixel maxima **Fig. 3.9J**) irrespective of LPS or LPS/fMLF/Sivelestat treatment. At 1-minute post stimulus, LPS/fMLF treated neutrophils develop 0.09 intracellular pixel maxima becoming significantly more fluorescent than untreated and LPS/fMLF Sivelestat conditions (<0.01 and 0.00 intracellular pixel maxima respectively **Fig. 3.9.J**). Bright intracellular signals in LPS/fMLF neutrophils are maintained for 4.5 minutes, enabling discrimination between activated and untreated neutrophils. At 7.5 minutes, LPS/fMLF signals lose statistical significance, but these signals still exceed those of LPS/fMLF Sivelestat treated or untreated neutrophils allowing activation detection under more stringent thresholding (**Fig. 3.9.J**).

Changes in neutrophil morphology (**Fig.3.9.E,F** and **H,I**), observed in concomitant brightfield images, showed all neutrophils becoming activated upon fMLF stimulation in the LPS/fMLF Sivelestat treated condition, as in the LPS/fMLF only condition.

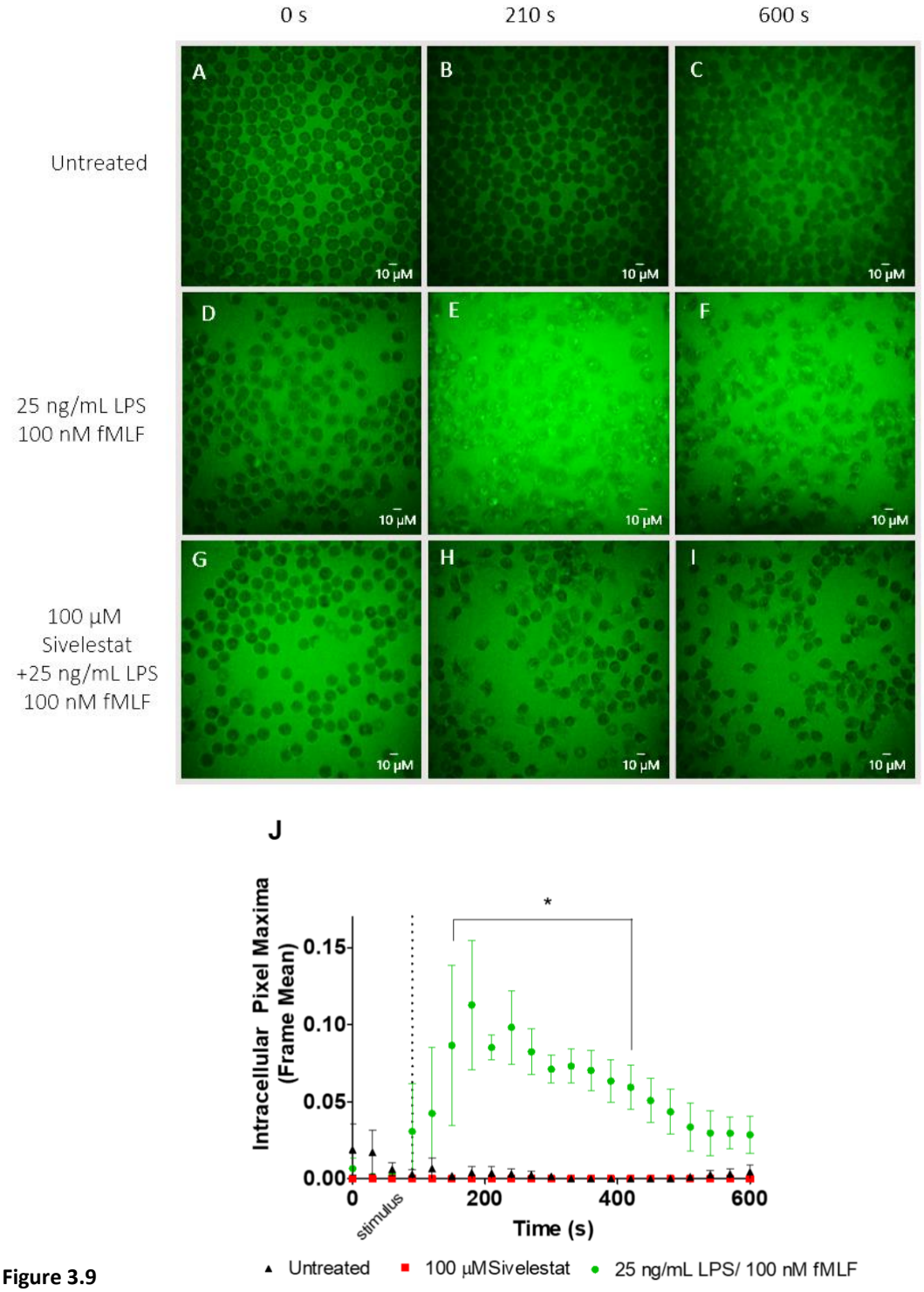

Figure 3.9

In response to bacterial products neutrophil activation is rapidly detectable with NAP

Images represent 10-minute time lapse of **A-C)** unstimulated neutrophils, **D-F)** neutrophils primed with 25 ng/mL LPS and activated with 100 nM fMLF and **G-I)** 100 µM Sivelestat followed by 25 ng/mL LPS and 100 nM fMLF treatment. **J)** Image analysis plotting mean intracellular fluorescence intensities of neutrophil populations at 30 second intervals. Graph values represent mean ± SEM, *P* values were calculated by two-way ANOVA and Bonferroni multiple comparisons test, **P*<0.05 n=3.

3.3.0 DETECTING NEUTROPHIL ACTIVATION ACROSS THE NEUTROPHIL LIFESPAN: WHOLE-CELL FLUORESCENCE

To investigate the effects of changing cell viability on neutrophil activation detection, neutrophils were incubated with and without 1 µM calcium ionophore over a twenty-hour period so that untreated and activated viable, apoptotic and necrotic populations could be compared by NAP staining. NAP was added to samples immediately following Percoll blood preparation, a 2-hour protocol (2 hrs) and then at 4 (6 hrs) and 16 (20 hrs) hour intervals. Flow cytometric analysis reveals that, apoptotic and necrotic populations comprise 6.2 and 2.5% of neutrophils respectively at 6 hours and 36.9 and 28.8% of neutrophils respectively at 20 hours. Following activation, NAP signal in viable activated neutrophils begins to plateau at 6 hours (173 MFI), achieving only slight increase at 20 hours (177 MFI, **Fig. 3.10.D**). By contrast NAP signal in viable untreated neutrophils remains low throughout the time course with NAP signals of 21.7, 21.0 and 37.0 MFI at 2, 6 and 20 hours respectively. Significant differences occur between activated and untreated viable neutrophils at 6 and 20 hours.

Following activation, NAP signal in apoptotic activated neutrophils increases 41.7 MFI/hr from 2 (53.8 MFI) to 6 (220.6 MFI) and then by 23.2 MFI/hr until the 20 hour timepoint (546.0 MFI, **Fig. 3.10.E**). Apoptotic untreated neutrophils show a similar trend in NAP staining to viable untreated neutrophils remaining low across the entire time course (24.1 MFI at 2 hrs, 23.9 MFI at 6 hrs) but increasing at 20 hours

(54.7 MFI). Despite the 9.3-fold increase in NAP signal at 6 hours, the only significant difference is observed at 20 hours.

Following activation, NAP signal in necrotic activated neutrophils shows the least variation in NAP signal generation over time (**Fig. 3.10.F**) increasing 20.4 MFI/hr from 2 hours (107.2 MFI) to 6 hours (188.6 MFI) and then 33.5 MFI/hr until the 20-hour timepoint (657.8 MFI). Although NAP signals in necrotic untreated neutrophils are the highest of the untreated populations (at 56.9, 58.3 and 90.0 MFI for the 2, 6 and 20-hour timepoints respectively) these are still relatively low values compared to activated viable and apoptotic cells. Significant differences occur between activated and untreated necrotic neutrophils at 6 and 20 hours.

Confocal microscopy of ageing neutrophil populations activated with 1 µM calcium ionophore in 3 µM NAP solution reveal distinct intracellular signal patterns for stimulated (**Fig. 3.10.H** bright intracellular puncta, green arrow), necrotic (whole-cell dim fluorescence, red arrow) and neutrophils before responding to stimulus, which are void of NAP signal appearing untreated (no fluorescence, grey arrow).

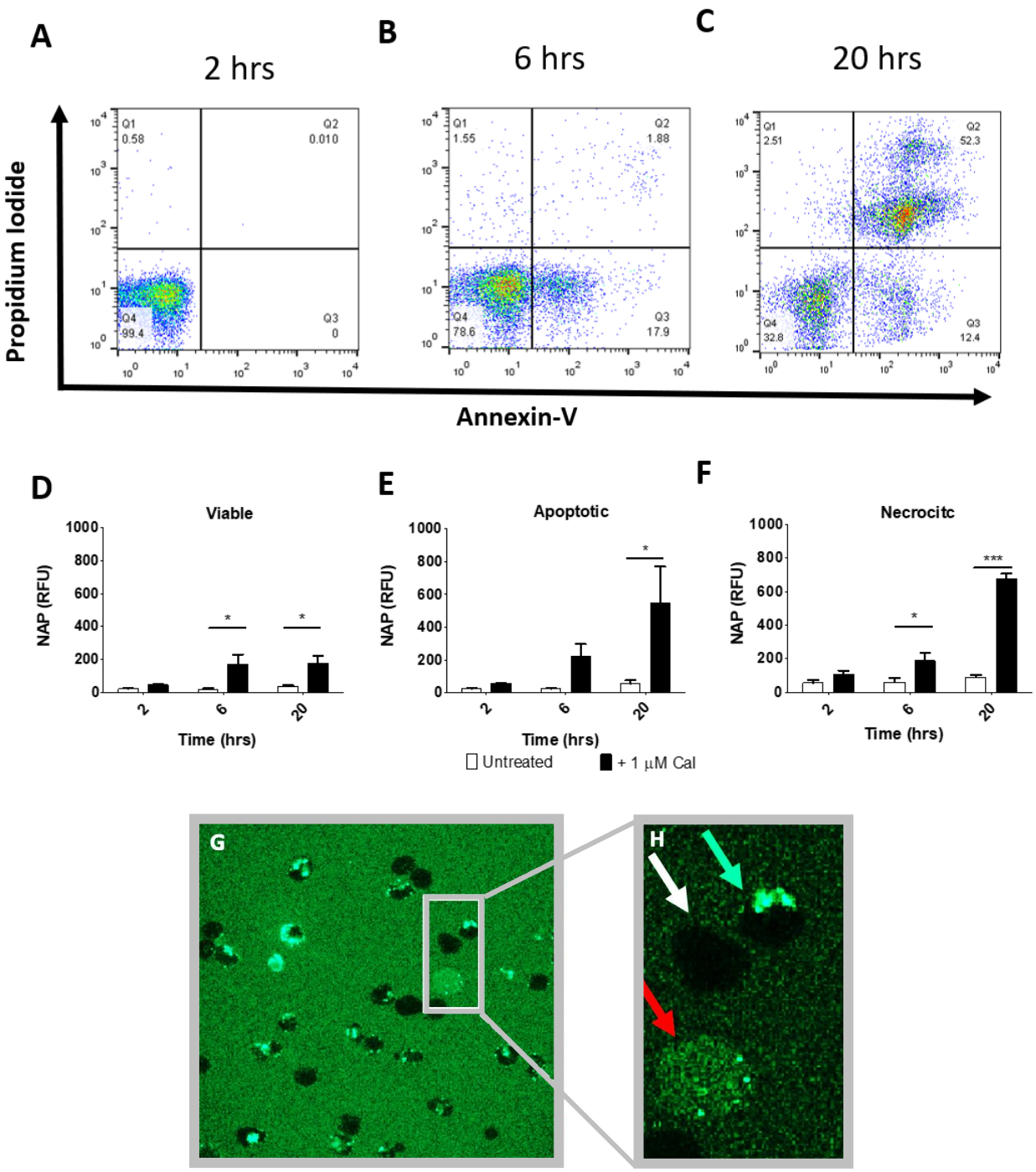

Figure 3.10 NAP continues to report activation as activated neutrophil populations age
Representative dot plots showing viable, apoptotic and necrotic neutrophil populations by propidium (1:300) iodide and annexin-V-AF647 (1:200) staining at **A)** 2 **B)** 6 and **C)** 20 hrs. Bar charts of 3 µM NAP staining in **D)** viable **E)** apoptotic and **F)** necrotic neutrophil populations, as determined by flow cytometry, show median fluorescence intensities of neutrophil populations with and without 1 µM calcium ionophore treatment at 2 hours. Values represent mean ± SEM, *P* values were calculated using two-way ANOVA and Bonferroni multiple comparisons test, * *P* <0.05, *** *P* <0.001, n=3. **G)** representative confocal image of activated neutrophils at 6 hrs **H)** magnified example of unactivated (grey arrow) activated (green arrow) and activated necrotic (red arrow) neutrophils.

3.3.1 DETECTING NEUTROPHIL ACTIVATION ACROSS THE NEUTROPHIL LIFESPAN: INTRACELLULAR FLUORESCENCE

Neutrophils accumulate NAP signal in different patterns of intracellular distribution when activation as opposed to necrosis leads to neutrophil staining (see **Fig. 3.10.H**). Confocal microscopy and image analysis were combined to interrogate the effect of changing neutrophil viability on NAP signal, specifically with regard to intracellular maxima pixels. Membrane impermeant DAPI staining shows significant increase in cell death in the untreated population by 20 hours generating 730, 994 and 2922 RFU at 2, 6 and 20 hrs respectively (**Fig. 3.11.M)**. The untreated population is increasingly composed of apoptotic and necrotic neutrophils over time (see **Fig. 3.10.A-C**) and this increase in DAPI staining is blocked by the addition of a pan-caspase inhibitor (QVD). Stimulating neutrophils with 1 µM calcium ionophore significantly increases DAPI staining immediately (at the 2-hour timepoint) with (1987 RFU) and without (2212 RFU) pan-caspase inhibitor treatment.

NAP signal shows a similar pattern of low staining in untreated and QVD treated neutrophils and high staining with 1 µM calcium ionophore treatment. These differences are much more pronounced such that a log scale is necessary to represent changes in NAP signal over time. By intracellular pixel maxima, increases in NAP signal in the mixed untreated population can be appreciated over time (1.9, 6.1 and 225.7 RFU and 2, 6 and 20 hours respectively) such that the 20-hour signal is significantly greater than the earlier timepoints. Activated to untreated

neutrophil NAP signal comparisons are also much clearer with 16.8- and 9.4-fold increases in NAP signal with activation at 2 and 6 hours respectively. At 20 hours untreated neutrophils show 1.6 times more NAP signal than activated neutrophils. Decrements in the fold change between untreated and activated NAP signals over time demonstrate increasing refractoriness to stimulus over time.

Although NAP signal shows increasing trends in both the QVD and QVD + calcium ionophore treatment groups over time, these groups show low fluorescence ($\leqslant$10 RFU and $\leqslant$31 RFU respectively) across the time course. These large reductions in NAP signal with the addition of QVD demonstrates a role for apoptosis in uninhibited caspase treatment groups.

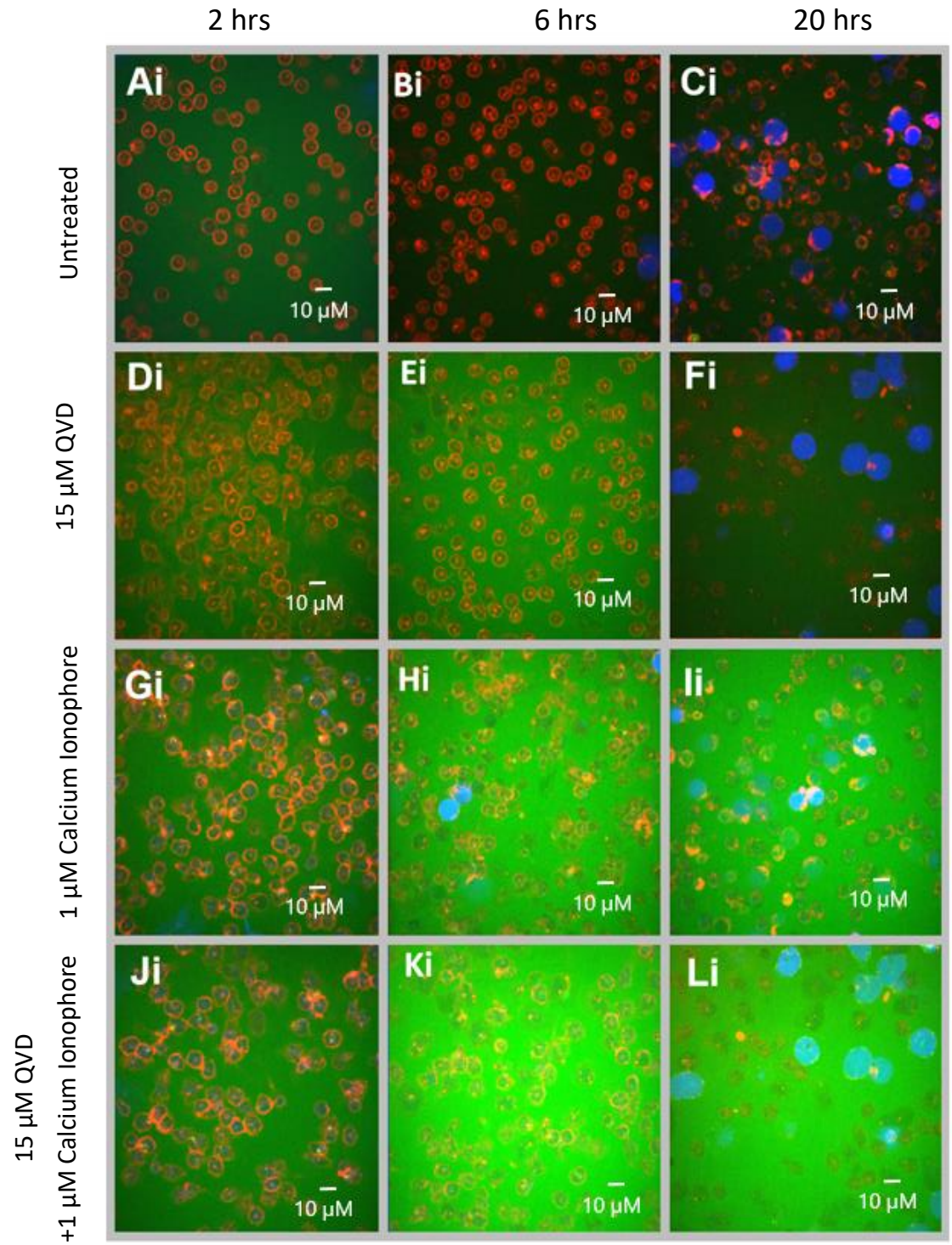

Figure 3.11 NAP detects neutrophil activation in stimulated, ageing neutrophil populations

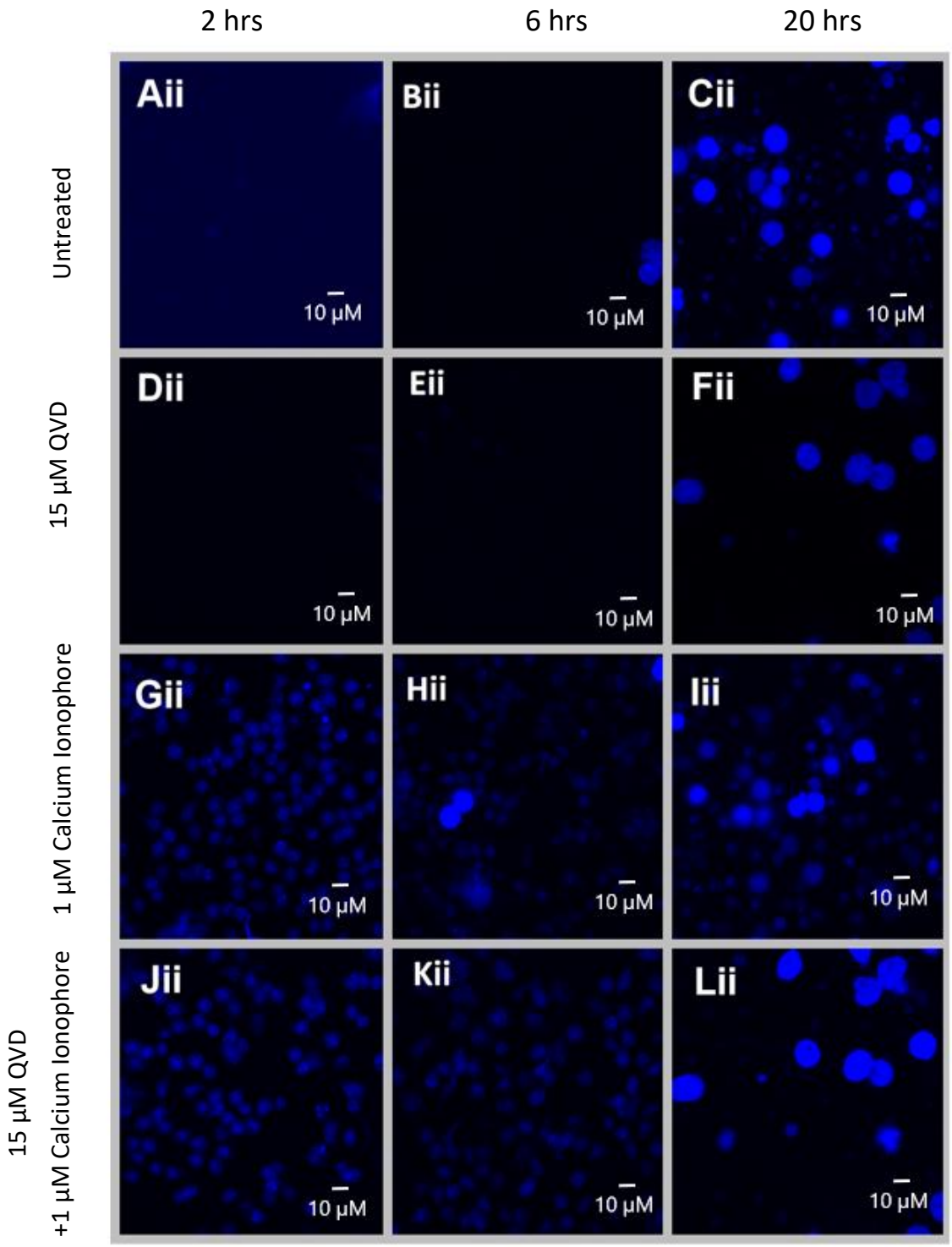

Figure 3.11 NAP detects neutrophil activation in stimulated, ageing neutrophil population

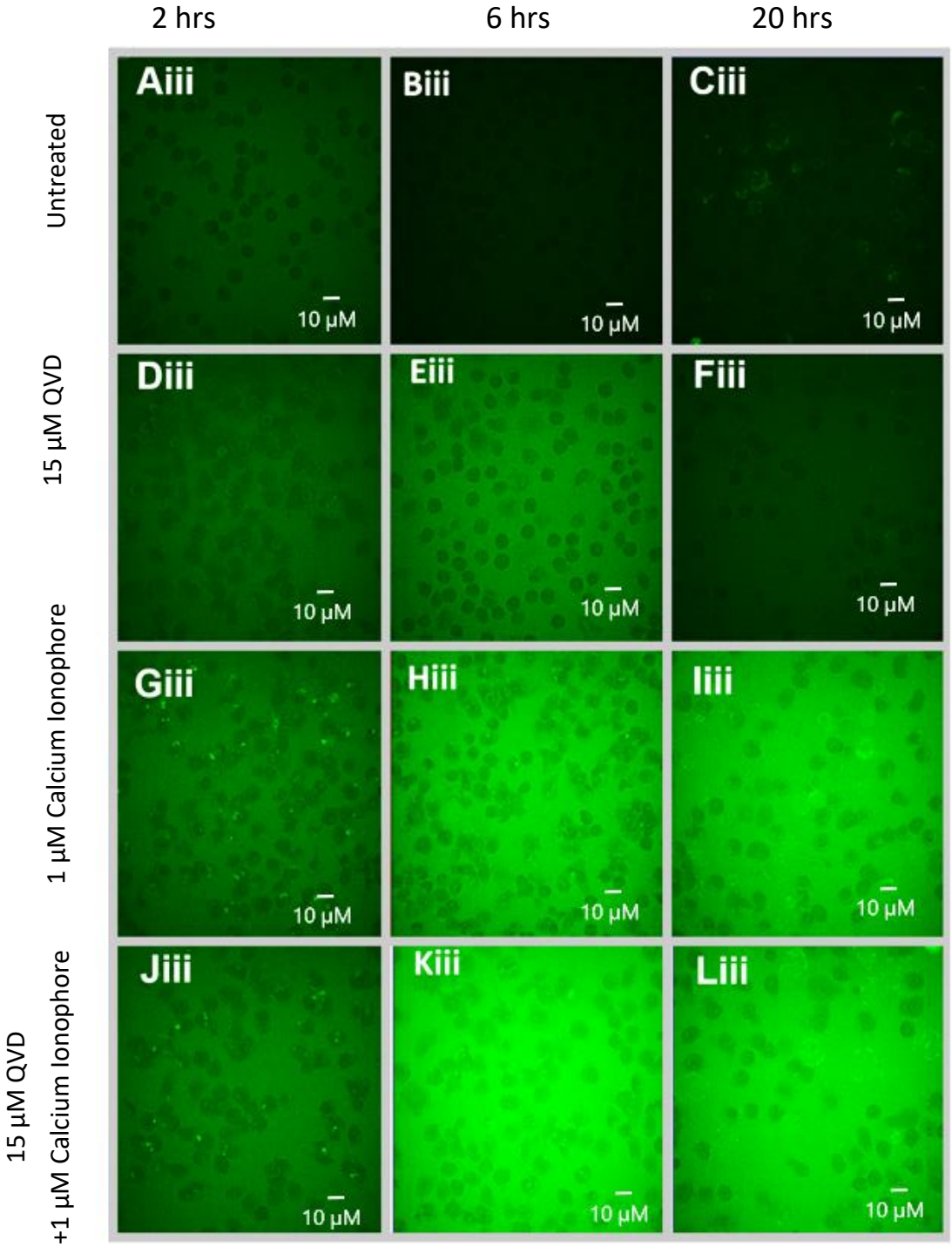

Figure 3.11 NAP detects neutrophil activation in stimulated, ageing neutrophil population

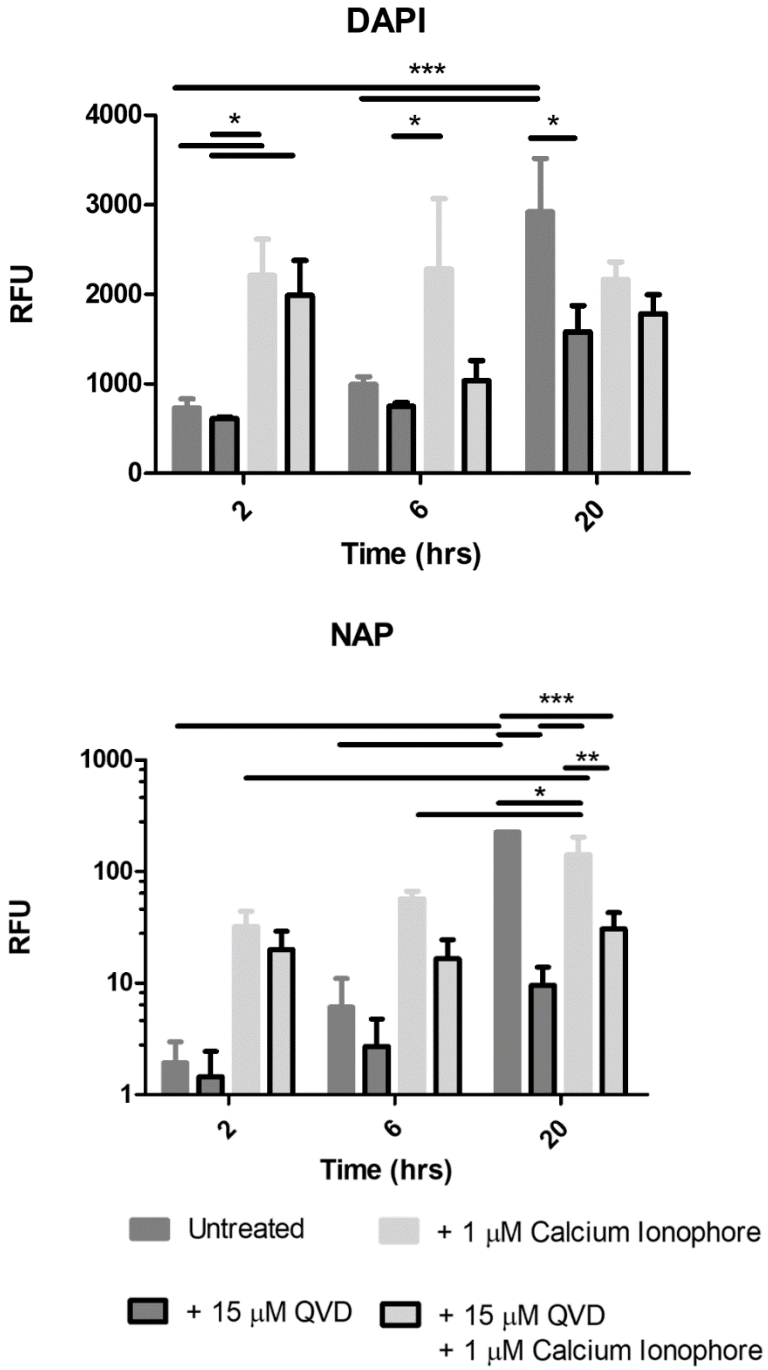

Figure 3.11 NAP detects neutrophil activation in stimulated, ageing neutrophil populations
Images represent neutrophils incubated **A-C)** without treatment **D-F)** with 15 μM QVD pan-caspase inhibitor **G-I)** with 1 μM calcium ionophore and **J-L)** with 15 μM QVD + 1 μM calcium ionophore at **A,D,G,J)**2 **B,E,H,K)** 6 and **C,F,I,L)** 20 hrs. Roman numerals represent **i)** merge **ii)** DAPI and **iii)** NAP images. Image analysis of **M)** DAPI images **N)** NAP images are shown, plotting mean intracellular fluorescence intensities of neutrophil populations. Values represent mean ± SEM, *P* values were calculated using two-way ANOVA and Bonferroni multiple comparisons test, *** *P* <0.001, n=3

3.3.2 SUMMARY

Neutrophil activation probe (NAP) is environmentally sensitive, principally to pH but also to temperature. 3 µM was identified as the standard NAP dose for use in subsequent experiments and although PR 3 and CG have some potential to influence NAP signal at this dose, in plate-reader assays, their contribution is negligible in confocal imaging assays in which HNE alone generates NAP signal. With neutrophil activation NAP fluorescence increases within 2 minutes, allowing activated neutrophils, now marked by bright intracellular puncta and extracellular fluorescence, to be parsed from dark untreated neutrophils. Neutrophil activation detection is reliable over the neutrophilic lifespan and NAP also affords the segregation of viable, apoptotic and necrotic neutrophils.

3.4.0 DISCUSSION

3.4.1 NAP CHARACTERISATION STUDIES WITH PURIFIED HUMAN NEUTROPHIL ELASTASE

NAP signal acquired from a system with active HNE depends on NAP and HNE concentrations, temperature, pH and the detection apparatus. Titrating NAP concentration has a proportional effect on its signal. NAP limit of detection could be considered in a variety of experimental set-ups however these permutations can be refined by considering appropriate restraints. Physiological restraints, such as a pathophysiological HNE concentration range (0-100 nM[173]) and practical restraints such as comparing data from subsequent assays. Within these limits, 0.5 µM is the

lowest concentration by which 100 nM HNE can be detected within one hour, by spectrometric analysis. There are many experimental alterations that may improve the limit of detection such as buffer alkylinization and the use of a more sensitive detection system such as afforded by confocal microscopy. However, the purpose of the limit of detection study was simply to understand spectrometric NAP signal detection over time, establishing experimental conditions for future studies. A concentration of 3 µM NAP was taken forward for further experimentation.

Temperature change can affect numerous cellular and experimental properties. The consistent effect of temperature on NAP signal between 35 and 40°C may limit its ability to interfere with deep tissue measurements of HNE activity *in vivo*. However, the signal variability that temperature introduces around 26°C could be an important consideration for HNE measurements at superficial or exposed surfaces and is important for several assays conducted at room temperature. Nonetheless, with an appropriate negative control, the effects of temperature and enzyme activity can be separated. One parameter that will impact all HNE measurements, *in vitro* or otherwise is pH. HNE is stored at pH 5 in neutrophil azurophil granules and alkalinisation to pH 9 takes place following the formation of the phagolysosome.[62] Therefore it is important to understand the effect of pH on HNE activity, particularly at pH 9 and under neutral conditions, under which the majority of extracellular HNE activity may take place. By measuring fluorescent emission of a coumarin-labelled substrate, the linear relationship between HNE activity and HNE concentration at pH 7 and 9 could be described by the following equation $V_{pH7} = \frac{V_{pH9}}{4}$ where V is the

fluorescent emission for a given concentration of HNE between 0 and 100 nM. This simple relationship may facilitate the use of mathematical tools, in understanding HNE dynamics in addition to fluorescence measurement. In the case of NAP, a similar mathematical relationship could not be revealed, and this may be due to the complexity introduced by fluorescein's pH-dependent quantum yield. Although alkalinisation was shown to promote HNE activity, the experiment could have been improved by finding the pH at which HNE activity achieves an upper limit and demonstrating the inverse effect due to acidification.

The effect of acidification on HNE activity was considered in subsequent experiments (**Fig 3.4** and **3.5**) which demonstrate reduced HNE activity at pH5 as expected. These experiments also demonstrate the low levels of NAP cleavage achieved by CG and PR3 and the minimal effect their activity has on NAP signal. HNE outcompetes CG and PR3 in the generation of NAP signal to the point that appropriate measurement thresholding could remove any contribution from competing enzymes as noise. In practice a clinical imaging biomarker would ideally provide readouts as quickly as possible and under 30 minutes. Measurements within these timeframes could favour the generation of HNE-specific NAP signal over other serprocidins which are slower to generate signal.

The effects of increasing dose on enzyme velocity provide mechanistic insight into NAP's selectivity for active HNE. There are 3 mechanisms for HNE's enhanced activity compared to other serprocidins, greater affinity for NAP, greater catalytic rate and increased sensitivity to alkalinisation. Serprocidins demonstrate a non-

linear relationship with substrate. HNE velocity is faster than that of PR3 or CG for the same change in NAP concentration, this indicates that HNE has either a higher affinity for NAP, a faster active site or both, when compared to other serprocidins. By taking the ratio of enzyme velocities at different serprocidin concentrations the effect of alkalinisation can be seen independently of affinity and catalytic constants. These ratios show that, in its interaction with NAP, HNE is more sensitive to alkalinisation-induced increased activity than other serprocidins.

Of the serprocidins, HNE has been demonstrated to have the fastest catalytic rate constant on interaction with endogenously derived substrates.[132] These differences help to explain NAP's HNE selectivity. Further work can be done to investigate the contributions of affinity and catalytic rate to this selectivity.

3.4.2 NAP CHARACTERISATION STUDIES WITH PRIMARY HUMAN NEUTROPHILS

By studying changes in adhesion molecule expression a clear indication of the extent of activation possible in primary human neutrophil assays was gained. Neutrophils acquired by Percoll blood preparation were suitably untreated to separate untreated populations from those stimulated by calcium ionophore. There is such a large difference between these untreated and pharmacologically stimulated groups indicates that the effects of weaker stimulation, as may be expected with physiological stimuli, may also be detected. The ability of NAP to report differences between the HNE activity of neutrophil-derived supernatants

with varying degrees of specific HNE-inhibition, also supports the concept of discerning between different physiological neutrophil populations which may be stimulated to release HNE and its inhibitors (such as elafin[174], SLPI[175] and serpinB1[171]) at varying concentrations. This work could have been furthered by determining if similar distinctions between neutrophil-derived supernatants could be made with endogenous inhibitors under physiological conditions. Although blocking NAP signal with Sivelestat, a specific inhibitor of HNE, supports the claim that NAP signal is selective for HNE activity, a full-block condition with a higher dose of Sivelestat would have done more to support this claim. Instead this was addressed in an imaging assay, where intracellular NAP signal was tracked over time. Despite a maximal stimulus of 10 µM calcium ionophore, full block was achieved with constant, 100 µM Sivelestat co-incubation. The rapid evolution of significant differences between uninhibited and 100 µM Sivelestat conditions demonstrate how quickly activated neutrophils can be separated from neutrophils without NAP signal. The two classes of neutrophils without NAP signal in this assay are Sivelestat inhibited activated neutrophils and, prior to stimulus, untreated neutrophils which were shown to be indistinguishable. The ability to distinguish between untreated and activated neutrophils rapidly and with a sustained difference between treatment groups may prove useful characteristics of NAP as a clinical biomarker. This work was repeated under more physiological experimental settings with 25 ng/mL LPS/ 100 nM fMLP stimulated neutrophils compared against untreated neutrophils across the entire time-course. It was important to use sufficiently low concentrations of bacterial products to recapitulate a physiologically

relevant bacterial inflammatory stimulus. Data following LPS/fMLF stimulation shows more variability between donors and loss of significance after 2.5 minutes of exposure to activating stimulus. The physiological data set also reported neutrophil activation 1 minute faster, and with a larger initial fold change, than the pharmacological setting. Comparisons between the pharmacological and physiological data sets are difficult to interpret as the later was collected on a spinning disk confocal microscope when the microscope used to collect the former, the Zeiss LSM 510 META confocal microscope, was replaced. To improve this assay, cell tracking could be used to isolate activated neutrophils for analysis, following the initial activity peak.

Finally, the effects of apoptosis and necrosis on activated neutrophil identification were considered. Image analysis revealed a consistent ability to discriminate between untreated and activated neutrophils despite ageing and the accrual of necrotic cells over a 20-hour time course. Imaging data also demonstrated different spatial and fluorescence patterns for untreated, activated and necrotic neutrophils. Flow cytometric analysis was used to confirm the ability to identify necrotic and activated viable neutrophils. Neutrophil populations can be segregated into untreated, activated, apoptotic and necrotic components using NAP signal.

CHAPTER 4:
CHARACTERISING NEUTROPHIL ACTIVATION USING VE200 IN VITRO

4.0.0 INTRODUCTION

HNE-targeted probes are designed to detect HNE and enable neutrophil labelling. This chapter aims to select a lead HNE-targeted probe and characterise probe-HNE interactions in terms of the dose and temporal dependence. Whether binding is irreversible is of interest as this is a necessary mechanistic requirement for targeted probes. The specificities of the lead targeted probe, binding neutrophils at the cellular level and HNE at the molecular level, are of particular interest. Satisfying these aims and interests, VE200 becomes an exciting candidate for multiplexed imaging with NAP. However, these two probes generate signal via mutually exclusive mechanisms relying on HNE active site inhibition or continuous activity respectively. The possibility of multiplexed NAP and VE200 imaging is evaluated with an emphasis on finding experimental optimal conditions. Finally, this chapter aims to understand whether VE200 has any ability to generate different signals for different viability states, this is important when imaging the relatively short-lived neutrophil.

4.1.0 IRREVERSIBLE INHIBITORS OF HNE

The oxidation of methionine 358 in α-1-PI reduced it's inhibitory effect against HNE 2000 fold and such a change may be achieved by reactive oxygen species release by activated neutrophils. α-1-PI and elaffin are susceptible to HNE cleavage-inactivation. To achieve more robust inhibition of HNE small molecule inhibitors which form irreversible bonds, have been synthesized. Sivelestat (ONO-5046) is an inhibitor of HNE which has been approved for clinical use in Japan and South Korea.[176,177] Sivelestat's relatively low affinity for HNE (K_i = 200 nM) and conflicting evidence concerning its clinical efficacy have kept this, the only clinically approved HNE inhibitor, out of other countries.[178] Squaretam and GW447631 are irreversible HNE inhibitors with inhibitory constants of 1.21 nM and 14 pM respectively.[130,179] Structure-activity relationship studies of 4-Oxo-β-lactams indicate that large effects on squaretam's inhibitory potency may be effected by linking a benzyl group to the lactam. Whether benzylation leads to improvement or reduction of inhibitory potency may rely on the moiety being replaced.[179]

4.1.1 SERINE PROTEASES

HNE is a serprocidin stored at millimolar concentrations in the azurophil granules of neutrophils.[180] Although HNE is chiefly a microbicidal protease, its broad substrate specificity allows neutrophils to use it intracellularly, extracellularly and in membrane-bound form for a variety of purposes. Phagocytosis, extravasation,[181] extracellular matrix remodelling,[182–184] cell-signalling,[185] mucus production,[186]

mucocilliary function[187] and NETosis[64] all have roles for HNE and a host of further interactions give the enzyme utility for other cell-types including monocytes, endothelial and adenocarcinoma cells. When released by activated neutrophils HNE can be used to destroy pathogens and promote neovascularization as part of tissue repair however sustained HNE release contributes to the pathophysiological sequalae of acute respiratory distress syndrome, lung adenocarcinoma, atherosclerosis and other chronic inflammatory diseases.

Craven et al. recently reported a probe that revealed neutrophil activation. This was designed to detect the serine proteases (serprocidins) using a pan-serprocidin substrate. A tri-branched probe was developed which maintains an optically super-silent ground state with a methyl red and fluorescein FRET pair on each of its three branches (**Figure 4.1.A**).[81] The structure facilitates internalisation by activated neutrophils and once in the phagolysosome, active serprocidins cleave the peptide sequences to remove the methyl red quenchers and generate a large fold increases in fluorescence (**Figure 4.1.B**). The probe generates bright intracellular puncta, in human neutrophils, within seconds of activation with pharmacological stimulus or bacterial coincubation. By adding the probe to whole blood in a simple, no-wash, no-lyse, flow cytometric assay, activated neutrophils could be profiled. Combining rapid signal generation and detailed cell-type specific analysis situates this pan-serprocidin probe as a promising patient-stratification biomarker for several chronic inflammatory diseases.

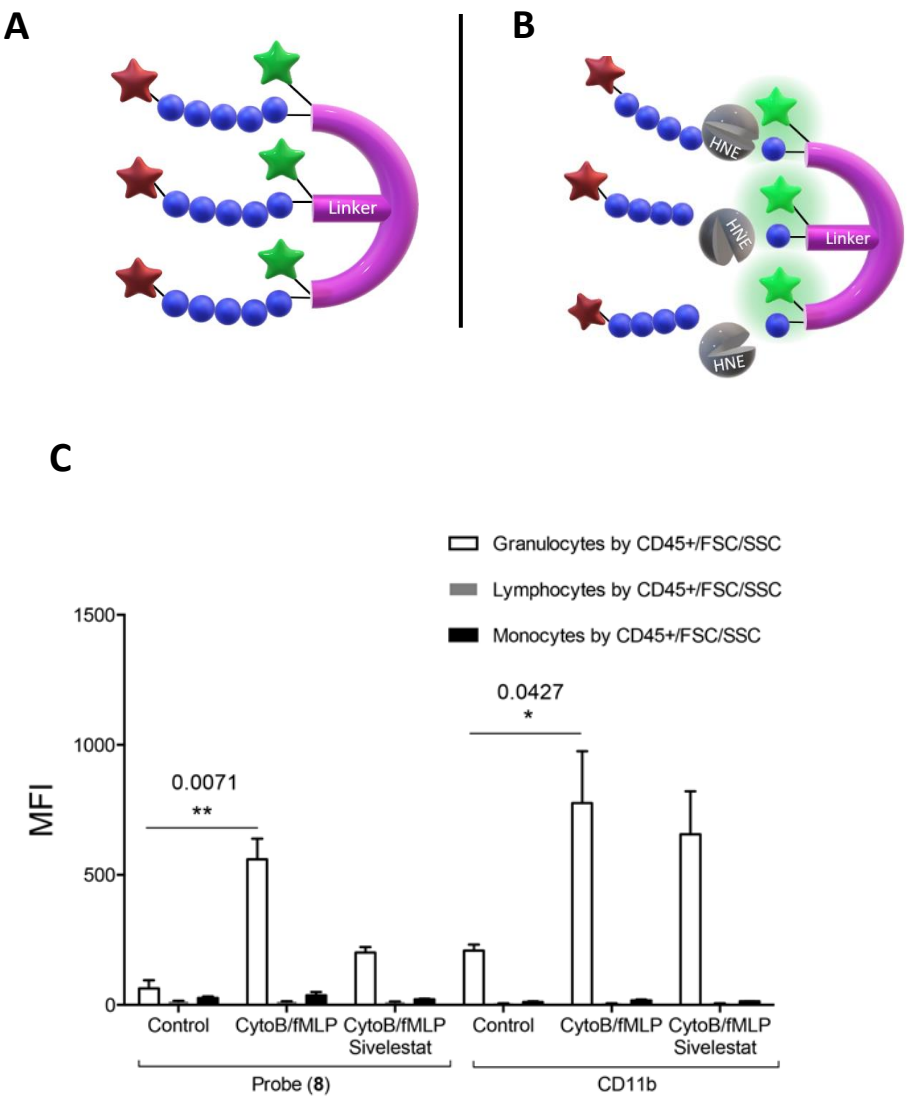

Figure 4.1 Activable FRET HNE Probe
Structure Craven et al.'s Probe **A)** before and **B)** after cleavage by active HNE and indicating associated FAM fluorescence. **C)** In a no-wash, no-lyse whole blood flow cytometric assay, neutrophils activated with bacterial products take up probe and upregulate CD11b. Fluorescent signal is blocked in activated neutrophils with 100 µM Sivelestat co-incubation, CD11b signal is not and neither signal is enhanced above untreated controls in lymphocytes or monocytes. Copyright Craven *et al.* 2018 and adapted under the licence CC BY 4.0.

The neutrophil elastase probe NE680 is a near-infrared multi-branched probe which is sensitive to cleavage by murine NE and HNE, amongst others (**Figure 4.2**).[120] It consists of a peptide sequence (PMAVVQSVP) flanked by a NIR fluorophores and conjugated to a poly-lysine dendrimer, which lengthens its plasma and tissue half-lives and results in internal quenching. Upon cleavage by proteases, NIR fluorescence emission is generated. NE680's quantification of NE activity was demonstrated *in vivo*, using LPS/fMLF challenged mice and by incubating murine lung sections in increasing doses of the NE-specific inhibitor, Sivelestat (**Figure 4.2.C-D**). Non-invasive, quantitative NE imaging was demonstrated using fluorescence molecular tomography.[120] Wang *et al.* demonstrated a similar dose dependent reduction in NIR fluorescence of NE680 could be achieved under more physiologically relevant conditions, using recombinant α-1-PI instead of Sivelestat.[188] Further studies using NE680 have revealed roles for NE in promoting neutrophil accumulation in atherosclerotic plaques, insulin resistance and arthritic pain, in murine models.[189–191] Although NE680 cleavage by HNE has been demonstrated *in vitro*, structural differences between the murine and human NE active sites and functional differences between murine and human neutrophils mean the clinical utility of NE680 has yet to be demonstrated.

Although a wealth of neutrophil probes have not reached *in vivo* studies, exciting developments in optical probe design are beginning to provide discriminatory power between related proteases. Despite their concomitant release from degranulating neutrophils, the various serprocidins perform distinct molecular functions.[192] Screening combinations of natural and unnatural amino acids by their

kinetic affinity and rate constants, Kasperkiewicz *et al.* designed a HNE probe with a 100-fold sensitivity surpassing the previous champion substrate designed by Korkmaz *et al.*, 100-fold.[193] The group's combinatorial substrate library technique generated substrate-based activatable probes and inhibitory, targeted probes and they have extended their approach to included counter selection which biases against the interference of substrate cleavage from similar protease families.[194,195] Finally, the recently synthesized fluorogenic toolbox contained unique substrate-fluorophore combinations for each of the four neutrophil serine proteases (HNE, proteinase 3, cathepsin G and neutrophil serine protease 4) and revealed for the first time their uneven distributions in azurophil granules.[196]

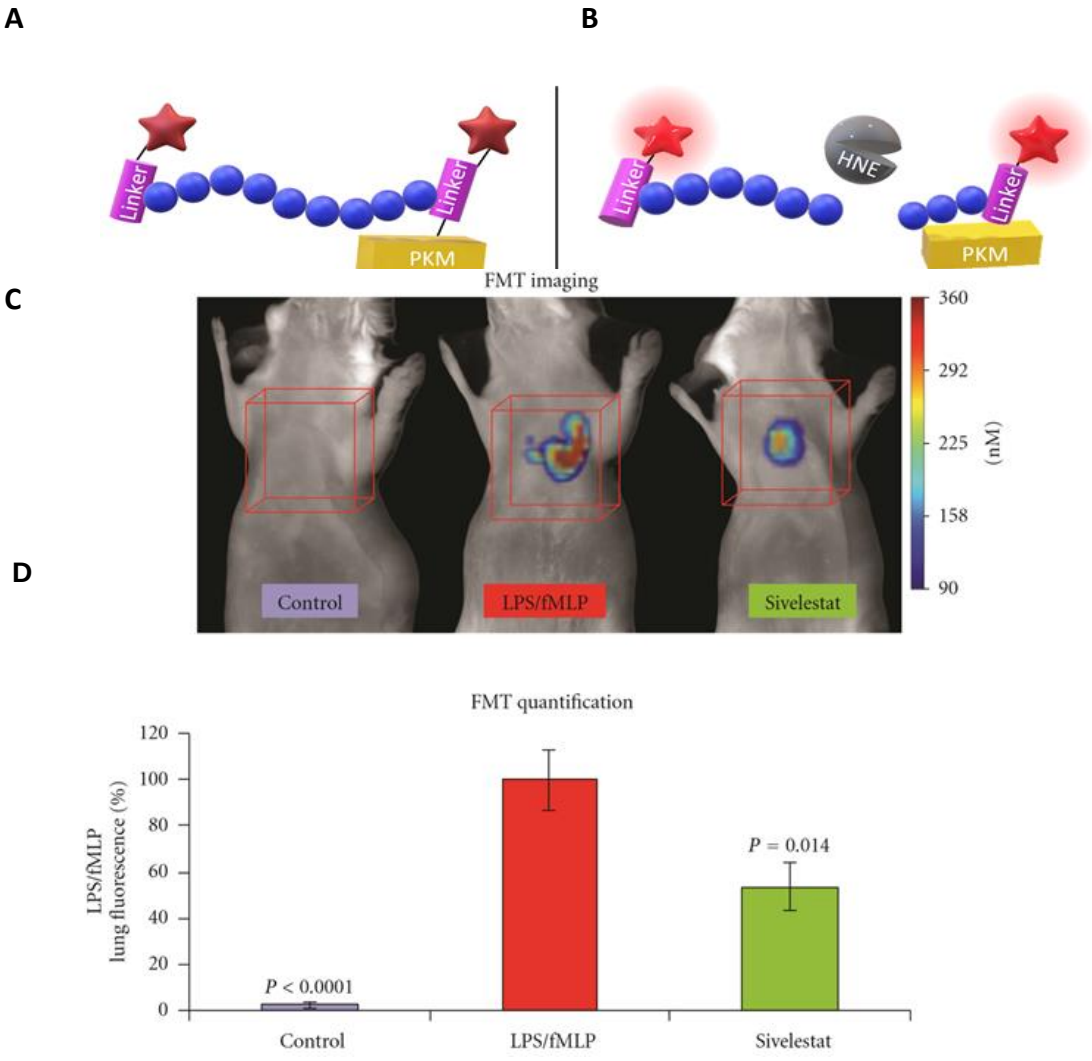

Figure 4.2 Schematic and in vivo function of NE680 FAST
Schematic representation of NE680 FAST before **A)** and after **B)** cleavage by active NE which alleviates fluorescence quenching. **C)** Fluorescence molecular tomography of NE680 FAST (4 nM intranasal) instilled into control, LPS/fMLP and LPS/fMLP mice treated with inhibitor. NIR signal is absent in untreated controls and reduced in sivelestat (5mg/kg intranasal) treated controls **D)** and mean concentration of fluorescence (in nM) was quantified in the lung area ROIs (orange cubes) for control (N=12), LPS/fMLP (N=16) and sivelestat (N=12) groups. **C-D)** Copyright 2011 Kossodo *et al.* and adapted under the CC BY 3.0 license.[120]

To enable clinical, functional neutrophil imaging via HNE activity at inflammatory sites a NAP was developed.[121] Using static quenching NAP's tribranched structure holds fluorescein moieties in close proximity limiting fluorescence. Each of these SmartProbe's three branches contain a HNE substrate sequence cleaved by the

active enzyme to generate large fold increases in fluorescent intensity. Encouraging results with NAP came from synthesising the SmartProbe to GMP standards and endomicroscopically imaging neutrophil activation in ventilated and perfused *ex vivo* human lungs.[197]

4.1.2 MONOCYTE ELASTASE AND PROBE SPECIFICITY

HNE is a fascinating enzyme acting intracellularly, extracellularly and at plasma membranes where it demonstrates broad substrate specificity (see **6.3.1 Substrates of HNE and the effects of their cleavage**) autocatalysis and inhibitor cleavage. Another quirk lay in the discovery of HNE within monocytes. Hatice *et al.* found approximately 40% of monocytes contained HNE but there are some important differences between this and neutrophilic HNE.[137] Monocytes were found to store 10-15 fold less HNE than neutrophils.[137] And the acidic, monocyte phagolysosome will produce far dimmer fluorescence than the alkalinised neutrophilic phagolysosome since both fluorescein fluorescence and HNE activity are reduced by acidification. These differences highlight biological and chemical mechanisms for a cell-type specific imaging technique however a third factor, the detector sensitivity of the imaging instrument, is also pertinent. Flow cytometry is more robust and sensitive technique for quantifying HNE-probe interactions than 20th century immunogold staining and electron microscopy. But flow cytometry is so sensitive that it may yield false positives across a large patient cohort. In a clinical setting *in situ* fibred microscopy may be the most relevant to clinical decision-making tool.

4.1.3 HNE-TARGETED PROBE TOXICITY

VE136 and VE200 were synthesized and tested for cytotoxicity by Dr. Vikki Evans. These probes were found to produce less than 2% cytotoxicity at 5 µM which is 12.5 and 50-fold in excess of the doses proposed for final phenotypic classification (see results section **5.3.1**) and FCE (see results section **5.4.2-3**) applications respectively. Furthermore no significant morphological changes were observed after neutrophils were incubated with VE200 for ninety minutes (see **figure 5.12 Xii)**. These targeted probes are therefore sufficiently non-toxic to warrant further investigation of their potential as *in vivo* components of a HNE phenotyping functional neutrophil classifier.

4.1.4 HYPOTHESIS AND AIMS:

Hypothesis: A HNE ligand-based probe can sensitively and specifically detect intracellular HNE activity enabling multiplexed imaging with NAP.

Aims:

1) Develop an assay for incomplete intracellular HNE inhibition using GW447631

i. Determine the Michaelis-Menton and catalysis constants for the HNE – AAPV interaction.
ii. Drawing on (i) kinetic understanding of the HNE-AAPV interaction use AAPV-AMC substrate to characterise GW447631 intracellular inhibition of HNE
iii. Drawing on (ii) understanding of GW447631 intracellular inhibition, determine the kinetics of HNE – GW447631 interaction in the presence of NAP.

2) Identify a lead HNE-targeted probe for multiplexed imaging with NAP in primary human neutrophils

i. Describe the fluorescent properties of the HNE targeted probe panel
ii. Select the lead HNE-targeted probe
iii. Describe the mechanism of VE200 interaction with HNE
iv. Determine the optimal VE200 imaging concentration
v. Identify an appropriate VE200 dose for multiplexed VE200 and NAP imaging in primary human neutrophils
vi. Determine if apoptosis and necrosis readouts can be achieved using multiplexed probe imaging

4.2.0 RESULTS

4.2.1 KINETICS OF THE HNE – AAPV SUBSTRATE INTERACTION

To understand the relationship between HNE enzyme velocity and AAPV-pNA concentration, kinetic constants were derived from a Michaelis-Menten curve. The Michaelis and catalysis constants are 172.5 nM and 25.3 s^{-1} respectively showing a relatively high-affinity binding takes place and substrate is rapidly converted into product.

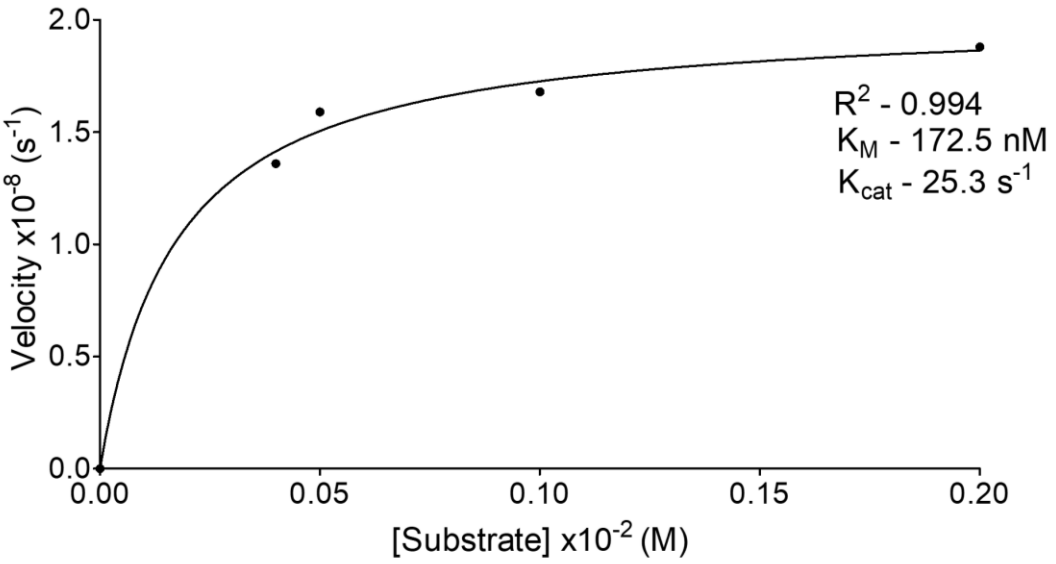

Figure 4.3 Kinetics of the HNE-AAPV interaction
Michaelis-Menten plot to determine the Michaelis constant and catalysis constant, measures of affinity and turnover rate respectively for the interaction between 10 nM HNE and AAPV-pNA substrate, n= 3.

4.2.2 GW447631 POTENCY IN PRIMARY HUMAN NEUTROPHIL LYSATES

By measuring enzyme activity across a broad GW447361 concentration range (0 – 1000 nM), a 50% inhibitory constant of 12.9 nM was interpolated. GW447361 shows a typical sigmoidal relationship between inhibitor concentration and enzyme velocity. Approximately 295 nM GW447631 fully inhibits a HNE concentration equivalent to the contents of five hundred thousand neutrophils. Importantly this assay also demonstrates dose dependent inhibition of neutrophil-derived HNE.

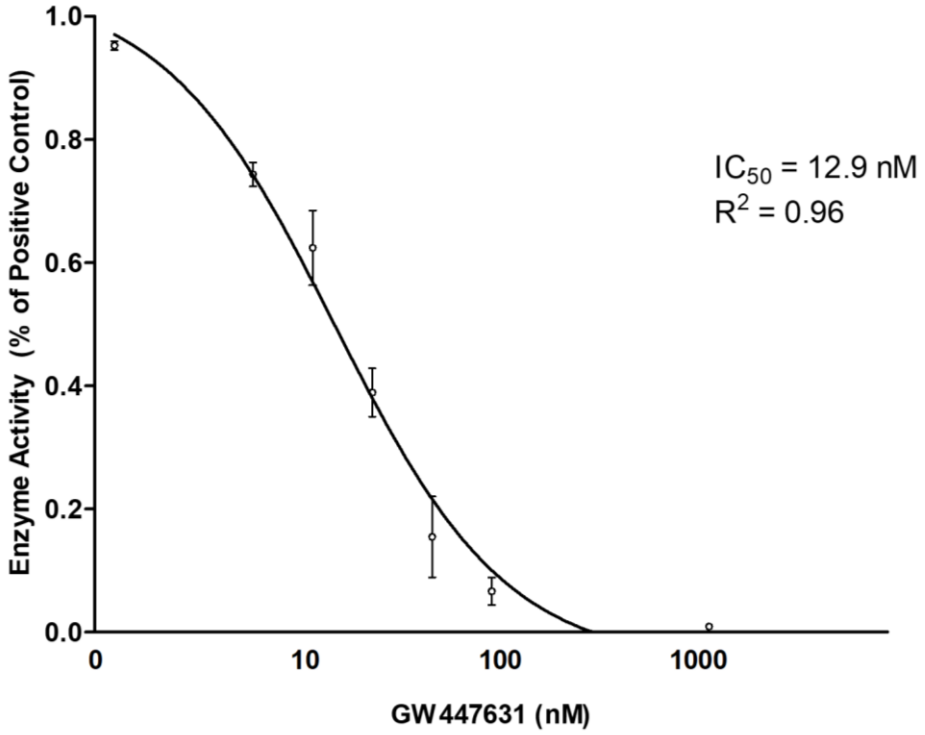

Figure 4.4 GW447631 dose dependently inhibits HNE in neutrophil lysates
Dose dependent inhibition of HNE was demonstrated by measuring AAPV-coumarin fluorescence in $2x10^7$/mL neutrophil-derived lysates after stimulation with 5 µM calcium ionophore. Lysates were treated with 0, 1, 5, 10, 20, 40, 80 and 1000 nM of GW447631. Values in the graph represent mean ± SEM, n=3.

4.2.3 GW447631 KINETIC ANALYSIS IN LIVE NEUTROPHILS

Further understanding of the GW447631 interaction with HNE was gained by time-lapse imaging of neutrophil activation under varying HNE inhibition. Visualising HNE activity with NAP shows large, bright, intracellular puncta in the absence of GW447631 and bright extracellular signal throughout the well (**Fig 4.5.A**). With increasing GW447631 concentration intracellular puncta decrease in size and number and extracellular fluorescence intensity decreases (**Fig 4.5.G**). At 10 µM GW447631 intracellular and extracellular signals of HNE activity are completely abrogated (**Fig 4.5.J**) by specific HNE inhibition[198] and neutrophils resemble the 100 µM Sivelestat condition. GW447631's dose dependent inhibition of HNE apparently occurs intracellularly and extracellularly, with readily detectable changes in signal intensity over time. Quantifying these changes shows a constant rate of NAP signal generation in the uninhibited condition and decreasing NAP signal over time in all GW447631 conditions. NAP signal shows dose and temporal dependence with HNE inhibition.

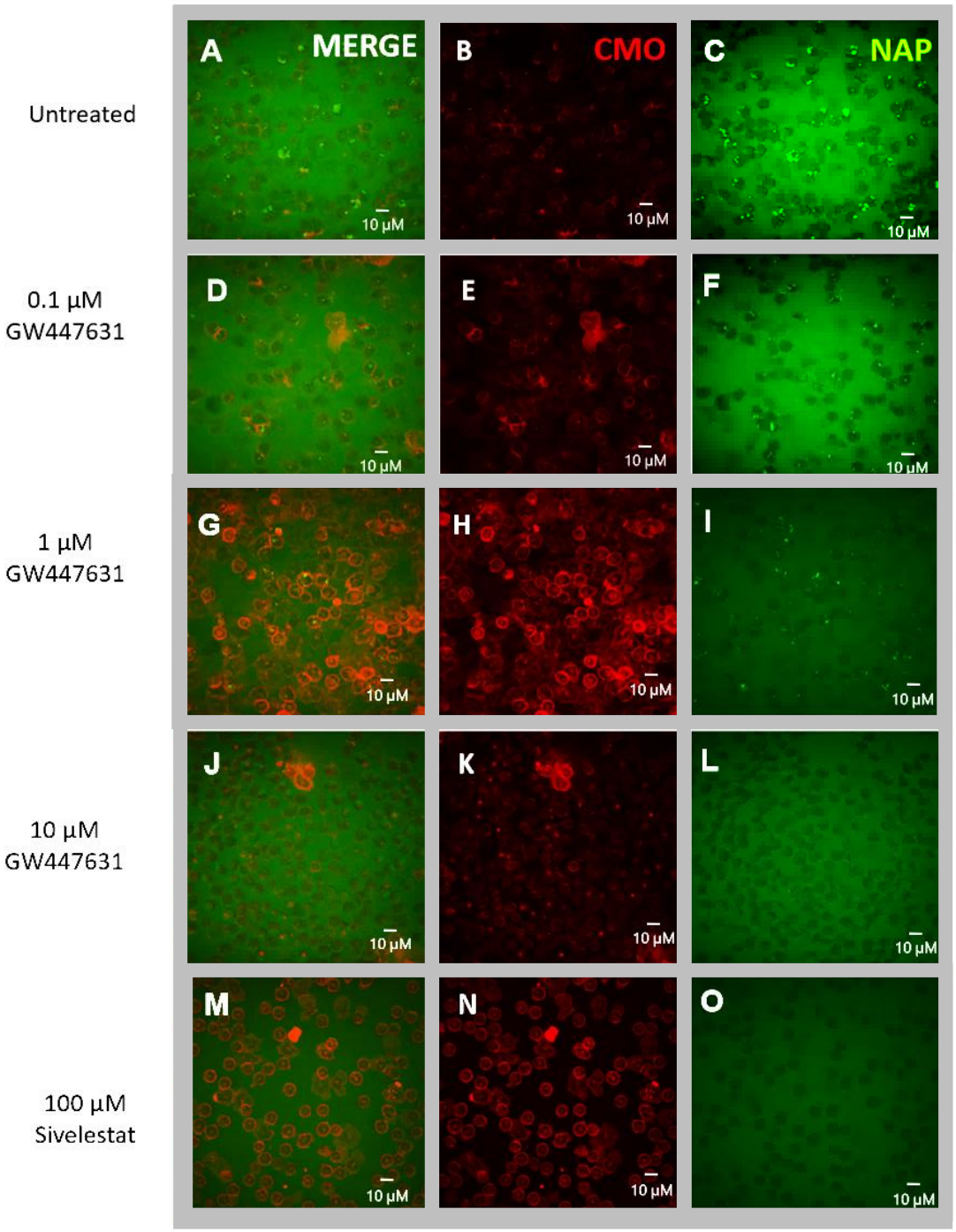

Figure 4.5 GW447631 displays dose dependent intracellular HNE inhibition

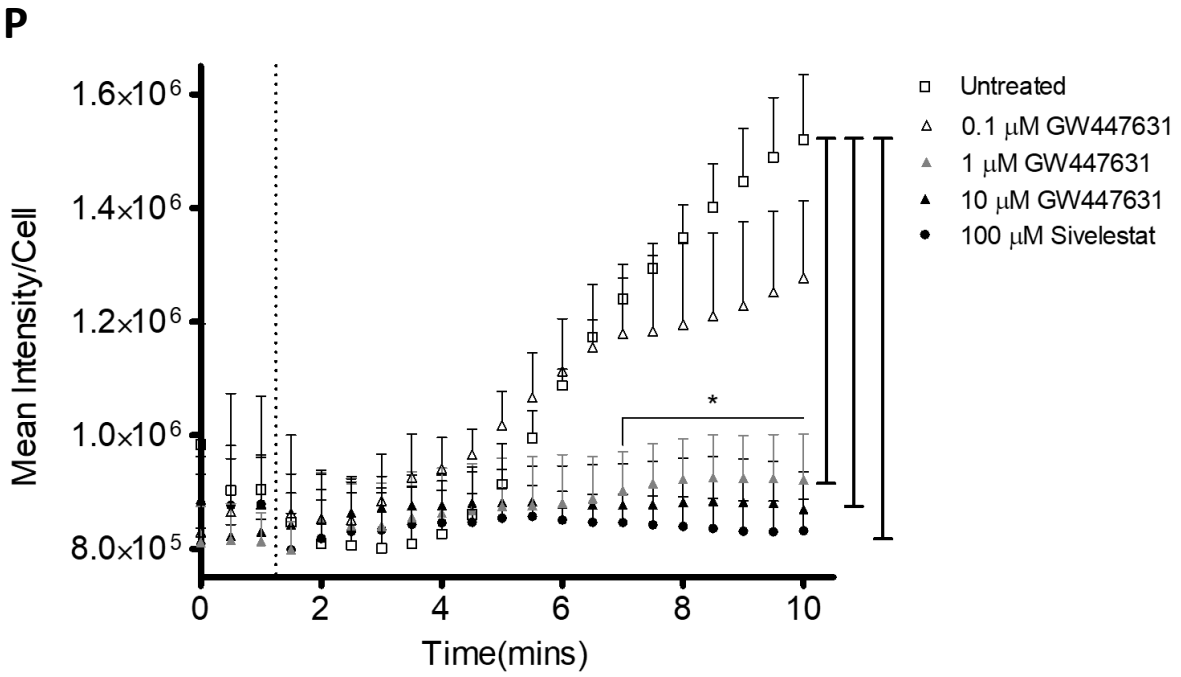

Figure 4.5 GW447631 displays dose dependent intracellular HNE inhibition
Spinning disk confocal microscopy of neutrophils incubated for 10 minutes with 3 μM NAP **A-C)** without HNE inhibitors, **D-F)** with GW447631 at 0.1 μM, **G-I)** 1 μM or **J-L)** 10 μM or **M-O)** with 100 μM Sivelestat. 10 μM calcium ionophore was added to all conditions immediately prior to the 120 s time point (dotted line). **P)** Image quantification shows intracellular NAP signal over time. Graph values represent mean ± SD and *P* values were calculated using one-way ANOVA and a Bonferroni post-test. *** *P* <0.001, n=3

4.2.4 FIBRONECTIN COATED WELLS AFFECT NEUTROPHIL ACTIVATION

Data from neutrophils that were incubated in wells for 15 mins, followed a gaussian distribution and showed an increased rate of NAP signal generation than those incubated for 5 mins (**Fig 4.6.A** slopes) which were non-parametric. However, these effects were reversed following pre-incubation with GW447631 so that neutrophils with only 5 mins incubation in wells demonstrated faster and parametric NAP signal generation, albeit from initially dimmer starting points than non-parametrically distributed, 15 mins counterparts (**Fig 4.6.B-D**). Differences between neutrophils following 5 and 15-minute well-incubations were significant under in each treatment group however there was a trend of dose-dependence with increased dose reducing the difference between the 5 and 15-minute incubations.

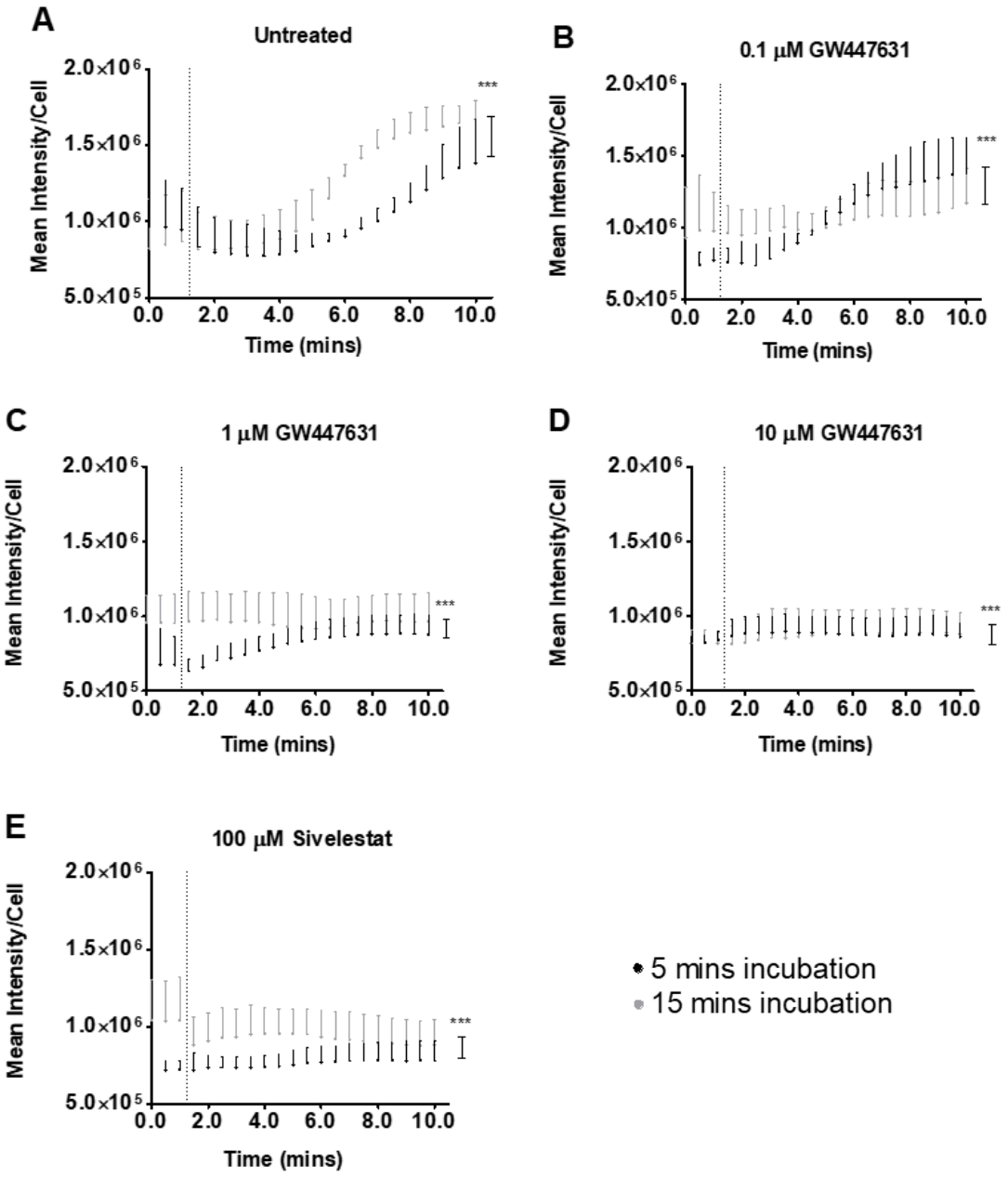

Figure. 4.6

GW447631 reverses the co-stimulatory effect of well-incubation on neutrophil activation

NAP signal over time for neutrophils incubated for 10 minutes with 3 µM NAP **A)** without HNE inhibitors, **B)** with GW447631 at 0.1 µM **C)** 1 µM or **D)** 10 µM or **E)** with 100 µM Sivelestat. 10 µM calcium ionophore was added to all conditions immediately prior to 120 s time point (dotted line). Neutrophils were adherent in wells for 5 mins (black dots) or 15 mins (grey dots). Graph values represent mean ± SD and *P* values, showing the difference between timepoint matched data, were calculated using two-way ANOVA and a Bonferroni post-test *** *P* <0.001. A D'Agostino and Pearson Omnibus normality test was performed, n=3

4.2.5 HNE ACTIVITY AFFECTS NEUTROPHIL SHAPE-CHANGE

When neutrophil radius was measured, across neutrophil populations, a trend of decreasing cell spreading was observed with increasing GW447631 dose. Untreated neutrophils maintained the widest mean radii across the 10-minute time-course and rapidly spread between 1.5 minutes, when stimulated, and 3.5 minutes before plateauing at 6 minutes. Neutrophils treated with 0.1 or 1 µM GW447631, or 100 µM Sivelestat, showed more gradual, linear cell spreading across the 10-minute time course. 10 µM GW447631 was the most potent HNE inhibiting condition and displayed no cell-spreading within 10 minutes.

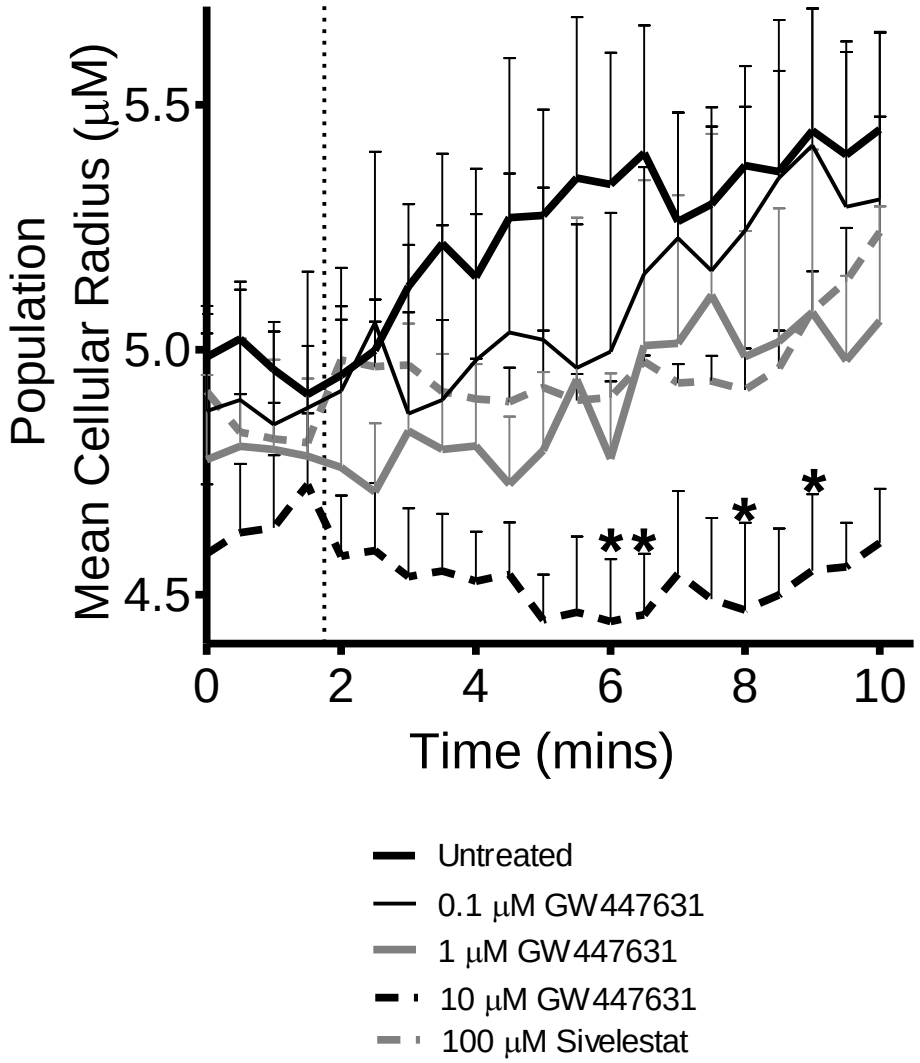

Figure. 4.7 High GW447631 dose reduces neutrophil activation dependent spreading
Mean neutrophil radius over time of neutrophils incubated for 10 minutes with 3 μM NAP without inhibitors, with 0.1, 1 or 10 μM GW447631 at or 100 μM Sivelestat. 10 μM calcium ionophore was added to all conditions immediately prior to 120 s time point (dotted line). Graph values represent means ± SEM. *P* values were calculated using two-way ANOVA and a Bonferroni post-test. * *P* <0.05, n=3

4.2.6 SPECTRAL CHARACTERISTICS OF THE HNE-TARGETED PROBE PANEL

Three targeted probes for HNE labelling were synthesized. Cy5 fluorophore was bound to either GW447361, a 4-oxo-β-lactam ring or a phenylated 4-oxo-β-lactam ring to synthesize VE136, VE200 and VE135 respectively. The emission and excitation spectra of the 3 targeted probes are similar with excitation/emission maxima of 650/675 (VE136), 650/665 (VE200) and 655/680 (VE135). Although emission spectra are very similar between probes, VE200 has a narrower excitation peak (RFU = 0.2 at 584 and 674 nM) than VE135 (RFU = 0.2 at 528 and 690 nM) or VE136 (RFU = 0.2 at 560 and 683 nM).

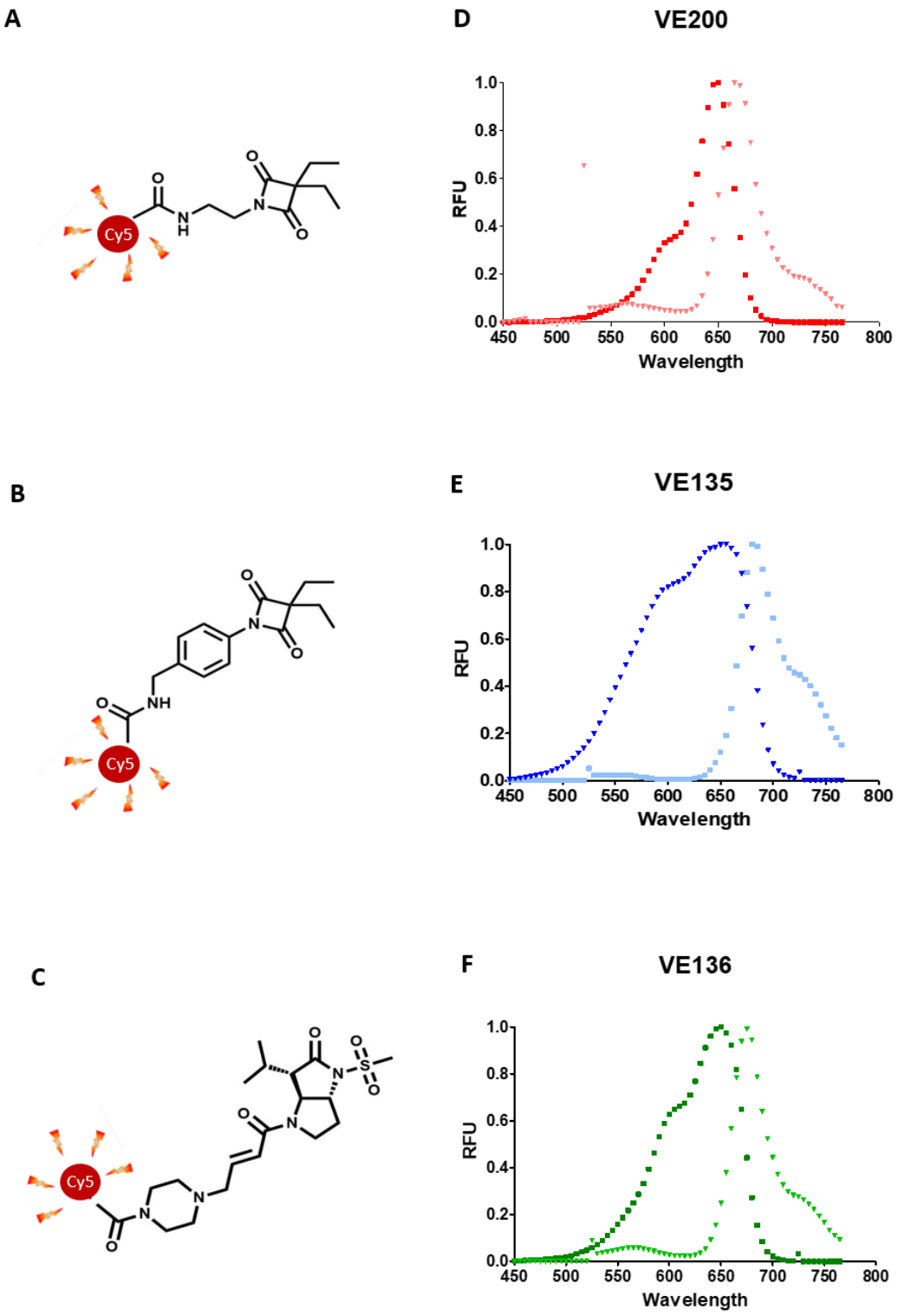

Figure 4.8 Structures and spectral properties of candidate HNE-targeted probes
Schematics showing inhibitor structure and fluorescence excitation and emission spectra for 10 µM cyanine-labelled HNE-targeted probes **A)** VE200 **B)** VE135 and **C)** VE136. Graph values represent mean ± SEM, n=3.

4.2.7 NEUTROPHIL SPECIFICITY OF HNE-TARGETED PROBES

To select a lead probe for further study, percentage labelling, after five minutes, was compared across PMN and PBMC populations of untreated and activated cells. Although it is possible for some 40% percent of monocytes to store and release HNE in quantities approximately 3% of the levels achieved by neutrophil degranulation,[137] this low level of HNE was undetectable in this assay. VE200 achieved the highest percentage labelling at 68%, and this occurred in the presence of neutrophils activated with 1 µM calcium ionophore. VE200 also displayed good selectivity for activated neutrophils demonstrating a 13.5-fold increase between untreated and activated neutrophils and less than 10% labelling of both PBMC conditions. Although not statistically significant, fluorescence fold increases of 1.6 and 2.9 for VE135 and VE136 respectively show a trend of neutrophil activation-induced fluorescence increase. With the lowest untreated to activated neutrophil labelling fold change and the highest percentage PBMC labelling, VE135 is not a neutrophil-specific label, nor does it enable the detection of neutrophil activation.

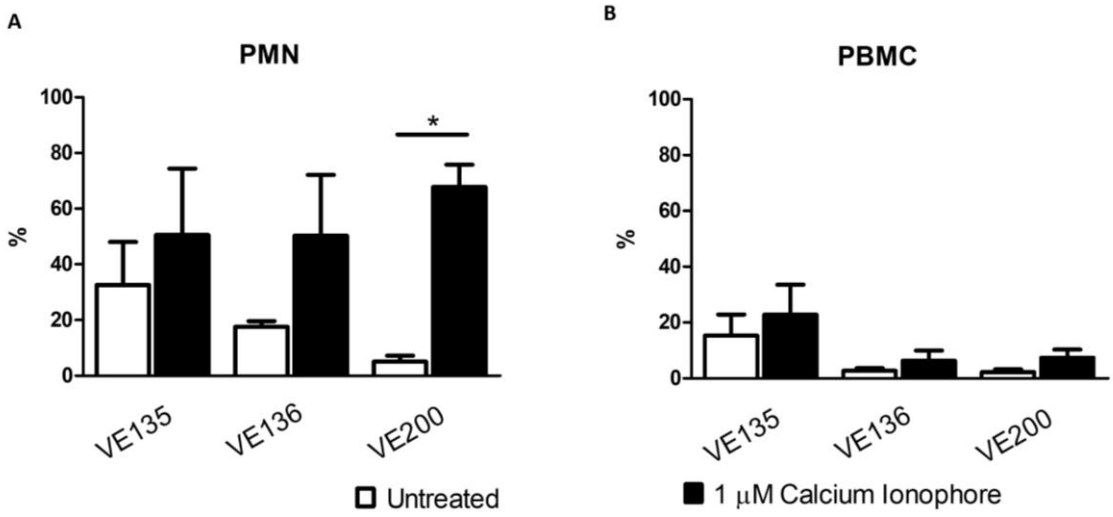

Figure 4.9 Cell-type specificity of HNE-targeted probes
Flow cytometric analysis showing percentage labelling cells, with 2 μM targeted probe, in **A)** PMN **B)** PBMC populations with and without calcium ionophore treatment. Graph values represent mean ± SEM and *P* values were calculated using one-way ANOVA and a Bonferroni post-test. * *P* <0.05, n=3.

4.2.8 VE136 SENSITIVELY DETECTS NEUTROPHIL ACTIVATION

Although VE200 outperformed VE136 for neutrophil activation detection, GW447631's high affinity HNE-binding revealed subtle and HNE-dependent changes in neutrophil activation (**Fig. 4.6 and 4.7**). To understand whether VE136, Cy5-labelled GW447631, could sensitively detect HNE release neutrophils were incubated with varying concentrations of PMA, for forty-five minutes, in the presence of VE136. Dose dependent labelling was achieved with neutrophils and not PBMCs, indicating neutrophil-specific VE136 labelling. Neutrophil-specificity of VE136 is further corroborated by the percentage-labelling after forty-five minutes of calcium ionophore incubation, this positive control data shows 94.5% of neutrophils are labelled and only 5.0% of PBMCs. However, the VE136 labelling interaction does not involve fluorescence unquenching and this necessitates comparisons of VE136 HNE labelling against false positive signals which can occur with free Cy5. When comparing PMA and calcium ionophore induced labelling in both groups to free Cy5 controls, neutrophil staining by VE136, in the presence of 10 and 50 nM PMA is less than that of Cy5 staining at 2000 nM PMA but VE136 staining from all other conditions (100, 200, 500, 1000 and 2000 nM PMA) exceed Cy5 staining, even at the maximal 2000 nM dose of PMA. There is no change in PBMC staining regardless of whether comparisons are made between pharmacological stimuli (PMA and calcium ionophore) or stain (VE136 and free Cy5), percentage PBMC staining ranges from 2.2% and 6.8%.

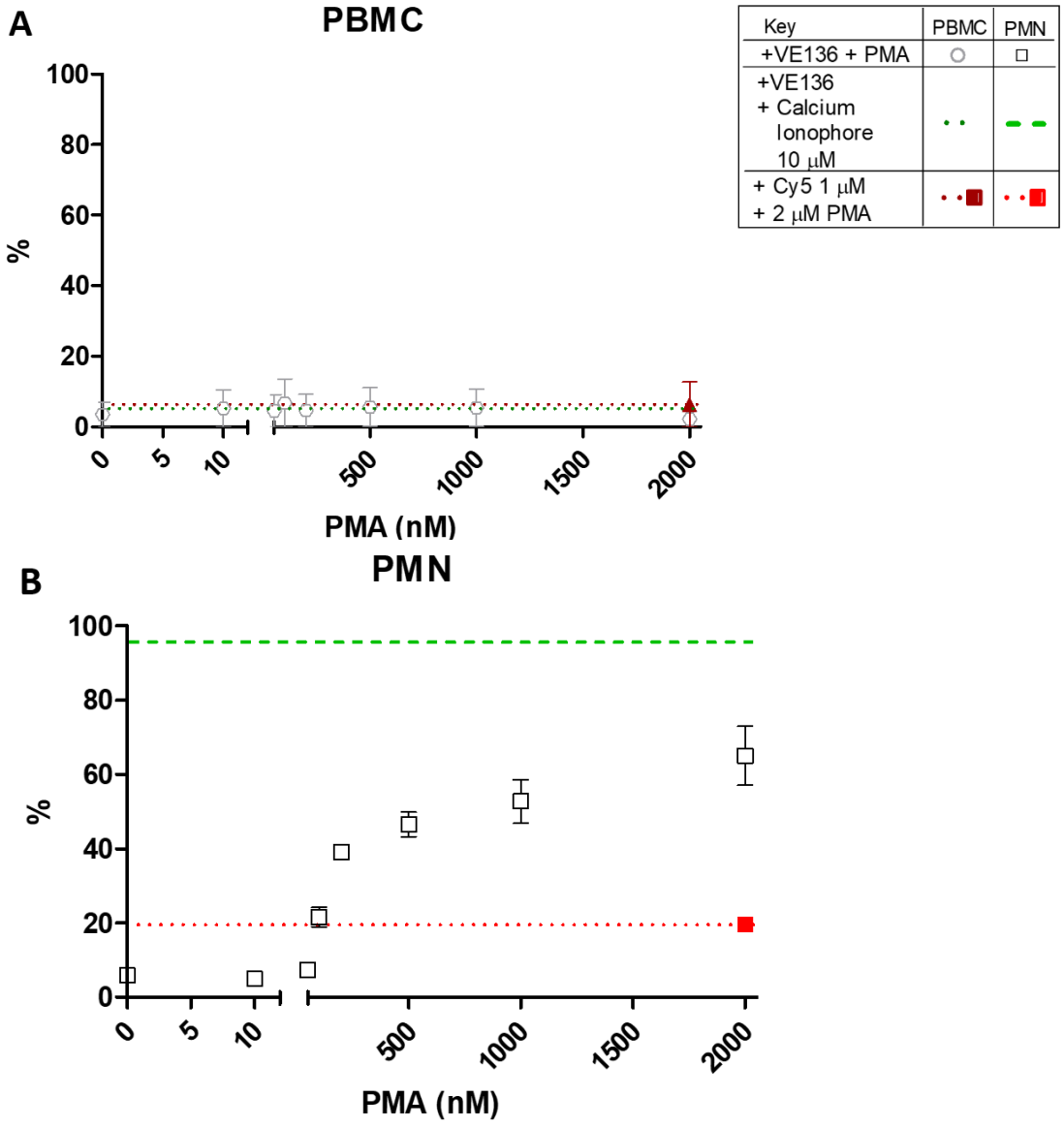

Figure 4.10 PMN specific VE136 is sensitive to varying PMA stimulation
Flow cytometric analysis showing percentage labelled PMN and PBMC, with 1 µM VE136 and 0, 10, 50, 100, 200, 500, 1000 or 2000 nM PMA. VE136 labelling is also compared to 10 µM calcium ionophore treatment positive controls. n=2. This experiment was not repeated further due to the limited availability of VE136, synthesized in house.

4.2.9 NEUTROPHIL-SPECIFIC TARGETED PROBES ARE HNE-SPECIFIC

VE136 and VE200 labelling were compared after 10 minutes of incubation with or without calcium ionophore (10 µM) treatment or calcium ionophore and Sivlestat (50 µM) treatment. In neutrophil populations, both probes showed increased labelling with stimulus which was abrogated by Sivelestat co-incubation. In PBMC populations, both probes show no variation between untreated, stimulated and stimulated/inhibited treatments. There is a trend toward more efficient neutrophil labelling with VE136 (65.6%, **Fig. 4.11.E**) over VE200 (58.0% **Fig. 4.11.F**), however the ratios of stimulated to untreated and stimulated to inhibited fluorescence also affect labelling efficiency. When comparing stimulated and untreated neutrophils, VE200 demonstrates a 34.2-fold increase in labelling efficiency with stimulation, as compared to 4.9-fold with VE136. When comparing stimulated and Sivelestat-treated, stimulated neutrophils, the trend is similar with VE200 demonstrating a 35.7-fold increase in labelling efficiency, without HNE-inhibition, as compared to 4.10-fold with VE136. These ratios demonstrate good HNE-specificity for both probes and more sensitive labelling with VE200. For both probes, all PBMC labelling falls below that of untreated neutrophils (13.8% VE136, 2.6% VE200, **Fig. 4.11.E and F**), a background level of neutrophil staining, demonstrating the neutrophil specificity of both probes. For its spectral compatibility with NAP (**Fig 4.7**) and its neutrophil and HNE-specific binding, (**Fig 4.9 and 4.11**) VE200 was selected as the lead probe for further investigation.

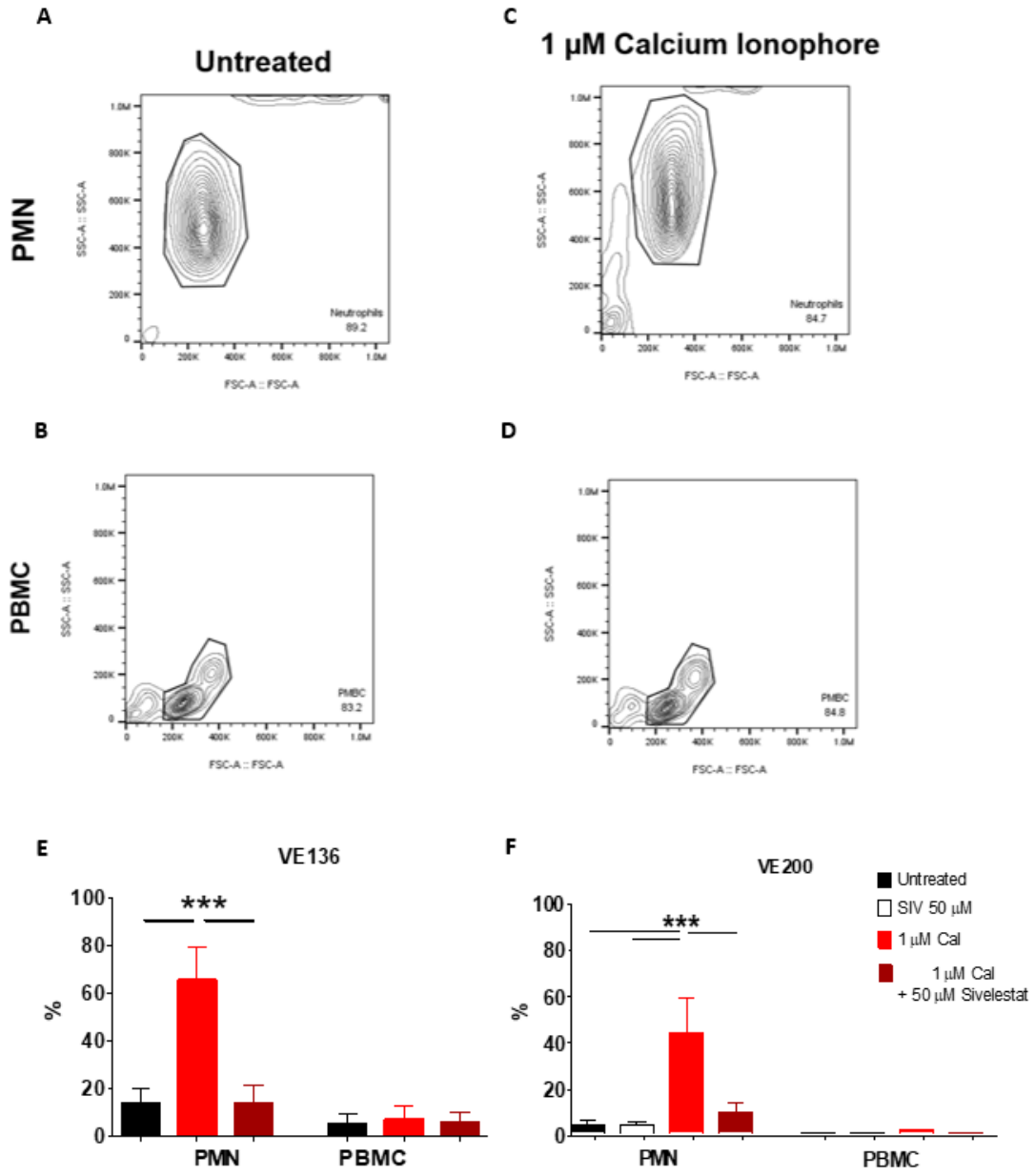

Figure 4.11 Cellular and molecular specificity of HNE-targeted probes
Flow cytometric analysis showing percentage labelled cells in PMN and PBMC populations with and without 10 µM calcium ionophore and 50 µM Sivelestat treatment. **A)** 1 µM VE136 specificity, n=4. **B)** 1 µM VE200 specificity, biological replicates shown individually, n=3. Graph values represent mean ± SEM of individual experiments. Graph values represent mean ± SEM and *P* values were calculated using two-way ANOVA and a Bonferroni post-test. *** *P* <0.001, n=4.

4.3.0 VE200 DEMONSTARTES IRREVERSIBLE INHIBITOR KINETICS

In the previous three comparative assays VE200 demonstrated best performance. VE200 fluorescence excitation characteristics which limit excitation from non-640 nm light compared to VE135 and VE136. And VE200 cellular and molecular specificity exceeded that of VE135 and VE136. Therefore, VE200 was selected for further characterisation and imaging experiments. VE200 shows dose dependent HNE binding when incubated with purified HNE (10 nM) and AAPV-AMC (1 mM). The 4-oxo-β-lactam ring inhibitor moiety should confer irreversible VE200 binding by suicide inhibition. According to Michaelis Menten phenomenology, the rate of inhibited product is proportional to the concentration of unbound VE200 remaining over time.[199] The goodness of fit (R^2= 0.93, **Fig. 4.12.A**) for the dose-dependence curve in **A)**, is indicative of a two-phase exponential decay in agreement with the mechanism of suicide inhibition. At 10 µM, VE200 inhibition of HNE activity increases with incubation time, this phenomenon is expected with irreversible inhibitors and does not occur with reversible inhibitors, which establish an equilibrium between bound and unbound forms to sustain a constant inhibitory effect over time.

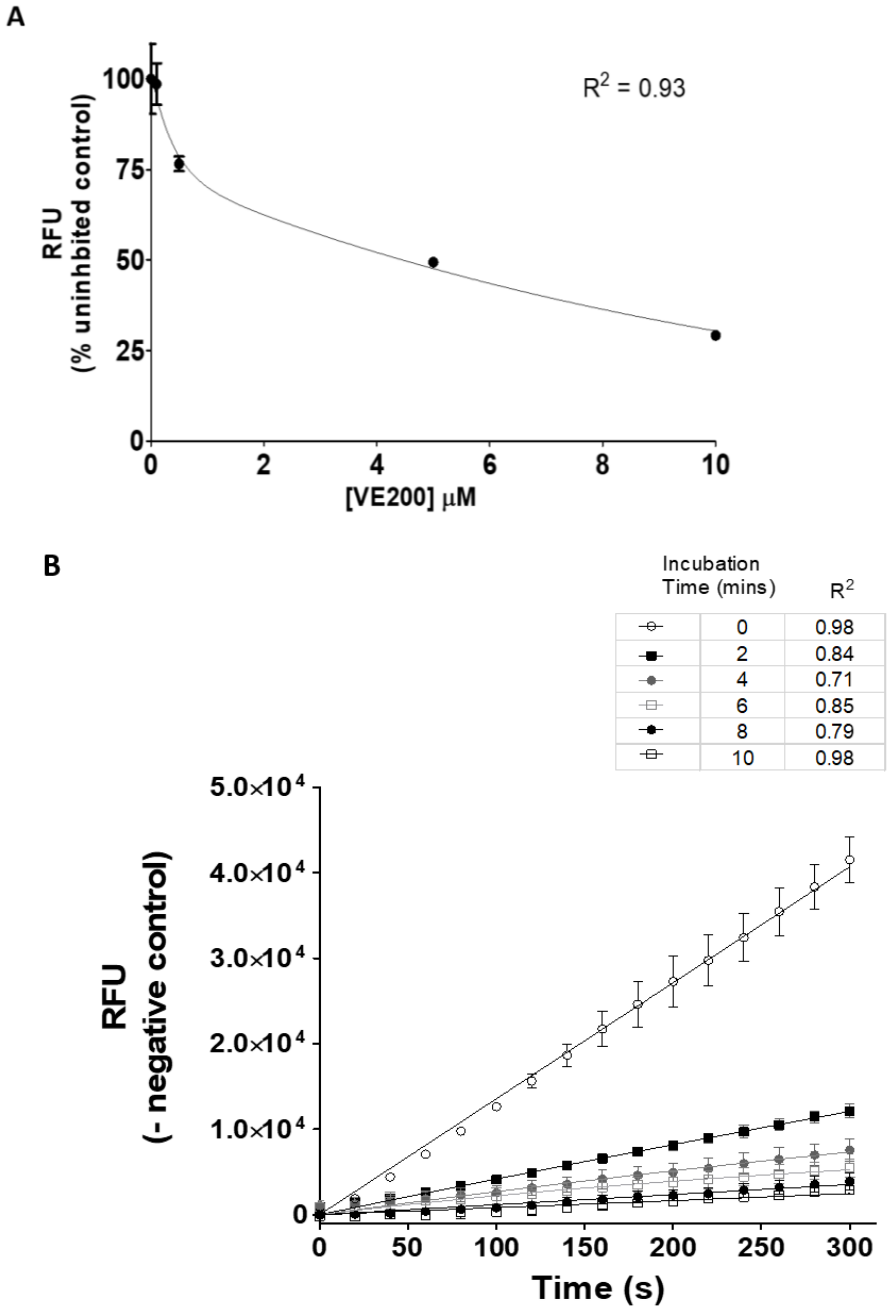

Figure 4.12 VE200 binds purified HNE irreversibly and with dose dependence
A) Dose dependent inhibition of 10 nM purified HNE by VE200 at 0.1, 0.5, 5 and 10 µM n= 3
B) Time-dependent inhibition of 10 nM purified HNE by 10 µM VE200 at 0, 2, 4, 6, 8 and 10 mins. Graph values represent mean ± SEM, n=3.

4.3.1 ESTABLISHING AN OPTIMAL IMAGING DOSE FOR VE200

VE200 labels neutrophils treated with 10 µM calcium ionophore (**Fig. 4.13F-J**) and remains excluded from untreated neutrophils (**Fig. 4.13A-E**) across a 100 – 2000 nM concentration range. Following pharmacological stimulation, VE200 labelling is dose dependent in neutrophils with a trend of exponential increase. Although untreated conditions yield low VE200 signal, this signal increases with neutrophil activation at each dose to facilitate activated neutrophil detection. The VE200 dose with the largest stimulation fold change is 500 nM in (**Fig. 4.13L**), when signal is quantified using a whole-frame histogram method and 200 nM in (**Fig. 4.13K**), when intracellular signal is quantified to the exclusion of extracellular space.

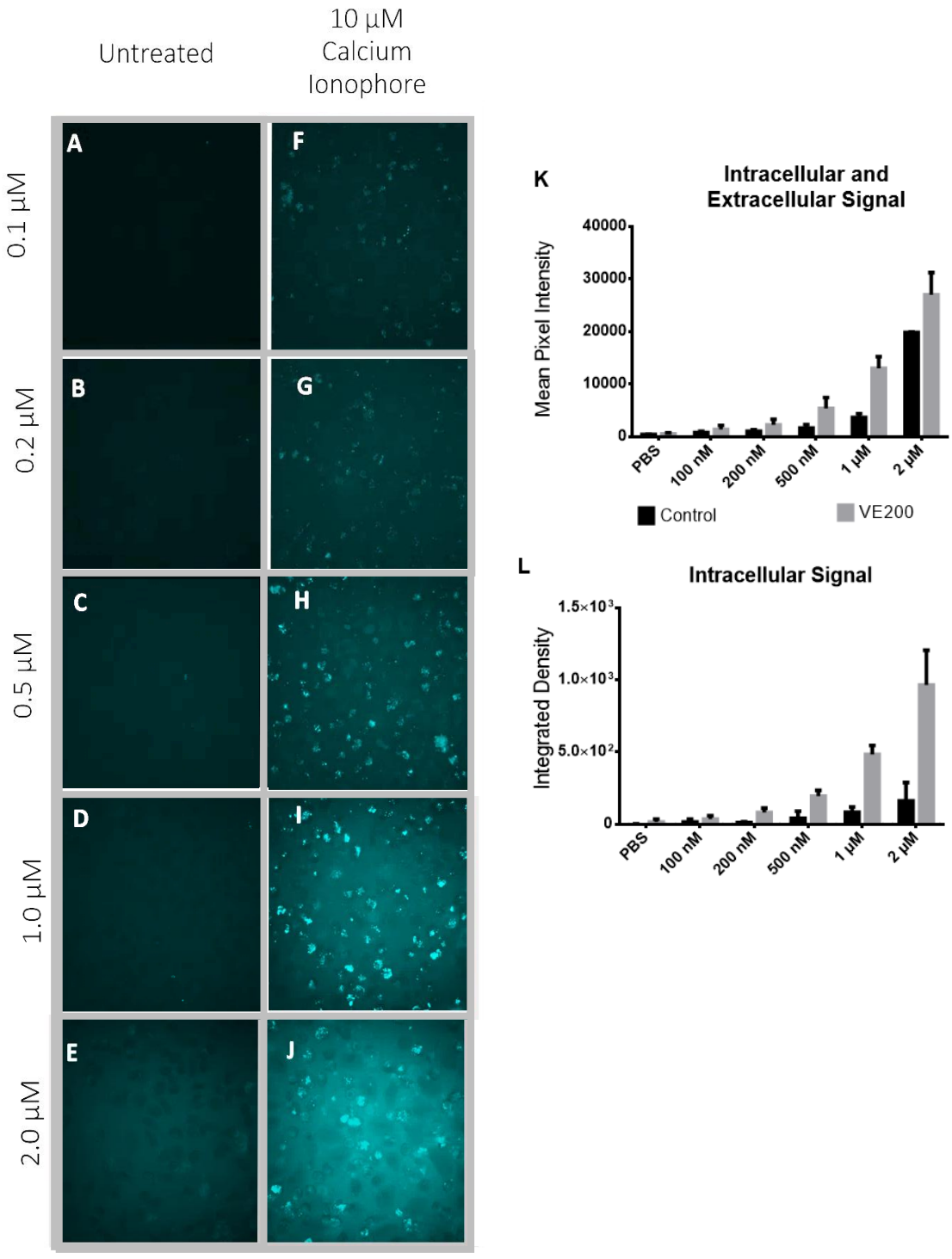

Figure 4.13 200 nM VE200 optimally enables activated neutrophil detection
Confocal microscopy of neutrophils incubated for 10 minutes with **A-E)** 0.1, 0.2, 0.5, 1 and 2 µM VE200 alone **D-F)** and in the presence of 10 µM calcium ionophore. Representative images, n=3.

4.3.2 VE200 LABELS NEUTROPHILS VIA ITS HNE-INHIBITOR MOIETY

Having established that VE200 labels stimulated neutrophils more efficiently than free Cy5 dye by flow cytometric analyses (**Fig. 4.9 and 4.11**), confocal microscopy was utilized to gain a subcellular understanding of VE200 labelling in neutrophils. After a single wash step, both VE200 and free Cy5 dye adsorb to and are endocytosed by neutrophils. Upon cellular stimulation, both labels are also capable of becoming concentrated in intracellular compartments in a punctate manner resembling NAP signalling. Image analysis was executed as described in **Chapter 2, 2.2.7** and showed no labelling with 0.2 µM free Cy5 irrespective of neutrophil activation status. Dose dependent increases in labelling occur in untreated and activated, Cy5 and VE200 treatment groups when compared at 0.2 and 2 µM. VE200 conditions consistently generate brighter cellular signals than their free Cy5 comparators, at both doses, with or without neutrophil activation. Stimulated neutrophils stained with VE200 showed significant fluorescence increase over all other conditions at 0.2 and 2 µM with fold-changes over the next brightest condition of 22.7 and 6.7 respectively.

When comparing across treatments, 2 µM free Cy5 labelling of stimulated neutrophils which have taken up dye, was not significantly different from untreated neutrophils labelled with 2 µM VE200, which have not yet taken up dye. Despite being the brightest of the four free Cy5 conditions, stimulated neutrophils labelled with 2 µM free Cy5 were still 1.8-fold dimmer than stimulated neutrophils labelled with 0.2 µM VE200.

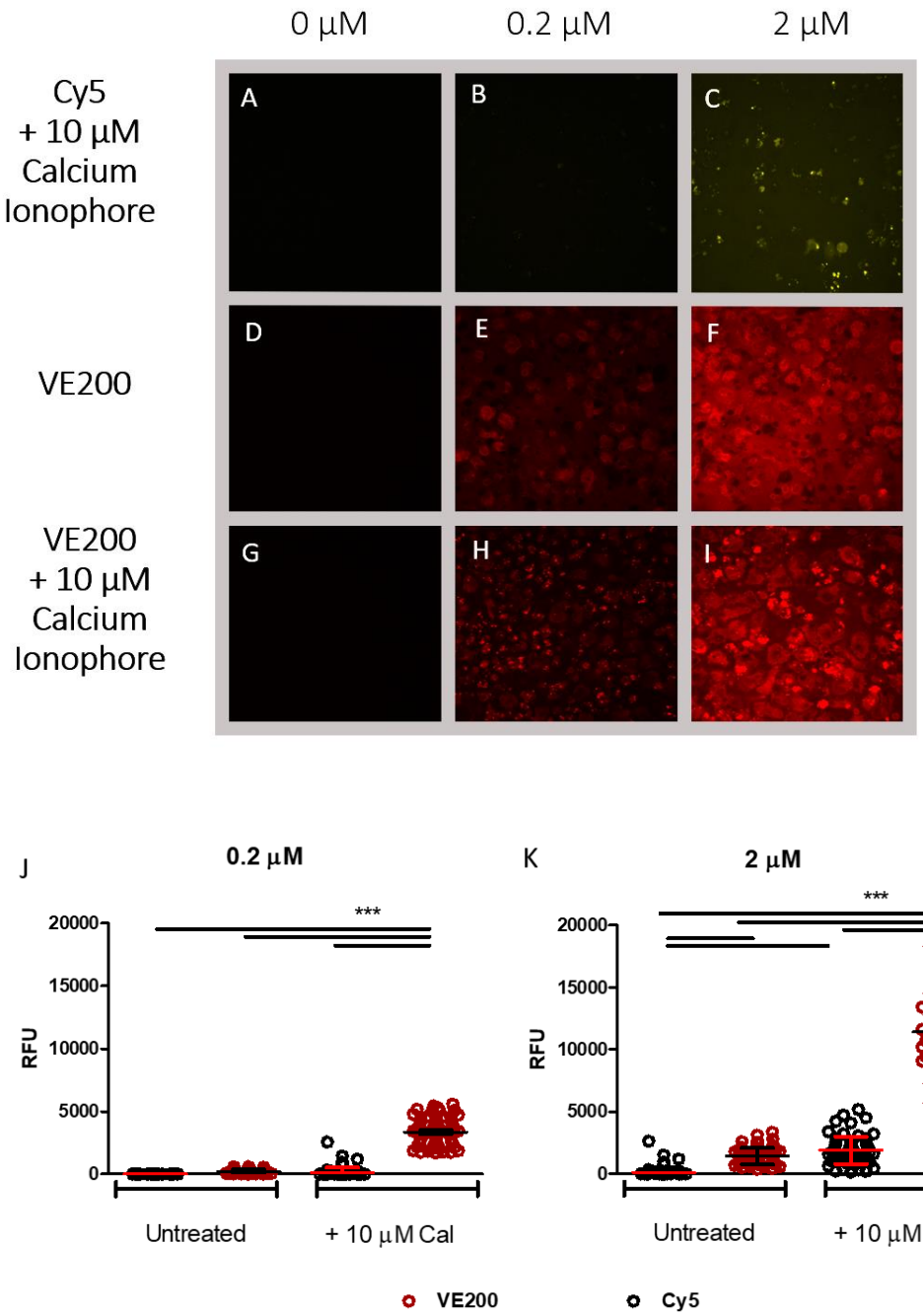

Figure 4.14 VE200 labels neutrophils more efficiently than Free Cy5
Confocal microscopy of neutrophils incubated for 10 minutes with **A-C)** free Cy5 dye and 10 µM calcium ionophore (Cal), **D-F)** VE200 and 10 µM calcium ionophore or **G-I)** VE200 alone. Cyanine-based reagents are at 0, 0.2 and 2 µM. Image quantification shows extent of cyanine-dye labelling in untreated and stimulated neutrophils for **J)** 0.2 and **K)** 2 µM incubations. Graph values represent mean ± SEM and *P* values were calculated using one-way ANOVA and a Bonferroni post-test. *** *P* <0.001, n=3

4.3.3 VE200 TITRATION ALLOWS MULTIPLEXING WITH NAP

NAP and VE200, as substrate- and inhibitor-based probes respectively, compete for active HNE. To evaluate the utility of multiplexed, NAP and VE200 imaging, VE200 was titrated to determine a concentration which would minimally block NAP signal while providing sufficient VE200 signal for the detection of neutrophil activation. Due to the bright and punctate nature of NAP signal, significant signal can be blocked before loss of signal becomes readily visible, highlighting the importance of image analysis techniques for objective, quantitative comparisons. An image analysis technique employed previously (see **Chapter 2, 2.2.7**) was re-applied. Although indistinguishable to the eye, NAP signal differences between untreated neutrophils in 3 µM NAP solution with 0 µM VE200 (1.1 kRFU), 0.2 µM VE200 (0.2 kRFU) and 2 µM VE200 (0.1 kRFU) were detectable (**Fig. 4.15G**), significant and VE200 dose dependent according to image analysis. As NAP signal is suppressed in the presence of an inhibitory probe, there may be a low level of neutrophil activation in the untreated population, image analysis therefore provides a sensitive measure of neutrophil activation in this assay. Importantly, NAP signal from calcium ionophore treated neutrophils show a 21.3-fold fluorescence increase (23.4 kRFU, **Fig. 4.15G**) over untreated neutrophils without VE200 co-incubation. Stimulated neutrophils co-incubated with 3 µM NAP and 0.2 µM or 2 µM VE200 display 71.1 % and 34.6 % full NAP signal respectively. This data implies a relationship of exponential decay between VE200 dose and NAP signal reduction whereby each log increase in VE200 dose halves NAP signal.

For the purposes of multiplexing in future experiments a dose of 200 nM VE200 will be sufficient to derive meaningful NAP and VE200 signal simultaneously from the same neutrophil.

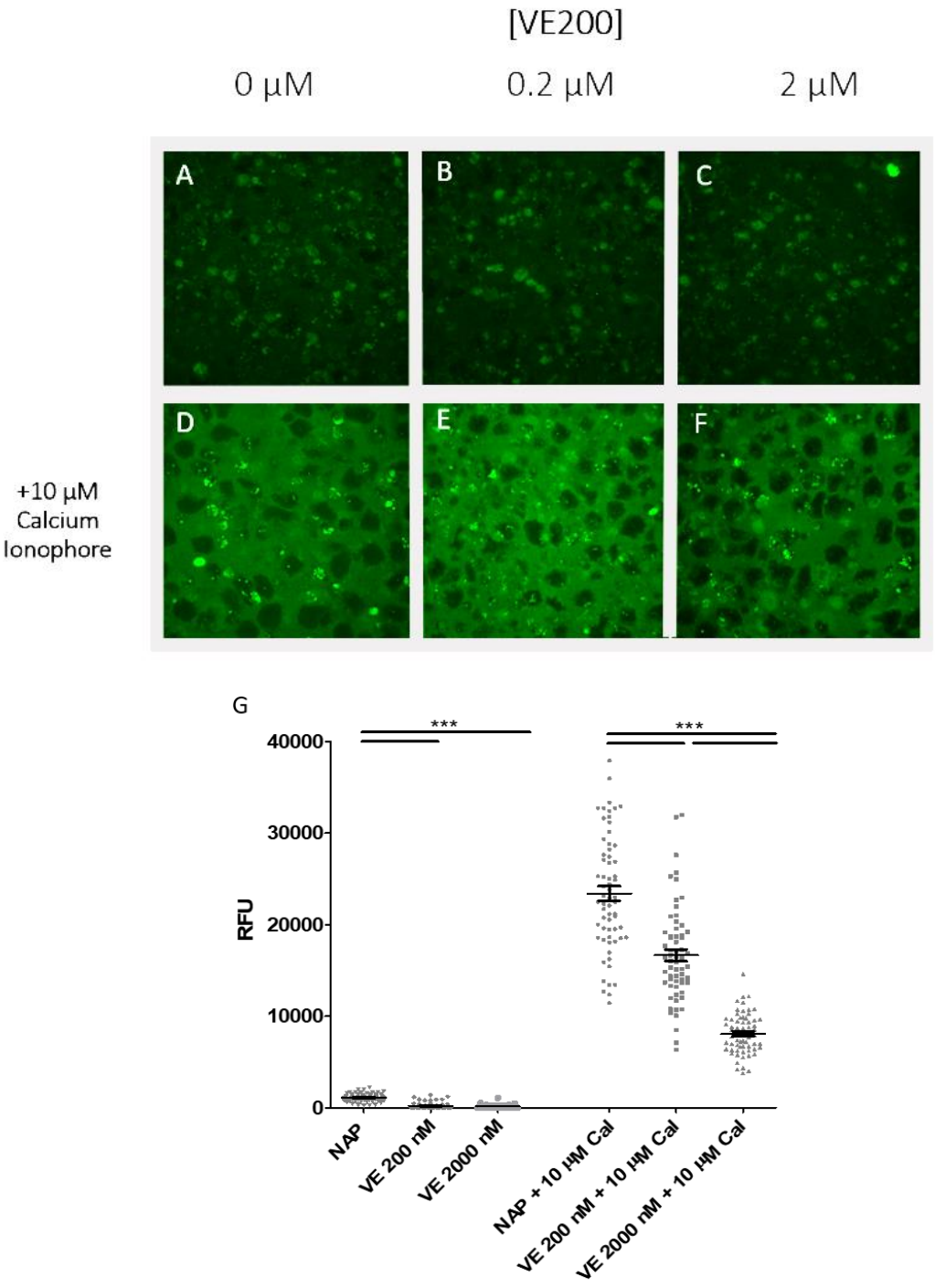

Figure 4.15 Low nanomolar VE200 doses enable multiplexed neutrophil labelling with NAP
Confocal microscopy of neutrophils incubated for 10 minutes with **A-C)** 3 µM NAP, **D-F)** 3 µM NAP and 10 µM calcium ionophore, in the presence of 0, 0.2 and 2 µM VE200. Image quantification shows extent of NAP signal elicited from untreated and stimulated neutrophils at varying VE200 concentrations. Graph values represent mean ± SEM and *P* values were calculated using one-way ANOVA and a Bonferroni post-test. *** *P* <0.001, n=3

4.3.4 DETECTING NEUTROPHIL ACTIVATION ACROSS THE NEUTROPHIL LIFESPAN: INTRACELLULAR FLUORESCENCE

Neutrophils are typically short-lived leukocytes. To evaluate VE200 staining in apoptotic and necrotic neutrophil populations, 100 nM VE200 was added to an imaging assay measuring DAPI staining over time (see **Fig. 3.11**). VE200 shows similar staining for untreated neutrophils at 2 (35.5 RFU) and 6 (45.9 RFU) hours, increasing 4.2-fold at 20 hours (194.2 RFU). Neutrophils treated with 1 µM calcium ionophore, at each timepoint, increase from 199.8 RFU at 2 hours to 356.7 RFU at 6 hours without increasing further at 20 hours (319.0 RFU). In the 15 µM QVD pan-caspase inhibitor (QVD) treatment group, VE200 signal is low at 24.9 RFU at 2 hours and peaks at 6 hours (7.2-fold increase from signal at 2 hours) before falling at 20 hours (2.0-fold increase from signal at 2 hours). With 15 µM QVD + 1 µM calcium ionophore treatment VE200 fluorescence rises at each time point from 2 (132.6 RFU), to 6 (202.8 RFU), to 20 hours (422.8 6 RFU). No VE200 signal is observed at any time point when neutrophils are pre-treated with 15 µM GW447631. Although membranous and intracellular fluorescence increases over time when ageing neutrophil populations are stained with either 3 µM NAP alone or with 100 nM VE200, differences in the rate of signal generation between timepoints create different trends of increasing signal for VE200 as compared with NAP (see **Fig. 3.11**). NAP staining reveals more distinctions between the various neutrophil populations in this assay. However, VE200 and NAP show different temporal patterns of increasing signal in untreated neutrophils, and neutrophils prevented from initiating apoptosis, with or without calcium ionophore stimulation.

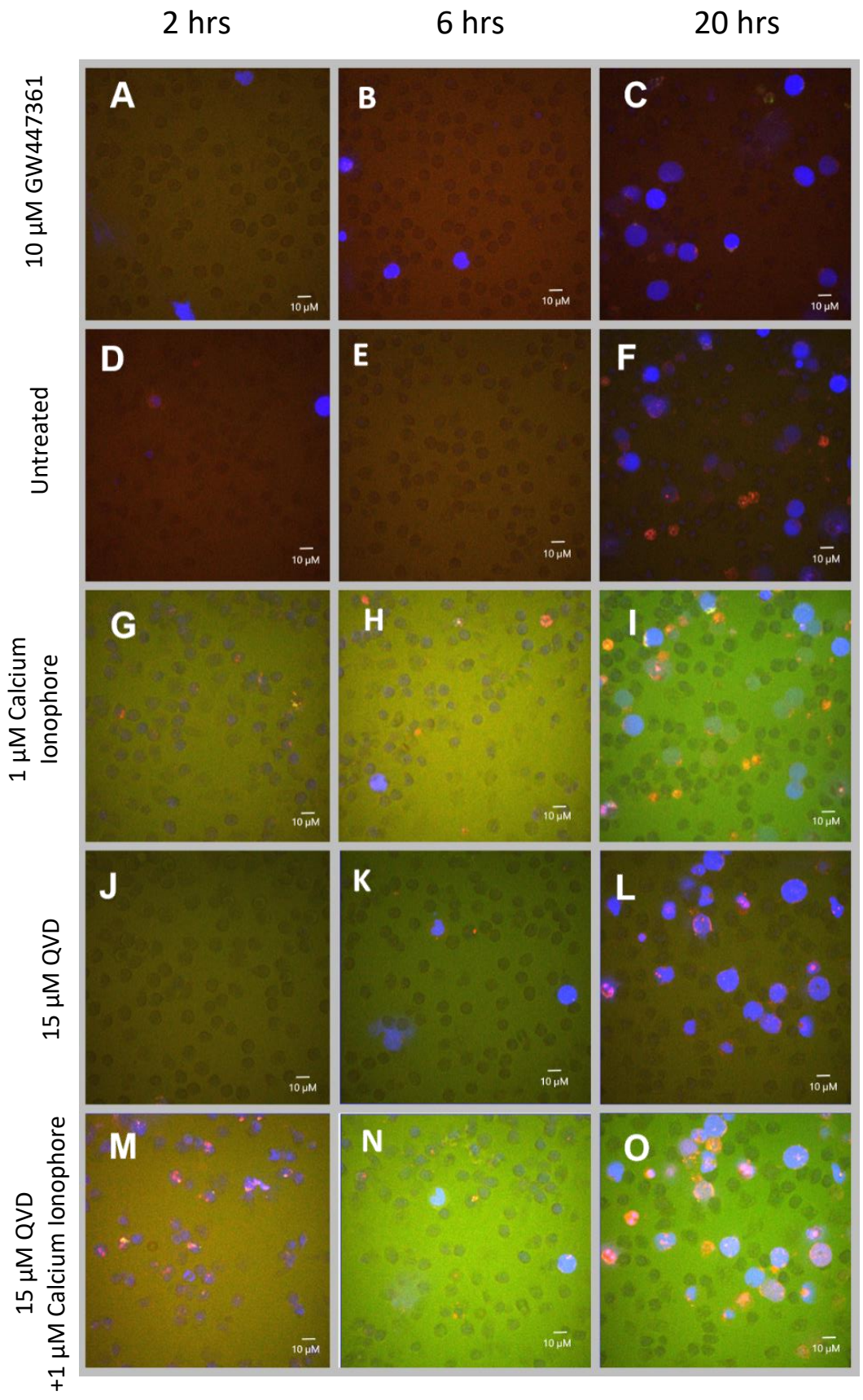

Figure 4.16 NAP and VE200 multiplex to report activation in ageing neutrophil populations

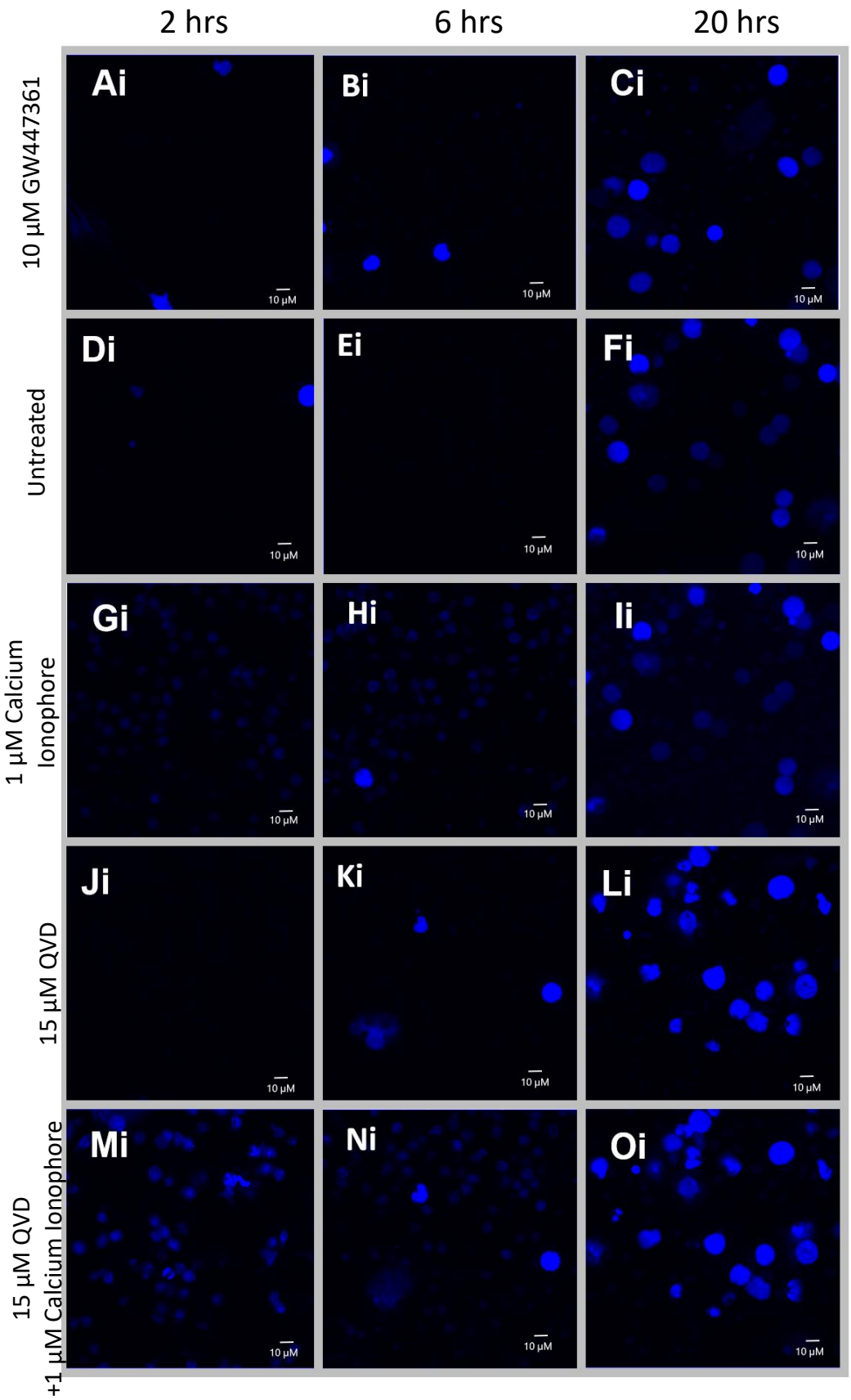

Figure 4.16 NAP and VE200 multiplex to report activation in ageing neutrophil populations

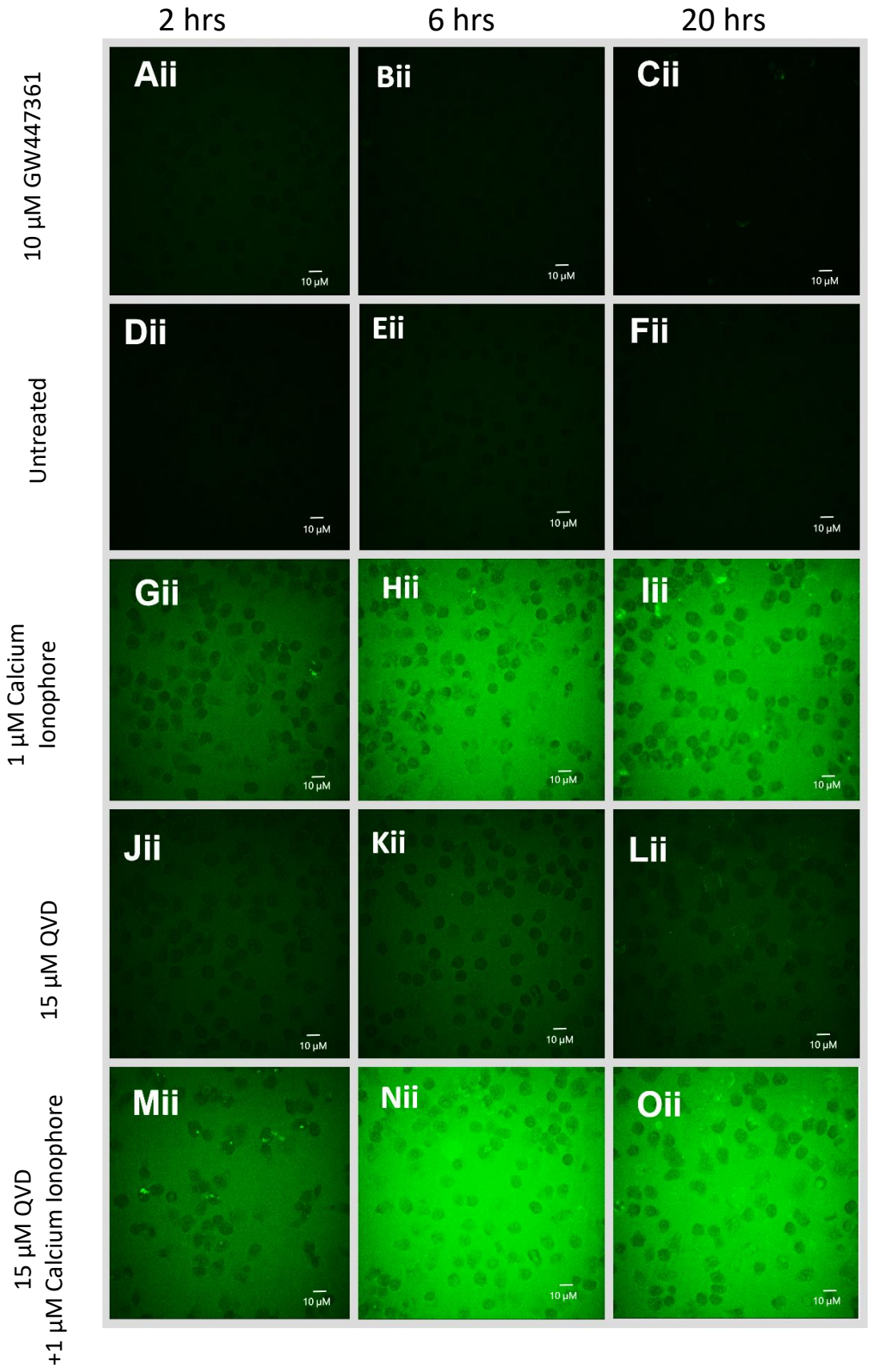

Figure 4.16 NAP and VE200 multiplex to report activation in ageing neutrophil populations

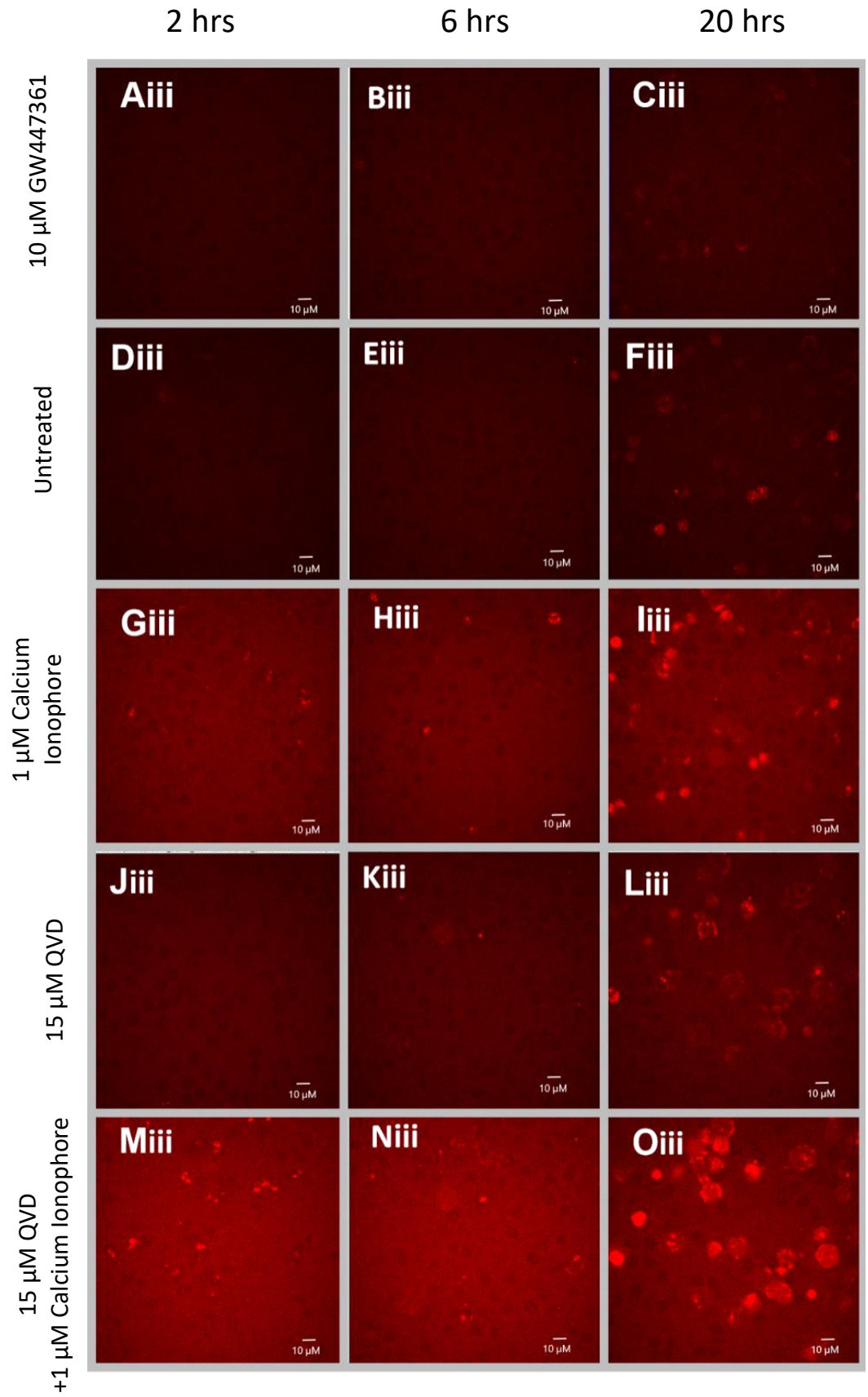

Figure 4.16 NAP and VE200 multiplex to report activation in ageing neutrophil populations

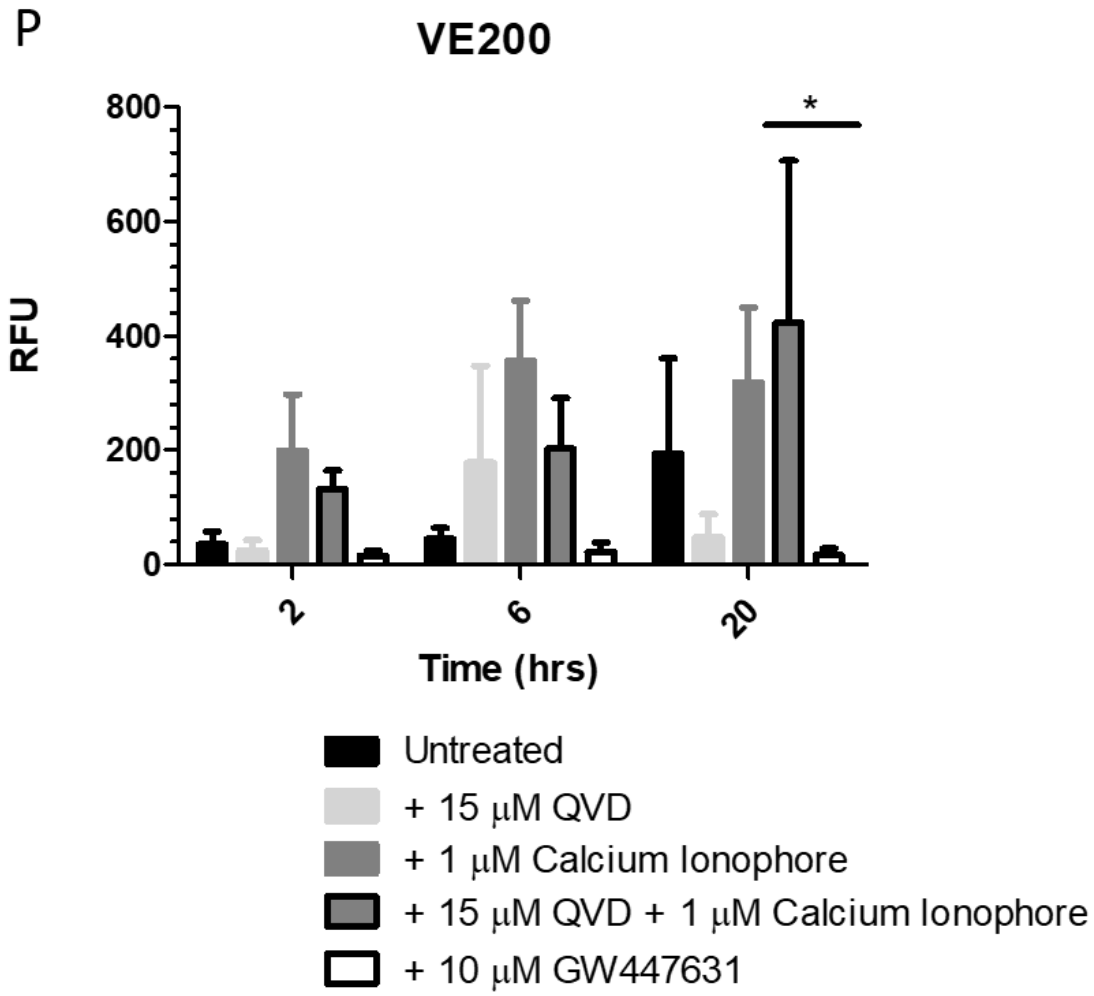

Figure 4.16 NAP and VE200 multiplex to report activation in ageing neutrophil populations
Images represent neutrophils incubated **A-C)** with 10 μM GW447631 **D-F)** without treatment **G-I)** with 1 μM calcium ionophore **J-L)** with 15 μM QVD pan-caspase inhibitor and **M-O)** with 15 μM QVD + 1 μM calcium ionophore at **A,D,G,J,M)** 2 **B,E,H,K,N)** 6 and **C,F,I,L,O)** 20 hrs. Roman numerals represent **i)** merge **ii)** DAPI and **iii)** NAP **iv)** VE200 images. **P)** Image analysis of VE200 images are shown, plotting mean intracellular fluorescence intensities of neutrophil populations. Values represent mean ± SEM, *P* values were calculated using two-way ANOVA and Bonferroni multiple comparisons test, * *P* <0.05, n=3

4.3.5 HNE-PROBE MULTIPLEXING ACROSS THE NEUTROPHIL LIFESPAN

To understand the effect of probe multiplexing on functional neutrophil imaging over time, 3 µM NAP and 100 nM VE200 were concomitantly added to ageing neutrophil populations at the point of imaging. Trends in NAP signal over time varied when 3 µM NAP was used to image HNE activity in ageing neutrophil populations, with and without 100 nM VE200 co-stain (see **Fig. 3.11**). Whether neutrophil populations aged untreated or under 15 µM pan-caspase inhibitor (QVD) treatment or 1 µM calcium ionophore treatment, 100 nM VE200 significantly reduced NAP staining at 20 hours (**Fig. 4.17.B and C**). The trend of NAP staining in the 15 µM QVD treatment group changed from increasing to decreasing at each timepoint when VE200 was added (**Fig. 4.17.B**). However, when neutrophils incubating in 15 µM QVD were challenged with 1 µM calcium ionophore at each timepoint there were no differences between NAP signal with or without the presence of 100 nM VE200 (**Fig. 4.17.D**).

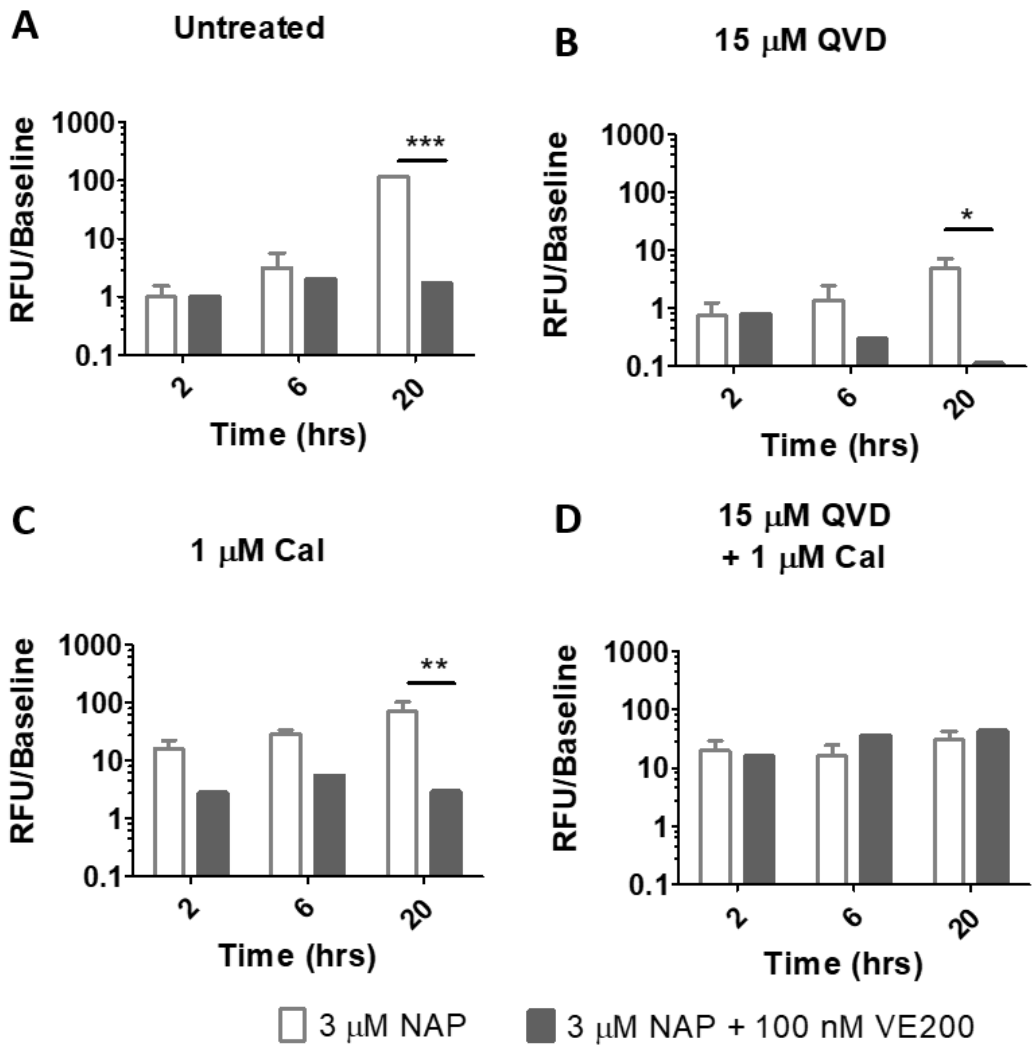

Figure 4.17 VE200 reduction of NAP signal is most pronounced at 20 hours
Image analysis of NAP images are shown, plotting mean intracellular fluorescence intensities of **A)** untreated, **B)** 15 μM QVD pan-caspase inhibitor **C)** 1 μM calcium ionophore (CaI) and **D)** 15 μM QVD pan-caspase inhibitor and 1 μM calcium ionophore treated neutrophil populations. Values represent mean ± SEM, *P* values were calculated using two-way ANOVA and Bonferroni multiple comparisons test, * *P* <0.05, ** *P* <0.01, *** *P* <0.001 n=3.

4.3.6 HNE-PROBE SIGNALS ARE NOT CORRELATED IN NEUTROPHIL APOPTOSIS

NAP and VE200 signals are least correlated when 10 µM GW447631 is present as this irreversible HNE inhibitor successfully outcompetes 100 nM VE200 without abrogating NAP signal. Probe signal decorrelation is most pronounced at the 20-hour timepoint (r^2=0.17). The conditions that show the highest correlations at 2, 6 and 20 hours are the 15 µM QVD conditions with (r^2=0.98, 0. 98 and 0.96 respectively) and without 1 µM calcium ionophore (r^2=0.92, 0. 88 and 0.83 respectively). At 2 and 20 hours, the untreated (r^2=0.97 and 0.80) and 1 µM calcium ionophore (r^2=0.94 and 0.78) conditions show high probe signal correlation however this falls at 6 hours to r^2=0.49 for untreated neutrophils and r^2=0.58 for activated neutrophils.

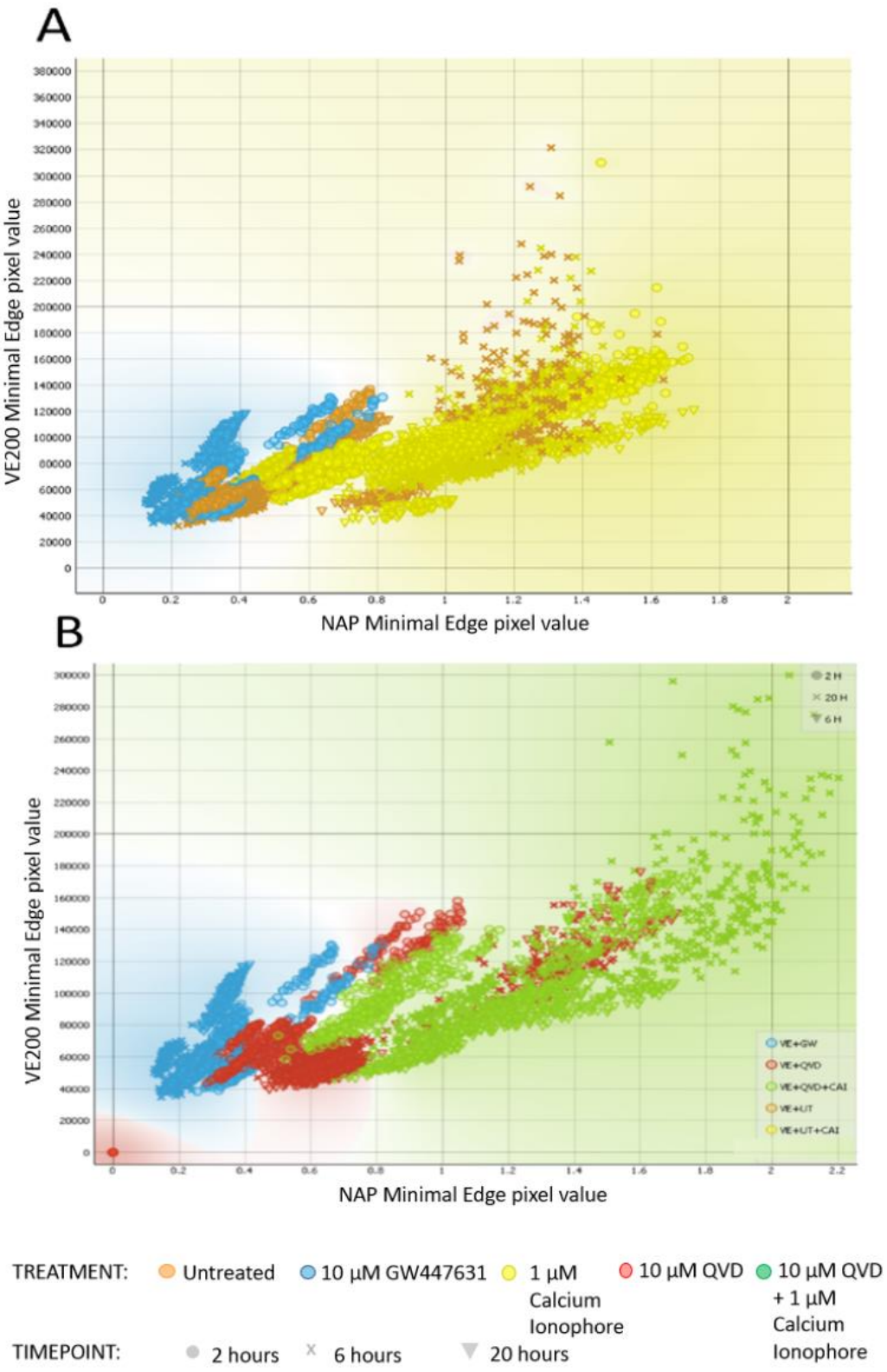

Figure 4.18 Correlation between NAP and VE200 signal decreases at 6 hours

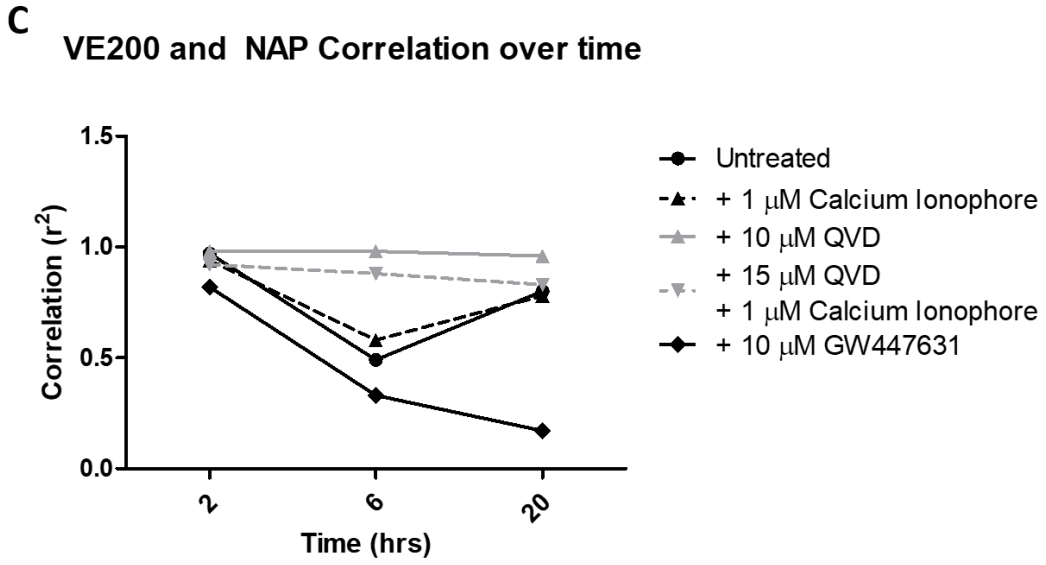

Figure 4.18 Correlation between NAP and VE200 signal decreases at 6 hours
NAP fluorescence is plotted against VE200 fluorescence for neutrophils **A)** without treatment (orange), under 1 μM calcium ionophore (yellow) treatment, under 10 μM GW447631 (blue) treatment **B)** under 15 μM QVD pan-caspase inhibitor, 15 μM QVD pan-caspase inhibitor + 1 μM calcium ionophore and 10 μM GW447631 (blue) treatment. Symbol shapes represent the 2 (circle) 6 (triangles) and 20-hour (crosses) timepoints. **C)** Correlations between NAP and VE200 signal for each population at each time point were plotted against time. Values represent cumulative raw data, n=3.

4.3.7 INITIAL KINETIC CHARACTERISATION OF GW447631 INHIBITORY CONSTANT

Determining the inhibitory constant of GW447631 proved technically difficult and will briefly be described. Initially progress curves were used to measure enzyme activity in a discontinuous measurement protocol. These curves have rectangular hyperbolic trends and their initial linear gradients (tangeants) must be extracted to begin the data reduction process for determining inhibitory constant. A curve-fitting approach using MatLab version R2017b can improve tangent measurements, fitting entire progress curves and interpolating tangent values. However, the approach via MatLab requires initial constants of a rectangular hyperbolic equation to be deduced individually, for numerous curves.

A fully automated data reduction approach for inhibitory constant measurement was developed using specialist enzyme kinetics curve-fitting software, GraFit version 7. In GraFit version 7, inputting the Michaelis Menten equation can be used to determine unknown values of inactivation constant and inhibitory constant. While using GraFit version 7 the technical parameters of enzyme kinetics experiments were re-evaluated leading to a continuous measurement assay. Implementing a continuous method significantly simplified work flow and reduced the risk of human error present in the discontinuous method. Using a continuous measurement assay, it became apparent that the combination of substrate and detection system, AAPV-AMC and BioTek II plate-reader, was not sensitive enough

for the purposes of this kinetic characterisation. AMC proved insufficiently bright to produce the fluorescent changes required to measure low enzyme velocities from 1-10 nM HNE. Increasing HNE concentration was not feasible because this necessitates exponential increase in substrate concentrations, as change in substrate concentration must be negligible throughout the experiment, to ensure the accuracy of data reduction.

A rhodamine labelled substrate was evaluated for its superior quantum yield compared to coumarin, this would increase the sensitivity of measurements, however the new substrate was found to be poorly water soluble and solubilising agents can reduce enzyme activity. Finally using AAPV-pNA in a continuous measurements assay and analysing data via GraFit version 7 proved to be the most useful method for an inhibitory constant assay.

The inhibitory constant of VE136 can be approximated at 14.3 nM. However, the combination of HNE concentration and AAPV-pNA remained suboptimal indicated by a slight increase in enzyme velocity over time in the plateau phase. This suggests that 10 nM HNE affected a non-negligible reduction in AAPV-pNA concentration, even at 1mM substrate.

4.3.8 SUMMARY

VE200 was the lead HNE-targeted probe candidate of a three-probe panel. VE200 has excellent cellular and molecular specificity and can be appropriately visualized at a 200 nM concentration. VE200 inhibits HNE irreversibly but the ability to image HNE with VE200 at low doses, limits its inhibitory effect such that multiplexing with NAP, an activity-based probe, is possible. Multiplexed NAP and VE200 imaging are useful in categorising neutrophils of varying ages and viability states with appropriate image analysis.

4.4.0 DISCUSSION

4.4.1 CHARACTERISATION OF GW447631 50% INHIBITORY CONSTANT

At 12.9 nM the IC50 of GW447631 in the lysate inhibition assay seems to indicate high binding affinity within the context of this assay. Importantly, neutrophil lysate HNE inhibition studies demonstrated that GW447631 is capable of inhibiting HNE derived from primary human neutrophil lysates. HNE is stored in neutrophil azurophil granules, complexed with sulfonated proteoglycan,[62] this physical barrier has to be overcome to inhibit HNE in this assay. Lysate preparation may be liberating proteoglycan from HNE active sites and allowing for interaction with GW447631. Alternatively, GW447631 may displace proteoglycan to bind HNE. Enzyme inhibition, by GW447631 follows the so-called suicide inhibition mechanism, a two-step process requiring HNE active site occupancy and inhibitor cleavage. Demonstrating that both steps of suicide inhibition can occur in neutrophil lysate is an encouraging outcome, meaning that this may be possible

with HNE-targeted probes. Neutrophil degranulation and neutrophil necrosis will also release HNE into the surrounding supernatant, however these processes are likely to liberate less HNE per second than the freeze-thaw cycles of lysate preparation. Hence the relatively high efficacy of GW447631 bodes well for its use as a sensitive and inherently safer optical probe, when fluorescently tagged, as low nanomolar concentrations of probe could be introduced to label neutrophils with minimal effects on other cellular processes.

4.4.2 INTRACELLULAR KINETIC IMAGING OF GW447631 INHIBITION

The ability to describe intracellular rates of enzyme activity may enable studies of HNE kinetics in cellular imaging assays. A variety of imaging platforms could facilitate this, including high-throughput screening *in vitro* and fluorescent endomicroscopy *in vivo*. Neutrophils transition between quiescent, primed and activated states and the ability to detect intracellular HNE rates may facilitate detecting these transitions. For example, following neutrophil priming, de-priming may occur. Neutrophil de-priming is understood to take place principally in the human lung[200] and may have significant impact on pulmonary inflammatory disease progression and the spreading of potentially harmful, activated neutrophils to distant organs following reverse transendothelial migration (rTEM).[18] Will deprimed neutrophils yield a different HNE rate than the more harmful rTEM neutrophils? If so, these rates could prove useful in assessing clinical disease. Future HNE kinetic imaging studies have the potential to answer this question. The current studies demonstrate that neutrophils are capable of increasing and decreasing NAP

fluorescence following LPS priming and fMLF stimulation. Characterising signal deceleration could prove useful in identifying different signal-loss mechanisms, so that LPS/fMLF treatment can be distinguished from de-priming by HNE imaging.

The effect of well dwell-time, prior to stimulation, may be expected to produce imperceptibly subtle changes in HNE activity however these are detectable with image-processing and sensitive NAP signalling. Longer incubation times may facilitate greater extents of integrin engagement in fibronectin coated wells, upregulating the extent of HNE release.[201] The trend of decreasing magnitude of well incubation effect with increasing GW447631 dose may be due to increased intracellular HNE inhibition, at higher doses, prior to degranulation. HNE inhibition also effects neutrophil spreading upon stimulation which implies the cleavage of fibronectin by HNE[23] facilitates cell-spreading. The effect on cell spreading does not appear to be due simply to the presence of drug since 100 µM Sivelestat had less effect than 10 µM GW447631. GW447631 has a more potent K_i than Sivelestat (0.014 nM vs. 200 nM) so that it can affect greater inhibition at lower doses than Sivelestat. The effects of these two drugs on cell-spreading also show GW447631 having greater effects than Sivelestat, despite a, log-fold, higher Sivelestat concentration. Because decrements in cell radius are on the scale of nanometres relatively large standard error is measured in this small sample size, increasing sample size could help to overcome this limitation.

4.4.3 FLOW CYTOMETRIC ANALYSIS OF HNE-TARGETED PROBE LABELLING

An important finding of the labelling efficiency experiments (**Fig. 4.11**) was the trend towards increased PBMC labelling with exposure to calcium ionophore. Although some increase in labelling may occur passively with calcium ionophore stimulating endocytosis there is some potential for this labelling to represent a HNE specific mechanism. 40% of monocytes contain and release HNE at concentrations that correspond to 3% degranulation from neutrophils.[137] It is possible for a very limited number of activated PBMCs to achieve HNE-specific VE200 labelling, however these quantities of HNE are very limited and prove undistinguishable from untreated conditions by flow cytometry. Another possible explanation for the PBMC trend is the presence of a very small number of neutrophils in the PBMC sample. A 3% neutrophil impurity would fall within the acceptable limits of PBMC purity following the Percoll blood preparation (95% purity limit) and enable 3×10^4 neutrophils to potentially influence fluorescent changes in PBMC staining upon activation. A small percentage of degranulating neutrophils may have released HNE onto the surfaces of PBMC where HNE can adhere by charge.[202] Finally, simple endocytosis may have led to the background levels of PBMC fluorescence. Increased with activation, endocytosis-dependent labelling can produce negligible levels of background fluorescence as **Fig. 4.14C** demonstrates with neutrophils and free Cy5 stain. Because there was no noticeable difference between monocyte-derived and lymphocyte-derived VE200 labelling a neutrophil impurity, seems the most plausible explanation for the statistically insignificant increase in HNE labelling with calcium

ionophore exposure. The most important conclusions for these studies are that VE136 and VE200 show good neutrophil specificity by virtue of specific HNE binding. VE200 showed the best cellular specificity and was taken forward.

4.4.4 SENSING GRADED NEUTROPHIL RESPONSES WITH HNE-TARGETED PROBE SIGNALS

The range of fluorescence intensities acquired by varying PMA dose indicates that targeted probes are capable of generating distinct signals for distinct levels of neutrophil activation. Appropriately titrated so as not to obfuscate NAP signal-related information, targeted probes could provide an additional layer of information for classifying neutrophils activated with varying stimulus intensities. This titration would be a trade-off between NAP signal and targeted probe signal detection. Because VE200 was taken forward for further experimentation, its signal to dose relationship was evaluated.

4.4.5 LIVE CELL VE200 DOSING AND IMAGE ANALYSIS

In **Fig. 4.13.K** and **L** VE200 signal of activated neutrophils is compared by whole-frame histogramming and intracellular puncta measurement respectively and these are both valid means of relaying the VE200 signal in images of activated neutrophils. In **Fig. 4.13.K** extracellular changes in VE200 signal are captured which contribute to the exponential rise in signal with increasing concentration. Intracellular measurements are more relevant than combined intracellular and extracellular measurements, for signal generation per cell. The subtle difference between measurements captured by the two image analysis techniques demonstrate the importance of appropriate use of image analysis to address the pursuit of specific hypotheses. With an understanding of VE200 specificity and optimal dose, it's ability to be multiplexed with NAP was considered.

4.4.6 CHARACTERISING VE200 AND NAP MULTIPLEXING

The enhanced labelling of VE200 over free Cy5 with neutrophil activation, demonstrates that the irreversible inhibition (see **Fig 4.12**) affected by its 4-oxo-β-lactam moiety, is responsible for increased activated neutrophil labelling. Combined with the similarities in the appearance and intracellular distribution of VE200 signal puncta and NAP signal puncta, VE200 seems effective in elucidating HNE in stimulated neutrophils. In untreated conditions, the increased fluorescence of VE200 compared to free Cy5 at 2 µM may be due to HNE-specific probe accumulation, in a minority of activated neutrophils. However, because Cy5 is

sensitive to photobleaching even under ambient light conditions, this difference could be due to more photobleaching in the free Cy5 condition at baseline. Although care is taken to protect both dyes from ambient light, making use of a more photo-stable fluorophore would resolve this concern. In the case of contaminating activated neutrophils, the addition of Sivelestat can be used to remove the unwanted effect. In the case of disproportionate photobleaching, a spectrometer reading taken at baseline could have compared detected and quantified any such difference.

The Olympus IX83 confocal spinning disk microscope enables each pixel to have a value from 0 to 65,535. The ability of NAP to detect low nanomolar HNE activity combined with such sensitive optical detection means that information inaccessible to the human eye, can be reported from imaging systems, with appropriate image analysis. Although most neutrophils are not in an activated state at the start of each experiment there is potential for a limited amount of neutrophil activation and/or death to occur during the three-hour Percoll blood preparation. The dose dependent suppression of NAP signal with VE200 co-incubation in untreated neutrophil populations indicates the presence of an activated neutrophil minority. Although baseline neutrophil activation was not investigated further in the context of probe multiplexing, the homogeneity of the untreated neutrophil population has been demonstrated by flow cytometry above (**Fig. 3.6**) and the 21.3-fold increase in NAP signal between untreated and activated neutrophil populations provides a sufficient assay window for the assessment of probe multiplexing. Normalising

activated conditions to untreated controls could remove the effects of different untreated baselines from the data.

4.4.7 NAP AND VE200 SIGNAL DECORRELATION FROM AGEING PMN POPULATIONS

Although both probes act on HNE, apoptosis appears to decorrelate NAP and VE200 probe signals. When neither caspases or HNE are inhibited, the greatest decreases in probe signal correlation are detected at 6 hours. In the untreated and 1 µM calcium ionophore stimulated populations probe signal correlation falls, by 50% and 48% respectively, at 6 hours. Similarly, 60% decorrelation occurs in the 10 µM GW447631 condition at 6 hours. Flow cytometric analysis shows the greatest difference between the 6 and 2-hour time points is in their apoptotic neutrophil content (see **Fig.3.10**). Importantly the necrotic population which may overwhelm apoptotic cell contributions, at 20 hours, cannot significantly affect signals, at this earlier time point. When apoptosis is reduced with 15 µM pan-caspase inhibitor correlation remains high (r^2>0.80) throughout the time course irrespective of stimulation with 1 µM calcium ionophore. It may be that HNE is inhibited in apoptotic neutrophils as intracellular membranes degrade and endogenous HNE inhibitors mix with HNE. At 20 hours, probe signal correlation is restored, in uninhibited, untreated and activated neutrophil populations, consistent with the complete loss of lipid membrane integrity associated with these predominantly necrotic neutrophil populations (see **Fig.3.10**). When neutrophils are untreated

both probes are dark and when neutrophils are activated/necrotic, both probes are at their brightest. Decorrelation may help specifically with apoptotic neutrophil detection when multiplexed imaging is implemented. Being able to distinguish between healthy, apoptotic and necrotic neutrophils using morphological and fluorescent information could provide meaningful patient stratification information for quantifying cell viability via fibred confocal endomicroscopy (FCE) *in vivo.* Immune cell functions such as efferocytosis could be analysed using this technique helping to distinguish between primary and secondary pathologies.

CHAPTER 5:

HNE IMAGING AS A NEUTROPHIL STRATIFICATION TOOL IN THE HUMAN LUNG

5.0.0 INTRODUCTION

The novel activable and targeted probes, NAP and VE200 are specific for and sensitive to HNE activity. FCE should therefore enable the enumeration of activated neutrophils using these probes. The work of this chapter is to establish if that is the case and to understand how much information can be derived from multiplexed HNE-imaging. More specifically, aiming to determine if statistical and machine learning techniques can be applied to imaging datasets such that neutrophils can be phenotyped as untreated, primed and activated.

5.1.0 THE STUDY OF HNE UNDER FIXATION

The protease-antiprotease hypothesis was formed from four observations 1) the marked potential of elastases to digest extracellular matrix producing macroscopic loss of function[203,204] 2) the identification of proteases that could be used to model pulmonary emphysema in animals[205] 3) the realization that α-1-antiprotease (α-1-PI) provides essential and specific regulation of neutrophil elastase[206] and 4) the association of α-1-PI deficiency with pulmonary emphysema.[207] This was the hypothesis that stimulated so much interest in neutrophil protease dysregulation in disease states which has lead to many clinical trials. Unfortunately the hypothesis was not complete and many clinical trials investigating the effects of synthetic HNE inhibitors have produced negative data, even in diseases with established protease dysregulation and even with evidence of *in vivo* elastolysis.[208–210] Major caveats to the assumption that increased HNE inhibitor administration will therapeutically correct HNE activity have arisen, these are mechanisms by which HNE escapes inhibition. Membranous HNE is resistant to endogenous inhibition and this is believed to be a steric hindrance effect.[211,212] As HNE molecules bind the external plasma membrane via electrostatic charge, these molecules can bind in orientations which obfuscate the active-site, preventing interaction with inhibitors. Perhaps more importantly, adherent neutrophils create interfaces with the substratum from which inhibitor molecules are largely excluded.[202] This exclusion is an important mechanism for utilising active HNE in the presence of HNE-inhibitors, as neutrophils can degranulate onto their substratum, concentrating HNE there. Although there is still much uncertainty surrounding the spatiotemporal dynamics of membranous

HNE accumulation and clearance, neutrophil fixation studies have helped to develop the current understanding.

Owen *et al.* produced the first report of membranous HNE and cathepsin G using fixed neutrophils and immunogold microscopy. In addition to finding cell-surface HNE inhibition-resistant Owen *et al.* found that fMLF and C5a stimulated two to three-fold increases in plasma membrane protease expression, whereas LPS concentrations as low as 100 fg/mL produced a ten-fold increase.[212] Korkmaz *et al.* synthesised a sensitive fluorogenic HNE substrate and used it to demonstrate full inhibition of membranous HNE. At equimolar concentrations, α-1-PI effectively blocked the HNE activity of unfixed neutrophils in solution but fixed samples retained their activity.[213] Korkmaz *et al.* also found that α-1-PI binding caused dissociation of HNE-α-1-PI from neutrophil plasma membranes.[213] Although Dwenger, Tost and Holle's dissociation experiments proved the existence of cell-surface binding sites for HNE[214], their claims of a specific receptor were perhaps disproven by Owen *et al.'s* identification of charge-based interactions with membranous heparin and chondroitin sulfate-containing proteoglycans, for HNE and cathepsin G.[215] A small fraction of proteoglycan associated serine proteases can bind β2-integrins expressed upon neutrophil activation.[18,216]

5.1.1 DIFFERENTIAL HNE RELEASE

Neutrophils respond in a myriad of ways to their various stimuli. Neutrophils may be primed or activated in response to stimuli, or both in response to sequential stimuli and they may be de-primed, all states that are distinguishable from neutrophil quiescence. Neutrophil priming is not a generic response but demonstrates cytokine-specificity. For example, platelet activating factor (PAF) and interferon γ (IFN-γ) both promote neutrophil adhesion[217,218], phagocytosis[219,220], degranulation[34,221] and inflammatory cytokine release[222,223] but they have opposite effects on chemotaxis[224,225] (PAF promoted) and apoptosis[226,227] (IFN-γ promoted). This is not surprising when we consider that the increased lipid-A content of Re-LPS primed neutrophils with increased ROS generation compared to the S-LPS glycoform, prior to fMLF stimulation.[228]

Rainger *et al.* found that C5a, fMLF and IL8 but not PAF were capable of eliciting HNE release. Although fMLF and PAF trigger cell adhesion pathways only the former lead to autocrine LTB4 signalling, stimulating HNE.[229] Although adherence was not necessary for HNE-release, adherent neutrophils, engaging CD11b/CD18 β2-integrins had a significantly increased degranulation response. Adhesion-mediated increases in degranulation may be quantal in nature such that the adhesion of priming stimuli and activating stimuli combine to elicit maximal degranulation. Because integrin expression and hence firm adhesion is a quantal process, different stimuli may promote varying extents of integrin expression, effecting stimulus-specific HNE release. This is not the case for all priming agents, PAF-mediated

superoxide production is CD11b independent.[230] The quantal release of protease inhibitors (elafin, SLPI and serpin B1) from neutrophils may provide a secondary level of chemokine-specific HNE activity modulation.[171,174,175]

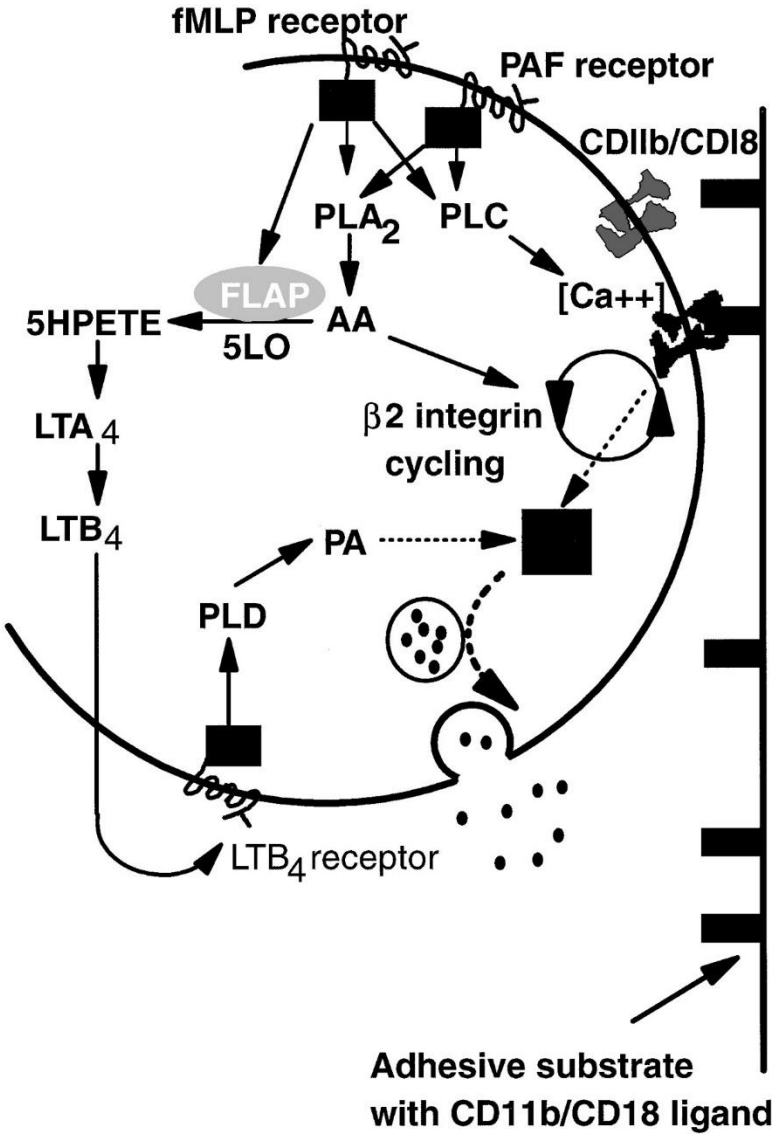

Figure 5.0 Signalling pathway for adhesion-enhanced chemokinetic degranulation
Copyright Rowley and Nash 1998 [229]

5.1.2 FIBRED CONFOCAL ENDOMICROSCOPY

Optical imaging apparatus have been developed to address a range of experimental requirements: super-resolution techniques more precisely describe subcellular dynamics, image cytometry improved the throughput of high-resolution imaging techniques, and the use of optical fibres enabled new confocal laser scanning microscopy paradigms *in vivo* (see **Chapter 1.2.1 - 1.2.4**). The Food and Drug Administration have approved one fibred confocal endomicroscopic system for human imaging, the CellVisio system, developed by Mauna Kea. However there are many experimental prototypes[143,231–234] for fibred confocal endomicroscopy (FCE) and the PROTEUS project have developed a system which incorporates chemical sensing and direct sampling/instillation interaction with the field of view.[235] Several hardware modifications enable different outcomes with FCE. Fibre bundles housing ~100, 000 fibres can form an image whereby each individual fibre contributes 1 pixel and acts as a confocal pinhole for proximal scanning confocal imaging.[236]

A single-mode fibre has a diameter of <10 µM and, surrounded by an outer cladding, transmits light by total internal reflection.[237] Single-mode fibres were advantageous for exceeding the limits of miniaturization and flexibility inherent in fibre-bundle imaging and delivering greater imaging resolution.[238] But single-mode fibre imaging had its own limitations including increased speckle noise, loss of multimodal light and a loss of field depth. Double-clad fibres have a fibre core, inner cladding and outer cladding, each with their own refractive index.[239] This improved on single-mode imaging limitations by using the inner-cladding to capture

multimodal light. Increasing light collection efficiency was useful for fibred Raman spectroscopy and multi-photon imaging but increasing field depth deviates from a confocal imaging regime. [238,240]

Multi-mode imaging was also described using a single imaging fibre the so called, single multi-mode imaging (SMMI). SMMI can image three-dimensional volumes at high resolution without the need for physical depth scanning making it a fast imaging paradigm for clinical applications.[241] SMMI can generate confocal images by digitally processing the image-volume.[242] Unfortunately this technique is not amenable to fibre-bending which is often necessary in a clinical imaging setting.[241] With this in mind, fibre bundles are currently the most clinically relevant FCE platform.

5.1.3 IMAGE ANALYSIS

The analysis of imaging data has become a field in its own right. Nuclear and plasma membrane stains added to the experimental set-up enable cell segmentatiaon and image cytometery. Fluorescence intensity is quantifiable using grayscale pixel values and comparable across images taken under identical conditions. Textural information is a particular advantage of image analysis as positional information may be imperceptible to the human eye and relay unique descriptors of cellular dynamics. Hundreds of variables can be measured by as variants of positional, fluorescence intensity and textural features within images and cells can be imaged and quantified under high-throughput conditions such that big data analysis

techniques may be required to approrpiately summarize data sets and visualize informative changes.

5.1.4 NEURAL NETWORKS

Artificial neural networks are sets of statistical algorithms inspired by neurobiology. Human neurons have input processes called dendrites and an output process, the axon which may branch for multiple connections to other neurons. These processes conduct the flow of information between the soma of connected neurons, where signals are integrated to control each neurons behaviour. With sufficient rules for action potential integration and firing the brain is capable of complex problem solving and image recognition was one area in which the human brain outperformed computer programs, until recently. Using the same principles, a neural network is comprised of input nodes, hidden layers, and output nodes. Digital images are in fact numbers with specified positions, vectors that lend themselves to mathematical manipulations such as thresholding, co-occurrence matrixes and non-linear functions. In a neural network, features of the original vectors can be taken as inputs, multiplication can be applied connections between nodes (weights) and non-linear functions can be applied at nodes (activation functions). Like the brain, multiple inputs can be received by each node in the network, in fact all the nodes of one layer interface with the nodes of immediately adjacent layers.

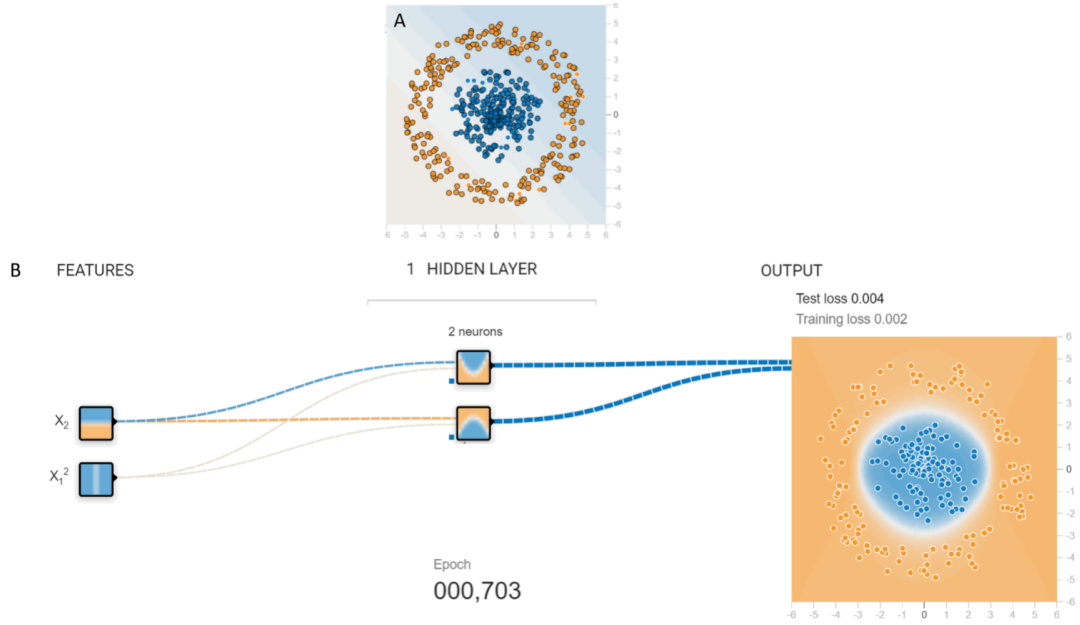

Figure 5.1 Schematic of an Artificial Neural Network
A) Classified input data **B)** Training on 50% of the sample, a single-layer perceptron, combined 2 features in 2 neurons to achieve an evaluation accuracy of 99.6% in 703 epochs. Line thickness indicates weight. Adapted from a tensor flow neural network online tool.[243]

There may be many hidden layers of nodes between the input and output layers resulting in a multilayer perceptron or none, a single layer perceptron. A training data set is used to inform the neural network of the vectors it should arrive at and this allows an error, a difference between the predicted and actual vectors to be calculated. Backpropagation allows the network to intelligently fine-tune each of its connections in a direction that minimizes error for the next epoch, a complete pass through the training set. Backpropagation minimizes the number of epochs required to generate a model with maximal classification accuracy for a given neural network architecture.

The inputs of traditional neural networks have been hundreds of features generated by image analysis software such as CellProfiler (Broad Institute, Cambridge, MA, USA). More recently, convolution neural networks have integrated

image analysis as a first.[244] This means that convolution neural networks can generate bespoke imaging features are generated to accommodate higher evaluation accuracies.

5.1.5 HYPOTHESIS AND AIMS

Hypothesis: Dual ligand and substrate-based HNE imaging can be used to functionally classify neutrophils with clinically meaningful sensitivity and specificity.

Aims:

1. **Develop a data-rich HNE-phenotyping assay**

i. Determine the effect of fixation on the NAP signal of purified HNE

ii. Determine the effect of fixation on the membranous NAP signal of primary human neutrophils

iii. Develop an immunofluorescence assay for functional HNE imaging using physiologically relevant stimuli

2. **Describe the level of resolution attainable between HNE-phenotypes**

i. Identify neutrophil activation via image cytometry using imaging textures and fluorescence intensities in univariate and bivariate analyses

ii. Functionally classify neutrophil treatment groups via image cytometry using imaging textures and fluorescence intensities:

   a. in univariate and bivariate analyses.

   b. in multivariate analyses of activation gated neutrophils combining principle components analysis and linear discriminants analysis.

   c. in multivariate analyses of all data via neural network classification

iii. Characterise the influence of time on phenotypic resolution

a. in univariate analyses of activation gated neutrophils

b. in multivariate analyses: Neural network classification of whole neutrophil populations by stimulus

Hypothesis: Neutrophil activation detection, via HNE-imaging, can be used to detect and quantify pulmonary adenocarcinoma.

1. **Detect neutrophil activation in human adenocarcinomatous pulmonary tissues using immunohistological patient slides.**
2. **Determine if any correlation exists between local activated neutrophil and Glut1 overexpressing cell counts using immunohistological patient slides.**

Hypothesis: Multiplexed probe HNE-phenotyping can be used to identify separate autologous neutrophil populations in the human lung.

1. **Detect neutrophil activation using FCE to image dual NAP and VE200 stained neutrophils**

i. In a 96-well plate formant

ii. In an *ex vivo* ventilated lung model

iii. Of separate populations in an *ex vivo* ventilated lung model

5.2.0 RESULTS

5.2.1 THE EFFECT OF FORMALDEHYDE FIXATION ON PURIFIED HUMAN HNE

To investigate the feasibility of detecting HNE using NAP on fixed neutrophils, formaldehyde was added to purified HNE at 6 dilutions. At 2, 4, 8 and 16% formaldehyde, the degree of HNE inhibition was significant compared to an untreated control (0% formaldehyde). HNE inhibition with formaldehyde demonstrates a relationship of one-phase exponential decay, with an asymptote tending towards 48% HNE activity. This indicates that formaldehyde fixation can achieve a maximum inhibitory effect of 52% HNE inhibition, within 10 minutes. 4% formaldehyde rendered 63% HNE activity compared to an untreated control and is a commonly used dilution. This level of inhibition was similar to 100 nM Sivelestat (61% activity) and incomplete inhibition at this dose informs the use of high Sivelestat concentrations in other studies (see **Fig 4.11 and. 5.12**). The 4% dilution informed the selection of a 4% PFA fixation condition for further fixed neutrophil studies (see **Fig. 5.3-5**).

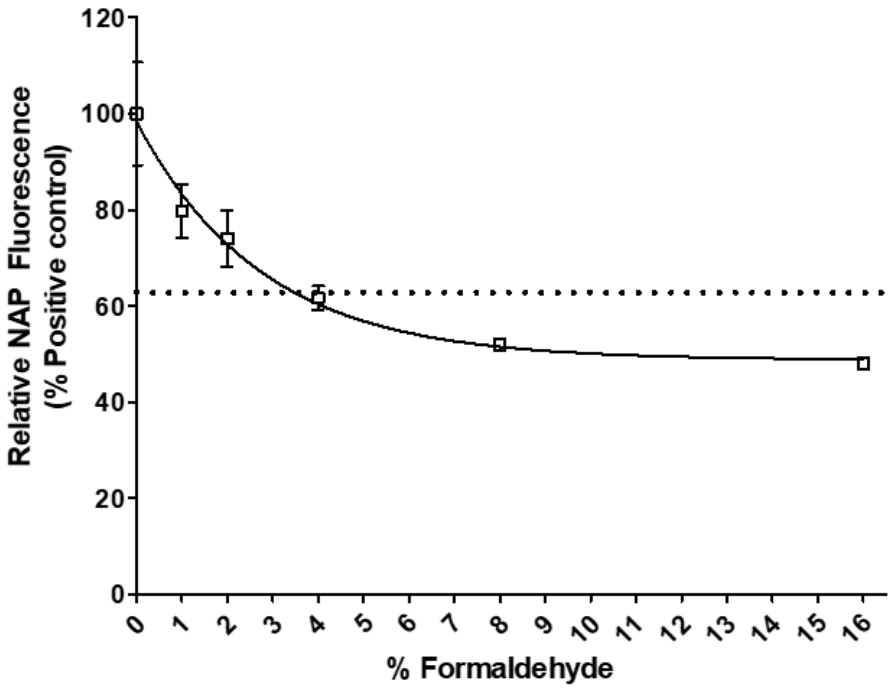

Figure 5.2 Formaldehyde can be titrated to preserve HNE activity
1 µM AAPV-AMC was co-incubated with 10 nM HNE and 100 nM Sivelestat (dotted line) or the following paraformaldehyde titrations 16, 8, 4, 2, 1 and 0% for 10 mins. AAPV-AMC fluorescence was detected using fluorescence spectroscopy. Graph values represent mean ± SEM, n=3.

5.2.2 THE EFFECT OF FORMALDEHYDE FIXATION ON NEUTROPHILIC HNE ACTIVITY AND IMMUNOFLUORESCENCE

When neutrophils are treated with bacterial products, CD11b upregulation is detectable using flow cytometry. Although the differences in NAP signal between untreated and activated neutrophil populations are statistically insignificant in this assay, a 2.8-fold increase in NAP fluorescence with neutrophil activation without fixation (**Fig. 5.3.C**) and a 1.9-fold increase with fixation (**Fig. 5.3.D**), both show NAP signal increasing with neutrophil activation. Previously discussed data demonstrates the ability to detect neutrophil activation, via confocal microscopy, when cells are stimulated with bacterial products (see **Fig.3.9**) and via flow cytometry, when cells are stimulated with calcium ionophore (see **Fig. 3.8**). Furthermore, the concomitant increase of NAP with CD11b-Alexa Fluor 647 fluorescence corroborates previous data that NAP signal detects neutrophil activation (**Fig. 5.3.A and B**). Fixation appears to increase NAP fluorescence (4.7-fold, **Fig. 5.3.E**) before neutrophil activation, while reducing anti-CD11b antibody binding (2.4-fold, **Fig. 5.3.F**).

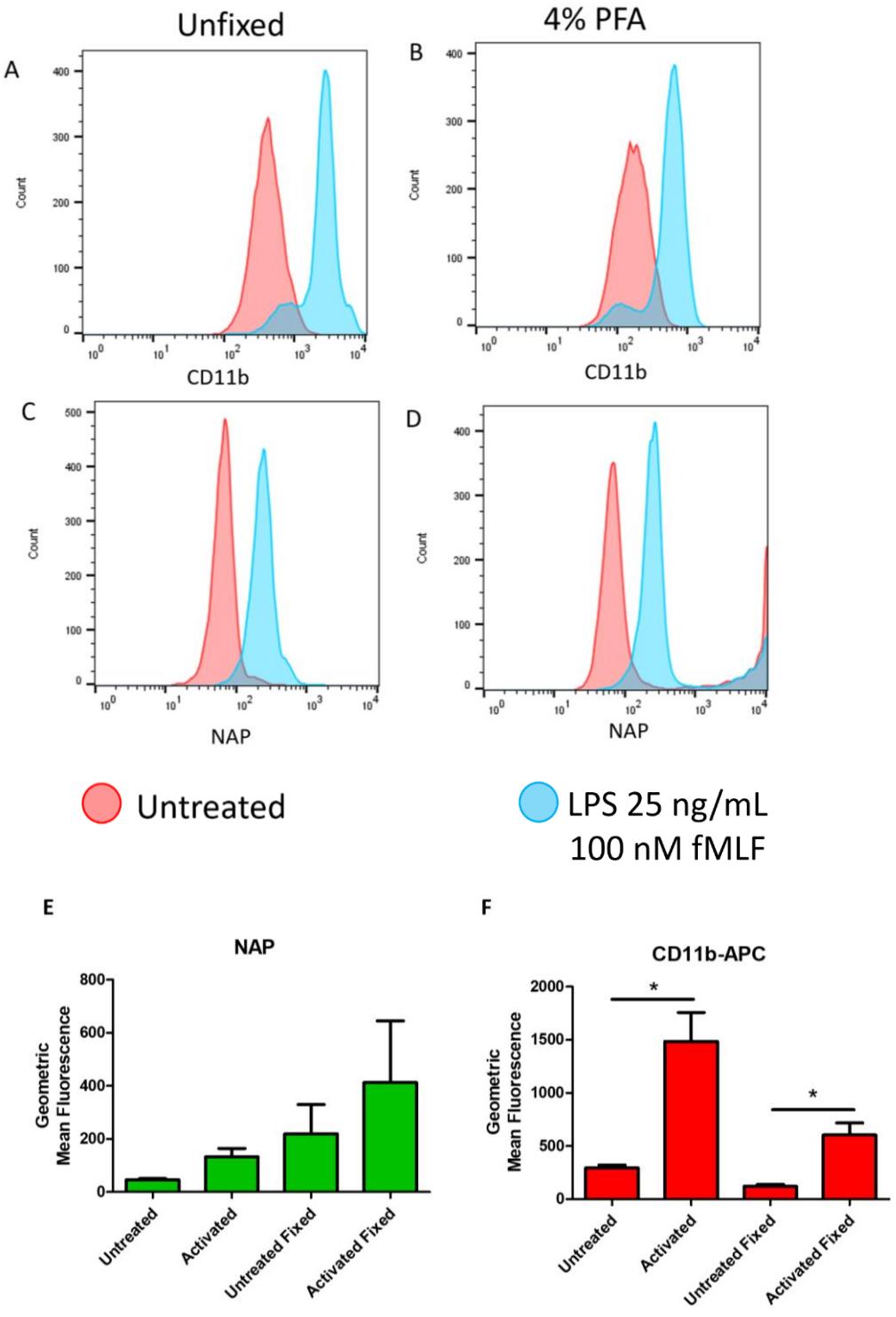

Figure 5.3 NAP can detect neutrophil activation after fixation
Flow cytometric analysis of untreated and activated (25 ng/mL LPS and 100 nM FMLF treated) neutrophil populations, with and without 4% paraformaldehyde fixation. Graph values represent mean of median fluorescence intensities ± SEM and *P* values were calculated using one-way ANOVA and a Bonferroni post-test. * *P* <0.05, n=3.

5.2.3 IMMUNOFLUORESCENT STAINING OF MEMBRANOUS HNE

In addition to its antimicrobial role within the phagolysosome, active HNE is degranulated into the extracellular space and onto plasma membranes. To assess the extent to which HNE becomes localized to neutrophil plasma membranes, following calcium ionophore stimulation, anti-HNE antibody was added to stimulated, fixed neutrophils. Despite showing large variations in shape, activated neutrophils are often wider at their basal surfaces (**Fig. 5.4.A**) than their apices (**Fig. 5.4.D**). CellMask^{TM} orange fluorescence intensity is dimmer at basal surfaces and brighter at apical surfaces. By scanning through confocal image slices and measuring CellMask^{TM} orange fluorescence intensity, a profile is generated which represents the distribution of plasma membrane in the z dimension. Changes in anti-HNE antibody fluorescence co-register with changes in CellMask^{TM} orange fluorescence, indicative of a spatial relationship between active HNE and plasma membrane from the basal to apical cell surfaces. The high degree of similarity between z profiles for both anti-HNE antibody and CellMask^{TM} orange demonstrates their colocalisation across groups of cells which suggests HNE is membranous in these samples.

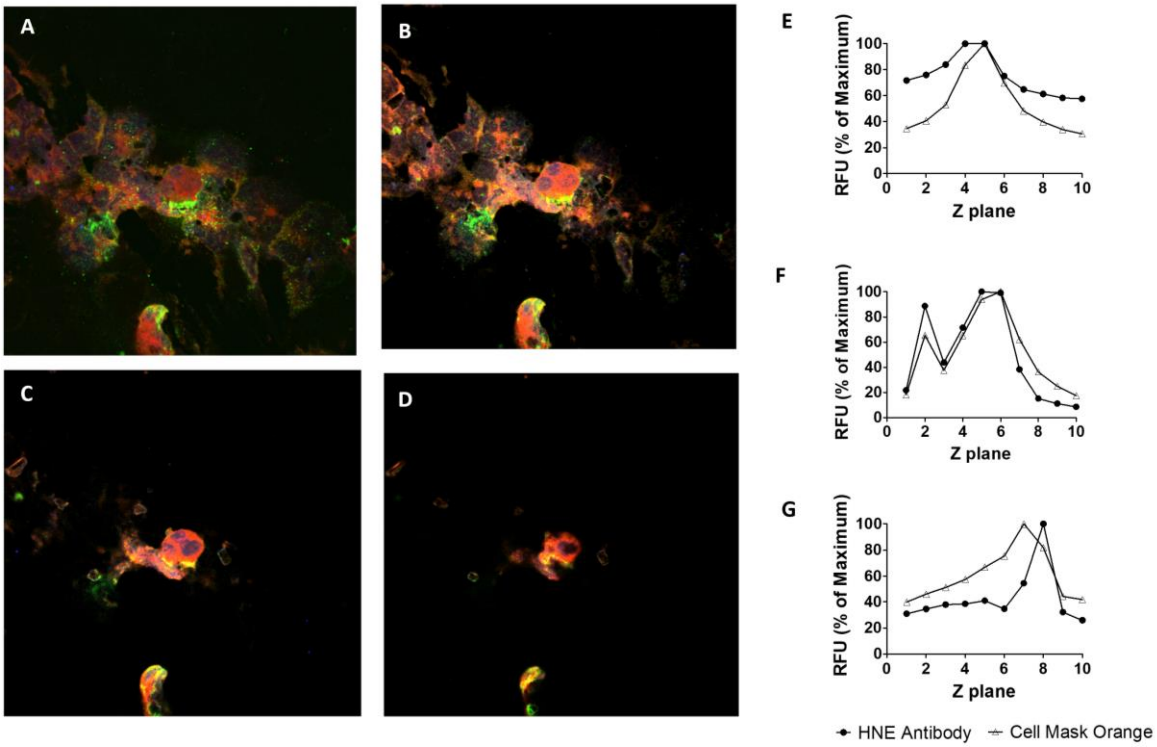

Figure. 5.4 Spatial Relationship between HNE and Plasma Membrane
A-D) Confocal microscopy of neutrophils, scanning through Z planes, incubated in 1 µM calcium ionophore, 2.5 µg/mL CellMask™ orange, fixed, incubated with 1 µM DAPI and immunolabelled with 1:200 anti-HNE antibody (abcam 68672). **E-G**) Graphs show image analysis measurements of CellMask™ orange and anti-HNE antibody fluorescence intensity scanning through Z planes. n=3

5.2.4 COMPARING HNE RELEASE AND ACTIVITY BY CHEMOKINETIC STIMULUS

To investigate whether neutrophils could be categorized into untreated, primed, activated, primed-activated categories by imaging HNE presence and activity, neutrophils were incubated under six conditions, fixed and compared via confocal imaging. For forty-five minutes neutrophils were incubated untreated (UT), or treated with 25 ng/mL Lipopolysaccharide (LPS), 100 nM platelet activating factor (PAF), 3 nM interleukin 8 (IL8), 1 nM or leukotriene B4 (LTB4). In a sixth condition neutrophils were incubated for thirty minutes with 25 ng/mL LPS before a fifteen-minute 100 nM N-formyl-Met-Leu-Phe incubation (FMLF). Although four percent PFA fixation introduced artefactual NAP signal in all conditions, untreated neutrophils (**Fig. 5.5 U-X**) are visibly dimmest in NAP signal. Neutrophils of the FMLF condition which were primed and subsequently activated are the brightest, by NAP staining. Individual neutrophils from each image were analysed and treatment populations compared by median relative fluorescence units. Image analysis revealed HNE immunofluorescence increased across treatment groups starting with UT and LPS as the dimmest, then PAF, IL8, LTB4 and FMLF as the brightest (**Fig. 5.5 Y**). NAP signals show the same trend with the exception of reduced NAP fluorescence under 3 nM IL8 stimulation (**Fig. 5.5 Z**). Logistic regression analyses show that HNE immunofluorescence and NAP fluorescence produce more accurate binary classification (between untreated and each treated neutrophil group) when combined with DAPI and CellMask^{TM} orange fluorescence and cell shape descriptors. Receiver-operator curves describe more accurate binary classification

when the classifier is trained with all imaging features than with HNE-imaging features only (**Fig. 5.5.Ai-Ji**). However, when reduced to HNE-imaging features only, true positive rate (TPR) decreases more for the LPS vs. UT distinction (-0.206 and -0.177 TPR for LPS and UT respectively **Fig. 5.5.Ai and Fi**) than for all other distinctions, (average for PAF, IL8, LTB4, FMLF = -0.110 ± 0.021 TPR **Fig. 5.5.Gi – Ji** and for their respective UTs = -0.050 ± 0.008 TPR **Fig. 5.5.Bi – Ei**). LPS fluorescence is least distinguishable from UT fluorescence by antibody and NAP staining (**Fig. 5.5.Y and Z**).

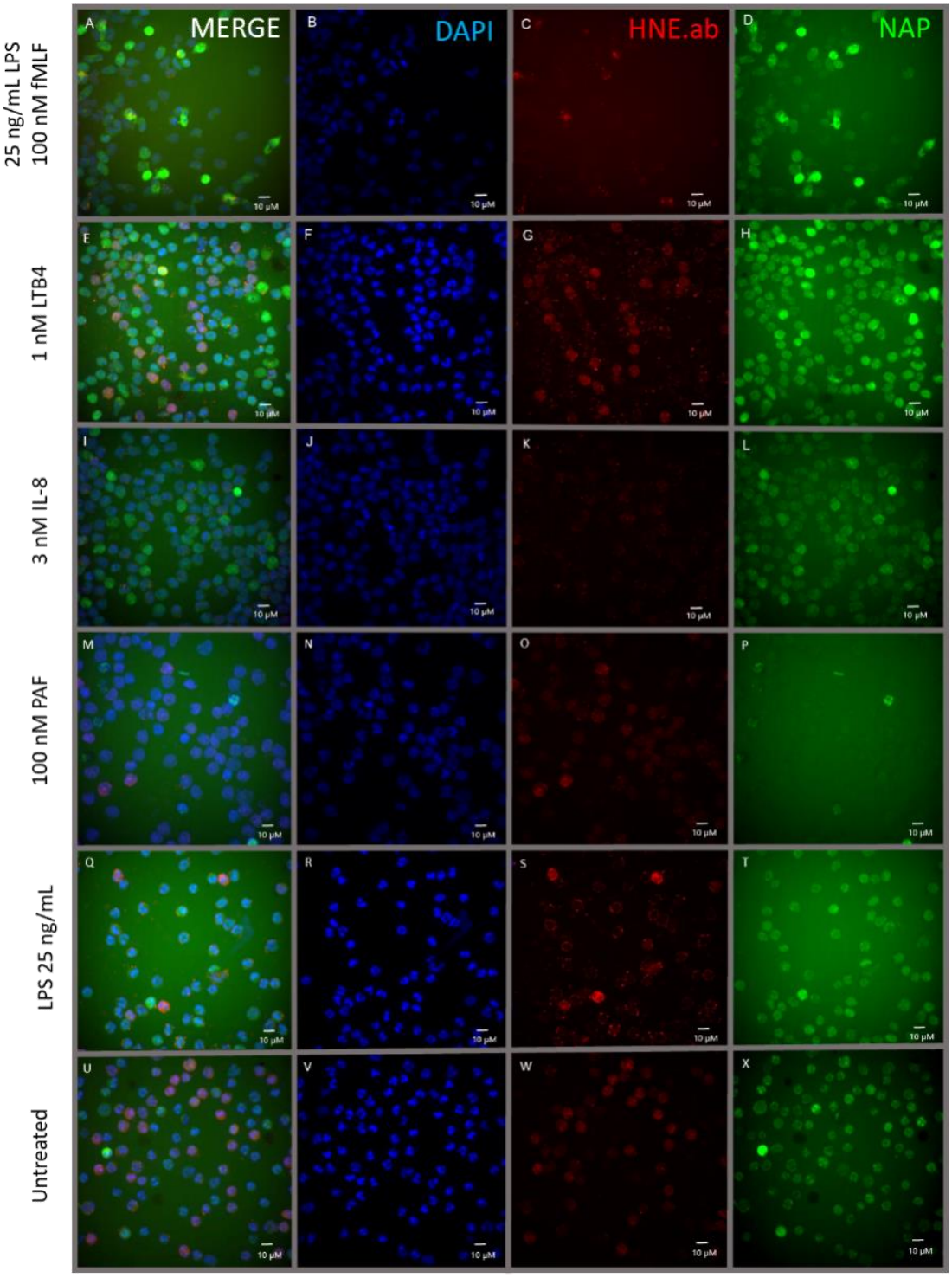

Figure. 5.5 HNE Immunofluorescence and NAP fluorescence are insufficient for binary classification

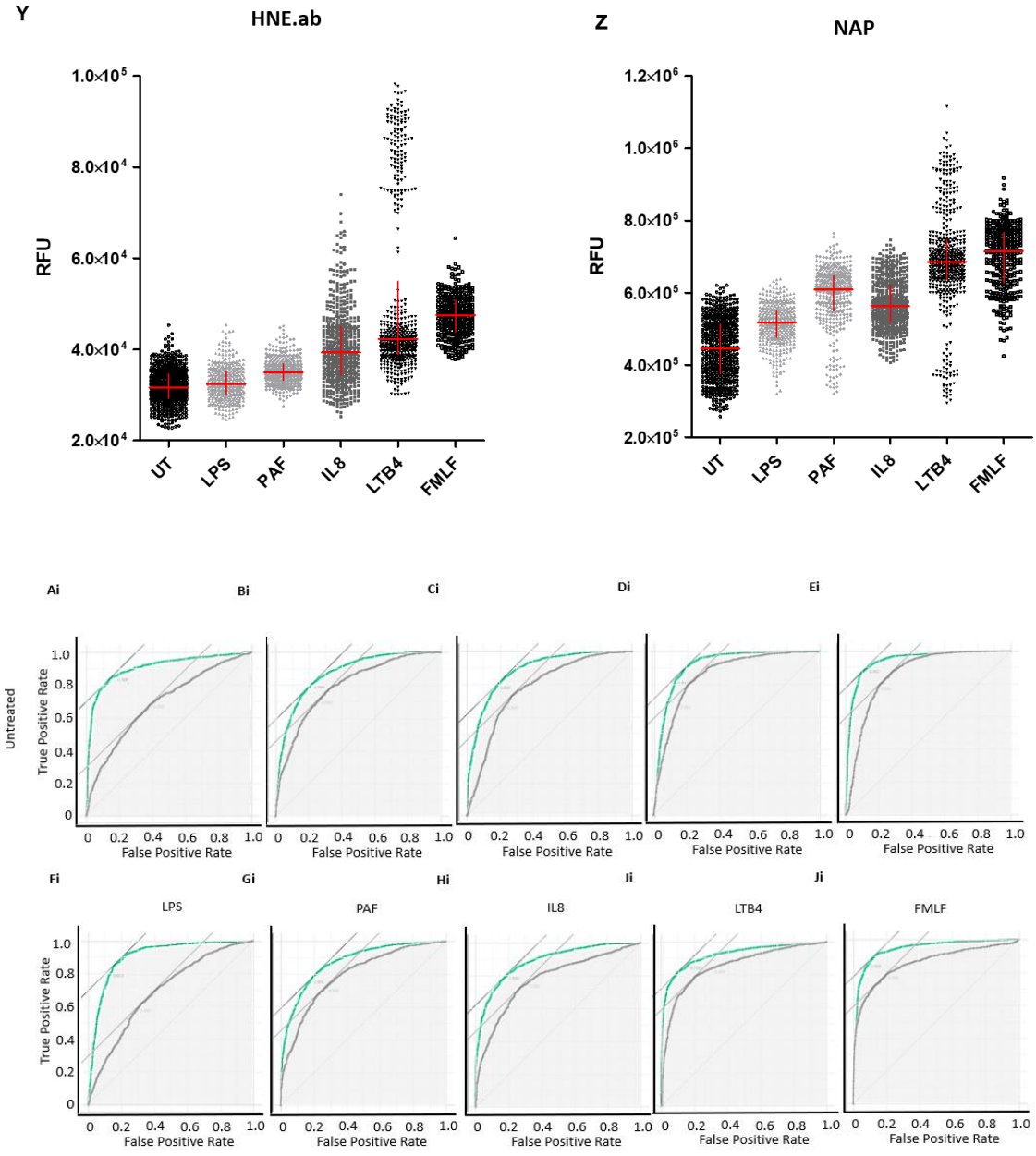

Figure. 5.5 HNE Immunofluorescence and NAP fluorescence are insufficient for binary classification Primary human neutrophils were pre-treated with **A-D)** 25 ng/mL LPS / 100 nM FMLF **E-H)** 1 nM LTB4 **I-L)** 3 nM IL-8 **M-P)** 100 nM PAF **Q-T)** 25 ng/mL LPS or **U-X)** untreated, fixed with 4% PFA and stained with a DNA stain (DAPI), a HNE activity probe (NAP) and immunolabelled with antibodies directed against HNE release. **Y-Z)** Data points represent fluorescence intensities of individual cells, red bars represent median and interquartile range. **Ai-Ji)** Receiver operator curves of logistic regression analyses, n=4

5.2.5 NEUTROPHIL ACTIVATION DETECTION BY HNE TEXTURAL FEATURES

Following chemokinetic stimulation, images of neutrophils were subjected to an image analysis pipeline for textural feature extraction. Textural features were statistically ranked to select the highest ranking or, optimal, texture feature. Optimal textural features were selected from each of the four imaging channels such that information from NAP, HNE antibody (HNE.ab), CellMask^{TM} Orange and DAPI staining could be compared. The ability of NAP to enter and fluorescently stain activated neutrophils to the exclusion of untreated neutrophils has been demonstrated previously (see **Fig. 3.8-10, 4.9** and **4.10**), this allows neutrophils with untreated levels of NAP or HNE.ab signal to be classed as “NAP dim” or “HNE.ab dim”. Fluorescently dim neutrophils do not have a clear activation phenotype based on HNE staining. Neutrophils with supra-untreated fluorescence were classed as “HNE.ab bright” or “NAP bright”, indicative of unambiguous neutrophil activation. The bright subgroups represent 2.6% and 6.3% of NAP and HNE.ab stained neutrophils respectively. HNE.ab bright neutrophils cannot be identified by NAP, DAPI or CellMask^{TM} Orange textural features, although CellMask^{TM} Orange texture distributions showed the least overlap between HNE.ab bright and dim neutrophil populations. NAP bright neutrophils cannot be identified by DAPI texture, although CellMask^{TM} Orange and HNE.ab textures produced bimodal distributions with relatively large separability for this data set: $2x10^6$ and $2.5x10^6$ units separate NAP dim and NAP bright medians for HNE.ab and CellMask^{TM} Orange distributions respectively. In the case of the HNE.ab texture distributions, the pronounced left-

skew of NAP dim neutrophils helps to distinguish this population from NAP bright cells. With inseparable dim and bright neutrophils across all textural features the probability of detecting only activated neutrophils less than 20% by all six strategies (**Fig. 5.6 B-D, F-H** red dotted lines).

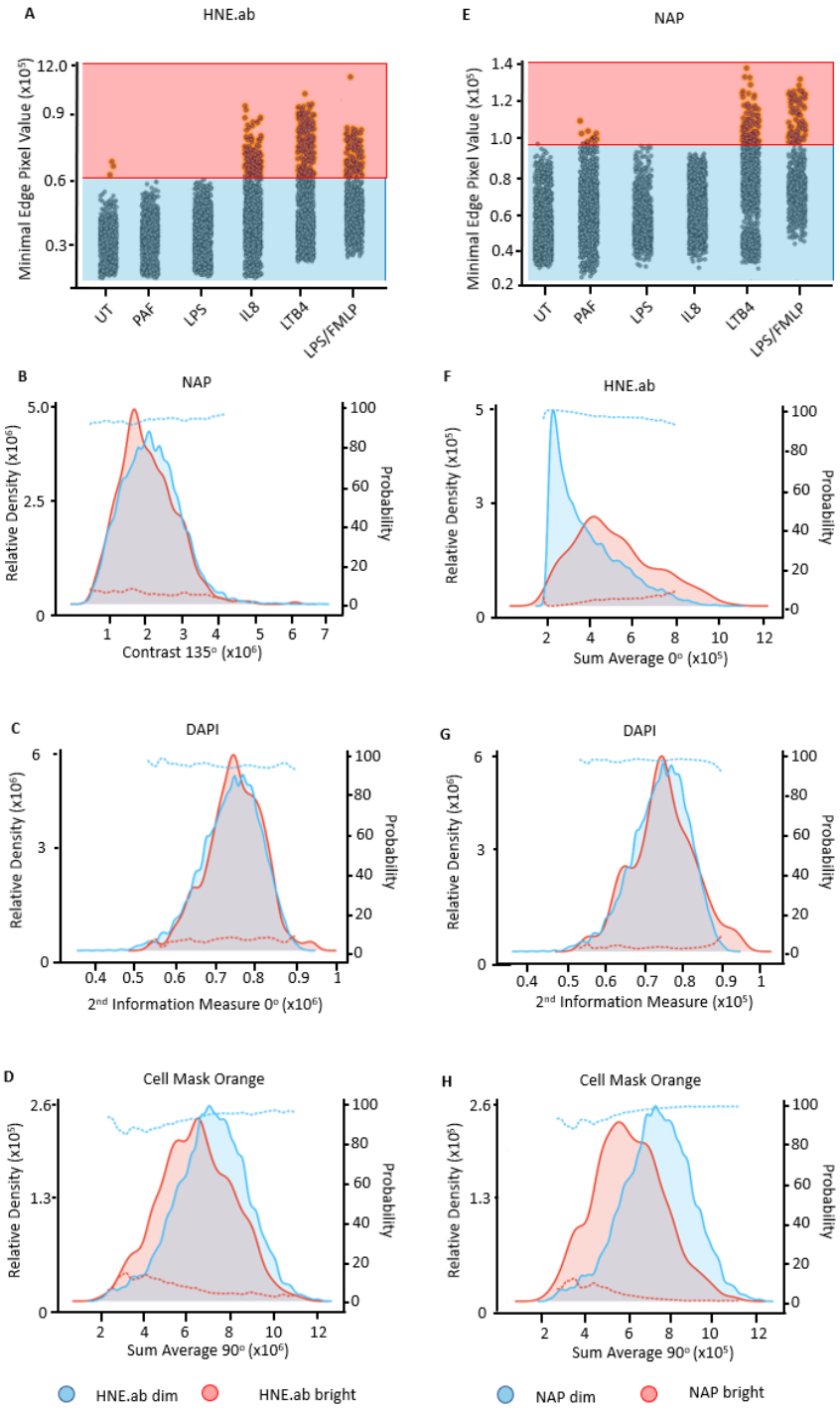

Figure. 5.6 Textural features exhibit insensitive identification of neutrophil activity
Image cytometric analysis of fixed untreated, primed and activated neutrophils. A fluorescence intensity threshold is applied to all neutrophil populations to distinguish between untreated and activated fluorescence in the **A**) HNE.ab and **E**) NAP channels individually. Neutrophils above and below the fluorescence threshold are represented as bright (red) or dim (blue) relative density histograms respectively, for untreated vs. activated neutrophil comparisons of **B**) NAP **F**) HNE.ab **C and G**) DAPI and **D and H**) CellMask™ Orange optimal textural features. The following neutrophil treatment groups are gated to contribute to bright (red) or dim (blue) histograms: untreated, 25ng/mL LPS, 1 nM LTB4, 25ng/mL LPS / 100nM FMLF, 3nM IL8 and 100 nM PAF, with dotted lines of the same colour showing classification probabilities. Histograms show all image cytometric data points, n=4.

5.2.6 NEUTROPHIL ACTIVATION DETECTION BY HNE INTENSITY FEATURES

Following chemokinetic stimulation, images of neutrophils were subjected to an image analysis pipeline for fluorescence intensity feature extraction. Optimal intensity features were objectively selected and gated for the identification of activated neutrophils as with textural features (see section **5.2.4**). The "bright" neutrophil subgroups represent 2.6% and 6.3% of NAP and HNE.ab stained neutrophils respectively (**Fig 5.7.A and E**). Using simple thresholding, HNE.ab bright neutrophils cannot be reliably identified by DAPI or CellMask^{TM} orange intensity features (**Fig. 5.7.C and D**). The probability of accurate HNE.ab bright neutrophil classification follows a trend of increase with increasing DAPI fluorescence (**Fig.5.7.C** red dotted line, maximum 50% probability at $1.7x10^5$ DAPI fluorescence). Probability and hence classification accuracy of HNE.ab bright neutrophils ranges from 70% to 100% between NAP fluorescence values of 1.1 - $1.4x10^6$ so that HNE.ab bright neutrophil can be identified by their NAP staining (**Fig. 5.7.B**). NAP bright neutrophil cannot be identified with DAPI or CellMask^{TM} Orange (**Fig.5.6.G and H**) staining and only reach 50% probability with HNE.ab staining(**Fig. 5.7.F**).

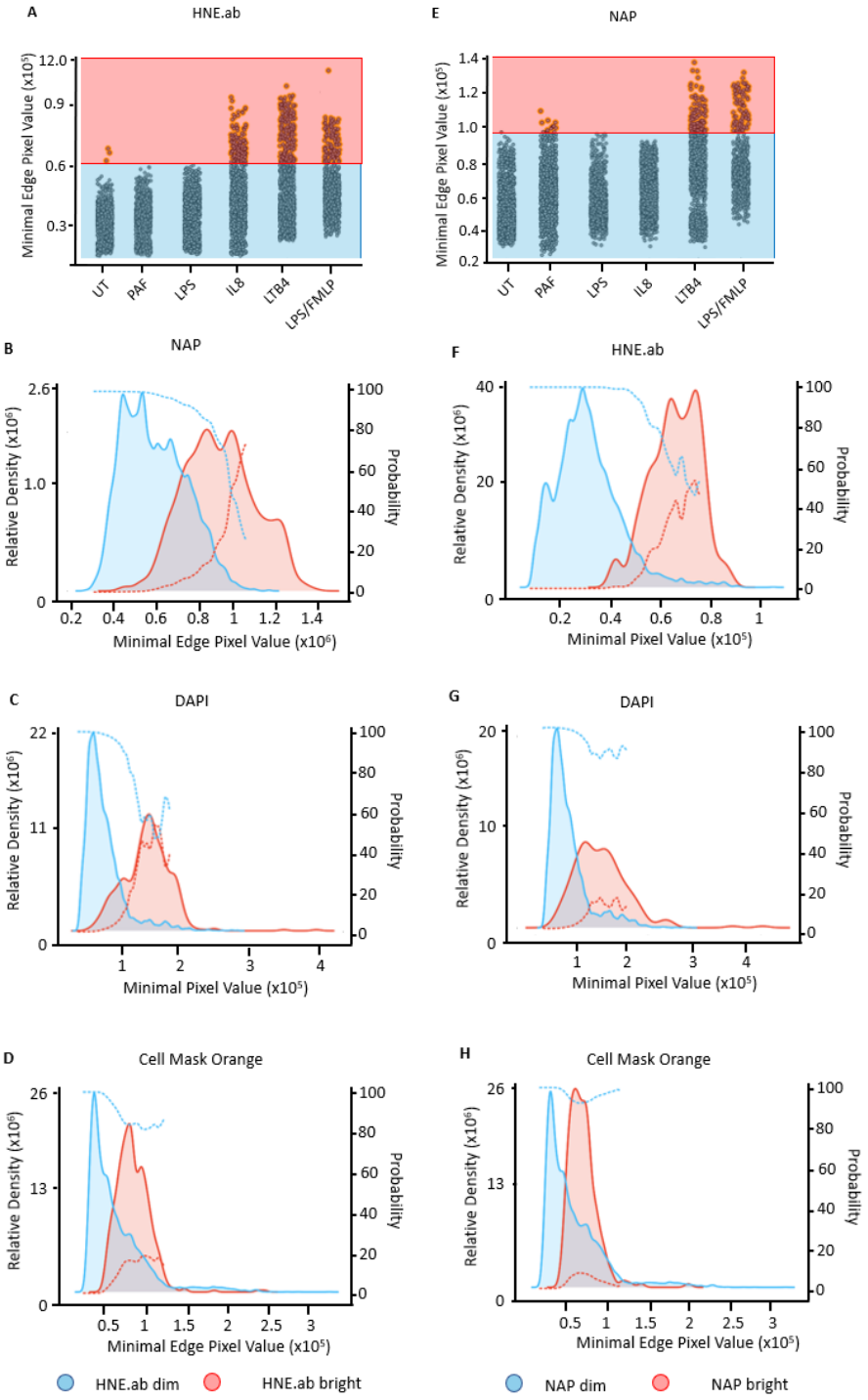

Figure. 5.7 Intensity features exhibit moderately sensitive identification of neutrophil activity
Image cytometric analysis of fixed untreated, primed and activated neutrophils. A fluorescence intensity threshold is applied to all neutrophil populations to distinguish between untreated and activated fluorescence in the **A**) HNE.ab and **E**) NAP channels individually. Neutrophils above the fluorescence threshold are represented as histograms in terms of their **B**) NAP F) HNE.ab **C and G**) DAPI and **D and H**) CellMask™ Orange optimal textural features. The following neutrophil treatment groups are gated to contribute to bright (red) or dim (blue) histograms: untreated, 25ng/mL LPS, 1 nM LTB4, 25ng/mL LPS / 100nM FMLF, 3nM IL8 and 100 nM PAF with dotted lines of the same colour showing classification probabilities. Histograms show all image cytometric data points, n=4.

5.2.7 STIMULUS-DEPENDENT NEUTROPHIL CLASSIFICATION BY HNE TEXTURAL FEATURES

To understand whether bivariate analyses would improve activated neutrophil identification, images of neutrophils were subjected to an image analysis pipeline for textural feature extraction. Activated neutrophils were gated out of the relevant treatment groups and analysed by optimal textural features, which were objectively derived as explained previously (see section **5.2.4**). The optimal textural features of NAP or HNE.ab bright neutrophils, from each imaging channel, were analysed for each treatment group. Although all textural features of all activated neutrophil distributions are multimodal, the presence of LTB4 or IL8 stimulation is somewhat distinguishable from other stimuli by their pronounced peak bifurcation via DAPI and CellMask^{TM} Orange texture analysis respectively (**Fig. 5.8.C and D**). PAF priming may be distinguishable from other activating stimuli by the relative inability of PAF to drive neutrophils into the NAP bright gate (**Fig. 5.8.F-G**). However, these distinctions are obscured by similarities between the ranges and medians of all activated neutrophil distributions. More robust classification of LTB4, HNE.ab bright neutrophils may be made at high values of DAPI texture (≥80% at values > $9x10^4$, **Fig. 5.8.C**) and CellMask^{TM} Orange texture (≥80 % at values >10^7, **Fig. 5.8.D**). LTB4 stimulated, HNE.ab bright neutrophils are also identifiable at low DAPI texture (≥80% at values <$2x10^6$, **Fig. 5.8C**). NAP bright, LTB4 neutrophils can be identified at high DAPI textures (≥90% at values >$11x10^6$, **Fig. 5.G**) as well as high or low CellMask^{TM} Orange textures (≥95% at values >$9.5x10^6$ or <$5.5x10^6$, **Fig. 5.8.H**).

NAP bright LPS/FMLF neutrophils can be classed as such with 90% accuracy at HNE.ab textures of ≥ 1.4 x10^6 (**Fig. 5.8.F**).

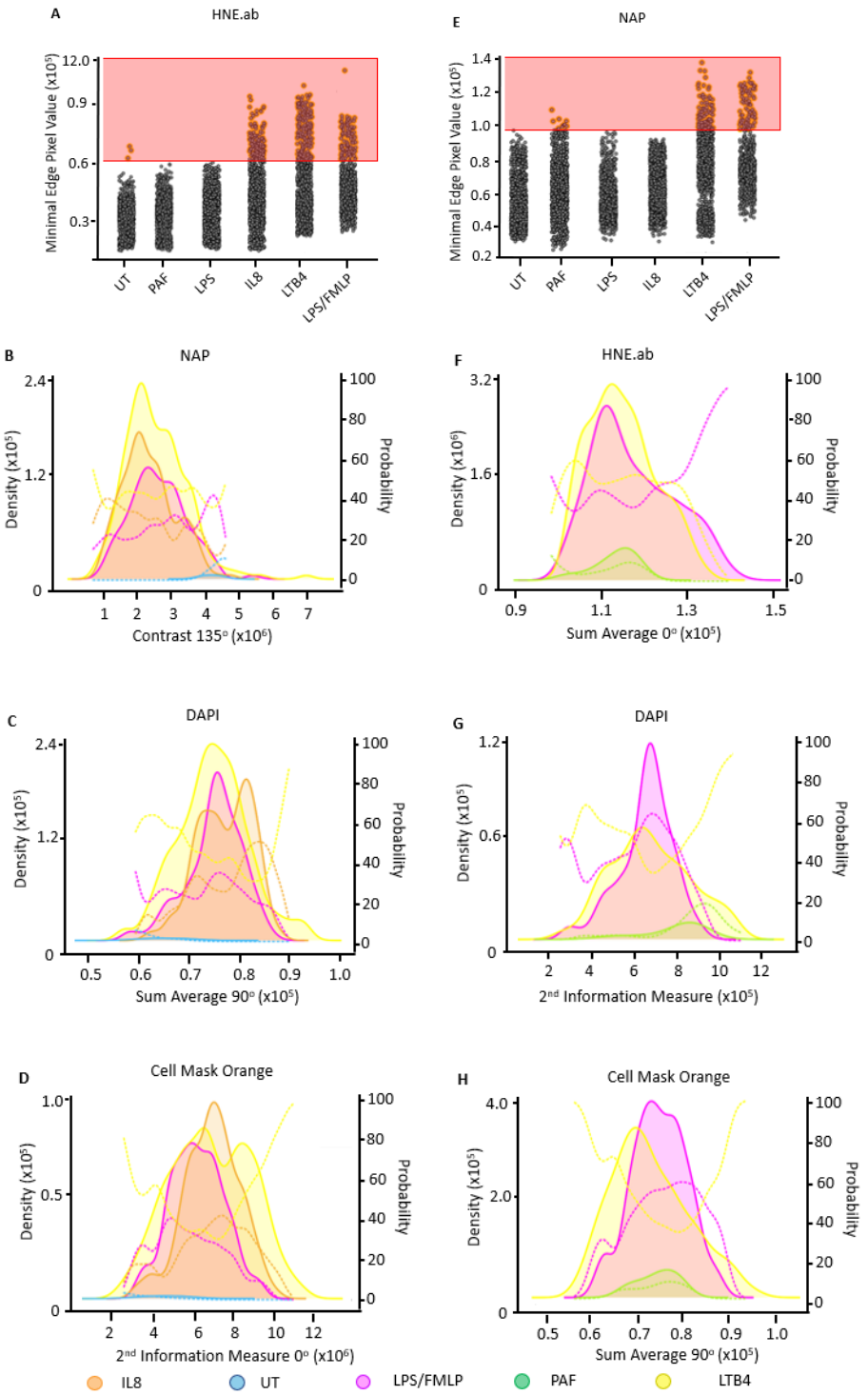

Figure. 5.8 Textural features exhibit insensitive classification of neutrophils by stimulus
Image cytometric analysis of fixed untreated, primed and activated neutrophils. A fluorescence intensity threshold is applied to all neutrophil populations to distinguish between untreated and activated fluorescence in the **A**) HNE.ab and **E**) NAP channels individually. Neutrophils above the fluorescence threshold are represented as histograms in terms of their **B**) NAP **F**) HNE.ab **C and G**) DAPI and **D and H**) CellMask™ Orange optimal textural features. The following neutrophil treatment groups are plotted as histograms: untreated (blue), 1 nM LTB4 (yellow), 25 ng/mL LPS/ 100 nM FMLF (pink), 3 nM IL8 (orange) and 100 nM PAF (green) with dotted lines of the same colour showing classification probabilities. Histograms show all image cytometric data points, n=4.

5.2.8 STIMULUS-DEPENDENT NEUTROPHIL CLASSIFICATION BY HNE INTENSITY FEATURES

To understand whether bivariate analyses would improve activated neutrophil identification, images of neutrophils were subjected to an image analysis pipeline for textural feature extraction. Activated neutrophils were gated out of the relevant treatment groups and analysed in terms of optimal fluorescence intensity features, which were objectively derived as explained previously (see section **5.2.4**). The optimal intensity features of NAP or HNE.ab bright neutrophils, from each imaging channel, were analysed for each treatment group. Although all the intensity features yield activated neutrophil distributions which are multimodal, the presence of LTB4 or IL8 stimulation is somewhat distinguishable from other stimuli by their pronounced peak bifurcation via DAPI and CellMask^{TM} Orange texture analysis respectively. PAF priming may be distinguishable from activating stimuli by the relative inability of PAF to drive neutrophils into the activated gate. Classifying distinctions are obscured by varying degrees of overlap between the ranges of all activated neutrophil distributions.

HNE.ab bright, IL8 stimulated neutrophils can be classified with 80% accuracy between 0.3 and 0.7 x10^6 NAP fluorescence units (**Fig. 5.9.B**). At 1x10^6 and between 1.2 and 1.3 x10^6 NAP fluorescence, HNE.ab bright neutrophils can be identified as LTB4 and LPS/FMLF stimulated respectively with 70% accuracy (**Fig. 5.9.B**). DAPI fluorescence units of 0.5 or ≥2.0 x10^6 can be used to classify HNE.ab bright neutrophils with 80% (LPS/FMLF) and 100% (LTB4) accuracy respectively (**Fig. 5.9.C**).

LPS/FMLF neutrophils can also be classified with high accuracy (80-100%) at low CellMask^{TM} Orange fluorescence intensity (0-0.5x10^5, **Fig. 5.9.D**). And HNE.ab bright IL8 neutrophils can be identified with 70% accuracy between 1 and 1.2x10^5 CellMask^{TM} Orange fluorescence (**Fig. 5.9.D**).

NAP bright neutrophils also demonstrate high classification accuracies particularly when HNE.ab fluorescence is measured. NAP bright neutrophils in all 3 activated populations were identifiable with 70% accuracy or more, with PAF and LTB4 neutrophils reaching 100% accuracy at low and high fluorescence ranges respectively. Other classification strategies (**Fig. 5.9.B-D, G,H** showed low accuracy for identifying PAF or untreated neutrophils, regardless of which HNE stain was the thresholding variable.

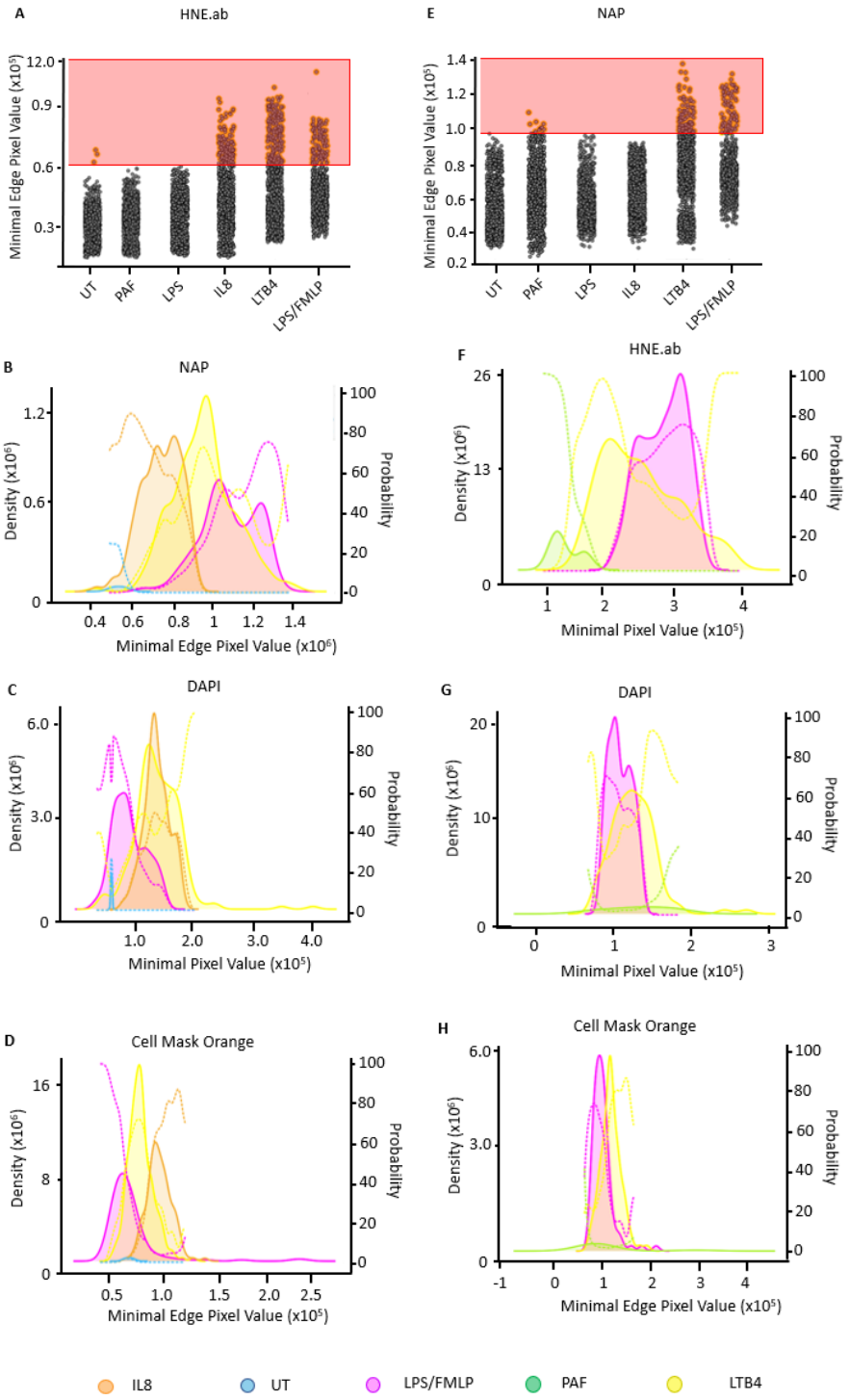

Figure. 5.9 Intensity features exhibit sensitive classification of neutrophils by stimulus
Image cytometric analysis of fixed untreated, primed and activated neutrophils. A fluorescence intensity threshold is applied to all neutrophil populations to distinguish between untreated and activated fluorescence in the **A**) HNE.ab and **E**) NAP channels individually. Neutrophils above the fluorescence threshold are represented as histograms in terms of their **B**) NAP **F**) HNE.ab **C and G**) DAPI and **D and H**) CellMask™ Orange optimal intensity features. The following neutrophil treatment groups are plotted as histograms: untreated (blue), 1 nM LTB4 (yellow), 25ng/mL LPS / 100nM FMLF (pink), 3nM IL8 (orange) and 100 nM PAF (green) with dotted lines of the same colour showing classification probabilities. Histograms show all image cytometric data points, n=4.

5.2.9 STIMULUS-DEPENDENT NEUTROPHIL CLASSIFICATION BY MULTIDIMENSIONAL HNE IMAGING FEATURES

Using linear combinations of the eight optimal features, eight principal components were produced which could be used to effectively cluster HNE.ab bright or NAP bright activated neutrophils, by chemokinetic treatment. Performing linear discriminant analysis on the eight principal components showed that distinct features spaces describe the activated neutrophils of each chemokinetic treatment. In eight-dimensional hyperplanes a gating strategy could be applied to HNE.ab bright neutrophils to identify LTB4, LTB4+SIV or LPS/FMLF neutrophils as distinct activated neutrophil populations. NAP bright neutrophils could be similarly classified to make distinctions between PAF, LTB4 and LTB4+SIV neutrophils.

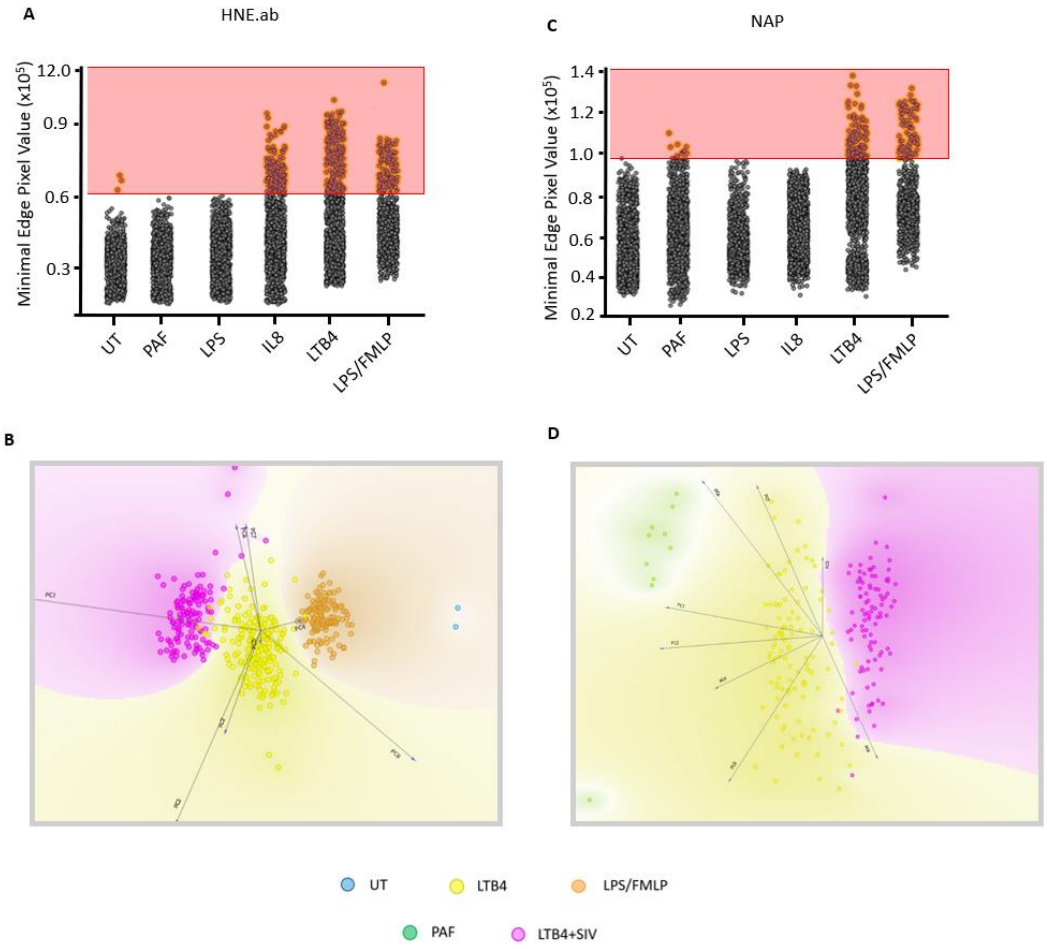

Figure. 5.10 Optimal textural and intensity features are sufficient for NAP and HNE.ab bright activated neutrophil subclassification

Image cytometric analysis of fixed untreated, primed and activated neutrophils. A fluorescence intensity threshold is applied to all neutrophil populations to distinguish between untreated and activated fluorescence in the **A)** HNE.ab and **C)** NAP channels individually. Linear discriminant analysis of principal components generates multidimensional score plots which show the clustering of neutrophils above the **B)** HNE.ab and **D)** NAP fluorescence thresholds respectively. The following neutrophil treatment groups are plotted: untreated (blue), 1 nM LTB4 (yellow), 25ng/mL LPS / 100nM FMLF (pink), 3nM IL8 (orange) and 100 nM PAF (green). All data points for each treatment group are shown, n=4.

5.3.0 STIMULUS-DEPENDENT CLASSIFICATION OF ENTIRE NEUTROPHIL POPULATIONS BY NEURAL NETWORK MODELLING

To evaluate the performance of machine learning algorithms when classifying not only supra-threshold neutrophils but entire neutrophil populations a neural network was modelled on image cytometric data sets generated by CellProfiler version 2.2. When classifying the six treatment groups the neural network achieved evaluation accuracies between 76.15% (PAF) and 81.49% (IL8) (**Fig. 5.11.A**) and an average evaluation accuracy of 79.01% across all classes (**Fig. 5.11.B**). Importantly accurate predictions, true positive rates, exceed false positive rates for all classes by at least 7.6-fold (false positive predictions which range from 0.84% - PAF misclassified as LPS/FMLF, to 10% - LPS misclassified as PAF, **Fig. 5.11.A**). Organised in order of stimulus intensity, the confusion matrix (**Fig. 5.11.A**) shows similar treatment groups are more readily confused. False positive rates are generally low, with an overall specificity of 94.98% (**Fig. 5.11.B**) and they are lowest at the corners of the confusion matrix where classes are most functionally distinct (untreated vs. LPS/FMLF activated). The greatest proportion of false positive untreated neutrophils (8.37%) are identified as primed (PAF) and the two strongest activating conditions, LTB4 and LPS/FMLF are associated with the least false positives (**Fig. 5.11.A**). Similarly, more PAF neutrophils are misclassified as LPS than any other class, both PAF and LPS are priming treatments. LTB4 and LPS/FMLF are more readily misclassified as each other than any other class. The strongest activating treatment, LPS/FMLF is most different from the untreated and priming classes (0.84-1.3% false positive rates **Fig. 5.11.A**).

A

		Actual (%)					
		UT	LPS	PAF	IL8	LTB4	LPS/FMLP
Predicted (%)	UT	79.67	3.6	8.37	4.27	1.92	2.09
	LPS	4.26	76.8	4.6	4.98	3.46	5.24
	PAF	4.92	10	76.15	5.34	3.85	3.14
	IL8	4.59	4.4	4.6	81.49	3.85	3.14
	LTB4	5.25	3.6	5.44	0.71	80.38	6.81
	LPS/FMLP	1.31	1.6	0.84	3.2	6.54	79.58

Scale (%)					
0	1	5	10	50	100

B

Sensitivity	0.7901
Specificity	0.9498

Figure. 5.11 Neural network classification of six distinct classes neutrophils following fixation
A) Confusion matrix, arranged by stimulus intensity, showing neural network classification performance. Image cytometric analysis of fixed untreated, 25ng/mL LPS, 100 nM PAF, 3nM IL8, 1 nM LTB4 and 25ng/mL LPS / 100nM FMLF treated neutrophils produced data for neural network classification. Evaluation accuracies are heat-mapped using a dark red (low) to dark green (high) colour scale, shown. Percentages for accurate classification are highlighted in black-bordered cells.
B) Sensitivity and specificity are calculated, n=4.

5.3.1 COMPARING HNE RELEASE AND ACTIVITY BY CHEMOKINETIC STIMULUS OVER TIME

To understand if classifying neutrophils by their HNE-phenotypes might be applied to COPD blood profiling in a live-cell formant, neutrophils were stained with VE200 and NAP and imaged at zero, forty-five and ninety minute time points. When neutrophils are co-stained with 100 nM VE200 and 3µM NAP, extracellular membranous and intracellular NAP fluorescence fluctuate in response to different stimuli (**Fig. 5.12.G and Gii, S and Sii**) whilst VE200 generates membranous and intracellular signals only (**Fig. 5.12.H and Hii, P and Pii**). Sivelestat in the LTB4+SIV condition blocks NAP signal across a ninety-minute timespan (**Fig. 5.12.C, Ci and Cii**) whereas VE200 signal decreases **Fig. 5.12.D, Di and Dii**), Sivelestat. Neutrophil morphology appears less rounded at forty-five and ninety minutes in FMLF, LTB4 and LTB4+SIV conditions (**Fig. 5.12.Cii and Ciii, Gii and Giii, Kii and Kiii**), than at zero minutes (**Fig. 5.12.C,G and K**).

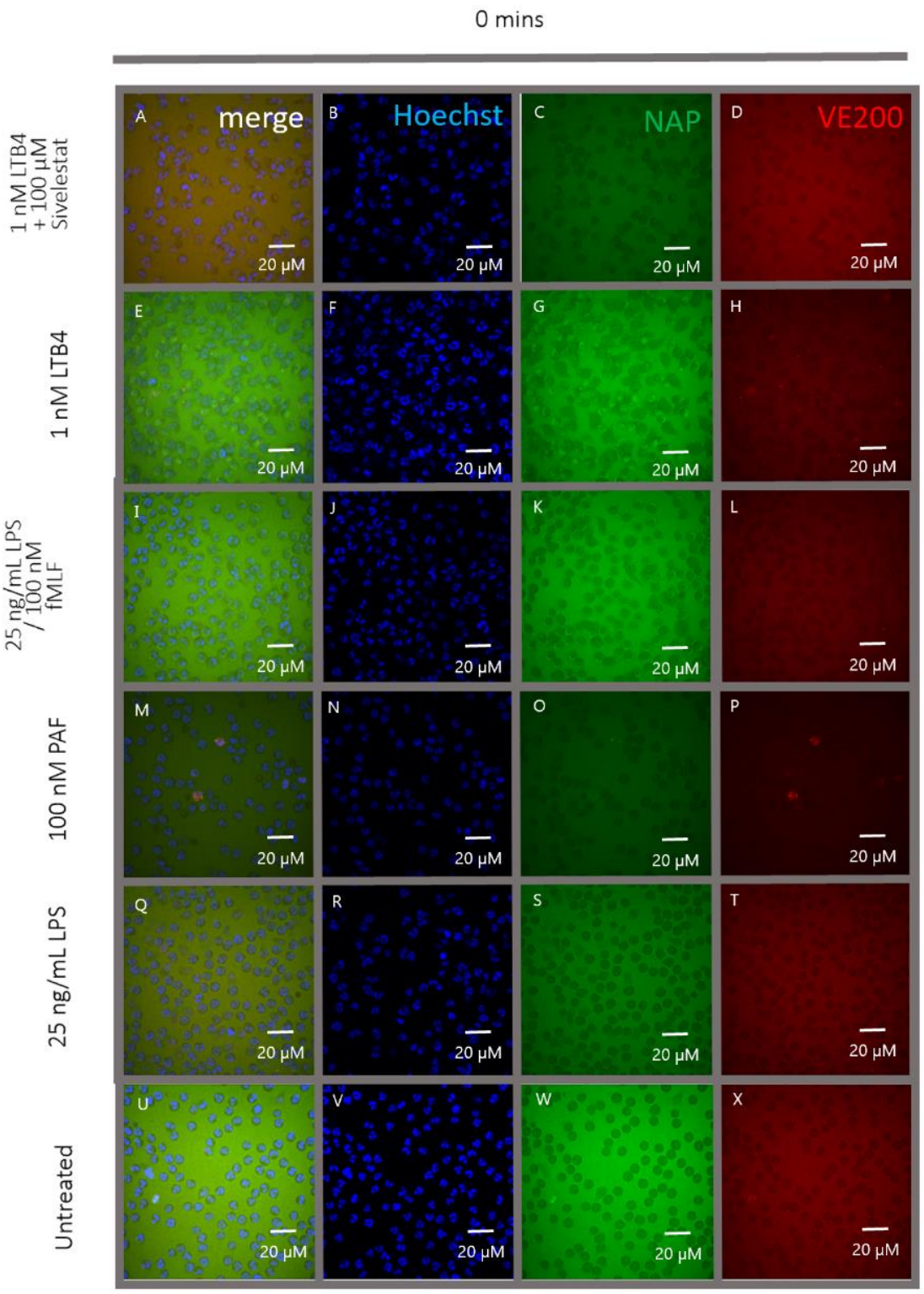

Figure. 5.12 Chemokinetic stimuli elicit varying HNE patterns in COPD patient neutrophils

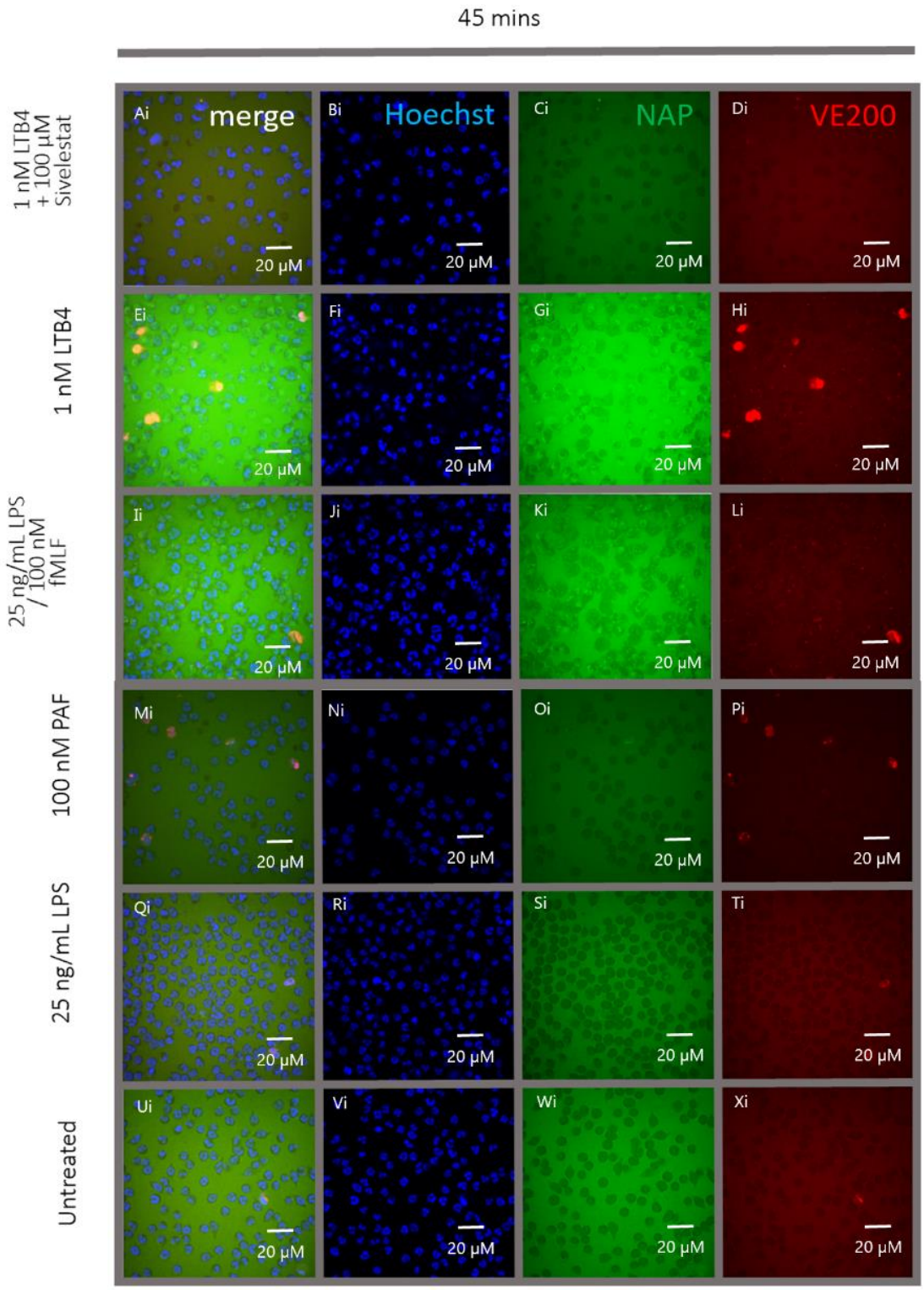

Figure. 5.12 Chemokinetic stimuli elicit varying HNE patterns in COPD patient neutrophils

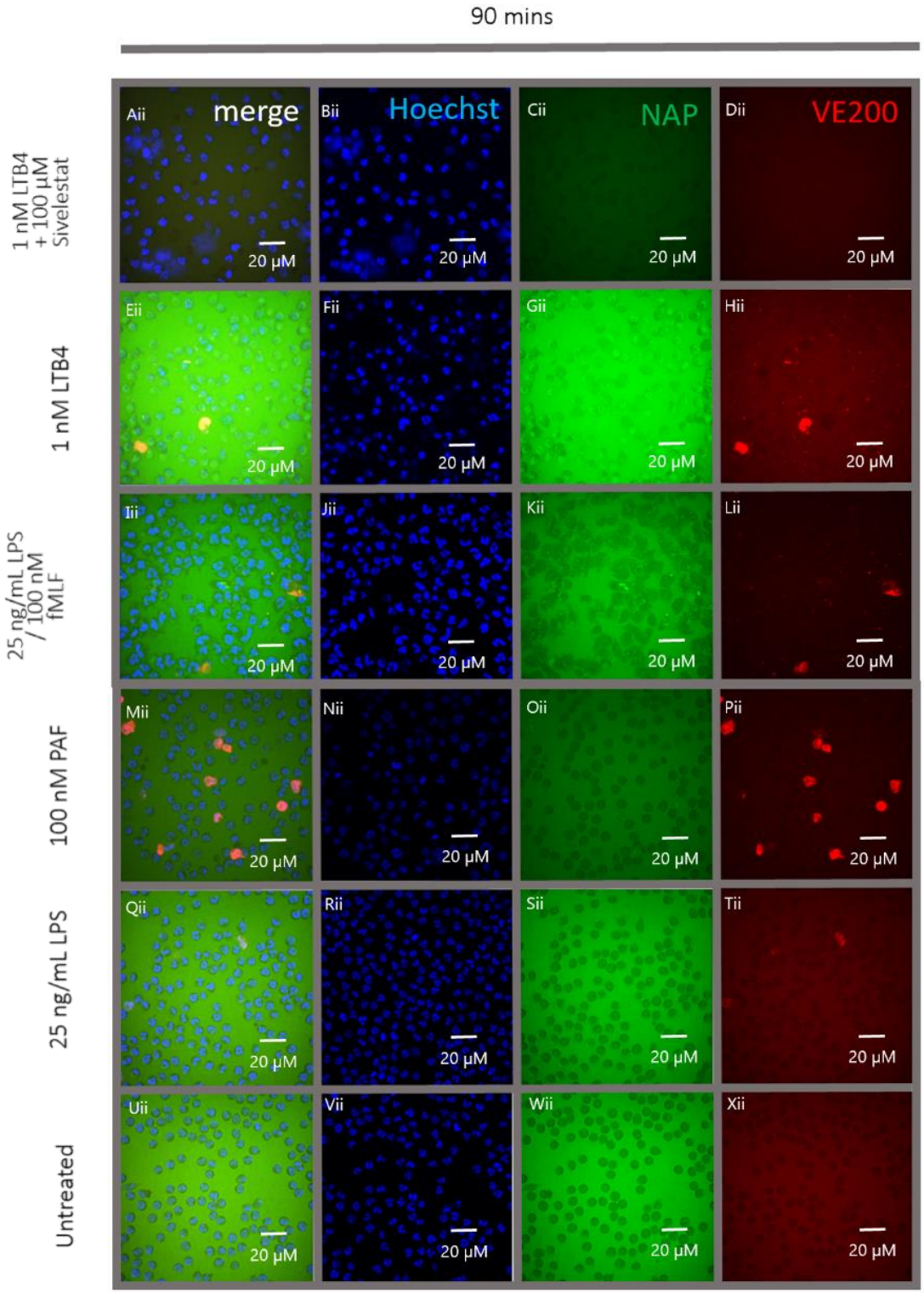

Figure. 5.12 Chemokinetic stimuli elicit varying HNE patterns in COPD patient neutrophils. The DNA of primary human neutrophils was labelled (Hoechst) before treatment with **A-D)** 25 ng/mL LPS / 100 nM FMLF **E-H)** 1 nM LTB4 **I-L)** 1 nM LTB4 / 100 µM Sivelestat **M-P)** 100 nM PAF **Q-T)** 25 ng/mL LPS or **U-X)** untreated. During treatment incubations neutrophils were concomitantly labelled with 100 nM HNE targeted probe (VE200) and 3 µM HNE activity probe (NAP). Imaging occurred at **A-X)** 0, **Ai-Xi)** 45 and **Aii-Xii)** 90 minutes, n=3.

5.3.2 QUANTIFYING NAP AND VE200 FLUORESCENCE OVER TIME

Comparing VE200 and NAP signal across all timepoints shows the effect of time on activated neutrophil staining. Increasing incubation time has little effect on VE200 fluorescence intensity. From zero to ninety minutes, median fluorescence increases 12.5 % from a lower quartile pixel value of 1.6 $x10^8$ to 1.8 $x10^8$ (**Fig. 5.13A**), similarly the interquartile range increases by only 4% of the range at baseline (1.5 $x10^7$ pixel values). Changes in NAP fluorescence over time more clearly follow trends of increasing median brightness and widening range. Pooling all treatment groups for comparisons across time, the median NAP fluorescence increases by 166%, and interquartile range increases by 23% over ninety minutes (**Fig 5.12B**).

The proportion of neutrophils, which exceed the maximal fluorescence of the untreated group at zero minutes, was analysed to understand the individual contributions of different chemokinetic treatment to the overall trends in **A)** and **B)**. This analysis corroborated previous findings with fixed neutrophils in which HNE-derived fluorescence increased from untreated to primed to activated conditions (see **Fig. 5.4**). The treatment group analysis also revealed that the LTB4+SIV condition has the highest proportion of activated neutrophils at zero and forty-five minute, by VE200 staining, with a mean activated percentage of 62.7% at zero minutes (**Fig. 5.13C**). However, at forty-five minutes VE200 staining had only increased by 0.7% and a 34.2% decrease was evident after ninety minutes. Other conditions that demonstrated greater increases in activated cell proportion at forty-five minutes. The untreated, LPS and LTB4 conditions showed increases of 9.4, 8.5,

and 34.2% respectively and these conditions went on to become more completely activated by ninety minutes, increasing by 13.8, 6.5 and 4.9% respectively. PAF activation seemed to decrease within the first forty-five minutes of incubation before increasing by 43.7% between the forty-five and ninety minutes timepoints, the largest change in activated neutrophil proportion detected by VE200 staining (**Fig. 5.13C)**. LPS/FMLF neutrophils seemed to decrease at both intervals, by 9.9% and then 16.1%.

Measuring the proportion of NAP bright neutrophils produced more homogenous results with all populations bar the LTB4+SIV condition showing their greatest increases from zero to forty-five minutes, and significant increases in percentage activated neutrophils (compared to zero minutes) for untreated and PAF conditions (see **Fig. 5.13D)**. The proportion of activated neutrophils increased by similar amounts across conditions, so that the order of least to most completely activated population was maintained. LPS and LTB4+SIV treatment were the exceptions to this trend, in order of decreasing HNE activity. The addition of Sivelestat renders the change in LTB4 NAP signal over time insignificant.

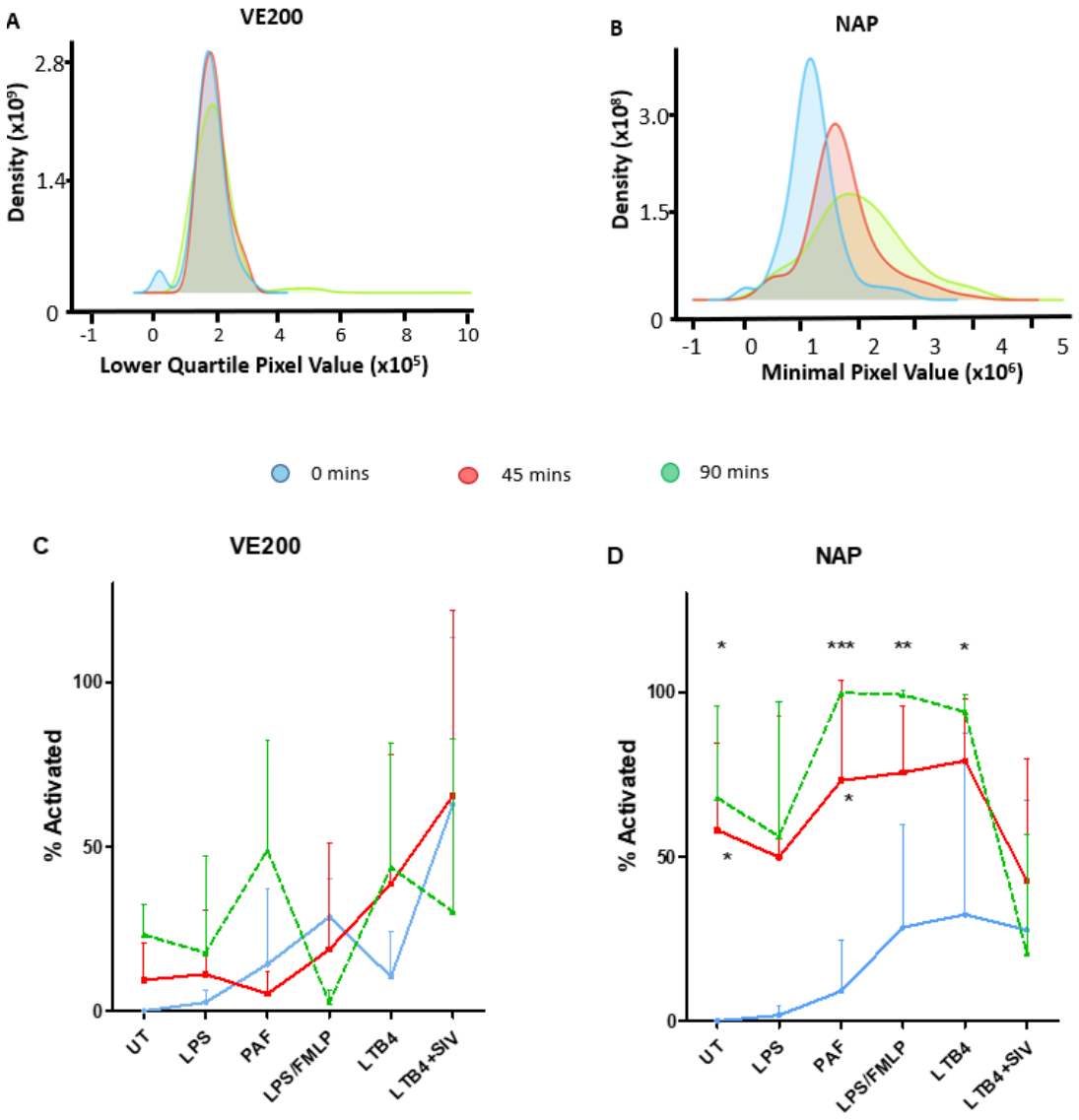

Figure. 5.13 VE200 and NAP label neutrophils with different temporal patterns
Image cytometry histograms of all neutrophils pooled at 0 (blue) 45 (red) and 90 mins (green) and plotted by optimal intensity **A)** VE200 and **B)** NAP features. All raw data is represented cumulatively. Line graphs showing individual chemokinetic treatment groups, imaged at 0 (solid black line), 45 (solid grey line) and 90 mins (dashed black line), in terms of optimal intensity **C)** VE200 and **D)** NAP features. The following neutrophil treatment groups are plotted: untreated (UT), 25ng/mL LPS, 100 nM PAF, 1 nM LTB4 with 100 µM Sivelestat, 1 nM LTB4 and 25ng/mL LPS / 100nM FMLF. Line graph values represent mean ± SD, *P* values were calculated by two-way ANOVA and Bonferroni multiple comparisons test, comparing against zero minute values, **P*<0.05 ***P*<0.01 ****P*<0.001 n=3

5.3.3 COMPARING NAP AND VE200 RATE OF LABELLING BY CHEMOKINETIC STIMULUS

In addition to measurements of fluorescence intensity and textural imaging features, imaging neutrophil responses to different chemokines over time yields information on the rate of change of measurements. Image analysis (see **Methods 2.5.5**) reveals the rate of change of NAP and VE200 fluorescence over 90 minutes. The LTB4+SIV condition constistently demonstrates the least change in NAP and VE200 signal overtime (**Fig. 5.14A and C**). Measuring NAP fluorescence rates, untreated, FMLF, LTB4 and LTB4+SIV conditions tended to plateau over the time course and untreated neutrophils display the shallowest, uninhibited rate of fluorescence increase (**Fig. 5.14A and B**). Unlike plateauing conditions, PAF fluorescence continues to accelerate across the time course even exceeding FMLF fluorescence at ninety minutes (**Fig. 5.14 B**). By VE200 rate of staining, PAF and LTB4 trends are similar to NAP rate of staining showing increasing and plateauing rates respectively (**Fig. 5.14 D**). FMLF staining however, follows opposing trends when it's rate of staining is measured, increasing over time with NAP and decreasing over time with VE200. Both HNE stains show FMLF rates plateauing at ninety minutes (**Fig. 5.14 B and D**).

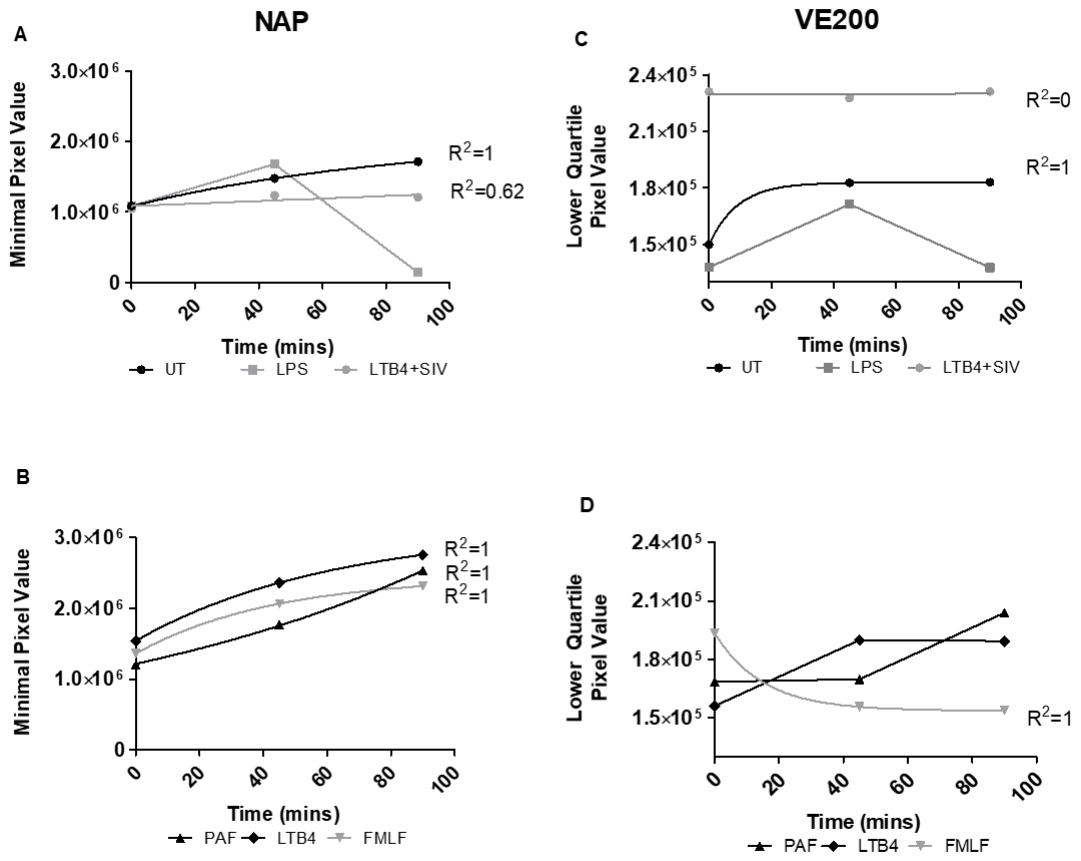

Figure. 5.14 Rate of HNE labelling may vary with chemokinetic specificity
Rate of neutrophil labelling is represented as **A,B)** NAP and **C,D)** VE200 optimal intensity feature measurement over time. untreated (black circles), 25ng/mL LPS (grey squares), 1 nM LTB4 and 100 µM Sivelestat (grey circles), 1 nM LTB4 (black diamonds) and 25ng/mL LPS / 100nM FMLF (grey triangles). Graph show image cytometric means of neutrophil populations, n=3.

5.3.4 STIMULUS-DEPENDENT NEUTROPHIL CLASSIFICATION BY MULTIDIMENSIONAL HNE FEATURES OVER TIME

When the eight most discriminatory features were used to generate principal components, linear discriminant analysis was performed as before (see **Fig. 5.10**) to cluster activated neutrophils by chemokinetic condition. VE200 fluorescence was a more stringent selection criterion than NAP fluorescence, yielding less bright neutrophils for cluster analysis, in fact LTB4, PAF and LPS treated neutrophils are completely lacking from the zero, forty-five and ninety-minute timepoints (bar 1 PAF neutrophil at zero minutes **Fig. 5.15D,E,F**) but these populations are represented by NAP bright neutrophil selection (**Fig. 5.15A,B,C**). Cluster analysis of NAP bright neutrophils achieves good clustering characteristics with clear delineation between chemokinetic treatment groups for most populations. Although limited, there is some ambiguity between priming conditions (PAF and LPS) at forty-five minutes (**Fig. 5.**15B) and between strong activated conditions (LTB4 and LPS/FMLF) at forty-five and ninety minutes (**Fig. 5.**15B **and C**). VE200 bright neutrophils (brighter than all untreated neutrophils at zero minutes) are clearly clustered with no ambiguity between untreated, LPS, PAF, LTB4, LTB4 + Sivelestat, or LPS/FMLF neutrophils (**Fig. 5.15 D,E,F**). Despite being abstracted by principle components analysis into an 8 dimensional hyperplane, which lacks clear relationship to a feature-space described by NAP and VE200 axes, treatment groups in the eight-dimensional principal component hyperplane are ordered by HNE release. The trend at ninety minutes for NAP and VE200 bright neutrophils, and at forty-five minutes for NAP bright neutrophils (with slight deviation from linearity for

VE200 bright neutrophils) show treatment groups are arranged linearly, in order of stimulus intensity, untreated, LPS, PAF, LTB4, LPS/FMLF neutrophils and the LTB4 with Sivelestat condition is aligned with LTB4 neutrophils perpendicular to this trend (**Fig. 5.15B,C,F**).

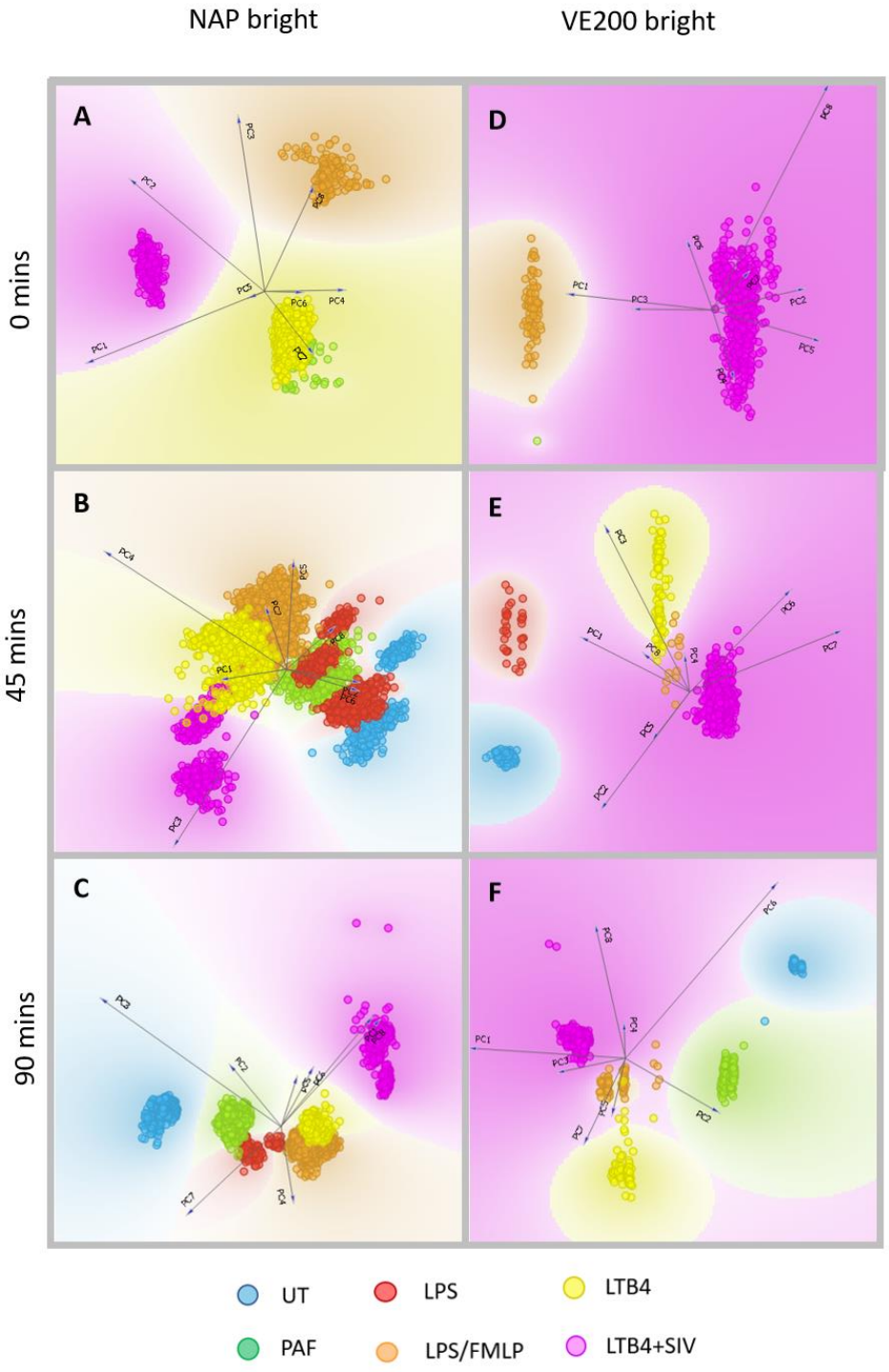

Figure. 5.15
VE200 classifies activated COPD neutrophils more specifically than NAP over time
Image cytometric analysis was applied to neutrophil populations to distinguish between untreated and activated fluorescence in the **A-C)** VE200 and **D-F)** NAP channels individually. Multidimensional score plots show neutrophil population clustering of at **A,D)** 0 mins, **B,E)** 45 mins and **C,F)** 90 mins. The following neutrophil treatment groups are plotted: untreated (blue), 25ng/mL LPS (red), 100 nM PAF (green) 1 nM LTB4 and 100 µM Sivelestat (purple), 1 nM LTB4 (yellow) and 25ng/mL LPS / 100nM FMLF (orange). All data points for each treatment group are shown, n=3.

5.3.5 STIMULUS-DEPENDENT CLASSIFICATION OF ENTIRE NEUTROPHIL POPULATIONS OVER TIME BY NEURAL NETWORK MODELLING

High classification accuracies and biologically relevant inferences were derived when fixed neutrophil populations were modelled using a neural network. To understand how neural network classification techniques might extend to live cell data, images from live neutrophils responding to physiologically relevant doses of stimulus were processed for neural network evaluation. All evaluation accuracies are above 79% bar the PAF class at 72.14%, the neural network demonstrates an overall sensitivity of 84.24% in this dataset (**Fig. 5.16B**). LTB4+SIV neutrophils are the most accurately identified with a true positive rate of 99.02% and all false positive rates below 0.77% across the remaining 5 neutrophil classes (**Fig. 5.16A**). The neural network shows a clear ability to identify functionally similar treatment groups with most false positives in each class falling in functionally similar classes, eg. 6.47% of untreated neutrophils are misclassified as the LPS neutrophils (**Fig. 5.16A**), the nearest to untreated in NAP and VE200 signal at each timepoint (see **Fig. 5.13C** and **D**) and all other classes have less than 2% false positive rates (**Fig. 5.16A**). Similarly, LPS/FMLF and LTB4 are more readily confused for each other and PAF neutrophils (6-9%) than for classes with low HNE release (0.22 – 2.73%, **Fig. 5.16A**). With an evaluation accuracy of 72.14% PAF neutrophils were the most difficult to classify (**Fig. 5.16A**). With each class representing all neutrophils from the zero, forty-five and ninety-minute timepoints, PAF neutrophils fall into the priming category at some timepoints (zero and forty-five minutes VE200, zero minutes NAP) and the activated category at subsequent timepoints by HNE response (see **Fig.**

5.13B and **D**). False positive analysis from the confusion matrix helps to highlight this ambiguity as PAF is the only class showing 5-10% measurements in 3 other classes.

A

		Actual (%)					
		LTB4+SIV	UT	LPS	PAF	LPS/FMLP	LTB4
Predicted (%)	LTB4+SIV	99.02	0.49	0.14	0	0.76	0.27
	UT	0.33	85.97	6.47	1.91	1.2	1.62
	LPS	0.22	8.16	79.31	8.65	2.17	2.97
	PAF	0	2.45	9.2	72.14	3.37	4.99
	LPS/FMLP	0.22	2.45	2.73	8.78	85.22	6.34
	LTB4	0.22	0.49	2.16	8.52	7.28	83.81

Scale (%)					
0	1	5	10	50	100

B

Sensitivity	0.8424
Specificity	0.9658

Figure. 5.16

A neural network classifies six neutrophil populations by chemokinetic stimulus using live-cell imaging data

A) Confusion matrix, arranged by HNE activity, showing neural network classification performance. Image cytometric analysis of fixed untreated, 1 nM LTB4 + 100 µM Sivelestat, 25ng/mL LPS, 100 nM PAF, 1 nM LTB4 and 25ng/mL LPS / 100nM FMLF treated neutrophils produced data for neural network classification. Data for each class was pooled across zero, forty-five and ninety-minute timepoints. Evaluation accuracies are heat-mapped using a dark red (low) to dark green (high) colour scale, shown. Percentages for accurate classification are highlighted in black-bordered cells.

B) Sensitivity and specificity are calculated, n=3.

5.3.6 STIMULUS-DEPENDENT CLASSIFICATION OF ENTIRE NEUTROPHIL POPULATIONS BY TIME-GROUPED NEURAL NETWORK MODELLING

A final machine learning analysis was undertaken to understand the effect of time on neural network classification. When data is organised by timepoint each individual class is more accurately classified leading to greater neural networks sensitivities at each timepoint than in the timepoint pooled analysis. Interestingly specificity improves less than sensitivity at each timepoint showing 0.9-2.1% increases whereas sensitivity increases by 3-9.2% (**Fig. 5.17B**). The distribution of false positives becomes increasingly limited to classes of the same activation state with the progression of time. At zero minutes the distribution of false positives through the confusion matrix shows little preference for cells in the grid, away from the green diagonal, the adjacent cells of which are functionally similar. By forty-five minutes there is a clear pattern of highest false positives along the diagonal with more distant false positive rates falling to <2.5%. Finally, at ninety minutes only 8 of the 30 false positive rates are >1% and these slightly higher rates identify two functional categories of low and high HNE activity (**Fig. 5.17A**). However, evaluation accuracy/sensitivity is >88% at each timepoint and at ninety minutes this reaches 93.44% **(Fig. 5.17B**), organising the six classes by stimulus and activation status.

A

Time (mins)			Actual (%)					
			LTB4+SIV	UT	LPS	PAF	LPS/FMLP	LTB4
0		LTB4+SIV	97.86	0	0.39	0	0.36	0.38
	Predicted	UT	0.36	90.54	2.36	3.6	1.82	1.89
	(%)	LPS	0	3.15	83.07	6	3.65	2.64
		PAF	0	2.7	5.91	83.6	0.36	7.55
		LPS/FMLP	1.79	0.9	2.36	0.4	89.42	2.64
		LTB4	0	2.7	5.91	6.4	4.38	84.91
45	Predicted	LTB4+SIV	99.34	1	0	0	0	0
	(%)	UT	0.66	87.06	3.95	0.46	0.74	0.78
		LPS	0	7.96	85.53	13.7	0.37	0.39
		PAF	0	1.49	7.24	77.17	5.9	3.53
		LPS/FMLP	0	1	1.64	6.39	86.35	7.45
		LTB4	0	1.49	1.64	2.28	6.64	87.84
90	Predicted	LTB4+SIV	99.13	0.51	0	0	0	0
	(%)	UT	0.58	93.33	2.67	0.42	0.25	0.82
		LPS	0.29	4.62	97.33	0	0	0
		PAF	0	0.51	0	88.66	5.94	3.27
		LPS/FMLP	0	0.51	0	8.4	90.35	4.08
		LTB4	0	0.51	0	2.52	3.47	91.84
			Scale (%)					
			0	1	5	10	50	100

B

Time (mins)	Sensitivity	Specificity
Σ	0.8424	0.9658
0	0.8823	0.9747
45	0.8721	0.9733
90	0.9344	0.9858

Figure. 5.17 Neural network classification improves with time-resolved image sets
A) Confusion matrix, arranged by HNE activity, showing neural network classification performance. Image cytometric analysis of fixed untreated, 1 nM LTB4 + 100 µM Sivelestat, 25ng/mL LPS, 100 nM PAF, 1 nM LTB4 and 25ng/mL LPS / 100nM FMLF treated neutrophils produced data for neural network classification. Data is arranged by class and timepoint. Evaluation accuracies are heat-mapped using a dark red (low) to dark green (high) colour scale, shown. Percentages for accurate classification are highlighted in black-bordered cells. **B)** Sensitivity and specificity are calculated, n=3.

5.3.7 NEUTROPHIL ACTIVATION DETECTION IN HUMAN LUNG ADENOCARCINOMA HISTOLOGICAL SAMPLES

To understand how HNE imaging may enable distinctions between quiescent and activated neutrophils in human tissues immunohistochemistry was performed on human spleen and lung adenocarcinoma tissue samples. The characteristic lobular nuclei of these polymorophonuclear granulocytes help to identify neutrophils, (**Fig. 5.18B and E**) coupled with bright HNE staining (**Fig. 5.18C and F**). In an adenocarinomatous setting, neutrophils show a trend of staining more brightly for HNE by immunohistochemistry (**Fig. 5.18G**) than in normal, healthy spleen. Morphological changes may provide more precise detection of neutrophil activation in human tissues. Neutrophils from lung adenocarcinoma tissue display a less circular morphology when compared to healthy splenic neutrophils (**Fig. 5.18C and F**). In cancerous lung tissue neutrophils appear to reorganise HNE into smaller regions such that the relationship between circularity and maximum diameter is altered (r=-0.66 for lung adenocaricinoma, -0.47 for spleen **Fig. 5.18H**).

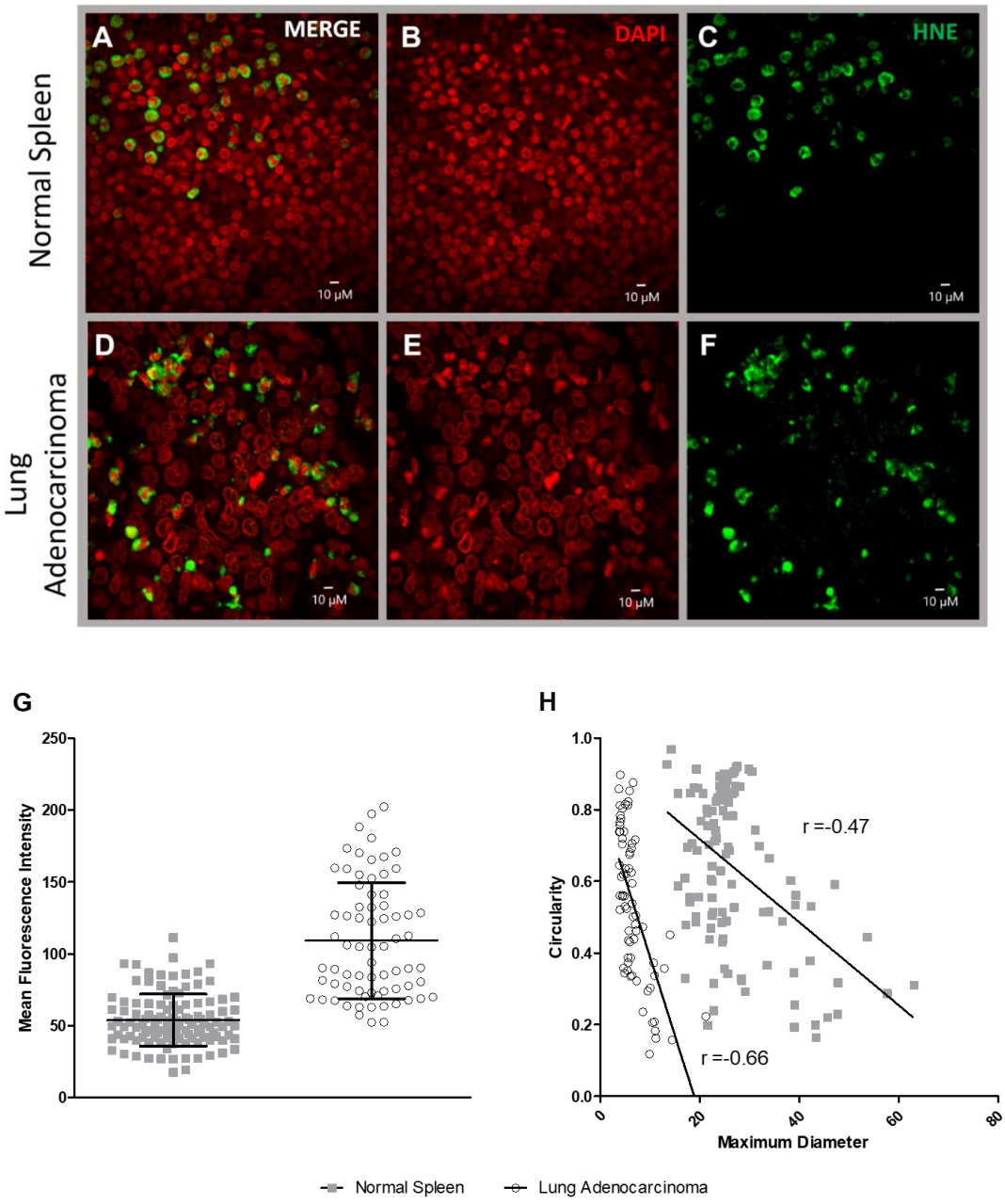

Figure 5.18
Immunohistological HNE imaging enables multiparametric neutrophil activation detection
Images show confocal microscopy of human **A-C)** spleen and **D-F)** lung adenocarcinoma cross-sections with nuclear staining (DAPI) and HNE immunostaining enhanced by tyramide signal amplification. Cross sections are shown as **A,D)** merge **B,E)** DAPI, **C,F)** HNE immunofluorescent images. **G)** Image analysis shows HNE fluorescence of individual neutrophils and **H)** correlation between neutrophil circularity and maximum (ferret) diameter, with Pearson coefficients, r, n=1.

5.3.8 SIGNIFICANCE OF NEUTROPHIL INFILTRATION IN HUMAN LUNG ADENOCARCINOMA HISTOLOGICAL SAMPLES

To understand how imaging neutrophil activation might contribute to lung adenocarcinoma detection, samples of human lung adenocarcinoma were acquired, sectioned and immunostained for HNE and the GLUT-1 glucose transporter, which is overexpressed on malignant epithelial cells. A correlation of 0.74 was found between HNE stained neutrophils and GLUT-1 bright cells. GLUT-1 bright cells in these sections were identified as highly likely to be malignant lung epithelial cells by a clinical pathologist.

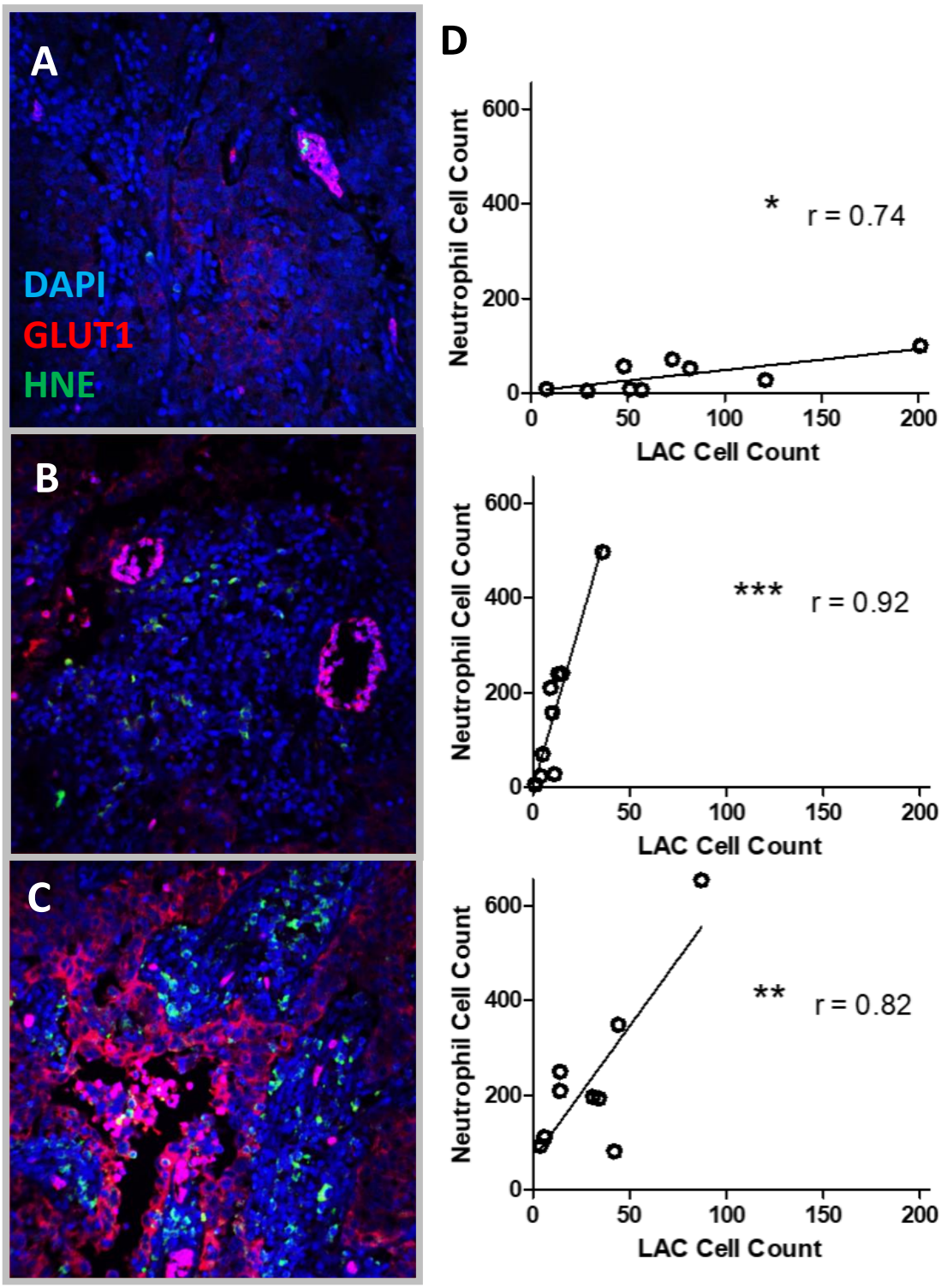

Figure 5.19 HNE staining correlates with GLUT1 staining in Human Lung Adenocarcinoma
Images show confocal microscopy of human lung adenocarcinoma cross-sections stained with DAPI (blue) and anti-GLUT-1 (red) and anti-HNE (green) antibodies. Sections with **A)** low **B)** medium and **C)** high numbers of GLUT-1 bright cells are shown. **D)** Image analysis shows the extent of correlation between the number of neutrophils and GLUT-1 bright cells in lung adenocarcinoma tissue, with Pearson coefficient, r, n=3.

5.3.9 DUAL-PROBE NEUTROPHIL ACTIVATION DETECTION BY FIBRED CONFOCAL ENDOMICROSCOPY *IN VITRO*

The fibred confocal imaging endomicroscope, Versicolour, (**Fig. 5.20.A**) was developed in-house. These images demonstrate the ability of Versicolour to detect neutrophil activation by NAP and VE200 staining *in vitro*. 3 µM NAP and 2 µM VE200 can be multiplexed for dual imaging of HNE presence and activity in neutrophils activated with 1 µM calcium ionophore (**Fig. 5.20.F-H**). Untreated neutrophils showed no staining in the 470 nm or 625 nm channels and 2 µM free Cy5 did not stain neutrophils regardless of calcium ionophore treatment (**Fig. 5.20.D and E**). All wells were re-imaged on a spinning-disk confocal microscope confirming the presence of neutrophils in all conditions and the increased NAP and VE200 fluorescence with activation (**Fig. 5.20.J**). NAP and VE200 co-localized staining and the absence of passive free Cy5 staining are confirmed by spinning-disk confocal microscopy. The apparent reduction in NAP signal with 2 µM VE200 co-staining is quantified elsewhere (see **Fig. 4.15**).

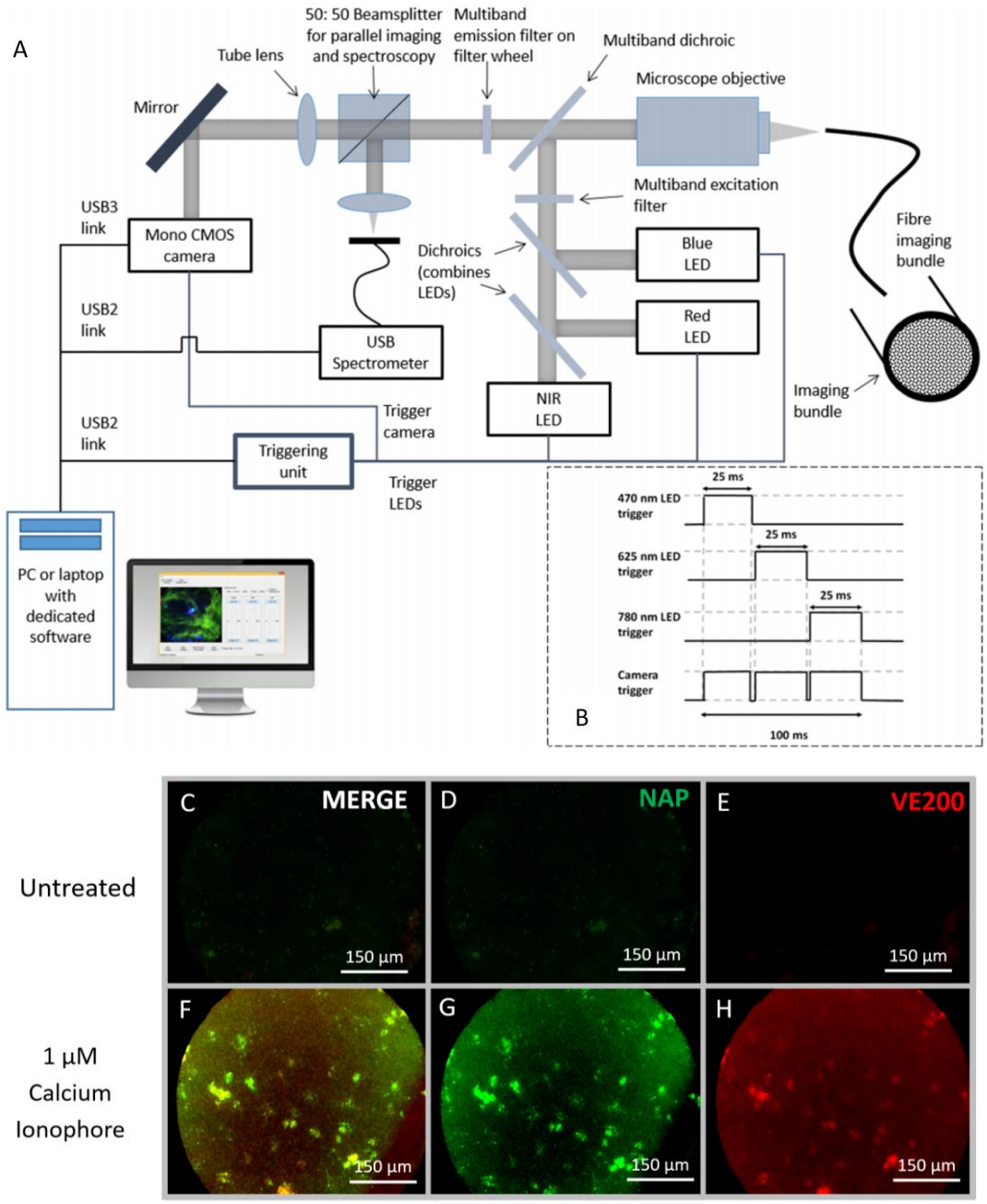

Figure 5.20 Activated neutrophils are visible via Versicolour fibred confocal endomicroscopy with multiplexed NAP and VE200

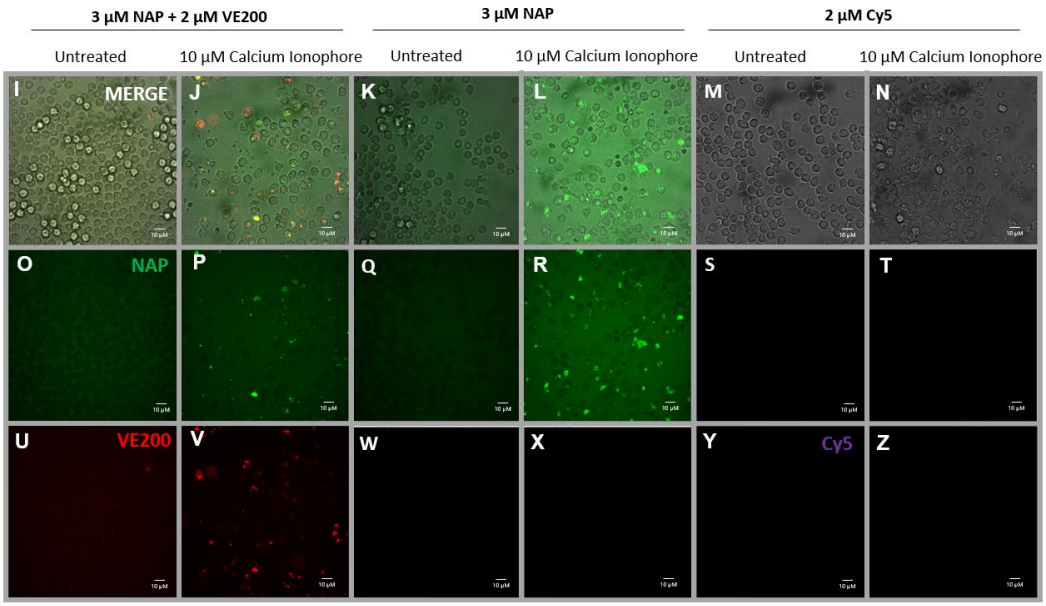

Figure 5.20 Activated neutrophils are visible via Versicolour fibred confocal endomicroscopy with multiplexed NAP and VE200

A) Electro-optical architecture of Versicolour, in-house fibred confocal endomicroscope and **B)** triggering sequence for 25-ms exposure time for each channel with 10 fps imaging speed for combined three-color imaging. A minor delay is introduced between pulses so that the camera hardware can accommodate image transfer.[245]

Images from Versicolour, showing **C-E)** untreated and **F-H)** 1 µM calcium ionophore stimulated neutrophils in **C,F)** merged, **D,G)** NAP and **E,H)** VE200 channels.

I-Z) Neutrophils that were imaged using Versicolor were subsequently imaged using spinning disk confocal microscopy: **I-N)** Merged, **O-T)** NAP and **U-Z)** VE200/Cy5 images are shown. Images compare untreated and 1 µM calcium ionophore stimulated neutrophils (**I,O,U** and **J,P,V** respectively) incubated with 3 µM NAP and 2 µM VE200, 3 µM NAP (**K,Q,W** and **L,R,X** respectively) or 2 µM free Cy5 dye **(M,S,Y** and **N,T,Z** respectively).

5.4.0 LOW SPATIAL RESOLUTION DUAL-PROBE NEUTROPHIL ACTIVATION DETECTION IN AN *EX VIVO* VENTILATED HUMAN LUNG

To evaluate how applicable *in vitro* versicolour imaging results are to a clinically relevant, pulmonary OMI scenario, neutrophils were acitvated and imaged in a human *ex vivo* lung ventilation (EVLV) model. Low reagent doses facilitate the relevance of EVLV to a clinical use case and a 200 nM VE200 dose, effecive in previous imaging experiements (see **Fig. 4.10-12**) was chosen rather than the 2 µM dose used in *in vitro* OMI experiments. At this low 200 nM VE200 dose, NAP signal was not obstructed by the presence VE200 and punctate NAP fluorecence is visible in calcium ionophore treated neutrophils. VE200 fluorescence was useful in indicating neutrophil activation as frames containing calicium ionophore stimulated neutrophils demonstrate bright fluorescence in the 625 nm channel, however the spatial relationship of VE200 signal to stimulated neutrophils is ambiguous with large regions of pixels at high values around regions that appear neutrophil-dense by NAP staining. Image processing clarifies the spatial resolution of both the 470 and 625 nm channels such that background signals are removed and contrast is increased and yet VE200 still has reduced low spatial resolution when compared to the precise puncta identifiable via EVLV NAP imaging. One advantage to VE200 neutrophil imaging is the complete lack of background signal in the absence of neutrophil activation whereas NAP signal is in constant competition with endogenous 488 nm autofluorescence.

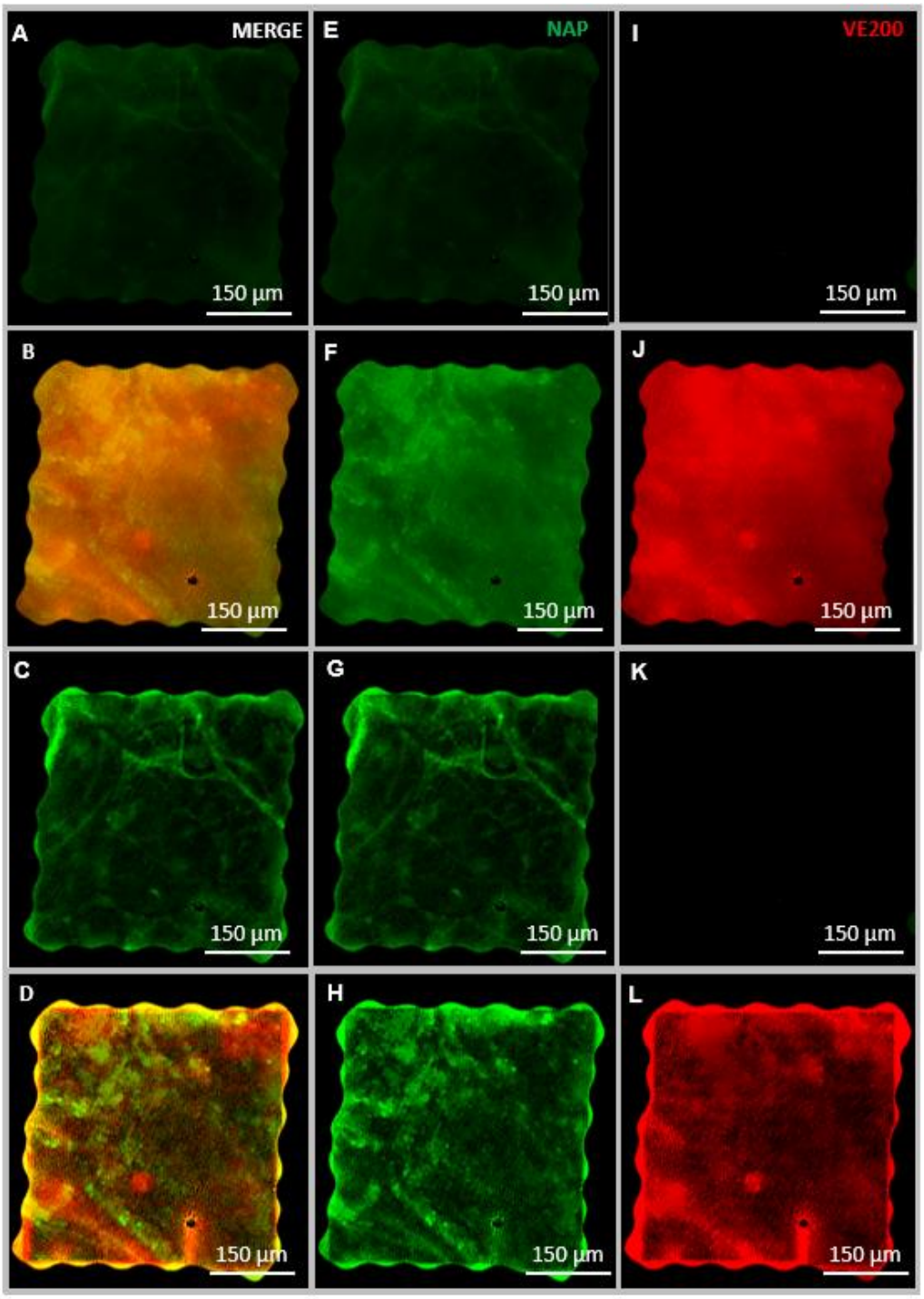

Figure 5.21 At 200 nM VE200, optical molecular imaging shows activated neutrophils are rapidly detected with low spatial resolution
Representative images from within an *ex vivo* ventilated human lung showing allogeneic neutrophils coated onto the interior alveolar surface. **A-D)** Merged images of 3 µM NAP and 200 nM VE200 images. **E-H)** NAP images, **I-l)** VE200 images. Untreated **A,E,I)** and **B,F,J)** 10 µM calcium ionophore stimulated neutrophils are shown **A,B,E,F,I,J)** before and **C,D,G,H,K,L)** after image processing, n=1. This experiment could not be repeated as human lungs are infrequently available for experimentation.

5.4.1 COMPARING TARGETED AND ACTIVABLE PROBE DETECTION SENSITIVITY IN AN *EX VIVO* VENTILATED HUMAN LUNG

Although activated neutrophils are more discretely resolved when imaged using NAP than VE200, frames containing activated neutrophils are instantly and unambiguously recognisable with 200 nM VE200 staining. Elastin fibres contribute a consistently low autofluorescence in the 470 nm channel and not in the 625 nm channel. Activated neutrophils stained with NAP appear distinctly brighter (median= 47 RFU, **Fig. 5.22.A** white squares) than lung tissue strcutures (median= 12 RFU, **Fig. 5.22.A** black circles), even via framewise image quantitifacition (histogramming and fluorescence thresholding) which does not individuate cells. In the presence of supraphysiological concentrations of activated neutrophils, VE200 appears to adsorb to surrounding lung structures with a similar level of fluorescence as activated neutrophils (median= 35 RFU, **Fig. 5.22.B and A** white squares), unless neutrophils have not been activated in which case there is no VE200 signal (**Fig.5.21.B** black circles). Interestingly, the magnitude of fluorescence increase when frames with activated neturophils are compared to those without is the same (+35 RRU) by both NAP and VE200 staining.

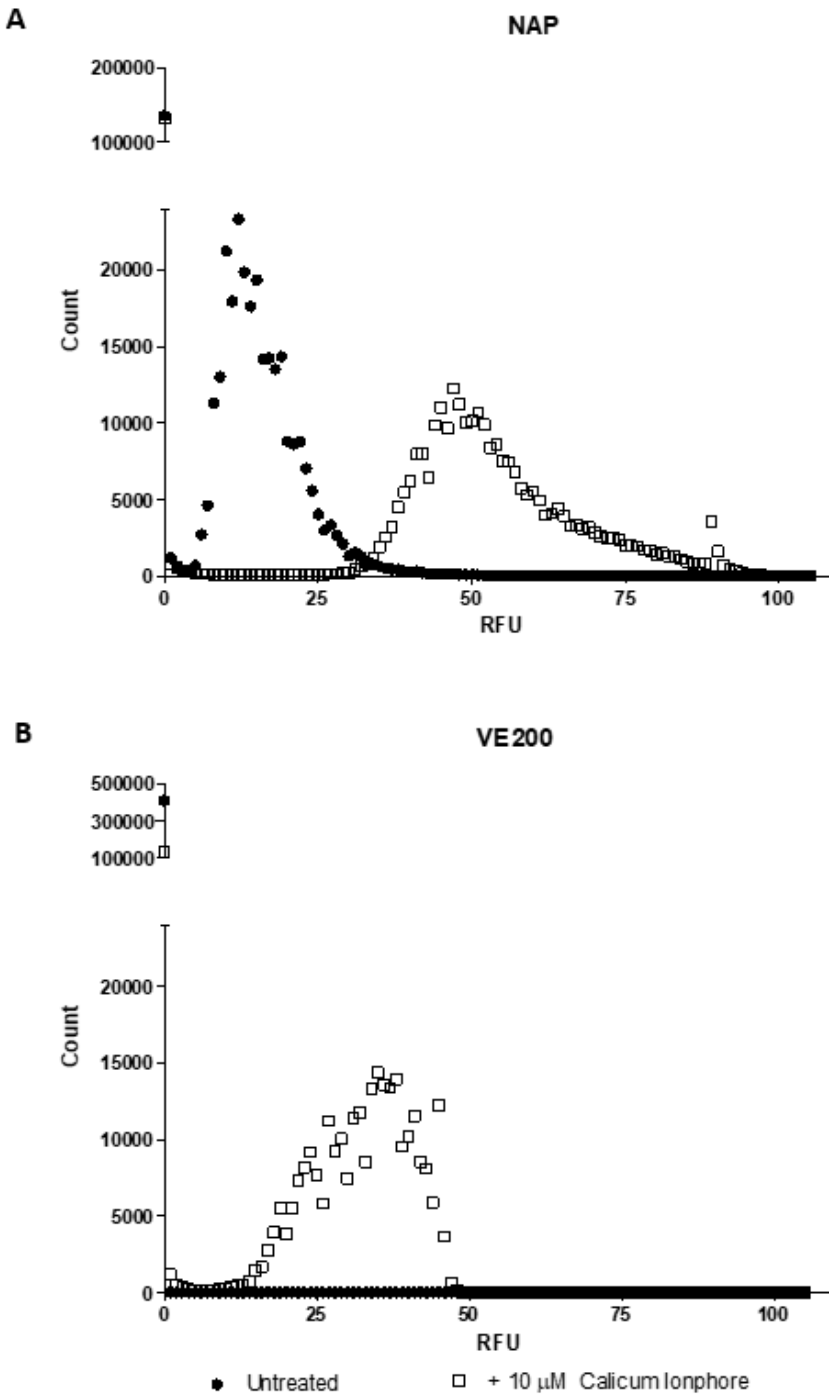

Figure 5.22 200 nM VE200 detects activated neutrophils despite low spatial resolution
Histograms of processed video frames acquired using Versicolour, optical molecular imaging. Images of neutrophils from within an *ex vivo* human lung were compared in untreated (black circles) or 10 μM calcium ionophore (white squares) stimulated states, n=1. This experiment could not be repeated as human lungs are infrequently available for experimentation.

5.4.2 HIGH SPATIAL RESOLUTION DUAL-PROBE NEUTROPHIL ACTIVATION DETECTION IN AN *EX VIVO* VENTILATED HUMAN LUNG

By increasing VE200 dose to 400 nM, activated nuetrophils become recognisable with spatial resolution of similar the to that of NAP. NAP signals persist in the presence of 400 nM VE200 and the multiplexing of these signals allows the identification of colocalized HNE labelling on calcium ionophore treated neutrophils in the EVLV model. As opposed to the complete lack of background in the 625 nm channel at 200 nM VE200, at 2400 nM there is a low level of featureless, background fluorescence. Comparing the maxima of the untreated and 10 µM calcium ionophore treated neutrophil conditions have comparable signal to noise ratios of 1.41 and 1.67 for NAP and VE200 respectively. Imporantly, these conditions allow for image thresholding to reduce untreated, background information to zero while maintaining signal from activated neutrophils. Activated neutrophils stain brightly and display a fluorescence blinking phenomenon, in both channels, as they pass between imaging core and inter-core cladding withing the multi-core imaging fibre. Background signals do not demonstrate blinking. Taking these imaging characterstics together, the spatial and temporal relationships of activated neutrophil signals combined with sharp differences in fluorescence intensity create an imaging paradigm in which activated neutrophils are readily identified from untreated neutrophils without fluorescence thresholding.

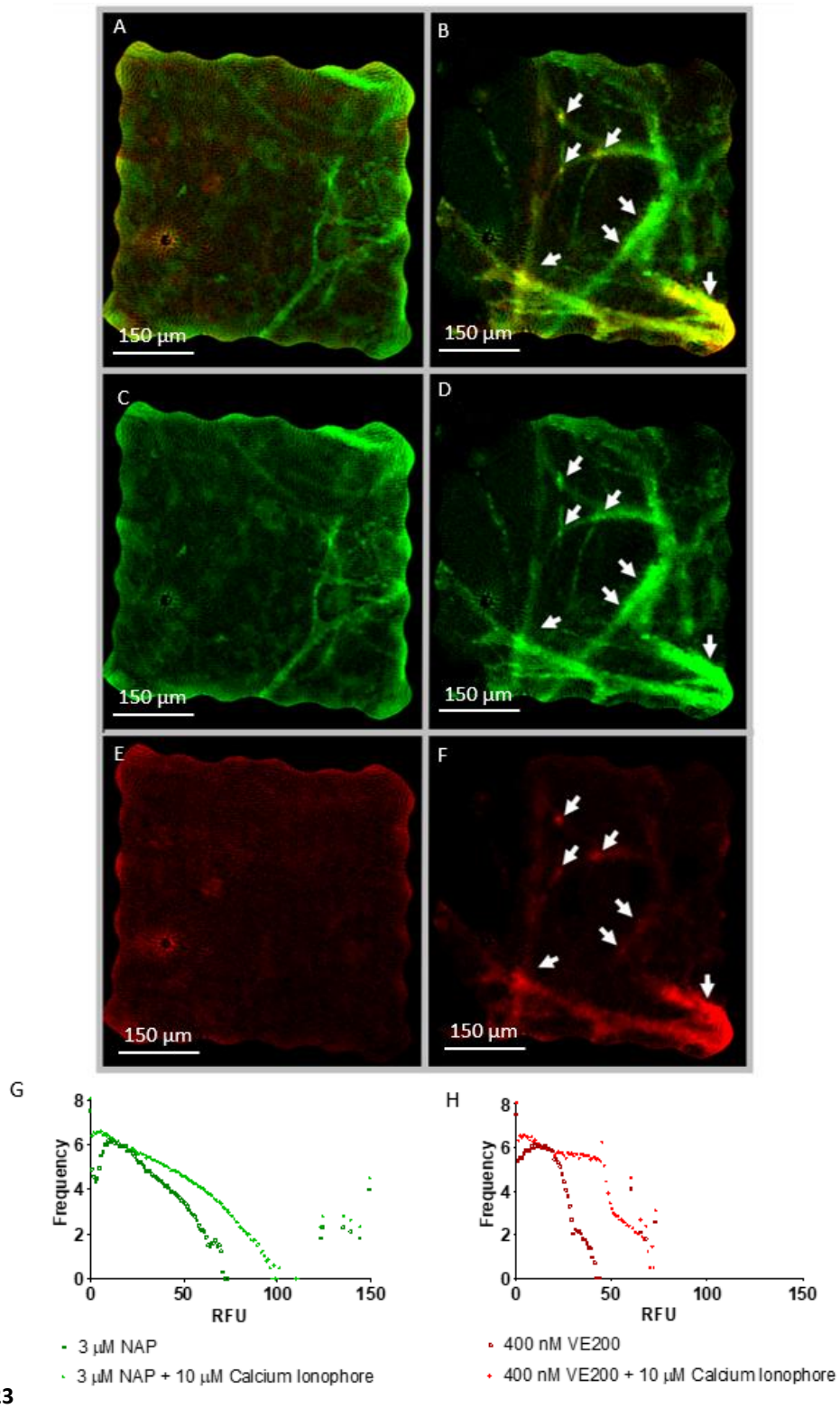

Figure 5.23

NAP and VE200 signals colocalize at sites of neutrophil activation in an *ex vivo* human lung

Representative images, acquired with Versicolour, from within an *ex vivo* ventilated human lung, of interior surface of an alveolus surface coated in allogeneic neutrophils. Neutrophils are instilled into the alveolar space **A,C,E)** untreated or **B,D,F)** stimulated with 10 µM calcium ionophore. Images are shown **A,B)** merged **C,D)** NAP **E,F)** VE200, n =1. This experiment could not be repeated as human lungs are infrequently available for experimentation.

5.4.3 SEPARATING ACTIVATED NEUTROPHILS POPULATIONS IN AN *EX VIVO* VENTILATED HUMAN LUNG

With 3 µM NAP and 400 nM VE200, the spatial resolution of HNE imaging was sufficiently high to distinguish separate waves of infused neutrophils in the EVLV model. When neutrophils, 10 µM calcium ionophore and NAP were co-administered to the alveolus, followed by neutrophils, 10 µM calcium ionophore and VE200, an elastin fibre was observed bearing clustered neutrophils, stained in alternating stripes of NAP and VE200 signal. A pattern of inverse proportion was observed as both probes varied in precisely opposite patterns of high and low signal intensity **Fig. 5.24.G**. It is likely that activated, adherent neutrophils covered the entire elastin fibre in continuous, bright NAP fluorescence after the first infusion. The second infusion, imaged within sixty seconds, could have introduced neutrophils with of approximately 400 nM VE200 removing NAP signal only where they contacted the elastin fibre **Fig. 5.24E**. Two populations of neutrophils are observed by differential staining of NAP and VE200.

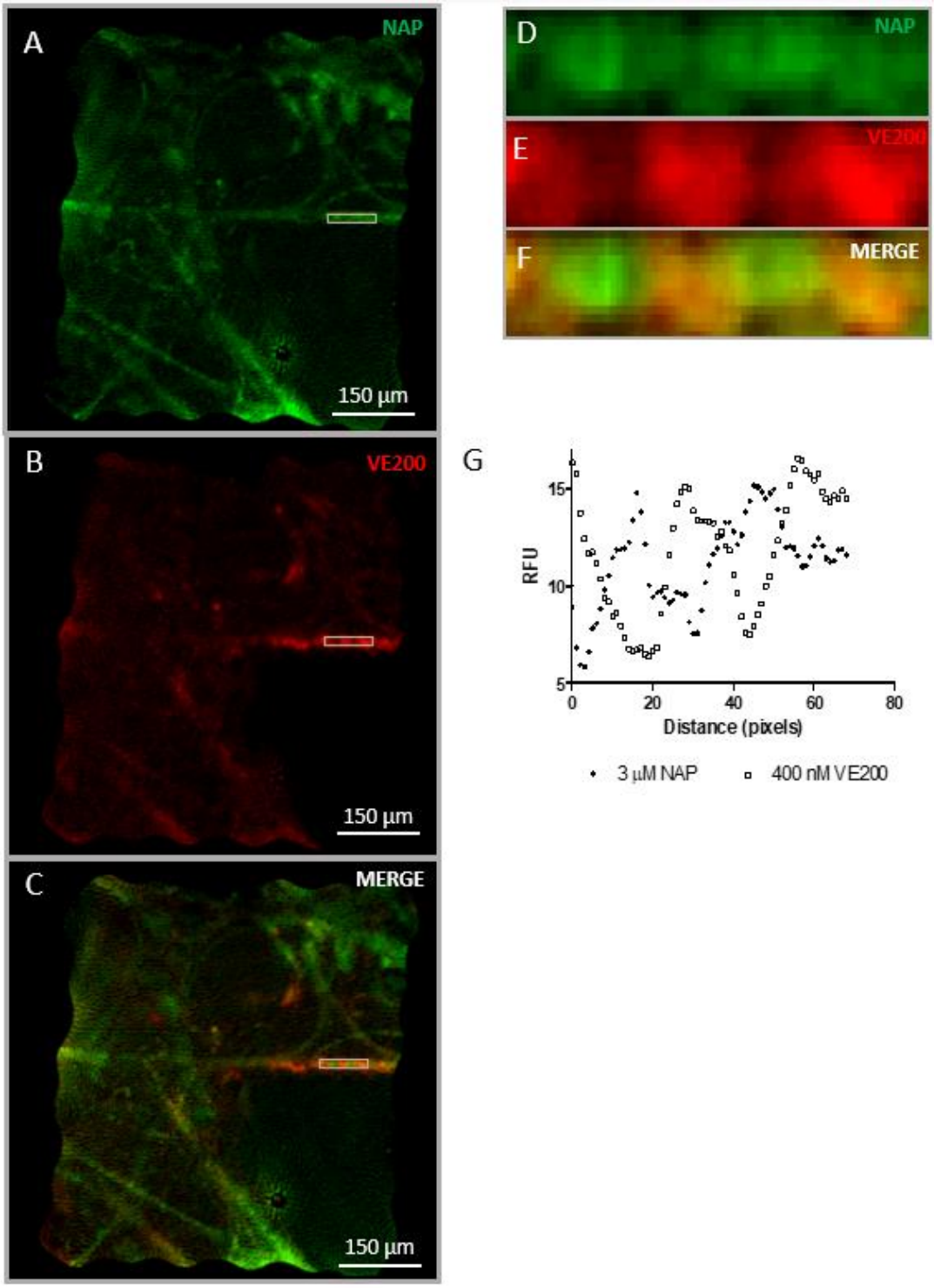

Figure 5.24 NAP signal is sensitive to VE200-mediated inhibition in human lung *ex vivo*
Representative images, acquired with Versicolour, from within an *ex vivo* ventilated human lung, of interior surface of an alveolus surface coated in allogeneic neutrophils. Neutrophils stimulated with 10 µM calcium ionophore are instilled into the alveolar space and shown as **A)** NAP only **B)** VE200 only and **C)** merge. Magnified **D)** NAP only **E)** VE200 only and **F)** merge images of a neutrophil coated elastin fibre (grey rectangle) are shown and **G)** analysed to plot fluorescence intensity across distance, n=1. This experiment could not be repeated as human lungs are infrequently available for experimentation.

5.4.4 SUMMARY

VE200, the HNE-targeted probe holds significant advantages over immunofluorescent HNE detection as a means of targeted HNE labelling. VE200 stains in minutes and it stains neutrophils without fixation, enabling dynamic imaging and improving NAP signal in multiplexed assays. The targeted and activable probes, VE200 and NAP combine to produce significant volumes of imaging data, accessible on a per cell basis. With multivariate analysis and neural network modelling, the dense network of information associated with individual images can be effectively mined to produce phenotypic classifiers. Combining chemistry, biology and data science techniques, neutrophils can be classified not just into untreated or activated classes but activated neutrophils can be subdivided by stimulus, neutrophil priming is detectable and subdivided by stimulus, so that nuanced neutrophil behaviour can be accurately described. In short, a versatile classification tool has been devised which describes a spectrum of neutrophil activation using live-cell imaging data. Finally, the ability to detect and quantify neutrophil activation via live-cell FCE, in a clinically-relevant *ex vivo* lung model, was demonstrated.

5.5.0 DISCUSSION

5.5.1 HNE ACTIVITY FOLLOWING FORMALDEHYDE FIXATION

Formaldehyde forms polymeric cross-links between proteins such as HNE and hence may interfere with HNE activity, reducing NAP signal. However, the inhibitory effect of fixation can be titrated. That neutrophils can be fixed without completely abrogating HNE activity is not a novel finding. Korkmaz *et al.* clearly demonstrate decreases in antibody affinity (andit-C63 and anti-CD16b) following 3% PFA/ 0.25% glutaraldehyde fixation but no change HNE activity[213]. Evidently NAP signal can be increased by gentle fixation conditions (**Fig. 5.2.E**) despite a reduction in HNE activity and this may have several explanations: 1) fixative may displace fluorescein moieties from the NAP dendrimer, 2) cleaved NAP fragments may interaction with fixative to accumulate on the surface of fixed neutrophils, 3) By cross-linking NAP molecules, fixative may increase the rate of NAP cleavage by allowing HNE to interact with NAP aggregates instead of isolated NAP molecules. The later may explain the appearance of a minority of neutrophils with a log-fold increase in NAP fluorescence, (**Fig. 5.2.D**) particularly as centrifugation may have concentrated NAP aggregates.

Because HNE activity is largely preserved and the effects of fixation on NAP signal generation present a systematic error, fixation artefacts can be removed from analysis by subtracting the fluorescence of a fixed untreated neutrophil control. Zin-based fixatives which may not require antibody-retrieval, may enhance fixed HNE activity measurements by removing formaldehyde, its cross-linking and fixation artefacts.[246]

5.5.2 MEMBRANOUS HNE IMMUNOFLUORESCENCE

Measuring HNE presence by immunofluorescence serves as a sensitive standard for validating NAP signals. Both methods enable signal amplification, detecting HNE under physiologically-relevant stimulation conditions, where individual neutrophils are expected to yield membranous HNE (mHNE) in the femtomolar to picomolar range.[212,213] Although the mHNE was discovered more recently than the degranulated and endosomal forms, mHNE contributes in a non-trivial manner to neutrophil activity. In addition to the sheer quantity of HNE that can be stored on the plasma membrane (in equilibrium with HNE in solution) mHNE is more resistant to alpha-1-antiprotease inhibition than degranulated HNE. As HNE is believed to adhere to plasma membranes by charge, the enzyme's active site may be less accessible to alpha-1-antiprotease when membrane bound than when in solution.[213] mHNE therefore presents an important caveat to the protease-antiprotease hypothesis by ensuring motile neutrophils can constantly evade HNE-inhibition, employing active mHNE at the plasma membrane-substrate interface. At this interface, inhibitor concentrations may fall to negligible levels. Clinical HNE biomarkers stand to be more informative when sensitive to mHNE and this sensitivity can be evaluated by correlation with immunofluorescence. This assay may have been improved descriptions of the extent to which mHNE was displaced by fixation. This contextualising data could have been gained by removing supernatants for measurements of HNE activity with and without fixation.

5.5.3 CHARACTERISING AND CLASSIFYING FIXED NEUTROPHIL POPULATIONS BY CHEMOKINETIC RESPONSE

NAP fluorescence and immunofluorescence increased with stimulus intensity under physiological doses of LPS, PAF, IL8, LTB4 and LPS/fMLF. The ability to categorize neutrophil activation into functional groups (untreated, primed, activated and primed-activated) by univariate analyses testifies to the precise control neutrophils exert over HNE release and activity. HNE release is tightly matched to the extent of activation a stimulus elicits, even at physiological doses which are often below the limit of detection of functional assays. This correlation highlights 1) the neutrophil's quantal release of granule contents, HNE and HNE inhibitor, modulating presence and activity of the protease in the inflammatory milieu.[174] 2) The sensitivity of image cytometry.

Image cytometry is the quantification of cellular populations from images, on a per cell basis, using image analysis. Often classification algorithms can be trained on information-dense images with high accuracy.[247] NAP enables image cytometry. HNE antibody and NAP fluorescence show the same overall pattern of increasing fluorescence intensity from untreated, to primed, to activated, to primed-activated neutrophils, validating the assertions that NAP can 1) detect increasing concentrations of HNE release under physiological stimulation 2) be used to identify neutrophils of different functional groups 3) describe neutrophil populations in

high-throughput assays. Taken together NAP imaging could inform a neutrophil classifier for automated neutrophil phenotyping.

Although textural features could be used to provide a more categorical rationale for classification than stronger or weaker fluorescence intensity, they make weaker distinctions between treatment groups. HNE may be localized to neutrophils in different treatment groups with similar patterns at the population level. The subtlety of HNE-derived textures may be compounded by the relatively small amounts of HNE released in response to physiological concentrations of stimulus, indeed over 90% of neutrophils resembled untreated cells in their HNE-staining under these conditions (see **Fig. 5.5.A and B**).

Similar trends help to validate NAP staining claims but differences in trends between stains are useful too. As HNE antibody staining and NAP staining relay subtly different pictures of neutrophil activation, a more nuanced phenotypic analysis is generated by their combination, enhancing the discriminatory power of classifiers. DAPI and CellMask^{TM} orange staining were added to the immunofluorescence assays to enable cell identification and segmentation for the image analysis pipeline. However, DAPI and CellMask^{TM} orange fluorescence intensity also displayed meaningful variance between treatment groups. Combining different sets of imaging data bivariate analyses had improved classification accuracies than univariate analyses (**Fig. 5.8**). This principle extends or greater accuracy with more information extends to higher order multivariate analyses. Principal components and linear discriminants analyses can create highly

informative multivariate data visualizations compared to univariate data visualization such as histograms and scatter graphs. With minor contributions from weakly segregating variables and greater contributions for variables that explain more sample variation, these orthogonal transformation techniques summarize large datasets in more informative, combinatorial axes. In this manner phenotypic clustering and classification accuracy can be optimized, creating the most appropriate multi-dimensional feature-space for data visualization.

Linear combinations of variables produce comprehensible and marked improvements in the informativeness of data visualisations and classification accuracy. However, machine learning techniques are not limited to linear transformations of data. Neural networks are capable of computing linear and nonlinear data transformations in parallel, estimating class identity, calculating estimation error and re-iterating along the fastest route to greatest accuracy. A simple neural network, outperformed linear classifiers, separating entire neutrophil populations including those with high similarity in linear comparisons.

5.5.4 CHARACTERISING LIVE NEUTROPHIL POPULATIONS BY PERCENTAGE ACTIVATION

Removing neutrophils within limits for untreated fluorescence from each treatment group allows the neutrophils with the most pronounced phenotype for each treatment group to be compared. There is a large degree of variation between donors by this method. It is important to visualise this variation as it highlights the varying degree to which neutrophil populations retain an “untreated” contingent when stimulated sub-maximally. Removing this large proportion of the data amplifies variation between treatment groups.

VE200 staining reveals less obvious neutrophil population differences than NAP and the two probes behave differently over time. VE200 staining could be amplified by increasing the concentration of probe used as only 100 nM is used compared to 3000 nM for NAP, however these doses minimize NAP signal reduction. Making use of the two different temporal patterns of VE200 and NAP will help to classify neutrophil populations across time.

5.5.5 CHARACTERISING RATE OF SIGNAL ACCUMULATION IN NEUTROPHIL POPULATIONS

Untreated and LPS treated neutrophils are difficult to separate by univariate analyses, however the temporal traces of these two populations deviate markedly between forty-five and ninety minutes. Similarly, 100 nM PAF elicited HNE responses akin to LTB4 and LPS/fMLF treatment groups in magnitude. Despite their similarities, PAF treated neutrophils arrive at these fluorescence intensities by a different means showing signal acceleration over time whereas the LTB4 and LPS/fMLF conditions show deceleration and plateauing. Stimulus-dependent signal deceleration may be related to differences in HNE degranulation. When Cepinskas *et al.* stimulated neutrophils with 100 nM PAF, with or without attachment to a HUVEC monolayer, HNE activity could not be detected in the surrounding supernatant, however HNE was released onto neutrophil plasma membranes.[17] Cepinskas *et al.* acknowledge that their inability to detect extracellular HNE release stands against the work of others such as Furuno *et al.*[248] and that this may be explained by their relatively shorter measurement interval (30 vs. 120 mins).[17] PAF-stimulated degranulation may occur in a delayed fashion compared with to LPS/FMLF-stimulated degranulation. If this is the case, HNE-staining acceleration may reflect HNE degranulation from a population of neutrophils. Differences in rate of signal generation could also be accounted for by differential corelease of endogenous inhibitors, such as elafin.[174] Alterations in HNE-release make NAP and VE200 signal generation kinetics an important element in classifying neutrophil

populations, particularly those that are rendered similar by absolute fluorescence measurements.

Decreasing the imaging interval and collecting data at more timepoints would clearly add clarity and robustness to this assay however this would require a more high-throughput imaging platform than the spinning-disk confocal microscope used, or reduction in the number of treatment groups. Importantly this technique is limited in its applicability to patient sample analysis. With an approximately three-hour Percoll blood purification step and the use of a confocal bench-top microscope sample analysis would not be performed in real time. As these probes demonstrate neutrophil specificity a whole blood sample may be analysed, significantly reducing readout lag-times. Because these measurements were taken *in vitro* they lack relevance to *in vivo* cell biology and this could be rectified with fibred confocal endomicroscopy (FCE) techniques of sufficient resolution and throughput.

5.5.6 CLASSIFYING LIVE NEUTROPHIL POPULATIONS BY CHEMOKINETIC RESPONSE

Principle components analysis and linear discriminants analysis combined make it possible to distinguish between a highly activated minority of neutrophils from untreated, primed, activated and a primed-activated treatment groups. The great advantage of these techniques is the generation of a multi-dimensional feature-space (taking combinatorial features as axes instead of raw features) in which neutrophils can be gated by their HNE-phenotype. Using neural network modelling HNE-phenotyping could be performed across entire neutrophil populations. The

neural network more readily confused neutrophils of the same functional mode (eg. one primed class for another) than other modes and ascribing less false positives to those modes which are most different in terms of HNE release. Therefore, the neural network demonstrates some ability to describe functional groups for HNE-phenotypes *a priori.*

Organization of neutrophil treatment groups into inhibited, primed and activated categories highlights the ability of machine learning to objectively reveal meaningful patterns in the data. 100 nM PAF stimulation seemed similar to activated neutrophils, eliciting similar levels of NAP staining as LTB4 and LPS/FMLF treatment at forty-five and ninety minutes (see **Fig. 5.13D**) and the fastest signal generation rates for both probes (see **Fig. 5.13B** and **D**). This may explain the increased confusion between this typically priming condition and the other activating treatment groups. Although losses in evaluation accuracy are minimal, the neural network seems to find PAF neutrophils most difficult to accurately identify because of their similarities to activated neutrophils. 100 nM PAF represents an interesting primed neutrophil population as it has been shown to increase neutrophil mHNE with undetectable release of HNE into the extracellular milieu.[17] However in this dataset strong PAF-dependent HNE responses indicate these cells are activated and hence PAF neutrophils are more accurately grouped with activating conditions than primed or untreated conditions. With an average evaluation accuracy of 84.24% for timepoint pooled data, temporally distinct waves of infiltrating neutrophils may still be accurately stimulus-classified irrespective of the duration of exposure to stimulus. This may be particularly useful in understanding chronic inflammatory

disease in which neutrophils may infiltrate a tissue at different times due to varying chemoattractants.

Neutrophils from COPD patients were prepared for this neural network analysis and a limitation of this study was the lack of willing, age-matched, healthy, smoking, volunteers, this would have elucidated disease-specific changes in HNE-phenotype, a tendency for increased PAF response in COPD neutrophils for example. However, comparison against healthy controls was not required to evaluate neural network classification between distinct neutrophil populations. Neural network data analysis could have also been improved by increasing the sample size or by collecting more complex data sets such as the use of fluorescence lifetime imaging might have allowed. For reasons of practicality neither of these approaches were pursued. Further work assessing the effect of neutrophil ageing, apoptosis and necrosis on stimulus-specific classification would provide useful insight into the stability of neural network performance over time. This neural network grouped HNE-phenotypes into functional modes *a priori* which lends credence to the idea that neutrophils can be classified via unsupervised machine learning techniques, but this must be investigated further.

5.5.7 NEUTROPHIL ACTIVATION DETECTION IN HUMAN LUNG ADENOCARICNOMA SAMPLES

Immunohistochemstry was used to identify activated neutrophils in human lung adenocarcinoma (LAC) samples, both by increased fluorescence intensity and shape change (see **Fig. 5.18**). As shown previously, neutrophils immunostained for HNE accrue NAP staining, post fixation (see **Fig. 5**). Hence the ability to detect neutrophil activation via immunostaining sets a precedent for NAP based neutrophil activation detection in LAC. The correlation between neutrophil count and GLUT-1 bright cell count in LAC samples is not surprising given that neutrophils are recruited to the tumour milieu and promote neutrophil recruitment. Neutrophil counting is understood to have prognostic significance with respect to many solid tumours including LAC however quantitation in the tumour milieu and image cytometric analyses (**Fig. 5.18**) may enhance the generalization and accuracy of quantitation techniques which currently rely on systemic circulation counts without classifying neutrophil activation. This study was limited by the single-marker identification of malignant epithelium. Although a clinical pathologist confirms the proposed identification is highly likely, transcription terminator factor 2 stain could have helped to corroborate malignant epithelial cell identification in these samples. GLUT-1 overexpression precedes GLUT-3 overexpression, in LAC, making it the earlier marker, both of which indicate intensifying tumour growth and poor survival.[249] Demonstrating a correlation between HNE and GLUT1 may therefore be sufficient to enable HNE stains to relay GLUT-1 prognostic information.

5.5.8 FIBRE-BASED NEUTROPHIL ACTIVATION DETECTION WITH MULTIPLEXED NAP AND VE200

When 3 µM NAP and 2 µM VE200 were multiplexed *in vitro* for neutrophil activation detection (**Fig. 5.20**) a key limitation was the lack of near-infrared plasma membrane stains. The three-colour imaging system, Versicolour was limited to two-colour imaging in practice. To confirm that Versicolour was detecting stained neutrophils, samples were imaged with 488 nm, 641 nm and brightfield channels via spinning-disk confocal microscopy. Nonetheless, VE200 and NAP signals were successfully multiplexed and imaged via FCE.

When neutrophil activation detection was attempted in the *ex vivo* lung ventilation model (EVLV), neutrophil and HNE-probe incubation times were decreased, to 1 minute, to improve the throughput of this rarely accessible model. 2 µM VE200 produced constant saturation in the 650 nm channel despite any concentration reductions due to regent volumes dispersing through the alveolar space. Neutrophil staining in the alveolar space via catheterised reagent instillation is significantly different from the same experiments in a 96-well plate format and well plate dose combinations were inappropriate in EVLV. Titration in EVLV showed optimal resolution and NAP multiplexing at 400 nM VE200.

Despite providing a relatively course level of image analysis, framewise histograms described imaging thresholds for the deletion of untreated frame signals such that neutrophil activation can be objectively measured using these images. Separating untreated and activated neutrophils by image analysis satisfies the first step

towards more sophisticated classification with EVLV data. Neutrophil activation can be detected in real-time in a ventilated lung using NAP and/or VE200. With calcium ionophore stimulation producing maximal HNE release, neutrophil activation detection occurs more readily than under gentler stimulation. It would be unsurprising if necrotic neutrophils were detectable using Versicolour and HNE probes as necrosis leads to maximal HNE release. Although neutrophils are effectively detected following priming and sub-maximal activating stimuli via confocal microscopy it is unclear whether FCE will facilitate equally robust HNE detection. Significant advances in the resolution of fibre-based microscopy have been made since the inception of Versicolour, improving image resolution and benefiting the application of machine learning techniques to clinical imaging data. Cell segmentation will be an important part of translating the classification techniques described (**Fig.s 5.14-16**) into an FCE technique. Stained neutrophils display a blinking phenomenon in the 650 and 370 nm channels. Being of comparable size to the imaging cores of the optical fibre, light from stained neutrophils is transiently obscured by cladding between imaging cores as the lung and fibre move. The cellular blinking phenomenon supports the detection of neutrophils as it is not present prior to stained neutrophil installation. With the application of appropriate image analysis tools, and in less densely populated fields of view, cellular blinking may be sufficient to extract individual cells from video frames for image cytometric analyses. Finally, the EVLV model recapitulates fluid dynamic properties of probe multiplexing that are important for FCE and sequential waves of inflammatory infiltrates can be modelled. Instilling two waves of activated

neutrophils into the same field of view, with NAP and then with VE200, made it possible to identify neutrophils from the primary and secondary installations respectively, by understanding changes in extracellular probe concentration and the antagonistic signal generation mechanisms of these HNE probes.

These findings are limited by the direct instillation of allogenic neutrophils into the alveolar space. The pulmonary remnant of the aorta can be connected to an artificial circulation of whole blood to add perfusion dynamics to the EVLV model and image neutrophil activation detection following extravasation. It was surprising to find that neutrophils were not sufficiently activated by instillation into an allogenic lung to become stained. A low level of neutrophil activation may have occurred and achieved insufficient HNE probe staining to be visible using Versicolour. The narrow and tortuous tracts of the pulmonary vasculature may considerably challenge, if not prevent, activated allogenic neutrophil extravasation. Whether or not this challenge can be overcome, the detection of neutrophils will provide previously inaccessible clarity into disease prognosis as work from Ionita *et al.* has already demonstrated in their study of hundreds of atherosclerotic plaques.[107] As image cytometric and neural network techniques become integrated with FCE, the clinician may be able to read a functionally categorized inflammatory sites, using information compressed from a multidimensional wealth of microscopic inflammatory details, informing her choice of disease management and treatment options.

CHAPTER 6:
SUMMARY AND FUTURE DIRECTIONS

6.1.0 CONCLUSIONS

In chapter one the biomarker potential of neutrophils was described. Short half-lives make for safer imaging paradigms as imaging reagents are rapidly cleared along with stained cells. At the same time, continuous neutrophil influx, makes neutrophil imaging useful over extensive, chronic inflammatory disease time-frames. Rapid response and accumulation are properties that allow labelled neutrophils to describe pathophysiological events quickly, with signal amplification. It can therefore be envisaged that cohorts of neutrophils will arrive at inflammatory sites, take up optical imaging agents and generate images which may be used to rapidly target patients to appropriate treatment groups. In a patient monitoring context, successive cohorts of infiltrating neutrophils may behave differently and the changes between cohorts maybe interpreted to describe treatment responsiveness. In addition to describing heterogeneity between neutrophil cohorts over time, indicating a trajectory, heterogeneity within each neutrophil population can be described at a given timepoint as a range of neutrophil activation states creates a granular picture of the inflammatory response. Optical molecular imaging is an inexpensive, specific and sensitive paradigm whereby the complexity of neutrophil biology can be organized into a versatile patient stratification tool. The work of this thesis concentrates on the development of such a tool.

6.1.1 CHAPTER THREE SUMMARY

In Chapter Three an activable optical imaging probe, Neutrophil Activation Probe (NAP) was characterised *in vitro* with purified HNE and primary human neutrophils. Chapter Three reported:

- 500nM NAP could be detected in a spectrometric system and a 3 µM concentration was useful in sensitive measurements of purified HNE activity without detector saturation.
- NAP signal proved temperature sensitive with maximal fluorescence at 26.1^{o}C
- Physiologically relevant HNE concentrations increase in activity under alkalinisation with predictable, linear dynamics. A 100-fold decrease in proton concentration yields a 4-fold increase in HNE activity.
- NAP fluorescence increases under alkalinisation.
- NAP is highly selective for HNE although at supra-physiological doses other serine proteases, cathepsin G and protease 3 can generate relatively small fractions of NAP signal.
- High NAP selectivity can be expected to be further increased in the phagolysosome where increasing serine protease and alkalinisation both effect greater contributions from HNE to NAP signal than other serine proteases.
- Calcium ionophore stimulation generates a large assay window within which to measure changes in neutrophil activation.

- NAP signal sensitively reports pharmacological modulation of HNE activity following calcium ionophore stimulation.
- Calcium ionophore stimulated primary human neutrophil's generate HNE-specific NAP signals which evolve with rapid kinetics and are stable over a ten minute time course. Subcellular NAP signals are readily quantified via image-analysis.
- LPS/fMLF stimulated primary human neutrophil's generate HNE-specific NAP signals which evolve with rapid kinetics and decay over a ten minute time course. The more subtle subcellular NAP signals induced by physiologically relevant stimuli are still readily quantified via image-analysis.
- NAP signals can be used to detect neutrophil activation in viable ageing neutrophils and in the presence of neutrophil apoptosis and necrosis, whether apoptotic or necrosis precede neutrophil activation or follow it. In mixed populations of viable apoptotic and necrotic neutrophils image analysis and fluorescence thresholding and intracellular distribution patterns may be used to select for cells of specific viability states.

6.1.2. CHAPTER FOUR SUMMARY

In chapter four a lead, HNE-targeted, optical imaging probe was selected from a panel of candidate probes developed in-house. VE200 was characterised *in vitro* with purified HNE and primary human neutrophils before its interaction with NAP was characterised. Finally, multiplexed HNE-imaging was conducted in an image cytometric assay investigating HNE dynamics across the neutrophil lifespan. Chapter four reported:

- GW447631 is a potent HNE inhibitor, which can abrogate NAP signal without appropriate titration.
- GW447631 achieves intracellular HNE inhibition and can reduce neutrophil shape-change upon stimulation.
- VE136 can be used to detect stimulus intensity as neutrophils release HNE with stimulus proportionality.
- VE200 detects neutrophil activation more sensitively than VE135 or VE136 and has improved neutrophil specificity over VE135. VE200 is therefore the lead HNE-targeted probe.
- VE200 displays neutrophil specificity among the leukocytes by virtue of its HNE specificity.
- Displaying biphasic binding kinetics and increased HNE inhibition over time, VE200 is an irreversibly binding HNE-targeted probe.

- Neutrophil activation is detected most sensitively by VE200 at a concentration of 200 nM when intracellular signal is quantified and 500 nM when extracellular signal is included in quantification.
- VE200 stains neutrophils with significantly increased efficiency compared to free Cy5 dye and at 200 nM, VE200 multiplexes 71.1% NAP signal is preserved in a multiplexed imaging assay.
- 3 μM NAP detects neutrophil activation and distinctions between viable, apoptotic and necrotic neutrophil populations more sensitively than 100 nM VE200. However, VE200's altered affinity for activated, viable, apoptotic and necrotic neutrophils adds discriminatory power when multiplexed with NAP.
- Image cytometry reveals that NAP and VE200 signals remain highly correlated in the presence of untreated, activated or necrotic neutrophils but become uncorrelated in the presence of apoptotic neutrophils.

6.1.3 CHAPTER FIVE SUMMARY

In chapter five the richness of imaging datasets generated via NAP and VE200 multiplexed imaging, was processed with the aim of classifying neutrophils by HNE-phenotype. Using image cytometry and the understanding of activation-detection by thresholding, established in chapters three and four, a simple classifier is used to parse overtly activated neutrophils by chemokinetic stimulus. Next a more complex classifier is used to parse all neutrophil imaged by chemokinetic stimulus. Finally, image cytometry is applied to human lung adenocarcinomatous tissue to detect neutrophil activation. And multiplexed HNE-imaging is applied via fibred-confocal endomicroscopy in an *ex vivo,* ventilated lung model. Chapter five reported:

- 63% of HNE activity is available for detection following gentle fixation, although fixation introduces artefactual NAP fluorescence. This enables membranous HNE detection in fixed samples of primary human neutrophils.
- HNE release follows a predictable trend of increase from untreated, primed, activated to primed-activated neutrophils. Imaging these treatment groups affords fluorescence intensity and textural data for the identification of activated neutrophils. By optimising combinations of imaging features neutrophils may be described in different classes, or chemokinetic phenotypes, occupying unique feature-spaces.
- Neural network modelling of multiplexed imaging data can produce specific and sensitive phenotypic classification of neutrophils responding to physiologically relevant stimuli, over time. Neural networks can organise

neutrophil phenotypes into functionally meaningful categories, *a priori*, facilitating the detection of abnormal activation responses.

- Image cytometry can be applied to HNE imaging in fixed human tissues to enable neutrophil multiparametric activation detection.
- HNE and the prognostic indicator GLUT-1 are positively correlated in lung adenocarcinoma.
- Via fibred-confocal microscopy multiplexed NAP and VE200 signals and hence neutrophil activation are detectable *in vitro*.
- Via fibred-confocal microscopy, multiplexed NAP and VE200 signals and hence neutrophil activation are detectable and quantifiable in an *ex vivo* ventilated lung model.
- Sequential NAP and VE200 staining can identify temporally distinct neutrophil populations in an *ex vivo* ventilated lung model.

6.2.1 LIMITATIONS AND FUTURE DIRECTIONS

There are several directions for future research that may prove useful to the fields of molecular imaging agent development, cellular phenotyping for optical molecular imaging and interventional clinical imaging. Although discussed in detail in chapters three to five, some key limitations of the current work warrant further discussion here.

6.2.2 IN VIVO RELEVANCE

The main limitation of the current work is the lack of *in vivo* studies supporting *in vitro* and *ex vivo* findings. Focusing on *in vitro* characterisation was necessary to understand how novel HNE imaging probes would relay information particularly in the destructive environment of the neutrophil's phagolysosome. The constraints of chemical synthesis also played a non-negligible role in the characterisation and development cycles of imaging agents. However, the *ex vivo* ventilated lung model contributes significantly to the argument for the clinical relevance of findings presented in chapter five. There are multiple avenues along which to develop this investigation: 1) instilling HNE imaging agents into animal models of disease for fibred confocal endomicroscopy at pertinent time points either *in vivo* or in inflamed organs of interest *ex* vivo. 2) Perfusing the *ex vivo* ventilated lung with human whole blood and delivering stimuli into the alveolar airspace to stimulate neutrophil extravasation would create a paradigm in which detection of the earliest inflammatory events may be evaluated. 3) Conducting a clinical trial to evaluate HNE imaging probes in diseased patients, wherein disease pathophysiology may impact on the quality of imaging data accessible. Options 2) and 3) may be preferable as the current characterisation has taken place using only human enzymes, primary human cells and tissues. Chapter three highlights the complex, multifactorial nature of probe signal generation *in vitro*, a matter which may be complicated further *in vivo* particular with the consideration of intrinsic tissue autofluorescence. Although autofluorescence can be removed from measurements of neutrophil activation in humans, the autofluorescence of tissues from different

species, and methods for its subtraction from signal, may vary significantly, potentially confounding inferences about probe sensitivity. Unpublished data from the Dhaliwal group shows sheep lungs are far more autofluorescent than human lungs by fibred confocal microscopy.

6.2.3 PHYSICAL LIMITATIONS TO THE CURRENT FIBRED CONFOCAL MICROSCOPY TECHNIQUE

Limited field of view and imaging resolution are limitations of the current fibred confocal endomicroscopy assays. However, both limitations can be resolved with existing technology. Recent technological advances in reflectance fibred microscopy enable multiple frames of a video to be automatically mosaiced creating 100 mm^2 or larger, fields of view without reduction in imaging resolution.[250] The resolution of the current fibred confocal microscopy apparatus can also be readily improved. Currently, graded refractive index lensed fibres achieve subcellular imaging resolutions to drive fibred microscopy into a similarly information-dense regime as benchtop confocal microscopy. With this in mind, the current technique to image and individually parse large numbers of neutrophils may be achieved in clinics in the near-future. This presents several areas of future research for neutrophil HNE-phenotyping. Neutrophils exist in numerous primed and activated states depending on their environment and activating stimuli and, due to the real-time nature of optical molecular imaging, transitory states may also be imaged. With this complexity in mind, it may be useful to investigate the minimum number of

neutrophil phenotypes which are necessary to make a given diagnosis or patient stratification decision and thereby expedite data acquisition and processing.

6.2.4 CONTEXTUALISED NEUTROPHIL QUANTITATION

The neutrophil to lymphocyte ratio (NLR) has been reported to be useful in making patient stratification decisions in across an impressive breadth of disease.[5–7,95–100] NLR seems a versatile means of translating inflammatory information into clinical decisions however, there is an important caveat to the implementation of NLR in a given patient cohort. The precise NLR thresholds dividing high and low risk cohorts are not stationary between patient cohorts and hence reported thresholds may prove unreliable in a new study. Although the number of neutrophils is contextualized by the number of lymphocytes in NLR calculations each neutrophil can exist in numerous states which may combine such two patients with the same NLR reach different outcomes. What may be required is a contextualised NLR which takes into consideration the activation state of specific immune cells, describing the compositions of inflammatory cell populations. The recent neutrophil to platelet ratio may be an attempt to address the limitations of NLR. A combined neutrophil-platelet-lymphocyte ratio may have advantages over NLR but the new ratio also lacks defined methodologies for establishing intra-cohort cut-offs.[251]

Despite their reliance on human operators, histological indices represent algorithms for assessing disease progression. Neutrophilia is quantified in histological indices, such as those used to score ulcerative colitis, but these scoring methods capture

much more information than the number of two or three cell-types. These comprehensive histological indices have been used to robustly compare patient strata for decades and seem a fitting model to learn from to address less-standardized quantitative, prognostic methods. However, histological scores also have their limitations, including the considerable time taken to produce readouts and intra-observer reproducibility.[252] With HNE-phenotyping the number and quality of neutrophils may be acquired in real-time, predicting disease stage and revealing the composition of neutrophil populations in a manner that may enable standardized thresholds to be applied. Other histological data such as autofluorescence or probe multiplexing may afford, may further inform image analysis algorithms to create more robust summaries of pathophysiology. These metrics may make neutrophil quantitation techniques for patient stratification applicable between patient cohorts.

6.2.5 SUMMARY

Neutrophil activation can be detected in an *ex vivo* human lung via fibred confocal endomicroscopy. Neutrophil imaging combined with image analysis and artificial intelligence can describe functionally different categories of neutrophil activation. This classification has exquisite precision, subdividing neutrophil priming and activation phenotypes by bacterial or lipid mediator stimulus. The diverse responses of neutrophils to stimuli may translate into meaningful optical readouts for patient stratification.

6.3.0 APPENDIX

6.3.1 SUBSTRATES OF HNE AND THE EFFECTS OF THEIR CLEAVAGE

Substrate/Effect	**Methods**	**Implication**	**Reference**
HNE	SDS-PAGE / SDS-PAGE, WB, Kinetic analysis	Reduced endogenous and synthetic inhibitor potency	253 / 254
Protease Inhibitors Elafin / SLPI / α1-PI	HPLC, WB / HPLC, WB / SDS-PAGE	Reduced inhibition / suicide inhibition and neutrophil chemoattraction	255 / 256 / 257
Protease Zymogens TIMP-1, pro-MMP-9 / pro-MMP-12	WB, SDS-PAGE / Zymography, reverse zymography	ECM remodelling, α-1-AP inactivation, neutrophil recruitment, impaired epithelial repair	258/259
Extracellular matrix Components Elastin / Decorin /Collagens I, IV and XVII and Laminin / meprin α/ fibronectin	SDS-PAGE / SDS-PAGE,WB / Mass spec., WB, Kinetic analysis / WB, Mass spec. /Fluoregenic substrate, CF BALF zymography / SDS-PAGE	ECM remodelling / neutrophil recruitment	19 / 20 / 25/ 21 / 22 / 23
NF-κB activation → Cathepsin B and MMP-2 upregulation	NE KO mouse model, WB, Zymography, RT-PCR	Pro-inflammatory	260
Antibodies IgG, IgA / IgM, IgM rheumatoid factor	SDS-PAGE / Radio-labelled protein elution	Enhanced degranulation of activated neutrophils	261,262 / 263

CD14	Flow Cytometry, SDS-PAGE, ELISA/ Flow Cytometry, WB	Impaired Monocyte LPS detection and reduced TNFα production / Reduced Fibroblast IL8 production	264 / 265
CD16	Flow cytometry and SDS-PAGE	Loss of antibody FC region sensitivity	266
Adhesion Molecules CD43 (neutrophil and T cell isoforms) and CD62P / ICAM-1	Flow cytometry and SDS-PAGE / Flow cytometry and SDS-PAGE	Partial cleavage – unknown effect on Leukocyte adhesion / Extravasation	266 / 267
TACE	WB, NB	TGF-α and Mucus Production	22,268
TLR2, TLR4, MD2	WB, IF of THP-1 macrophages	Impaired antimicrobial processes	269
Cytokines TNFα, Interleukins: 1β, 2, 3, 4,6, 8, 10, 12p40, 12p70 G-CSF, GM-CSF, IFNα2, IFNγ, MCP-1, MIP-1α, MIP-1β	ELISA with HNE inhibitor control		269
TNF, IL6 and IL8 mRNA transcription KD	Q-PCR of THP-1 macrophages		269
NF-κB nuclear translocation KD	IF of THP-1 macrophages		269
Surfactant Protein D	Fragment analysis by SDS-PAGE and HPLC		166

IL-2R and IL-6R	Flow cytometry and Dot blot/ Flow cytometry and Reverse-Phase HPLC	Impaired T cell adherence and migration	270
IL8 production	ELISA	Pro-inflammatory, neutrophil recruitment	22,260
Intercellular Adhesion Molecules Epithelial Cadherin, JAM-C	Fragment analysis by SDS-PAGE and HPLC	Loss of (pulmonary) epithelium integrity	271
PML-RARα	WB and murine KO	Acute promyelocytic leukaemia pathophysiology	272
Flagellin	WB and SDS-PAGE	Reduced immunogenicity	273
VEGF	SDS-PAGE and Mass-spec. / Migration assays	Altered VEGF receptor signalling, Macrophage and endothelial progenitor cell recruitment	56,274
Thrombin / Anti-thrombin III	SDS-PAGE/ two-dimensional immuno-electrophoresis	Anti- and pro-coagulation effects	275/276
Low density lipoproteins (Apolipoprotein-B and Apolipoprotein-A-II)	SDS-PAGE	Dyslipidaemia, atheromatous plaque formation	277
Vitamin D-binding protein	SDS-PAGE, autoradiography	Loss of C5a chemotaxis promoting effect	278

Phosphatidyl Serine Receptor	Flow Cytometry	Impairing both efferocytosis and TGFβ production	164
Complement component 3bi and Complement Receptor 1		Impaired phagocytosis and superoxide production	279

Table 7.0 Pleiotropic effects of HNE activity demonstrated *in vitro*

HNE – Human Neutrophil Elastase

SLPI – secretory leukocyte protease inhibitor

TACE – Tumour necrosis factor alpha converting enzyme

TNF-α -Tumour necrosis factor alpha

GCSF – Granulocyte colony stimulating factor

GM-CSF- Granulocyte-macrophage colony stimulating factor
VEGF – Vascular endothelial growth factor
TLR- Toll-like Receptor

MMP – Matrix metalloprotease

TIMP – Tissue inhibitor of metalloprotease

IL – Interleukin

IG – immunoglobulin

ICAM-1 intercellular adhesion molecule 1

WB – Western blot

NB – Northern Blot

SDS-PAGE – sodium dodecyl sulphate polyacrylamide gel electrophoresis

KO – Knock-out

KD – Knockdown

6.3.2 STATISTICAL RANKING FOR OBJECTIVE FEATURE SELECTION

HNE Immunofluorescence

NAP Texture and Intensity

	#	Info. gain	Gain ratio	Gini	ANOVA
Intensity_MinIntensityEdge_sumNAP		0.226	0.113	0.050	361.404
Intensity_MinIntensity_sumNAP		0.225	0.113	0.050	359.551
Intensity_LowerQuartileIntensity_sumNAP		0.207	0.104	0.047	370.948
Intensity_MeanIntensityEdge_sumNAP		0.206	0.103	0.047	406.222
Intensity_MedianIntensity_sumNAP		0.198	0.099	0.045	360.238
Intensity_MeanIntensity_sumNAP		0.197	0.098	0.045	367.116
Intensity_MaxIntensityEdge_sumNAP		0.197	0.098	0.043	333.403
Intensity_UpperQuartileIntensity_sumNAP		0.194	0.097	0.043	349.734
Intensity_MaxIntensity_sumNAP		0.182	0.091	0.039	281.007
Intensity_IntegratedIntensityEdge_sumNAP		0.176	0.088	0.037	260.792
Intensity_IntegratedIntensity_sumNAP		0.133	0.067	0.029	189.817
Intensity_StdIntensityEdge_sumNAP		0.121	0.061	0.026	81.038
Intensity_StdIntensity_sumNAP		0.065	0.033	0.014	61.354
Texture_Contrast_sumNAP_3_135		0.057	0.029	0.013	119.977
Texture_DifferenceEntropy_sumNAP_3_135		0.057	0.028	0.013	110.183
Texture_DifferenceVariance_sumNAP_3_135		0.057	0.028	0.013	111.111
Intensity_MADIntensity_sumNAP		0.056	0.028	0.013	56.440
Texture_DifferenceEntropy_sumNAP_3_45		0.056	0.028	0.013	106.496
Texture_Contrast_sumNAP_3_45		0.055	0.028	0.013	118.202
Texture_DifferenceVariance_sumNAP_3_45		0.053	0.027	0.012	110.298
Texture_InverseDifferenceMoment_sumNAP_3_135		0.052	0.026	0.012	91.035
Texture_Correlation_sumNAP_3_135		0.051	0.026	0.010	103.950
Texture_InfoMeas1_sumNAP_3_135		0.049	0.025	0.010	87.710
Texture_Entropy_sumNAP_3_45		0.048	0.024	0.012	61.016
Texture_InverseDifferenceMoment_sumNAP_3_45		0.048	0.024	0.011	87.963
Texture_Entropy_sumNAP_3_135		0.047	0.024	0.012	60.255
Texture_InfoMeas2_sumNAP_3_135		0.045	0.022	0.009	97.616
Texture_AngularSecondMoment_sumNAP_3_45		0.044	0.022	0.011	13.771
Texture_DifferenceEntropy_sumNAP_3_90		0.044	0.022	0.010	83.869
Texture_Correlation_sumNAP_3_45		0.044	0.022	0.009	100.359
Texture_InfoMeas1_sumNAP_3_45		0.044	0.022	0.009	88.510
Texture_AngularSecondMoment_sumNAP_3_135		0.044	0.022	0.011	13.880
Texture_DifferenceVariance_sumNAP_3_90		0.043	0.022	0.009	82.647
Texture_DifferenceVariance_sumNAP_3_0		0.042	0.021	0.009	82.090
Texture_DifferenceEntropy_sumNAP_3_0		0.042	0.021	0.009	80.614
Texture_InfoMeas1_sumNAP_3_0		0.042	0.021	0.009	79.187
Texture_Correlation_sumNAP_3_0		0.042	0.021	0.009	86.757
Texture_Entropy_sumNAP_3_0		0.041	0.021	0.010	51.818
Texture_Contrast_sumNAP_3_0		0.041	0.020	0.009	85.729
Texture_InfoMeas2_sumNAP_3_45		0.041	0.020	0.008	97.341
Texture_Correlation_sumNAP_3_90		0.041	0.020	0.008	83.075
Texture_InverseDifferenceMoment_sumNAP_3_90		0.040	0.020	0.009	74.384
Texture_Entropy_sumNAP_3_90		0.040	0.020	0.010	52.994
Texture_InfoMeas1_sumNAP_3_90		0.040	0.020	0.008	80.305
Texture_InfoMeas2_sumNAP_3_0		0.040	0.020	0.008	87.822
Texture_InverseDifferenceMoment_sumNAP_3_0		0.039	0.019	0.008	68.496
Texture_InfoMeas2_sumNAP_3_90		0.038	0.019	0.008	84.849
Texture_AngularSecondMoment_sumNAP_3_90		0.038	0.019	0.009	12.933
Texture_AngularSecondMoment_sumNAP_3_0		0.037	0.018	0.009	12.544
Texture_SumVariance_sumNAP_3_90		0.036	0.018	0.009	52.278
Texture_Variance_sumNAP_3_90		0.034	0.017	0.008	54.922
Texture_SumVariance_sumNAP_3_0		0.033	0.017	0.008	52.035
Texture_Variance_sumNAP_3_135		0.033	0.017	0.008	56.017
Texture_Variance_sumNAP_3_45		0.032	0.016	0.008	52.155
Texture_SumEntropy_sumNAP_3_90		0.032	0.016	0.008	41.288
Texture_SumVariance_sumNAP_3_135		0.032	0.016	0.007	47.524
Texture_SumVariance_sumNAP_3_45		0.031	0.016	0.007	47.141
Texture_SumEntropy_sumNAP_3_0		0.031	0.015	0.008	42.925
Texture_Variance_sumNAP_3_0		0.030	0.015	0.007	48.722
Texture_SumEntropy_sumNAP_3_135		0.029	0.015	0.007	39.791
Texture_SumAverage_sumNAP_3_0		0.029	0.014	0.007	25.596
Texture_SumAverage_sumNAP_3_90		0.028	0.014	0.007	25.928
Texture_SumEntropy_sumNAP_3_45		0.027	0.013	0.006	39.402
Texture_SumAverage_sumNAP_3_135		0.026	0.013	0.006	22.762
Texture_SumAverage_sumNAP_3_45		0.025	0.012	0.006	22.884
Intensity_MassDisplacement_sumNAP		0.023	0.011	0.005	33.770
Texture_Gabor_sumNAP_3		0.010	0.005	0.002	13.284
Location_MaxIntensity_X_sumNAP		0.004	0.002	0.001	4.842
Location_CenterMassIntensity_X_sumNAP		0.003	0.002	0.001	4.643
Location_CenterMassIntensity_Y_sumNAP		0.002	0.001	0.000	2.284
Location_MaxIntensity_Y_sumNAP		0.002	0.001	0.000	2.290

HNE Immunofluorescence

HNE.ab Texture and Intensity

	#	Info. gain	Gain ratio	Gini	ANOVA
Intensity_MinIntensityEdge_sumHNE		0.168	0.084	0.032	307.865
Intensity_MinIntensity_sumHNE		0.160	0.080	0.030	306.550
Intensity_LowerQuartileIntensity_sumHNE		0.098	0.049	0.022	81.244
Intensity_MedianIntensity_sumHNE		0.085	0.043	0.019	47.178
Intensity_MeanIntensityEdge_sumHNE		0.081	0.041	0.017	107.234
Intensity_MeanIntensity_sumHNE		0.076	0.038	0.016	57.380
Intensity_MaxIntensity_sumHNE		0.075	0.037	0.019	140.039
Intensity_StdIntensity_sumHNE		0.071	0.036	0.018	111.116
Intensity_IntegratedIntensityEdge_sumHNE		0.070	0.035	0.015	139.330
Intensity_UpperQuartileIntensity_sumHNE		0.067	0.033	0.015	47.283
Intensity_StdIntensityEdge_sumHNE		0.066	0.033	0.016	119.599
Intensity_MaxIntensityEdge_sumHNE		0.060	0.030	0.014	119.087
Intensity_IntegratedIntensity_sumHNE		0.052	0.026	0.011	79.934
Texture_SumAverage_sumHNE_3_45		0.048	0.024	0.011	80.871
Texture_SumAverage_sumHNE_3_0		0.047	0.024	0.011	81.256
Texture_SumAverage_sumHNE_3_90		0.047	0.024	0.011	81.148
Texture_SumAverage_sumHNE_3_135		0.046	0.023	0.011	81.566
Texture_AngularSecondMoment_sumHNE_3_0		0.045	0.023	0.010	90.105
Texture_InverseDifferenceMoment_sumHNE_3_0		0.045	0.023	0.011	87.155
Texture_AngularSecondMoment_sumHNE_3_45		0.045	0.022	0.010	87.802
Texture_AngularSecondMoment_sumHNE_3_135		0.044	0.022	0.010	87.882
Texture_AngularSecondMoment_sumHNE_3_90		0.044	0.022	0.010	89.699
Texture_InverseDifferenceMoment_sumHNE_3_90		0.044	0.022	0.010	86.170
Texture_InverseDifferenceMoment_sumHNE_3_135		0.043	0.021	0.010	86.818
Intensity_MADIntensity_sumHNE		0.043	0.021	0.009	69.821
Texture_Entropy_sumHNE_3_0		0.042	0.021	0.010	87.701
Texture_Entropy_sumHNE_3_135		0.042	0.021	0.010	87.694
Texture_SumEntropy_sumHNE_3_0		0.041	0.021	0.010	87.729
Texture_InverseDifferenceMoment_sumHNE_3_45		0.041	0.020	0.009	83.265
Texture_Entropy_sumHNE_3_90		0.041	0.020	0.010	87.583
Texture_SumEntropy_sumHNE_3_135		0.041	0.020	0.009	85.959
Texture_Entropy_sumHNE_3_45		0.041	0.020	0.009	86.703
Texture_SumEntropy_sumHNE_3_45		0.040	0.020	0.009	85.768
Texture_SumEntropy_sumHNE_3_90		0.040	0.020	0.009	86.996
Intensity_MassDisplacement_sumHNE		0.033	0.016	0.008	27.690
Texture_DifferenceEntropy_sumHNE_3_90		0.032	0.016	0.007	68.056
Texture_DifferenceEntropy_sumHNE_3_0		0.032	0.016	0.007	67.852
Texture_DifferenceEntropy_sumHNE_3_45		0.032	0.016	0.007	68.169
Texture_DifferenceEntropy_sumHNE_3_135		0.031	0.015	0.007	69.507
Texture_Gabor_sumHNE_3		0.028	0.014	0.007	62.853
Texture_SumVariance_sumHNE_3_90		0.028	0.014	0.007	45.418
Texture_SumVariance_sumHNE_3_135		0.028	0.014	0.006	44.596
Texture_SumVariance_sumHNE_3_0		0.027	0.014	0.006	46.084
Texture_SumVariance_sumHNE_3_45		0.027	0.013	0.006	44.869
Texture_Variance_sumHNE_3_0		0.027	0.013	0.006	49.576
Texture_Variance_sumHNE_3_90		0.026	0.013	0.006	48.769
Texture_Variance_sumHNE_3_135		0.024	0.012	0.006	46.334
Texture_Variance_sumHNE_3_45		0.024	0.012	0.005	48.718
Texture_Correlation_sumHNE_3_135		0.022	0.011	0.005	33.144
Texture_Correlation_sumHNE_3_0		0.020	0.010	0.005	34.552
Texture_InfoMeas2_sumHNE_3_135		0.020	0.010	0.005	35.676
Texture_Contrast_sumHNE_3_135		0.020	0.010	0.004	39.925
Texture_InfoMeas2_sumHNE_3_90		0.020	0.010	0.005	34.703
Texture_Contrast_sumHNE_3_45		0.019	0.010	0.004	37.268
Texture_Correlation_sumHNE_3_90		0.019	0.009	0.005	33.840
Texture_Contrast_sumHNE_3_0		0.019	0.009	0.004	32.147
Texture_Correlation_sumHNE_3_45		0.018	0.009	0.004	34.723
Texture_InfoMeas2_sumHNE_3_0		0.018	0.009	0.004	34.309
Texture_InfoMeas2_sumHNE_3_45		0.018	0.009	0.004	35.095
Texture_Contrast_sumHNE_3_90		0.017	0.009	0.004	32.070
Texture_InfoMeas1_sumHNE_3_45		0.011	0.005	0.002	8.343
Texture_DifferenceVariance_sumHNE_3_0		0.010	0.005	0.002	17.223
Texture_DifferenceVariance_sumHNE_3_90		0.010	0.005	0.002	18.650
Texture_DifferenceVariance_sumHNE_3_135		0.010	0.005	0.002	20.078
Texture_DifferenceVariance_sumHNE_3_45		0.010	0.005	0.002	20.474
Texture_InfoMeas1_sumHNE_3_135		0.010	0.005	0.002	8.233
Texture_InfoMeas1_sumHNE_3_90		0.010	0.005	0.002	4.161
Texture_InfoMeas1_sumHNE_3_0		0.009	0.005	0.002	3.541
Location_CenterMassIntensity_X_sumHNE		0.003	0.002	0.001	4.649
Location_MaxIntensity_X_sumHNE		0.003	0.002	0.001	4.581
Location_CenterMassIntensity_Y_sumHNE		0.002	0.001	0.000	2.278
Location_MaxIntensity_Y_sumHNE		0.002	0.001	0.000	2.531

Multiplexed VE200 and NAP Time-lapsed imaging

NAP Intensities

	#	Info. gain	Gain ratio	Gini	ANOVA
Intensity_MaxIntensity_sumNAP		0.541	0.270	0.121	1460.475
Intensity_MaxIntensityEdge_sumNAP		0.540	0.270	0.121	1457.647
Intensity_MinIntensity_sumNAP		0.539	0.269	0.118	1363.899
Intensity_MedianIntensity_sumNAP		0.539	0.269	0.121	1415.895
Intensity_UpperQuartileIntensity_sumNAP		0.538	0.269	0.122	1429.734
Intensity_MeanIntensity_sumNAP		0.538	0.269	0.121	1417.943
Intensity_LowerQuartileIntensity_sumNAP		0.536	0.268	0.120	1402.074
Intensity_MinIntensityEdge_sumNAP		0.534	0.267	0.117	1372.602
Intensity_MeanIntensityEdge_sumNAP		0.528	0.264	0.118	1413.386
Intensity_IntegratedIntensityEdge_sumNAP		0.318	0.159	0.084	384.507
Intensity_IntegratedIntensity_sumNAP		0.232	0.116	0.059	217.086
Intensity_StdIntensity_sumNAP		0.222	0.111	0.059	428.157
Intensity_MADIntensity_sumNAP		0.199	0.099	0.054	343.150
Intensity_StdIntensityEdge_sumNAP		0.198	0.099	0.052	395.970
Intensity_MassDisplacement_sumNAP		0.028	0.014	0.007	60.638

NAP Textures

	#	Info. gain	Gain ratio	Gini	ANOVA
Texture_SumAverage_sumNAP_3_0		0.070	0.035	0.017	152.639
Texture_SumAverage_sumNAP_3_90		0.068	0.034	0.017	153.841
Texture_SumAverage_sumNAP_3_135		0.067	0.033	0.017	148.730
Texture_SumAverage_sumNAP_3_45		0.065	0.033	0.016	149.645
Texture_Gabor_sumNAP_3		0.060	0.030	0.014	90.002
Texture_SumVariance_sumNAP_3_90		0.045	0.022	0.011	101.776
Texture_SumVariance_sumNAP_3_135		0.044	0.022	0.011	97.969
Texture_SumVariance_sumNAP_3_0		0.042	0.021	0.011	96.847
Texture_SumVariance_sumNAP_3_45		0.042	0.021	0.011	94.448
Texture_InfoMeas2_sumNAP_3_90		0.039	0.020	0.010	89.088
Texture_InfoMeas1_sumNAP_3_90		0.039	0.020	0.009	85.607
Texture_SumEntropy_sumNAP_3_45		0.039	0.019	0.010	75.835
Texture_InfoMeas2_sumNAP_3_0		0.038	0.019	0.009	79.269
Texture_SumEntropy_sumNAP_3_0		0.037	0.019	0.010	74.356
Texture_SumEntropy_sumNAP_3_90		0.037	0.018	0.009	74.585
Texture_Variance_sumNAP_3_90		0.037	0.018	0.009	86.918
Texture_SumEntropy_sumNAP_3_135		0.037	0.018	0.009	76.433
Texture_Variance_sumNAP_3_45		0.036	0.018	0.009	80.824
Texture_Variance_sumNAP_3_0		0.036	0.018	0.009	82.106
Texture_InfoMeas1_sumNAP_3_0		0.035	0.017	0.009	75.659
Texture_Variance_sumNAP_3_135		0.034	0.017	0.009	82.507
Texture_Correlation_sumNAP_3_90		0.033	0.016	0.008	57.606
Texture_InfoMeas2_sumNAP_3_135		0.032	0.016	0.008	64.161
Texture_InfoMeas2_sumNAP_3_45		0.029	0.015	0.007	64.344
Texture_Correlation_sumNAP_3_0		0.029	0.014	0.007	51.215
Texture_InfoMeas1_sumNAP_3_135		0.028	0.014	0.007	57.279
Texture_InfoMeas1_sumNAP_3_45		0.027	0.014	0.007	52.203
Texture_InverseDifferenceMoment_sumNAP_3_90		0.022	0.011	0.005	37.963
Texture_Correlation_sumNAP_3_135		0.018	0.009	0.004	31.849
Texture_Correlation_sumNAP_3_45		0.018	0.009	0.004	31.440
Texture_Contrast_sumNAP_3_90		0.015	0.007	0.004	14.622
Texture_InverseDifferenceMoment_sumNAP_3_0		0.014	0.007	0.003	25.324
Texture_Entropy_sumNAP_3_45		0.014	0.007	0.004	22.780
Texture_Entropy_sumNAP_3_135		0.013	0.007	0.004	21.858
Texture_InverseDifferenceMoment_sumNAP_3_135		0.013	0.006	0.003	19.136
Texture_DifferenceEntropy_sumNAP_3_90		0.012	0.006	0.003	17.301
Texture_Entropy_sumNAP_3_90		0.011	0.005	0.003	14.326
Texture_Entropy_sumNAP_3_0		0.010	0.005	0.003	15.133
Texture_AngularSecondMoment_sumNAP_3_45		0.009	0.005	0.002	11.060
Texture_AngularSecondMoment_sumNAP_3_135		0.009	0.005	0.002	9.790
Texture_DifferenceVariance_sumNAP_3_90		0.009	0.005	0.003	7.790
Texture_Contrast_sumNAP_3_0		0.009	0.005	0.002	7.653
Texture_InverseDifferenceMoment_sumNAP_3_45		0.009	0.004	0.002	13.566
Texture_DifferenceEntropy_sumNAP_3_0		0.008	0.004	0.002	10.864
Texture_DifferenceVariance_sumNAP_3_0		0.007	0.004	0.002	7.291
Texture_AngularSecondMoment_sumNAP_3_0		0.007	0.003	0.002	7.141
Texture_DifferenceVariance_sumNAP_3_135		0.006	0.003	0.002	2.145
Texture_AngularSecondMoment_sumNAP_3_90		0.006	0.003	0.002	6.488
Texture_Contrast_sumNAP_3_45		0.005	0.002	0.001	2.961
Texture_Contrast_sumNAP_3_135		0.004	0.002	0.001	2.414
Texture_DifferenceVariance_sumNAP_3_45		0.004	0.002	0.001	4.516
Texture_DifferenceEntropy_sumNAP_3_45		0.004	0.002	0.001	2.027
Texture_DifferenceEntropy_sumNAP_3_135		0.003	0.002	0.001	1.225

Multiplexed VE200 and NAP Time-lapsed imaging

VE200 Intensities

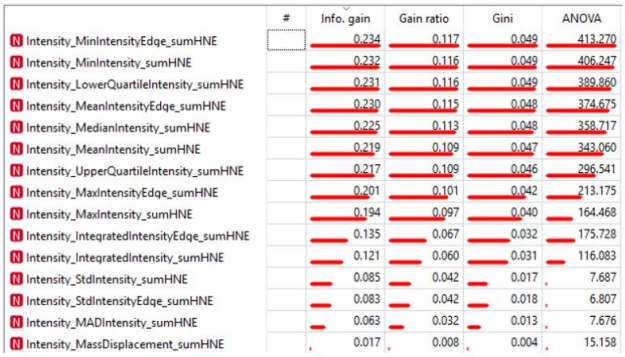

	#	Info. gain	Gain ratio	Gini	ANOVA
Intensity_MinIntensityEdge_sumHNE		0.234	0.117	0.049	413.270
Intensity_MinIntensity_sumHNE		0.232	0.116	0.049	406.247
Intensity_LowerQuartileIntensity_sumHNE		0.231	0.116	0.049	389.860
Intensity_MeanIntensityEdge_sumHNE		0.230	0.115	0.048	374.675
Intensity_MedianIntensity_sumHNE		0.225	0.113	0.048	358.717
Intensity_MeanIntensity_sumHNE		0.219	0.109	0.047	343.060
Intensity_UpperQuartileIntensity_sumHNE		0.217	0.109	0.046	296.541
Intensity_MaxIntensityEdge_sumHNE		0.201	0.101	0.042	213.175
Intensity_MaxIntensity_sumHNE		0.194	0.097	0.040	164.468
Intensity_IntegratedIntensityEdge_sumHNE		0.135	0.067	0.032	175.728
Intensity_IntegratedIntensity_sumHNE		0.121	0.060	0.031	116.083
Intensity_StdIntensity_sumHNE		0.085	0.042	0.017	7.687
Intensity_StdIntensityEdge_sumHNE		0.083	0.042	0.018	6.807
Intensity_MADIntensity_sumHNE		0.063	0.032	0.013	7.676
Intensity_MassDisplacement_sumHNE		0.017	0.008	0.004	15.158

VE200 Textures

	#	Info. gain	Gain ratio	Gini	ANOVA
Texture_SumAverage_sumHNE_3_0		0.061	0.030	0.017	97.253
Texture_SumAverage_sumHNE_3_90		0.060	0.030	0.017	98.152
Texture_SumAverage_sumHNE_3_135		0.059	0.029	0.016	93.317
Texture_SumAverage_sumHNE_3_45		0.059	0.029	0.016	93.839
Texture_AngularSecondMoment_sumHNE_3_0		0.030	0.015	0.009	20.216
Texture_AngularSecondMoment_sumHNE_3_135		0.029	0.015	0.008	17.718
Texture_AngularSecondMoment_sumHNE_3_90		0.028	0.014	0.008	20.154
Texture_AngularSecondMoment_sumHNE_3_45		0.026	0.013	0.008	18.005
Texture_InverseDifferenceMoment_sumHNE_3_0		0.026	0.013	0.006	24.841
Texture_Entropy_sumHNE_3_135		0.025	0.013	0.007	24.543
Texture_Gabor_sumHNE_3		0.025	0.012	0.006	19.144
Texture_Entropy_sumHNE_3_90		0.024	0.012	0.007	32.263
Texture_Entropy_sumHNE_3_0		0.024	0.012	0.007	31.758
Texture_InverseDifferenceMoment_sumHNE_3_90		0.024	0.012	0.006	20.067
Texture_Entropy_sumHNE_3_45		0.023	0.011	0.007	26.057
Texture_InverseDifferenceMoment_sumHNE_3_45		0.021	0.011	0.005	13.498
Texture_Contrast_sumHNE_3_0		0.021	0.011	0.005	15.465
Texture_SumEntropy_sumHNE_3_135		0.021	0.011	0.006	27.450
Texture_DifferenceEntropy_sumHNE_3_0		0.020	0.010	0.005	19.948
Texture_Variance_sumHNE_3_90		0.020	0.010	0.006	3.067
Texture_SumEntropy_sumHNE_3_45		0.019	0.010	0.006	29.212
Texture_Contrast_sumHNE_3_90		0.019	0.010	0.004	11.633
Texture_SumEntropy_sumHNE_3_90		0.019	0.009	0.005	26.457
Texture_DifferenceEntropy_sumHNE_3_135		0.018	0.009	0.004	14.846
Texture_DifferenceVariance_sumHNE_3_135		0.018	0.009	0.005	23.680
Texture_Contrast_sumHNE_3_45		0.018	0.009	0.005	13.729
Texture_DifferenceEntropy_sumHNE_3_90		0.018	0.009	0.004	14.044
Texture_InverseDifferenceMoment_sumHNE_3_135		0.018	0.009	0.004	16.465
Texture_Contrast_sumHNE_3_135		0.017	0.009	0.004	14.326
Texture_SumEntropy_sumHNE_3_0		0.017	0.008	0.005	23.120
Texture_DifferenceEntropy_sumHNE_3_45		0.016	0.008	0.004	12.379
Texture_DifferenceVariance_sumHNE_3_45		0.016	0.008	0.004	23.355
Texture_Variance_sumHNE_3_45		0.016	0.008	0.005	4.011
Texture_Variance_sumHNE_3_135		0.016	0.008	0.004	3.033
Texture_Variance_sumHNE_3_0		0.016	0.008	0.005	5.693
Texture_DifferenceVariance_sumHNE_3_0		0.015	0.008	0.003	13.452
Texture_DifferenceVariance_sumHNE_3_90		0.015	0.007	0.003	11.555
Texture_SumVariance_sumHNE_3_135		0.015	0.007	0.004	5.004
Texture_Correlation_sumHNE_3_135		0.014	0.007	0.003	20.752
Texture_SumVariance_sumHNE_3_45		0.014	0.007	0.004	4.700
Texture_SumVariance_sumHNE_3_0		0.013	0.006	0.004	3.028
Texture_Correlation_sumHNE_3_45		0.013	0.006	0.003	18.678
Texture_SumVariance_sumHNE_3_90		0.012	0.006	0.003	4.149
Texture_Correlation_sumHNE_3_0		0.012	0.006	0.002	13.805
Texture_Correlation_sumHNE_3_90		0.011	0.006	0.002	12.496
Texture_InfoMeas2_sumHNE_3_135		0.010	0.005	0.002	11.221
Texture_InfoMeas1_sumHNE_3_0		0.010	0.005	0.002	10.007
Texture_InfoMeas2_sumHNE_3_0		0.009	0.004	0.002	12.044
Texture_InfoMeas1_sumHNE_3_135		0.008	0.004	0.002	6.542
Texture_InfoMeas2_sumHNE_3_90		0.008	0.004	0.002	10.429
Texture_InfoMeas1_sumHNE_3_90		0.007	0.004	0.002	8.193
Texture_InfoMeas2_sumHNE_3_45		0.006	0.003	0.001	9.063
Texture_InfoMeas1_sumHNE_3_45		0.006	0.003	0.001	4.510

Multiplexed VE200 and NAP Time-lapsed imaging

DAPI Intensities

	#	Info. gain	Gain ratio	Gini	ANOVA
Intensity_MinIntensity_sumDAPI		0.321	0.161	0.064	256.379
Intensity_MinIntensityEdge_sumDAPI		0.321	0.161	0.064	256.081
Intensity_LowerQuartileIntensity_sumDAPI		0.314	0.157	0.068	265.779
Intensity_MedianIntensity_sumDAPI		0.295	0.148	0.075	316.890
Intensity_MeanIntensityEdge_sumDAPI		0.246	0.123	0.056	151.018
Intensity_MeanIntensity_sumDAPI		0.246	0.123	0.061	189.959
Intensity_UpperQuartileIntensity_sumDAPI		0.243	0.122	0.063	168.523
Intensity_MADIntensity_sumDAPI		0.210	0.105	0.050	289.536
Intensity_IntegratedIntensity_sumDAPI		0.180	0.090	0.055	63.278
Intensity_StdIntensity_sumDAPI		0.175	0.087	0.048	115.293
Intensity_MaxIntensityEdge_sumDAPI		0.166	0.083	0.043	29.979
Intensity_MaxIntensity_sumDAPI		0.155	0.078	0.047	124.623
Intensity_IntegratedIntensityEdge_sumDAPI		0.145	0.072	0.044	46.813
Intensity_MassDisplacement_sumDAPI		0.115	0.058	0.029	182.719
Intensity_StdIntensityEdge_sumDAPI		0.109	0.054	0.031	18.390

DAPI Textures

	#	Info. gain	Gain ratio	Gini	ANOVA
Texture_AngularSecondMoment_sumDAPI_3_90		0.154	0.077	0.035	219.073
Texture_AngularSecondMoment_sumDAPI_3_0		0.152	0.076	0.035	219.808
Texture_SumEntropy_sumDAPI_3_135		0.137	0.068	0.031	243.211
Texture_SumEntropy_sumDAPI_3_45		0.131	0.065	0.029	239.360
Texture_SumEntropy_sumDAPI_3_0		0.124	0.062	0.029	251.116
Texture_SumEntropy_sumDAPI_3_90		0.124	0.062	0.029	250.803
Texture_AngularSecondMoment_sumDAPI_3_45		0.118	0.059	0.026	206.996
Texture_AngularSecondMoment_sumDAPI_3_135		0.118	0.059	0.026	208.072
Texture_SumAverage_sumDAPI_3_0		0.118	0.059	0.031	150.292
Texture_Correlation_sumDAPI_3_90		0.118	0.059	0.031	71.501
Texture_SumAverage_sumDAPI_3_90		0.117	0.058	0.031	150.169
Texture_Correlation_sumDAPI_3_0		0.111	0.055	0.029	69.114
Texture_Entropy_sumDAPI_3_90		0.110	0.055	0.024	195.966
Texture_InfoMeas1_sumDAPI_3_0		0.110	0.055	0.028	93.732
Texture_InfoMeas1_sumDAPI_3_90		0.107	0.053	0.027	94.520
Texture_SumAverage_sumDAPI_3_45		0.105	0.052	0.027	157.860
Texture_Entropy_sumDAPI_3_0		0.104	0.052	0.023	195.973
Texture_SumAverage_sumDAPI_3_135		0.104	0.052	0.027	157.972
Texture_InverseDifferenceMoment_sumDAPI_3_90		0.101	0.050	0.023	151.587
Texture_SumVariance_sumDAPI_3_90		0.097	0.048	0.028	41.154
Texture_SumVariance_sumDAPI_3_0		0.096	0.048	0.028	40.244
Texture_InverseDifferenceMoment_sumDAPI_3_0		0.096	0.048	0.022	149.881
Texture_Entropy_sumDAPI_3_135		0.088	0.044	0.019	203.355
Texture_Correlation_sumDAPI_3_135		0.087	0.043	0.021	57.940
Texture_Entropy_sumDAPI_3_45		0.086	0.043	0.018	201.093
Texture_SumVariance_sumDAPI_3_45		0.086	0.043	0.025	30.662
Texture_SumVariance_sumDAPI_3_135		0.085	0.042	0.024	30.216
Texture_Correlation_sumDAPI_3_45		0.081	0.041	0.020	60.227
Texture_InverseDifferenceMoment_sumDAPI_3_135		0.075	0.037	0.016	176.894
Texture_Variance_sumDAPI_3_0		0.075	0.037	0.022	43.248
Texture_InverseDifferenceMoment_sumDAPI_3_45		0.073	0.036	0.015	171.170
Texture_Variance_sumDAPI_3_90		0.072	0.036	0.021	42.405
Texture_Gabor_sumDAPI_3		0.070	0.035	0.021	97.305
Texture_Variance_sumDAPI_3_45		0.068	0.034	0.020	37.843
Texture_Variance_sumDAPI_3_135		0.065	0.033	0.019	37.667
Texture_InfoMeas1_sumDAPI_3_135		0.065	0.032	0.015	95.701
Texture_InfoMeas1_sumDAPI_3_45		0.062	0.031	0.014	91.326
Texture_InfoMeas2_sumDAPI_3_0		0.061	0.030	0.016	55.355
Texture_InfoMeas2_sumDAPI_3_90		0.060	0.030	0.016	55.852
Texture_DifferenceEntropy_sumDAPI_3_135		0.059	0.029	0.014	130.457
Texture_DifferenceEntropy_sumDAPI_3_90		0.053	0.027	0.012	122.080
Texture_DifferenceEntropy_sumDAPI_3_90		0.053	0.027	0.012	122.080
Texture_DifferenceEntropy_sumDAPI_3_45		0.052	0.026	0.012	128.989
Texture_DifferenceEntropy_sumDAPI_3_0		0.049	0.025	0.011	121.300
Texture_Contrast_sumDAPI_3_135		0.043	0.021	0.010	72.075
Texture_Contrast_sumDAPI_3_90		0.041	0.021	0.009	59.847
Texture_InfoMeas2_sumDAPI_3_135		0.040	0.020	0.009	37.195
Texture_Contrast_sumDAPI_3_0		0.039	0.020	0.009	56.739
Texture_InfoMeas2_sumDAPI_3_45		0.038	0.019	0.009	35.968
Texture_Contrast_sumDAPI_3_45		0.036	0.018	0.008	68.621
Texture_DifferenceVariance_sumDAPI_3_135		0.023	0.012	0.007	38.267
Texture_DifferenceVariance_sumDAPI_3_45		0.023	0.012	0.006	42.711
Texture_DifferenceVariance_sumDAPI_3_90		0.018	0.009	0.004	43.979
Texture_DifferenceVariance_sumDAPI_3_0		0.015	0.008	0.004	39.507

Multiplexed VE200 and NAP Time-lapsed imaging

CellMask™ Orange Intensities

	#	Info. gain	Gain ratio	Gini	ANOVA
Intensity_UpperQuartileIntensity_sumCellMask		0.270	0.135	0.070	737.910
Intensity_MedianIntensity_sumCellMask		0.260	0.130	0.065	801.389
Intensity_IntegratedIntensityEdge_sumCellMask		0.258	0.129	0.066	508.735
Intensity_LowerQuartileIntensity_sumCellMask		0.256	0.128	0.063	860.873
Intensity_MeanIntensity_sumCellMask		0.252	0.126	0.063	765.882
Intensity_MinIntensity_sumCellMask		0.248	0.124	0.057	654.025
Intensity_MinIntensityEdge_sumCellMask		0.246	0.123	0.057	646.202
Intensity_MeanIntensityEdge_sumCellMask		0.215	0.108	0.055	799.112
Intensity_IntegratedIntensity_sumCellMask		0.209	0.104	0.057	376.933
Intensity_MaxIntensity_sumCellMask		0.180	0.090	0.053	253.595
Intensity_MaxIntensityEdge_sumCellMask		0.176	0.088	0.050	374.708
Intensity_MADIntensity_sumCellMask		0.175	0.087	0.052	321.097
Intensity_StdIntensityEdge_sumCellMask		0.144	0.072	0.043	349.693
Intensity_StdIntensity_sumCellMask		0.135	0.067	0.040	215.393
Intensity_MassDisplacement_sumCellMask		0.052	0.026	0.011	127.577

CellMask™ Orange Textures

	#	Info. gain	Gain ratio	Gini	ANOVA
Texture_SumAverage_sumCellMask_3_90		0.067	0.033	0.017	140.206
Texture_SumAverage_sumCellMask_3_0		0.066	0.033	0.016	139.862
Texture_InfoMeas1_sumCellMask_3_0		0.065	0.032	0.016	150.145
Texture_SumAverage_sumCellMask_3_135		0.064	0.032	0.016	135.287
Texture_SumAverage_sumCellMask_3_45		0.064	0.032	0.016	133.934
Texture_InfoMeas1_sumCellMask_3_90		0.063	0.032	0.015	147.555
Texture_AngularSecondMoment_sumCellMask_3_0		0.063	0.031	0.016	96.955
Texture_AngularSecondMoment_sumCellMask_3_90		0.061	0.030	0.015	98.201
Texture_InverseDifferenceMoment_sumCellMask_3_0		0.058	0.029	0.014	66.510
Texture_Entropy_sumCellMask_3_0		0.057	0.029	0.014	59.431
Texture_InverseDifferenceMoment_sumCellMask_3_90		0.057	0.028	0.014	65.667
Texture_Entropy_sumCellMask_3_90		0.057	0.028	0.014	60.776
Texture_AngularSecondMoment_sumCellMask_3_135		0.056	0.028	0.014	97.432
Texture_InverseDifferenceMoment_sumCellMask_3_45		0.056	0.028	0.014	55.256
Texture_AngularSecondMoment_sumCellMask_3_45		0.055	0.028	0.014	97.204
Texture_SumEntropy_sumCellMask_3_0		0.054	0.027	0.014	51.456
Texture_SumEntropy_sumCellMask_3_90		0.052	0.026	0.014	54.366
Texture_InfoMeas1_sumCellMask_3_45		0.051	0.026	0.012	129.121
Texture_InverseDifferenceMoment_sumCellMask_3_135		0.050	0.025	0.012	57.787
Texture_Entropy_sumCellMask_3_135		0.049	0.025	0.013	53.813
Texture_Entropy_sumCellMask_3_45		0.049	0.024	0.013	53.117
Texture_InfoMeas1_sumCellMask_3_135		0.048	0.024	0.011	123.088
Texture_InfoMeas2_sumCellMask_3_0		0.046	0.023	0.010	99.026
Texture_InfoMeas2_sumCellMask_3_90		0.042	0.021	0.009	96.688
Texture_SumEntropy_sumCellMask_3_135		0.041	0.021	0.011	45.120
Texture_Correlation_sumCellMask_3_0		0.041	0.020	0.009	87.902
Texture_Correlation_sumCellMask_3_45		0.039	0.020	0.009	80.845
Texture_InfoMeas2_sumCellMask_3_45		0.039	0.020	0.009	92.552
Texture_SumEntropy_sumCellMask_3_45		0.039	0.019	0.010	45.343
Texture_Correlation_sumCellMask_3_90		0.039	0.019	0.008	89.090
Texture_InfoMeas2_sumCellMask_3_135		0.039	0.019	0.009	85.730
Texture_Correlation_sumCellMask_3_135		0.036	0.018	0.008	78.016
Texture_DifferenceEntropy_sumCellMask_3_0		0.036	0.018	0.009	44.538
Texture_DifferenceEntropy_sumCellMask_3_90		0.035	0.017	0.009	42.140
Texture_DifferenceEntropy_sumCellMask_3_45		0.032	0.016	0.009	29.398
Texture_DifferenceEntropy_sumCellMask_3_135		0.029	0.015	0.008	31.281
Texture_Contrast_sumCellMask_3_0		0.026	0.013	0.007	34.893
Texture_Contrast_sumCellMask_3_90		0.026	0.013	0.007	37.632
Texture_Gabor_sumCellMask_3		0.025	0.012	0.007	34.354
Texture_Contrast_sumCellMask_3_45		0.024	0.012	0.006	22.529
Texture_Variance_sumCellMask_3_45		0.024	0.012	0.007	11.010
Texture_Variance_sumCellMask_3_90		0.023	0.012	0.007	10.999
Texture_SumVariance_sumCellMask_3_90		0.022	0.011	0.006	21.988
Texture_Contrast_sumCellMask_3_135		0.022	0.011	0.006	26.351
Texture_Variance_sumCellMask_3_0		0.022	0.011	0.007	12.638
Texture_SumVariance_sumCellMask_3_0		0.022	0.011	0.006	21.772
Texture_Variance_sumCellMask_3_135		0.021	0.010	0.006	9.265
Texture_SumVariance_sumCellMask_3_135		0.019	0.009	0.005	26.137
Texture_SumVariance_sumCellMask_3_45		0.018	0.009	0.005	25.892
Texture_DifferenceVariance_sumCellMask_3_45		0.014	0.007	0.004	18.492
Texture_DifferenceVariance_sumCellMask_3_90		0.014	0.007	0.004	23.283
Texture_DifferenceVariance_sumCellMask_3_0		0.013	0.007	0.004	19.248
Texture_DifferenceVariance_sumCellMask_3_135		0.012	0.006	0.004	19.369

6.3.3 BIBLIOGRAPHY

1. Guthrie, L. A. Priming of neutrophils for enhanced release of oxygen metabolites by bacterial lipopolysaccharide. Evidence for increased activity of the superoxide-producing enzyme. *J. Exp. Med.* **160**, 1656–1671 (1984).

2. Brinkmann, V. *et al.* Neutrophil Extracellular Traps Kill Bacteria. *Science (80-.).* **303**, 1532–1535 (2004).

3. Lee, T. H. "Me-too" products—friend or foe? *N. Engl. J. Med.* **350**, 211–212 (2004).

4. Ionita, M. G. *et al.* High neutrophil numbers in human carotid atherosclerotic plaques are associated with characteristics of rupture-prone lesions. *Arterioscler. Thromb. Vasc. Biol.* **30**, 1842–1848 (2010).

5. Bowen, R. C. *et al.* Neutrophil-to-lymphocyte ratio as prognostic indicator in gastrointestinal cancers: a systematic review and meta-analysis. *Oncotarget* **8**, 32171–32189 (2017).

6. Templeton, A. J. *et al.* Prognostic role of neutrophil-to-lymphocyte ratio in solid tumors: A systematic review and meta-analysis. *J. Natl. Cancer Inst.* **106**, (2014).

7. Zhao, C. *et al.* Validation and optimization of the Systemic Inflammation-Based modified Glasgow Prognostic Score in predicting postoperative outcome of inflammatory bowel disease: Preliminary data. *Sci. Rep.* **8**, 1–8 (2018).

8. de Jager, C. P. C. *et al.* Lymphocytopenia and neutrophil-lymphocyte count ratio predict bacteremia better than conventional infection markers in an emergency care unit. *Crit. Care* **14**, R192 (2010).

9. Yilmaz, H., Cakmak, M., Inan, O., Darcin, T. & Akcay, A. Can neutrophil-lymphocyte ratio be independent risk factor for predicting acute kidney injury in patients with severe sepsis? *Ren. Fail.* **37**, 225–229 (2015).

10. Mauer, A., Athens, J., Ashenbrucker, H., Cartwright, G. & Wintrobe, M. Leukokinetic Studies. II. A Method for Labelling Granulocytes in vitro with Radioactive Diisopropylfluorophosphate (DFP). **39**, 1481–1486 (1960).

11. Athens, J. W. *et al.* Leukokinetic studies. III. The distribution of granulocytes in the blood of normal subjects. **40**, 159–164 (1960).

12. Marshall, B. T. *et al.* Direct observation of catch bonds involving cell-adhesion molecules. *Nature* **423**, 190–193 (2003).

13. Sundd, P. *et al.* Slings enable neutrophil rolling at high shear. *Nature* **488**, 399–403 (2012).

14. Sundd, P. *et al.* Quantitative dynamic footprinting microscopy reveals mechanisms of neutrophil rolling. *Nat. Methods* **7**, 821–824 (2010).

15. Wang, S., Dangerfield, J. P., Young, R. E. & Nourshargh, S. PECAM-1, α6 integrins and neutrophil elastase cooperate in mediating neutrophil transmigration. *J. Cell Sci.* **118**, 2067–2076 (2005).

16. Yang, L. *et al.* ICAM-1 regulates neutrophil adhesion and transcellular migration of TNF-α-activated vascular endothelium under flow. *Blood* **106**, 584–592 (2005).

17. Cepinskas, G., Sandig, M. & Kvietys, P. R. PAF-induced elastase-dependent neutrophil transendothelial migration is associated with the mobilization of elastase to the neutrophil surface and localization to the migrating front. **1945**, 1937–1945 (1999).

18. Colom, B. *et al.* Leukotriene B4-Neutrophil Elastase Axis Drives Neutrophil Reverse Transendothelial Cell Migration InVivo. *Immunity* **42**, 1075–1086 (2015).

19. Tyagi, S. C. & Simon, S. R. Regulation of neutrophil elastase activity by elastin-derived peptide. *J. Biol. Chem.* **268**, 16513–16518 (1993).

20. Li, Y. *et al.* Solar ultraviolet irradiation induces decorin degradation in human skin likely via neutrophil elastase. *PLoS One* **8**, e72563 (2013).

21. Arecco, N. *et al.* Elastase levels and activity are increased in dystrophic muscle and impair myoblast cell survival, proliferation and differentiation. *Sci. Rep.* **6**, 24708 (2016).

22. Bergin, D. A. *et al.* Activation of the epidermal growth factor receptor (EGFR) by a novel metalloprotease pathway. *J. Biol. Chem.* **283**, 31736–44 (2008).

23. McDonald, J. A. & Kelley, D. G. Degradation of fibronectin by human leukocyte elastase. Release of biologically active fragments. *J. Biol. Chem.* **255**, 8848–8858 (1980).

24. Steadman, R. *et al.* Laminin cleavage by activated human neutrophils yields proteolytic fragments with selective migratory properties. *J. Leukoc. Biol.* **53**, 354–365 (1993).

25. Lin, L. *et al.* Neutrophil elastase cleaves the murine hemidesmosomal protein BP180/type XVII collagen and generates degradation products that modulate experimental bullous pemphigoid. *Matrix Biol.* **31**, 38–44 (2012).

26. Gresham, H. D. *et al.* Domain-specific interactions between entactin and neutrophil integrins: G2 domain ligation of integrin α3β1 and E domain ligation of the leukocyte response integrin signal for different responses. *J. Biol. Chem.* **271**, 30587–30594 (1996).

27. Clark, R. A., Wikner, N. E., Doherty, D. E. & Norris, D. A. Cryptic chemotactic activity of fibronectin for human monocytes resides in the 120-kDa fibroblastic cell-binding fragment. *J. Biol. Chem.* **263**, 12115–12123 (1988).

28. Adair-Kirk, T. L. & Senior, R. M. Fragments of extracellular matrix as mediators of inflammation. *Int. J. Biochem. Cell Biol.* **40**, 1101–1110 (2008).

29. Gong, L. *et al.* Promoting effect of neutrophils on lung tumorigenesis is mediated by CXCR2 and neutrophil elastase. *Mol. Cancer* **12**, 1–14 (2013).

30. Liu, X. *et al.* Bidirectional regulation of neutrophil migration by mitogen-activated protein kinases. *Nat. Immunol.* **13**, 457–464 (2012).

31. Boneschansker, L., Jorgensen, J., Ellett, F., Briscoe, D. M. & Irimia, D. Convergent and Divergent Migratory Patterns of Human Neutrophils inside Microfluidic Mazes. *Sci. Rep.* **8**, 1887 (2018).

32. Lämmermann, T. *et al.* Neutrophil swarms require LTB4 and integrins at sites of cell death in vivo. *Nature* **498**, 371 (2013).

33. Chou, R. C. *et al.* Lipid-Cytokine-Chemokine Cascade Drives Neutrophil Recruitment in a Murine Model of Inflammatory Arthritis. *Immunity* **33**, 266–278 (2010).

34. Andréasson, E., Önnheim, K. & Forsman, H. The subcellular localization of the receptor for platelet-activating factor in neutrophils affects signaling and activation characteristics. *Clin. Dev. Immunol.* **2013**, 456407 (2013).

35. Dancey, J. T., Deubelbeiss, K. A., Harker, L. A. & Finch, Clemen. A. Neutrophil kinetics in man. *J. Clin. Invest.* **58**, 705–715 (1976).

36. Dresch, C., Najean, Y. & Beauchet, J. In vitro 51Cr and 32P-DFP labeling of granulocytes in man. *J. Nucl. Med.* **12**, 774–784 (1971).

37. Pillay, J. *et al.* In vivo labeling with 2H2O reveals a human neutrophil lifespan of 5.4 days. *Blood* **116**, 625–627 (2010).

38. Kolaczkowska, E. & Kubes, P. Neutrophil recruitment and function in health and inflammation. *Nat. Rev. Immunol.* **13**, 159 (2013).

39. Haslett, C., Guthrie, L. A., Kopaniak, M. M., Johnston, R. B. & Henson, P. M. Modulation of multiple neutrophil functions by preparative methods or trace concentrations of bacterial lipopolysaccharide. *Am. J. Pathol.* **119**, 101–10 (1985).

40. Tak, T., Tesselaar, K., Pillay, J., Borghans, J. A. M. & Koenderman, L. What's your age again? Determination of human neutrophil half-lives revisited. *J. Leukoc. Biol.* **94**, 595–601 (2013).

41. Colotta, F., Re, F., Polentarutti, N., Sozzani, S. & Mantovani, A. Modulation of granulocyte survival and programmed cell death by cytokines and bacterial products. *Blood* **80**, 2012–2020 (1992).

42. Futosi, K., Fodor, S. & Mócsai, A. Neutrophil cell surface receptors and their intracellular signal transduction pathways. *Int. Immunopharmacol.* **17**, 638–650 (2013).

43. Berger, M. *et al.* Neutrophils express distinct RNA receptors in a non-canonical way. *J. Biol. Chem.* **287**, 19409–19417 (2012).

44. Ekman, A.-K. & Cardell, L. O. The expression and function of Nod-like receptors in neutrophils. *Immunology* **130**, 55–63 (2010).

45. Huang, C. & Niethammer, P. Tissue Damage Signaling Is a Prerequisite for Protective Neutrophil Recruitment to Microbial Infection in Zebrafish. *Immunity* (2018). doi:10.1016/j.immuni.2018.04.020

46. McDonald, B. *et al.* Intravascular Danger Signals Guide Neutrophils to Sites of Sterile Inflammation. *Science (80-.).* **330**, 362 LP – 366 (2010).

47. Wang, T. *et al.* Plasma neutrophil elastase and elafin as prognostic biomarker for acute respiratory distress syndrome: a multicenter survival and longitudinal prospective observation study. *Shock Inj. Inflammation, Sepsis Lab. Clin. Approaches* **48**, 168–174 (2017).

48. Auner, B. *et al.* Circulating leukotriene B4 identifies respiratory complications after trauma. *Mediators Inflamm.* **2012**, (2012).

49. Rabquer, B. J. *et al.* Junctional Adhesion Molecule-C Is a Soluble Mediator of Angiogenesis. *J. Immunol.* **185**, 1777 LP – 1785 (2010).

50. Manetti, M. *et al.* Differential expression of junctional adhesion molecules in different stages of systemic sclerosis. *Arthritis Rheum.* **65**, 247–257 (2013).

51. Kohri, K., Ueki, I. F., Nadel, J. A. Y. A., Ueki, I. F. & Nadel, J. A. Neutrophil elastase induces mucin production by ligand- dependent epidermal growth factor receptor activation. **0130**, 531–540 (2002).

52. Shao, M. X. G. & Nadel, J. A. Neutrophil Elastase Induces MUC5AC Mucin Production in Human Airway Epithelial Cells via a Cascade Involving Protein Kinase C, Reactive Oxygen Species, and TNF- -Converting Enzyme. *J. Immunol.* **175**, 4009–4016 (2005).

53. Caffery, B. *et al.* MUC1 expression in Sjogren's syndrome, KCS, and control subjects. *Mol. Vis.* **16**, 1720–1727 (2010).

54. Mun, C. *et al.* A Phase I/II Placebo-Controlled Randomized Pilot Clinical Trial of Recombinant Deoxyribonuclease (DNase) Eye Drops Use in Patients With Dry Eye Disease. *Transl. Vis. Sci. Technol.* **8**, 10 (2019).

55. Leclercq, A. *et al.* Involvement of intraplaque hemorrhage in atherothrombosis evolution via neutrophil protease enrichment Abstract : The pathological remodeling of the ar- terial wall

in atherosclerosis involves protease ac- independent predictor of recurrent ischemic event. *J. Leukoc. Biol.* **82**, 1420–1429 (2007).

56. Kurtagic, E., Rich, C. B., Buczek-Thomas, J. A. & Nugent, M. A. Neutrophil Elastase-Generated Fragment of Vascular Endothelial Growth Factor-A Stimulates Macrophage and Endothelial Progenitor Cell Migration. *PLoS One* **10**, e0145115 (2015).

57. Coffelt, S. B., Wellenstein, M. D. & De Visser, K. E. Neutrophils in cancer: Neutral no more. *Nat. Rev. Cancer* **16**, 431–446 (2016).

58. Yamashita, J., Tashiro, K., Yoneda, S., Kawahara, K. & Shirakusa, T. Local Increase in Polymorphonuclear Leukocyte Elastase Is Associated With Tumor Invasiveness in Non-small Cell Lung Cancer. *Chest* **109**, 1328–1334 (1996).

59. Houghton, A. M. *et al.* Neutrophil Elastase-Mediated Degradation of IRS-1 Accelerates Lung Tumor Growth. **16**, 219–223 (2010).

60. Lamb, F. S. *et al.* Endotoxin Priming of Neutrophils Requires Endocytosis and NADPH Oxidase-dependent Endosomal Reactive Oxygen. **287**, 12395–12404 (2012).

61. Levine, A. P., Duchen, M. R., de Villiers, S., Rich, P. R. & Segal, A. W. Alkalinity of Neutrophil Phagocytic Vacuoles Is Modulated by HVCN1 and Has Consequences for Myeloperoxidase Activity. *PLoS One* **10**, e0125906 (2015).

62. Reeves, E. P. *et al.* Killing activity of neutrophils is mediated through activation of proteases by K+ flux. *Nature* **416**, 291–297 (2002).

63. Wang, X., Qin, W., Zhang, Y., Zhang, H. & Sun, B. Endotoxin promotes neutrophil hierarchical chemotaxis via the p38-membrane receptor pathway. *Oncotarget* **7**, 74247–74258 (2016).

64. Papayannopoulos, V., Metzler, K. D., Hakkim, A. & Zychlinsky, A. Neutrophil elastase and myeloperoxidase regulate the formation of neutrophil extracellular traps. *J. Cell Biol.* **191**, 677–691 (2010).

65. Fuchs, T. a *et al.* Novel cell death program leads to neutrophil extracellular traps. *J. Cell Biol.* **176**, 231–41 (2007).

66. Gupta, A. K. *et al.* Activated endothelial cells induce neutrophil extracellular traps and are susceptible to NETosis-mediated cell death. *FEBS Lett.* **584**, 3193–3197 (2010).

67. Pilsczek, F. H. *et al.* A Novel Mechanism of Rapid Nuclear Neutrophil Extracellular Trap Formation in Response to Staphylococcus aureus. *J. Immunol.* **185**, 7413 LP – 7425 (2010).

68. Yipp, B. G. & Kubes, P. NETosis : how vital is it ? **122**, 2784–2795 (2019).

69. M. Minsky. Memoir on Inventing the Confocal Scanning Microscope. *Scanning* **10**, 128–138 (1987).

70. Carter, M. & Shieh, J. *Guide to Research Techniques in Neuroscience*. (Academic Press, Elsevier, 2015).

71. Lenderink, E., Lucassen, G. W., van Kemenade, P. M., Steenwinkel, M.-J. S. T. & Vink, A. A. In vivo measurements of epidermal thickness with optical coherence tomography and confocal laser scanning microscopy: a comparison of methods. in *Coherence Domain Optical Methods in Biomedical Science and Clinical Applications VI* **4619**, 194–201 (International Society for Optics and Photonics, 2002).

72. Gigan, S. Optical microscopy aims deep. *Nat. Photonics* **11**, 14 (2017).

73. Hein, B., Willig, K. I. & Hell, S. W. Stimulated emission depletion (STED) nanoscopy of a fluorescent protein-labeled organelle inside a living cell. *Proc. Natl. Acad. Sci.* **105**, 14271–

14276 (2008).

74. Stuker, F., Ripoll, J. & Rudin, M. Fluorescence molecular tomography: principles and potential for pharmaceutical research. *Pharmaceutics* **3**, 229–274 (2011).

75. Ntziachristos, V., Tung, C.-H., Bremer, C. & Weissleder, R. Fluorescence molecular tomography resolves protease activity in vivo. *Nat. Med.* **8**, 757–761 (2002).

76. Cotte, Y. *et al.* Marker-free phase nanoscopy. *Nat. Photonics* **7**, 113 (2013).

77. Dorward, D. A. *et al.* Technical advance: autofluorescence-based sorting: rapid and nonperturbing isolation of ultrapure neutrophils to determine cytokine production. *J. Leukoc. Biol.* **94**, 193–202 (2013).

78. Schaafsma, B. E. *et al.* The clinical use of indocyanine green as a near-infrared fluorescent contrast agent for image-guided oncologic surgery. *J. Surg. Oncol.* **104**, 323–332 (2011).

79. Alander, J. T. *et al.* A review of indocyanine green fluorescent imaging in surgery. *J. Biomed. Imaging* **2012**, 7 (2012).

80. Kossodo, S. *et al.* Noninvasive In Vivo Quantification of Neutrophil Elastase Activity in Acute Experimental Mouse Lung Injury. *Int. J. Mol. Imaging* **2011**, 11 pages (2011).

81. Craven, T. H. *et al.* Super-silent FRET Sensor Enables Live Cell Imaging and Flow Cytometric Stratification of Intracellular Serine Protease Activity in Neutrophils. *Sci. Rep.* **8**, 1–10 (2018).

82. Panizzi, P. *et al.* Oxazine conjugated nanoparticle detects in vivo hypochlorous acid and peroxynitrite generation. *J. Am. Chem. Soc.* **131**, 15739–15744 (2009).

83. Mendive-Tapia, L. *et al.* Spacer-free BODIPY fluorogens in antimicrobial peptides for direct imaging of fungal infection in human tissue. *Nat. Commun.* **7**, 10940 (2016).

84. Sun, Y. *et al.* Intraoperative visualization of the tumor microenvironment and quantification of extracellular vesicles by label-free nonlinear imaging. *Sci Adv* **4**, eaau5603 (2018).

85. Harz, M. *et al.* Analysis of single blood cells for CSF diagnostics via a combination of fluorescence staining and micro-Raman spectroscopy. *Analyst* **133**, 1416–1423 (2008).

86. Zhang, R. R. *et al.* Beyond the margins: real-time detection of cancer using targeted fluorophores. *Nat. Rev. Clin. Oncol.* **14**, 347–364 (2017).

87. Yserbyt, J., Dooms, C., Janssens, W. & Verleden, G. M. Endoscopic advanced imaging of the respiratory tract: exploring probe-based confocal laser endomicroscopy in emphysema. *Thorax* **73**, 188–190 (2018).

88. Fuchs, F. S. *et al.* Confocal laser endomicroscopy for diagnosing lung cancer in vivo. *Eur. Respir. J.* **41**, 1401–1408 (2013).

89. Krstajić, N. *et al.* Two-color widefield fluorescence microendoscopy enables multiplexed molecular imaging in the alveolar space of human lung tissue. *J. Biomed. Opt.* **21**, 46009 (2016).

90. East, J. E. *et al.* Advanced endoscopic imaging: European Society of Gastrointestinal Endoscopy (ESGE) Technology Review. *Endoscopy* **48**, 1029–1045 (2016).

91. Ducourthial, G. *et al.* Development of a real-time flexible multiphoton microendoscope for label-free imaging in a live animal. *Sci. Rep.* **5**, 1–9 (2015).

92. Koch, M., Symvoulidis, P. & Ntziachristos, V. Tackling standardization in fluorescence molecular imaging. *Nat. Photonics* **12**, 505–515 (2018).

93. Staderini, M., Megia-Fernandez, A., Dhaliwal, K. & Bradley, M. Peptides for optical medical imaging and steps towards therapy. *Bioorg. Med. Chem.* **26**, 2816–2826 (2018).

94. Garland, M., Yim, J. J. & Bogyo, M. A Bright Future for Precision Medicine: Advances in Fluorescent Chemical Probe Design and Their Clinical Application. *Cell Chem. Biol.* **23**, 122–136 (2016).

95. de Jager, C. P. C. *et al.* Lymphocytopenia and neutrophil-lymphocyte count ratio predict bacteremia better than conventional infection markers in an emergency care unit. *Crit. Care* **14**, R192 (2010).

96. Yilmaz, H., Cakmak, M., Inan, O., Darcin, T. & Akcay, A. Can neutrophil-lymphocyte ratio be independent risk factor for predicting acute kidney injury in patients with severe sepsis? *Ren. Fail.* **37**, 225–229 (2015).

97. Angkananard, T., Anothaisintawee, T. & Thakkinstian, A. Neutrophil lymphocyte ratio and risks of cardiovascular diseases: A systematic review and meta-analysis. *Atherosclerosis* **263**, e159–e160 (2017).

98. Xu, T. *et al.* The relationship between neutrophil-to-lymphocyte ratio and diabetic peripheral neuropathy in Type 2 diabetes mellitus. *Med. (United States)* **96**, e8289 (2017).

99. F, T., H, Y. & T, X. Predictive Value of Neutrophil to Lymphocyte Ratio in Patients With Acute Exacerbation of Chronic Obstructive Pulmonary Disease. *PLoS One* **13**, e0204377 (2018).

100. Dundar, Z. D. *et al.* Neutrophil-Lymphocyte Ratio in Patients with Pesticide Poisoning. *J. Emerg. Med.* **47**, 286–293 (2014).

101. Birch, G. P., Campbell, T., Bradley, M. & Dhaliwal, K. Optical Molecular Imaging of Inflammatory Cells in Interventional Medicine–An Emerging Strategy . *Frontiers in Oncology* **9**, 882 (2019).

102. Bressenot, A. *et al.* Comparing histological activity indexes in UC. *Gut* **64**, 1412–1418 (2015).

103. Zhao, C. *et al.* Validation and optimization of the Systemic Inflammation-Based modified Glasgow Prognostic Score in predicting postoperative outcome of inflammatory bowel disease: preliminary data. *Sci. Rep.* **8**, 747 (2018).

104. Li, S., Cao, W., Han, J., Tang, B. & Sun, X. The diagnostic value of white blood cell, neutrophil, neutrophil-to-lymphocyte ratio, and lymphocyte-to-monocyte ratio in patients with primary angle closure glaucoma. *Oncotarget* **8**, 68984–68995 (2017).

105. Xu, T. *et al.* The relationship between neutrophil-to-lymphocyte ratio and diabetic peripheral neuropathy in Type 2 diabetes mellitus. *Med. (United States)* **96**, (2017).

106. Biller, J. & Thies, W. When to Operate in Carotid Artery Disease. *Am. Fam. Physician* **61**, 400–406 (2000).

107. Ionita, M. G. *et al.* High neutrophil numbers in human carotid atherosclerotic plaques are associated with characteristics of rupture-prone lesions. *Arterioscler. Thromb. Vasc. Biol.* **30**, 1842–1848 (2010).

108. Bian, F. *et al.* Desiccating Stress-Induced MMP Production and Activity Worsens Wound Healing in Alkali-Burned Corneas. *Investig. Opthalmology Vis. Sci.* **56**, 4908–4919 (2015).

109. Tibrewal, S. *et al.* Hyperosmolar stress induces neutrophil extracellular trap formation: Implications for dry eye disease. *Investig. Ophthalmol. Vis. Sci.* **55**, 7961–7969 (2014).

110. Hong, J. *et al.* In vivo confocal microscopy of conjunctival goblet cells in patients with Sjögren's syndrome dry eye. *Br. J. Ophthalmol.* **94**, 1454–1458 (2010).

111. Yoo, D. *et al.* Release of Cystic Fibrosis Airway Inflammatory Markers from Pseudomonas aeruginosa –Stimulated Human Neutrophils Involves NADPH Oxidase-Dependent Extracellular DNA Trap Formation . *J. Immunol.* **192**, 4728–4738 (2014).

112. Berisha, F., Feke, G. T., Trempe, C. L., McMeel, J. W. & Schepens, C. L. Retinal abnormalities in early Alzheimer's disease. *Investig. Ophthalmol. Vis. Sci.* **48**, 2285–2289 (2007).

113. Ramirez, A. I. *et al.* The role of microglia in retinal neurodegeneration: Alzheimer's disease, Parkinson, and glaucoma. *Front. Aging Neurosci.* **9**, 1–21 (2017).

114. Bazan, N. G. Neuroprotectin D1-mediated anti-inflammatory and survival signaling in stroke, retinal degenerations, and Alzheimer's disease. *J. Lipid Res.* **50**, S400–S405 (2009).

115. Langhorst, J., Boone, J., Lauche, R., Rueffer, A. & Dobos, G. Faecal Lactoferrin, Calprotectin, PMN-elastase, CRP, and White Blood Cell Count as Indicators for Mucosal Healing and Clinical Course of Disease in Patients with Mild to Moderate Ulcerative Colitis: Post Hoc Analysis of a Prospective Clinical Trial. *J Crohns Colitis* **10**, 786–794 (2016).

116. Kok, K. *et al.* Human neutrophil elastase degrades the therapeutic monoclonal antibodies effective in IBD. *J. Crohn's Colitis* **12**, S146 (2018).

117. Xu, Y. *et al.* Curcumin inhibits tumor proliferation induced by neutrophil elastase through the upregulation of α1-antitrypsin in lung cancer. *Mol. Oncol.* **6**, 405–417 (2012).

118. Bekes, E. M. *et al.* Tumor-recruited neutrophils and neutrophil TIMP-free MMP-9 regulate coordinately the levels of tumor angiogenesis and efficiency of malignant cell intravasation. *Am. J. Pathol.* **179**, 1455–1470 (2011).

119. Wu, L., Saxena, S., Awaji, M. & Singh, R. K. Tumor-associated neutrophils in cancer: Going pro. *Cancers (Basel).* **11**, (2019).

120. Kossodo, S. *et al.* Noninvasive in vivo quantification of neutrophil elastase activity in acute experimental mouse lung injury. *Int. J. Mol. Imaging* **2011**, 581406 (2011).

121. Craven, T. *et al.* In-situ imaging of neutrophil activation in the human alveolar space with neutrophil activation probe and pulmonary optical endomicroscopy. *Lancet* **387**, **Suppl**, S31- (2016).

122. Zhou, J. *et al.* Real-time detection of implant-associated neutrophil responses using a formyl peptide receptor-targeting NIR nanoprobe. *Int. J. Nanomedicine* **7**, 2057–2068 (2012).

123. Pellico, J. *et al.* In vivo imaging of lung inflammation with neutrophil-specific 68Ga nano-radiotracer. *Sci. Rep.* **7**, 1–10 (2017).

124. Ramoji, A. *et al.* Toward a spectroscopic hemogram: Raman spectroscopic differentiation of the two most abundant leukocytes from peripheral blood. *Anal. Chem.* **84**, 5335–5342 (2012).

125. Zeng, Y. *et al.* Label-free in vivo imaging of human leukocytes using two-photon excited endogenous fluorescence. *J. Biomed. Opt.* **18**, 40504 (2013).

126. Korkmaz, B. *et al.* Design and use of highly specific substrates of neutrophil elastase and proteinase 3. *Am. J. Respir. Cell Mol. Biol.* **30**, 801–807 (2004).

127. Kasperkiewicz, P. *et al.* Design of ultrasensitive probes for human neutrophil elastase through hybrid combinatorial substrate library profiling. *Proc. Natl. Acad. Sci.* **111**, 2518 (2014).

128. Luisetti, M. *et al.* Studies of MR 889, a new synthetic proteinase inhibitor. *Biochem. Biophys. Res. Commun.* **165**, 568–573 (1989).

129. Macdonald, S. J. F. *et al.* The discovery of a potent, intracellular, orally bioavailable, long duration inhibitor of human neutrophil elastase—GW311616A a development candidate. *Bioorg. Med. Chem. Lett.* **11**, 895–898 (2001).

130. Macdonald, S. J. F. *et al.* Discovery of further pyrrolidine trans-lactams as inhibitors of human neutrophil elastase (HNE) with potential as development candidates and the crystal structure of HNE complexed with an inhibitor (GW475151). *J. Med. Chem.* **45**, 3878–3890 (2002).

131. Mehta, J. L. *et al.* Neutrophil elastase inhibitor ICI 200,880 protects against attenuation of coronary flow reserve and myocardial dysfunction following temporary coronary artery occlusion in the dog. *Cardiovasc. Res.* **28**, 947–956 (1994).

132. Korkmaz, B. *et al.* Discriminating between the activities of human neutrophil elastase and proteinase 3 using serpin-derived fluorogenic substrates. *J. Biol. Chem.* **277**, 39074–39081 (2002).

133. Locke, L. W. *et al.* A Novel Neutrophil-Specific PET Imaging Agent: cFLFLFK-PEG-64Cu. *J. Nucl. Med.* **50**, 790–797 (2009).

134. Yang, X. *et al.* Targeting formyl peptide receptor 1 of activated macrophages to monitor inflammation of experimental osteoarthritis in rat. *J. Orthop. Res.* **34**, 1529–1538 (2016).

135. Xiao, L. *et al.* A novel near-infrared fluorescence imaging probe for in vivo neutrophil tracking. *Mol Imaging* **11**, 372–382 (2012).

136. Xiao, L. *et al.* Synthesis of the Cyanine 7 labeled neutrophil-specific agents for noninvasive near infrared fluorescence imaging. *Bioorganic Med. Chem. Lett.* **20**, 3515–3517 (2010).

137. Hatice, K., Campbell, E. J. & Kuhn III, C. Elastase and Cathepsin and G of Human Subcellular Granules Monocytes : to Heterogeneity. *J. Histochem. Cytochem.* (1990).

138. Puppels, G. J. *et al.* Studying single living cells and chromosomes by confocal Raman microspectroscopy. *Nature* **347**, 301–303 (1990).

139. Puppels, G. J., Garritsen, H. S., Segers-Nolten, G. M., de Mul, F. F. & Greve, J. Raman microspectroscopic approach to the study of human granulocytes. *Biophys. J.* **60**, 1046–1056 (1991).

140. Otto, C., Sijtsema, N. M. & Greve, J. Confocal Raman microspectroscopy of the activation of single neutrophilic granulocytes. *Eur. Biophys. J.* **27**, 582–589 (1998).

141. van Manen, H. J., van Bruggen, R., Roos, D. & Otto, C. Single-cell optical imaging of the phagocyte NADPH oxidase. *Antioxidants Redox Signal.* **8**, 1509–1522 (2006).

142. Llewellyn, M. E., Barretto, R. P. J., Delp, S. L. & Schnitzer, M. J. Minimally invasive high-speed imaging of sarcomere contractile dynamics in mice and humans. *Nature* **454**, 784 (2008).

143. Williams, R. M. *et al.* Strategies for High Resolution Imaging of Epithelial Ovarian Cancer by Laparoscopic Nonlinear Microscopy. *Transl. Oncol.* **3**, 181–194 (2010).

144. Brown, C. M. *et al. In vivo* imaging of unstained tissues using a compact and flexible multiphoton microendoscope. **17**, 4 (2012).

145. Avlonitis, N. *et al.* Highly specific, multi-branched fluorescent reporters for analysis of human neutrophil elastase. *Org. Biomol. Chem.* **11**, 4414–4418 (2013).

146. Robinson, P. J. Differential stimulation of protein kinase C activity by phorbol ester or calcium/phosphatidylserine in vitro and in intact synaptosomes. *J. Biol. Chem.* **267**, 21637–21644 (1992).

147. Berridge, M. J. Inositol trisphosphate and diacylglycerol as second messengers. *Biochem. J.*

220, 345 (1984).

148. Majumdar, S., Rossi, M., Fujiki, T. & Phillips, W. Protein kinase C isotypes and signaling in neutrophils. Differential substrate specificities of a translocatable calcium-and phospholipid-dependent beta-protein kinase. *J. Biol. Chem.* **266**, 9285–9294 (1991).

149. Igumenova, T. I. Dynamics and Membrane Interactions of Protein Kinase C. *Biochemistry* **54**, 4953–4968 (2015).

150. Pinton, P., Giorgi, C., Siviero, R., Zecchini, E. & Rizzuto, R. Calcium and apoptosis: ER-mitochondria Ca 2+ transfer in the control of apoptosis. *Oncogene* **27**, 6407 (2008).

151. Huang, Y. & Putney, J. W. Relationship between intracellular calcium store depletion and calcium release-activated calcium current in a mast cell line (RBL-1). *J. Biol. Chem.* **273**, 19554–19559 (1998).

152. Dahlgren, C. & Karlsson, A. Ionomycin-induced neutrophil NADPH oxidase activity is selectively inhibited by the serine protease inhibitor diisopropyl fluorophosphate. *Antioxidants Redox Signal.* **4**, 17–25 (2002).

153. Gupta, A. K., Giaglis, S., Hasler, P. & Hahn, S. Efficient neutrophil extracellular trap induction requires mobilization of both intracellular and extracellular calcium pools and is modulated by cyclosporine A. *PLoS One* **9**, e97088 (2014).

154. Gray, R. D. *et al.* Activation of conventional protein kinase C (PKC) is critical in the generation of human neutrophil extracellular traps. *J. Inflamm. (Lond).* **10**, 12 (2013).

155. Radic, M. & Neeli, I. Opposition between PKC isoforms regulates histone deimination and neutrophil extracellular chromatin release . *Frontiers in Immunology* **4**, 38 (2013).

156. Luckasen, J. R., White, J. G. & Kersey, J. H. Mitogenic Properties of a Calcium Ionophore, A23187. *Proc. Natl. Acad. Sci.* **71**, 5088 LP – 5090 (1974).

157. Babcock, D. F., First, N. L. & Lardy, H. A. Action of ionophore A23187 at the cellular level. Separation of effects at the plasma and mitochondrial membranes. *J. Biol. Chem.* **251**, 3881–3886 (1976).

158. Kao, J. P. Y., Li, G. & Auston, D. A. Practical aspects of measuring intracellular calcium signals with fluorescent indicators. in *Methods in cell biology* **99**, 113–152 (Elsevier, 2010).

159. Serhan, C. N., Korchak, H. M. & Weissmann, G. PGBX, a prostagandin derivative, mimics the action of the calcium ionophore A23187 on human neutrophils. *J. Immunol.* **125**, 2020–2024 (1980).

160. Korkmaz, B., Attucci, S., Jourdan, M.-L., Juliano, L. & Gauthier, F. Inhibition of Neutrophil Elastase by 1-Protease Inhibitor at the Surface of Human Polymorphonuclear Neutrophils. *J. Immunol.* **175**, 3329–3338 (2005).

161. Witko-Sarsat, V. *et al.* Presence of Proteinase 3 in Secretory Vesicles: Evidence of a Novel, Highly Mobilizable Intracellular Pool Distinct From Azurophil Granules: Presented in part at the 17th European Workshop on the Cell Biology of Phagocytes, Catania, Italy, May 1998. *Blood* **94**, 2487–2496 (1999).

162. Kantari, C. *et al.* Proteinase 3, the Wegener autoantigen, is externalized during neutrophil apoptosis: evidence for a functional association with phospholipid scramblase 1 and interference with macrophage phagocytosis. *Blood* **110**, 4086–4095 (2007).

163. Martin, K. R. *et al.* Proteinase 3 is a phosphatidylserine-binding protein that affects the production and function of microvesicles. *J. Biol. Chem.* **291**, 10476–10489 (2016).

164. Vandivier, R. W. *et al.* Elastase-mediated phosphatidylserine receptor cleavage impairs apoptotic cell clearance in cystic fibrosis and bronchiectasis. *J. Clin. Invest.* **109**, 661–670 (2002).

165. Henriksen, P. A., Devitt, A., Kotelevtsev, Y. & Sallenave, J. M. Gene delivery of the elastase inhibitor elafin protects macrophages from neutrophil elastase-mediated impairment of apoptotic cell recognition. *FEBS Lett.* **574**, 80–84 (2004).

166. Hirche, T. O. *et al.* Neutrophil Elastase Mediates Innate Host Protection against Pseudomonas aeruginosa. *J. Immunol.* **181**, 4945–4954 (2008).

167. Yang, R. *et al.* Neutrophil elastase enhances the proliferation and decreases apoptosis of leukemia cells via activation of PI3K/Akt signaling. *Mol. Med. Rep.* **13**, 4175–4182 (2016).

168. Oltmanns, U., Sukkar, M. B., Xie, S., John, M. & Chung, K. F. Induction of human airway smooth muscle apoptosis by neutrophils and neutrophil elastase. *Am. J. Respir. Cell Mol. Biol.* **32**, 334–341 (2005).

169. Hou, H.-H. *et al.* PlGF mediates neutrophil elastase-induced airway epithelial cell apoptosis and emphysema. *Respir. Res.* **15**, 106 (2014).

170. Grechowa, I., Horke, S., Wallrath, A., Vahl, C.-F. & Dorweiler, B. Human neutrophil elastase induces endothelial cell apoptosis by activating the PERK-CHOP branch of the unfolded protein response. *FASEB J.* **31**, 3868–3881 (2017).

171. Baumann, M., Pham, C. T. N. & Benarafa, C. SerpinB1 is critical for neutrophil survival through cell-autonomous inhibition of cathepsin G. *Blood* **121**, 3900–3907 (2013).

172. Rafiq, K., Hanscom, M., Valerie, K., Steinberg, S. F. & Sabri, A. Novel Mode for Neutrophil Protease Cathepsin G–Mediated Signaling: Membrane Shedding of Epidermal Growth Factor Is Required for Cardiomyocyte Anoikis. *Circ. Res.* **102**, 32–41 (2008).

173. Gramegna, A. *et al.* Neutrophil elastase in bronchiectasis. *Respir. Res.* **18**, 211 (2017).

174. King, A. E., Critchley, H. O. D., Sallenave, J.-M. & Kelly, R. W. Elafin in human endometrium: an antiprotease and antimicrobial molecule expressed during menstruation. *J. Clin. Endocrinol. Metab.* **88**, 4426–4431 (2003).

175. Klimenkova, O. *et al.* A lack of secretory leukocyte protease inhibitor (SLPI) causes defects in granulocytic differentiation. *Blood* **123**, 1239–1249 (2014).

176. Aikawa, N. *et al.* Reevaluation of the efficacy and safety of the neutrophil elastase inhibitor, Sivelestat, for the treatment of acute lung injury associated with systemic inflammatory response syndrome; a phase IV study. *Pulm. Pharmacol. Ther.* **24**, 549–554 (2011).

177. Aikawa, N. & Kawasaki, Y. Clinical utility of the neutrophil elastase inhibitor sivelestat for the treatment of acute respiratory distress syndrome. *Ther. Clin. Risk Manag.* **10**, 621–629 (2014).

178. von Nussbaum, F. & Li, V. M.-J. Neutrophil elastase inhibitors for the treatment of (cardio) pulmonary diseases: Into clinical testing with pre-adaptive pharmacophores. *Bioorg. Med. Chem. Lett.* **25**, 4370–4381 (2015).

179. Mulchande, J. *et al.* 4-Oxo-β-lactams (azetidine-2,4-diones) are potent and selective inhibitors of human leukocyte elastase. *J. Med. Chem.* **53**, 241–253 (2010).

180. Hirche, T. O. *et al.* Neutrophil elastase mediates innate host protection against Pseudomonas aeruginosa. *J. Immunol.* **181**, 4945 (2008).

181. Young, R. E. *et al.* Neutrophil Elastase (NE)-Deficient Mice Demonstrate a Nonredundant Role

for NE in Neutrophil Migration, Generation of Proinflammatory Mediators, and Phagocytosis in Response to Zymosan Particles In Vivo. *J. Immunol.* **172**, 4493–4502 (2004).

182. Ferry, G., Lonchampt, M. & Pennel, L. and. Activation of MMP-9 by neutrophil elastase in an in vivo model of acute lung injury. *FEBS Lett.* **402**, 111–115 (1997).

183. Jackson, P. L. *et al.* Human neutrophil elastase-mediated cleavage sites of MMP-9 and TIMP-1: implications to cystic fibrosis proteolytic dysfunction. *Mol. Med.* **16**, 1 (2010).

184. Oltmanns, U., Sukkar, M. B., Xie, S., John, M. & Chung, K. F. Induction of human airway smooth muscle apoptosis by neutrophils and neutrophil elastase. *Am. J. Respir. Cell Mol. Biol.* **32**, 334–341 (2005).

185. Benabid, R. *et al.* Neutrophil elastase modulates cytokine expression: Contribution to host defense against pseudomonas aeruginosa-induced pneumonia. *J. Biol. Chem.* **287**, 34883–34894 (2012).

186. Shao, M. X. G. & Nadel, J. A. Neutrophil Elastase Induces MUC5AC Mucin Production in Human Airway Epithelial Cells via a Cascade Involving Protein Kinase C, Reactive Oxygen Species, and TNF- -Converting Enzyme. *J. Immunol.* **175**, 4009–4016 (2005).

187. Smallman, L. A., Hill, S. L. & Stockley, R. A. Reduction of ciliary beat frequency in vitro by sputum from patients with bronchiectasis: A serine proteinase effect. *Thorax* **39**, 663–667 (1984).

188. Wang, M. *et al.* Understanding Lung Deposition of Alpha-1 Antitrypsin in Acute Experimental Mouse Lung Injury Model Using Fluorescence Microscopy. *Int. J. Mol. Imaging* **2016**, 1–11 (2016).

189. Glinzer, A. *et al.* Targeting Elastase for Molecular Imaging of Early Atherosclerotic Lesions. *Arterioscler. Thromb. Vasc. Biol.* **37**, 525–533 (2017).

190. Talukdar, S. *et al.* Neutrophils mediate insulin resistance in mice fed a high-fat diet through secreted elastase. *Nat. Med.* **18**, 1407–1412 (2012).

191. Muley, M. M. *et al.* Neutrophil elastase induces inflammation and pain in mouse knee joints via activation of proteinase-activated receptor-2. *Br. J. Pharmacol.* **173**, 766–777 (2016).

192. Wiedow, O. & Meyer-Hoffert, U. Neutrophil serine proteases: Potential key regulators of cell signalling during inflammation. *J. Intern. Med.* **257**, 319–328 (2005).

193. Kasperkiewicz, P. *et al.* Design of ultrasensitive probes for human neutrophil elastase through hybrid combinatorial substrate library profiling. *Proc. Natl. Acad. Sci.* **111**, (2014).

194. Kasperkiewicz, P. *et al.* Determination of extended substrate specificity of the MALT1 as a strategy for the design of potent substrates and activity-based probes. *Sci. Rep.* **8**, 1–10 (2018).

195. Poreba, M. *et al.* Counter Selection Substrate Library Strategy for Developing Specific Protease Substrates and Probes. *Cell Chem. Biol.* **23**, 1023–1034 (2016).

196. Kasperkiewicz, P., Altman, Y., D'Angelo, M., Salvesen, G. S. & Drag, M. Toolbox of Fluorescent Probes for Parallel Imaging Reveals Uneven Location of Serine Proteases in Neutrophils. *J. Am. Chem. Soc.* **139**, 10115–10125 (2017).

197. Wu, L., Saxena, S., Awaji, M. & Singh, K. R. Tumor-Associated Neutrophils in Cancer: Going Pro. *Cancers (Basel).* **11**, (2019).

198. Macdonald, S. J. F. *et al.* Discovery of further pyrrolidine trans-lactams as inhibitors of human neutrophil elastase (HNE) with potential as development candidates and the crystal structure

of HNE complexed with an inhibitor (GW475151). *J. Med. Chem.* **45**, 3878–3890 (2002).

199. Fersht, A. *Structure and mechanism in protein science. A guide to enzyme catalysis and protein folding*. (W.H. Freeman and Company, 1999).

200. Sapey, E. & Stockley, R. A. Red, amber and green: the role of the lung in de-priming active systemic neutrophils. (2014).

201. Lu, H. *et al.* LFA-1 is sufficient in mediating neutrophil emigration in Mac-1-deficient mice. *J. Clin. Invest.* **99**, 1340–1350 (1997).

202. Campbell, E. J. & Campbell, M. A. Pericellular proteolysis by neutrophils in the presence of proteinase inhibitors: Effects of substrate opsonization. *J. Cell Biol.* **106**, 667–676 (1988).

203. Thomas, L. Reversible collapse of rabbit ears after intravenous papain, and prevention of recovery by cortisone. *J. Exp. Med.* **104**, 245–252 (1956).

204. Turino, G. M., Lourenco, R. V. & McCracken, G. H. Role of connective tissues in large pulmonary airways. *J. Appl. Physiol.* **25**, 645–653 (1968).

205. Senior, R. M. *et al.* The induction of pulmonary emphysema with human leukocyte elastase. *Am. Rev. Respir. Dis.* **126**, 469–475 (1977).

206. Gross, P., Pfitzer, E. A., Tolker, E., Babyak, M. A. & Kaschak, M. Experimental emphysema: its production with papain in normal and silicotic rats. *Arch. Environ. Heal. An Int. J.* **11**, 50–58 (1965).

207. Laurell, C.-B. & Eriksson, S. The electrophoretic α; 1-globulin pattern of serum in α; 1-antitrypsin deficiency. *Scand. J. Clin. Lab. Invest.* **15**, 132–140 (1963).

208. Luisetti, M. *et al.* MR889, a neutrophil elastase inhibitor, in patients with chronic obstructive pulmonary disease: a double-blind, randomized, placebo-controlled clinical trial. *Eur. Respir. J.* **9**, 1482–1486 (1996).

209. Vogelmeier, C., Aquino, T. O., O'Brien, C. D., Perrett, J. & Gunawardena, K. A. A randomised, placebo-controlled, dose-finding study of AZD9668, an oral inhibitor of neutrophil elastase, in patients with chronic obstructive pulmonary disease treated with tiotropium. *COPD J. Chronic Obstr. Pulm. Dis.* **9**, 111–120 (2012).

210. Chapman, K. R. *et al.* Intravenous augmentation treatment and lung density in severe α1 antitrypsin deficiency (RAPID): a randomised, double-blind, placebo-controlled trial. *Lancet* **386**, 360–368 (2015).

211. Bangalore, N. & Travis, J. Comparison of properties of membrane bound versus soluble forms of human leukocytic elastase and cathepsin G. *Biol. Chem. Hoppe. Seyler.* **375**, 659–666 (1994).

212. Owen, C. A., Campbell, M. A., Sannes, P. L., Boukedes, S. S. & Carolina, N. Cell Surface-bound Elastase and Cathepsin G on Human Neutrophils: A Novel, Non-Oxidative Mechanism by Which Neutrophils Focus and Preserve Catalytic Activity of Serine Proteinases. *J. Cell Biol.* **131**, 775–789 (1995).

213. Korkmaz, B., Attucci, S., Jourdan, M.-L. M.-L., Juliano, L. & Gauthier, F. Inhibition of Neutrophil Elastase by 1-Protease Inhibitor at the Surface of Human Polymorphonuclear Neutrophils. *J. Immunol.* **175**, 3329–3338 (2005).

214. Dwenger, A., Tost, P. & Holle, W. Evaluation of Elastase and α1-Proteinase Inhibitor-Elastase Uptake by Polymorphonuclear Leukocytes and Evidence of an Elastase-Specific Receptor. *Clin. Chem. Lab. Med.* **24**, 299–308 (1986).

215. Campbell, E. J. & Owen, C. A. The sulfate groups of chondroitin sulfate- and heparan sulfate-containing proteoglycans in neutrophil plasma membranes are novel binding sites for human leukocyte elastase and cathepsin G. *J. Biol. Chem.* **282**, 14645–14654 (2007).

216. Campbell, E. J. Human leukocyte elastase, cathepsin G, and lactoferrin: family of neutrophil granule glycoproteins that bind to an alveolar macrophage receptor. *Proc. Natl. Acad. Sci.* **79**, 6941–6945 (1982).

217. Kulkarni, S., Woollard, K. J., Thomas, S., Oxley, D. & Jackson, S. P. Conversion of platelets from a proaggregatory to a proinflammatory adhesive phenotype: role of PAF in spatially regulating neutrophil adhesion and spreading. *Blood* **110**, 1879–1886 (2007).

218. Klebanoff, S. J. *et al.* Effects of gamma-interferon on human neutrophils: protection from deterioration on storage. *Blood* **80**, 225–234 (1992).

219. Rosales, C. & Brown, E. Two mechanisms for IgG Fc-receptor-mediated phagocytosis by human neutrophils. *J. Immunol.* **146**, 3937–3944 (1991).

220. Melby, K., Midtvedt, T. & Degre, M. Effect of human leukocyte interferon on phagocytic activity of polymorphonuclear leukocytes. *Acta Pathol. Microbiol. Scand. Ser. B Microbiol.* **90**, 181–184 (1982).

221. Cassatella, M. A. *et al.* Interferon-gamma activates human neutrophil oxygen metabolism and exocytosis. *Immunology* **63**, 499 (1988).

222. N Aquino, E. *et al.* Proteomic analysis of neutrophil priming by PAF. *Protein Pept. Lett.* **23**, 142–151 (2016).

223. Humphreys, J. M., Hughes, V. & Edwards, S. W. Stimulation of protein synthesis in human neutrophils by γ-interferon. *Biochem. Pharmacol.* **38**, 1241–1246 (1989).

224. Shalit, M., Dabiri, G. A. & Southwick, F. S. Platelet-activating factor both stimulates and" primes" human polymorphonuclear leukocyte actin filament assembly. *Blood* **70**, 1921–1927 (1987).

225. Aas, V., Lappegard, K. T., Siebke, E. M. & Benestad, H. B. Modulation by interferons of human neutrophilic granulocyte migration. *J. Interf. cytokine Res.* **16**, 929–935 (1996).

226. Khreiss, T., József, L., Chan, J. S. D. & Filep, J. G. Activation of extracellular signal-regulated kinase couples platelet-activating factor-induced adhesion and delayed apoptosis of human neutrophils. *Cell. Signal.* **16**, 801–810 (2004).

227. Perussia, B., Kobayashi, M., Rossi, M. E., Anegon, I. & Trinchieri, G. Immune interferon enhances functional properties of human granulocytes: role of Fc receptors and effect of lymphotoxin, tumor necrosis factor, and granulocyte-macrophage colony-stimulating factor. *J. Immunol.* **138**, 765–774 (1987).

228. Kabanov, D. S. & Prokhorenko, I. R. Involvement of Toll-like receptor 4 and Fc receptors gamma in human neutrophil priming by endotoxins from Escherichia coli. *Biochem.* **78**, 185–193 (2013).

229. Rowley, A. F. & Nash, G. B. Adhesion-dependent release of elastase from human neutrophils in a novel, flow-based model: Specificity of different chemotactic agents. *Blood* **92**, 4819–4827 (1998).

230. Read, R. A., Moore, E. E., Moore, F. A., Carl, V. S. & Banerjee, A. Platelet-activating factor-induced polymorphonuclear neutrophil priming independent of CD11b adhesion. *Surgery* **114**, 308–313 (1993).

231. Knittel, J., Schnieder, L., Buess, G., Messerschmidt, B. & Possner, T. Endoscope-compatible

confocal microscope using a gradient index-lens system. *Opt. Commun.* **188**, 267–273 (2001).

232. Liang, C., Descour, M. R., Sung, K.-B. & Richards-Kortum, R. Fiber confocal reflectance microscope (FCRM) for in-vivo imaging. *Opt. Express* **9**, 821–830 (2001).

233. Delaney, P. M., Harris, M. R. & King, R. G. Fiber-optic laser scanning confocal microscope suitable for fluorescence imaging. *Appl. Opt.* **33**, 573–577 (1994).

234. Jabbour, J. M., Saldua, M. A., Bixler, J. N. & Maitland, K. C. Confocal endomicroscopy: instrumentation and medical applications. *Ann. Biomed. Eng.* **40**, 378–397 (2012).

235. Choudhary, T. R. *et al.* High fidelity fibre-based physiological sensing deep in tissue. *Sci. Rep.* **9**, 7713 (2019).

236. Gmitro, A. F. & Aziz, D. Confocal microscopy through a fiber-optic imaging bundle. *Opt. Lett.* **18**, 565–567 (1993).

237. Saleh, B. E. A. & Teich, M. C. *Fundamentals of photonics*. (John Wiley & Sons, 2019).

238. Yelin, D., Bouma, B. E., Yun, S. H. & Tearney, G. J. Double-clad fiber for endoscopy. *Opt. Lett.* **29**, 2408–2410 (2004).

239. Oh, G., Chung, E. & Yun, S. H. Optical fibers for high-resolution in vivo microendoscopic fluorescence imaging. *Opt. Fiber Technol.* **19**, 760–771 (2013).

240. Myaing, M. T. *et al.* Enhanced two-photon biosensing with double-clad photonic crystal fibers. *Opt. Lett.* **28**, 1224–1226 (2003).

241. Choi, Y. *et al.* Scanner-free and wide-field endoscopic imaging by using a single multimode optical fiber. *Phys. Rev. Lett.* **109**, 1–5 (2012).

242. Loterie, D. *et al.* Digital confocal microscopy through a multimode fiber. *Opt. Express* **23**, 23845 (2015).

243. Smilkov, D., Carter, S., Karpathy, A. & Olah, C. Tensor Flow Neural Network Playground. Available at: https://playground.tensorflow.org/#activation=tanh&batchSize=10&dataset=circle&regDataset=reg-plane&learningRate=0.03&regularizationRate=0&noise=0&networkShape=4,2&seed=0.81877&showTestData=false&discretize=false&percTrainData=50&x=true&y=true&xTimesY=fal.

244. Dürr, O. & Sick, B. Single-Cell Phenotype Classification Using Deep Convolutional Neural Networks. *J. Biomol. Screen.* **21**, 998–1003 (2016).

245. Krstajić, N., Mills, B., Murray, I. & Marshall, A. Low-cost high sensitivity pulsed endomicroscopy to visualize tricolor optical signatures. *J. Biomed. Opt.* **23**, 1 (2018).

246. Mori, H. *et al.* Introduction of zinc-salt fixation for effective detection of immune cell related markers by immunohistochemistry. **43**, 883–889 (2016).

247. Pierzchalski, A., Mittag, A. & Tárnok, A. *Recent Advances in Cytometry Part A: Instrumentation, Methods*. (Academic Press, 2011).

248. Furuno, T., Mitsuyama, T., Hidaka, K., Tanaka, T., & Hara, N. The Role of Neutrophil Elastase in Human Pulmonary Artery Endothelial Cell Injury. *Int. Arch. Allergy Immunol.* **122**, 262–269 (1997).

249. Younes, M., Brown, R. W., Stephenson, M., Gondo, M. & Cagle, P. T. Overexpression of Glut1 and Glut3 in stage I nonsmall cell lung carcinoma is associated with poor survival. *Cancer* **80**, 1046–1051 (1997).

250. Kose, K. *et al.* Automated video-mosaicking approach for confocal microscopic imaging in vivo: an approach to address challenges in imaging living tissue and extend field of view. *Sci. Rep.* **7**, 10759 (2017).

251. Mercier, J. & Voutsadakis, I. A. The platelets-neutrophils to lymphocytes ratio: a new prognostic marker in metastatic colorectal cancer. *J. Gastrointest. Oncol.* **9**, 478–486 (2018).

252. Bressenot, A. *et al.* Comparing histological activity indexes in UC. *Gut* **64**, 1412–1418 (2015).

253. Fu, Z., Thorpe, M., Akula, S., Chahal, G. & Hellman, L. T. Extended Cleavage Specificity of Human Neutrophil Elastase, Human Proteinase 3, and Their Distant Ortholog Clawed Frog PR3—Three Elastases With Similar Primary but Different Extended Specificities and Stability . *Frontiers in Immunology* **9**, 2387 (2018).

254. Dau, T., Sarker, R. S. J., Yildirim, A. O., Eickelberg, O. & Jenne, D. E. Autoprocessing of neutrophil elastase near its active site reduces the efficiency of natural and synthetic elastase inhibitors. *Nat. Commun.* **6**, 1–8 (2015).

255. Guyot, N. *et al.* Elafin, an elastase-specific inhibitor, is cleaved by its cognate enzyme neutrophil elastase in sputum from individuals with cystic fibrosis. *J. Biol. Chem.* **283**, 32377–32385 (2008).

256. Weldon, S. *et al.* Decreased levels of secretory leucoprotease inhibitor in the Pseudomonas-infected cystic fibrosis lung are due to neutrophil elastase degradation. *J. Immunol.* **183**, 8148–8156 (2009).

257. Banda, B. M. J., Rice, A. G., Griffin, G. L. & Senior, R. M. The inhibitory complex of human alpha 1-proteinase inhibitor and human leukocyte elastase is a neutrophil chemoattractant. **167**, (1988).

258. Jackson, P.L., Xu, X., Wilson, L., Weathington, N.M., Clancy, J.P., Blalock, J.E. and Gaggar, A. Human neutrophil elastase-mediated cleavage sites of MMP-9 and TIMP-1: implications to cystic fibrosis proteolytic dysfunction. *Mol. Med.* **16**, 1 (2010).

259. Shapiro, S. D. *et al.* Neutrophil elastase contributes to cigarette smoke-induced emphysema in mice. *Am. J. Pathol.* **163**, 2329–35 (2003).

260. Geraghty, P. *et al.* Neutrophil elastase up-regulates cathepsin B and matrix metalloprotease-2 expression. *J. Immunol.* **178**, 5871–5878 (2007).

261. Eckle, I., Kolb, G., Heiser, C. & Havemann, K. Stimulation of neutrophil elastase and myeloperoxidase release by IgG fragments. *Clin. Exp. Immunol.* **81**, 352–356 (1990).

262. Döring, G. *et al.* Elastase from polymorphonuclear leucocytes: a regulatory enzyme in immune complex disease. *Clin. Exp. Immunol.* **64**, 597–605 (1986).

263. Prince, H. E., Folds, J. D., Modrzakowski, M. C. & Spitznagel, J. K. A comparative analysis of human IgM rheumatoid factor degradation by purified elastase and total granule extracts from human polymorphonuclear leukocytes. *Inflammation* **4**, 27–35 (1980).

264. Le-Barillec, K., Si-Tahar, M., Balloy, V. & Chignard, M. Proteolysis of monocyte CD14 by human leukocyte elastase inhibits lipopolysaccharide-mediated cell activation. *J. Clin. Invest.* **103**, 1039–1046 (1999).

265. Nemoto, E. *et al.* Cleavage of CD14 on human gingival fibroblasts cocultured with activated neutrophils is mediated by human leukocyte elastase resulting in down-regulation of lipopolysaccharide-induced IL-8 production. *J. Immunol.* **165**, 5807–5813 (2000).

266. Remold-O'Donnell, E. & Parent, D. Specific sensitivity of CD43 to neutrophil elastase. *Blood* **86**, 2395–2402 (1995).

267. Champagne, B., Tremblay, P., Cantin, A. & Pierre, Y. S. Proteolytic cleavage of ICAM-1 by human neutrophil elastase. *J. Immunol.* **161**, 6398–6405 (1998).

268. Fischer, B. M. & Voynow, J. A. Neutrophil elastase induces MUC 5AC gene expression in airway epithelium via a pathway involving reactive oxygen species. *Am. J. Respir. Cell Mol. Biol.* **26**, 447–452 (2002).

269. Domon, H. *et al.* Neutrophil Elastase Subverts the Immune Response by Cleaving Toll-Like Receptors and Cytokines in Pneumococcal Pneumonia . *Frontiers in Immunology* **9**, 732 (2018).

270. Bank, U. *et al.* Selective proteolytic cleavage of IL-2 receptor and IL-6 receptor ligand binding chains by neutrophil-derived serine proteases at foci of inflammation. *J. Interf. cytokine Res.* **19**, 1277–1287 (1999).

271. Boxio, R. *et al.* Neutrophil elastase cleaves epithelial cadherin in acutely injured lung epithelium. *Respir. Res.* **17**, 129 (2016).

272. Lane, A. A. & Ley, T. J. Neutrophil elastase cleaves PML-RARα and is important for the development of acute promyelocytic leukemia in mice. *Cell* **115**, 305–318 (2003).

273. López-Boado, Y. S., Espinola, M., Bahr, S. & Belaaouaj, A. Neutrophil Serine Proteinases Cleave Bacterial Flagellin, Abrogating Its Host Response-Inducing Activity. *J. Immunol.* **172**, 509–515 (2004).

274. Kurtagic, E., Jedrychowski, M. P. & Nugent, M. A. Neutrophil elastase cleaves VEGF to generate a VEGF fragment with altered activity. *Am. J. Physiol. Lung Cell. Mol. Physiol.* **296**, L534–L546 (2009).

275. Brower, M. S., Walz, D. A. & Garry, K. E. Human neutrophil elastase alters human alpha-thrombin function: limited proteolysis near the gamma-cleavage site results in decreased fibrinogen clotting and platelet-stimulatory activity. *Blood* **69**, 813–819 (1987).

276. Jochum, M., LANDER, S., HEIMBURGER, N. & Fritz, H. Effect of human granulocytic elastase on isolated human antithrombin III. *Hoppe-Seyler´ s Zeitschrift für Physiol. Chemie* **362**, 103–112 (1981).

277. Polacek, D., Byrne, R. E., Fless, G. M. & Scanu, A. M. In vitro proteolysis of human plasma low density lipoproteins by an elastase released from human blood polymorphonuclear cells. *J. Biol. Chem.* **261**, 2057–2063 (1986).

278. DiMartino, S. J., Shah, A. B., Trujillo, G. & Kew, R. R. Elastase controls the binding of the vitamin D-binding protein (Gc-globulin) to neutrophils: a potential role in the regulation of C5a co-chemotactic activity. *J. Immunol.* **166**, 2688–2694 (2001).

279. Tosi, M. F., Zakem, H. & Berger, M. Neutrophil elastase cleaves C3bi on opsonized pseudomonas as well as CR1 on neutrophils to create a functionally important opsonin receptor mismatch. *J. Clin. Invest.* **86**, 300–308 (1990).